# EXPERIMENTAL STUDIES ON SHOCK BOUNDARY LAYER INTERACTIONS USING MICRO-RAMPS AT MACH 5

A report submitted to the University of Manchester for
the degree of Doctor of Philosophy
in the Faculty of Engineering and Physical Sciences

2013

By
Mohd R. Saad
School of Mechanical Aerospace & Civil Engineering

# Contents

# List of Tables

# List of Figures

# Abstract

Shock boundary layer interactions (SBLI) is an undesirable event occurring in high-speed air-breathing propulsion system that stimulates boundary layer separation due to adverse pressure gradients and consequently lead to flow distortion and pressure loss in the intake section. Therefore it is essential to apply flow control mechanisms to prevent this phenomenon. This study involves a novel flow control device called micro-ramp, which is a part of the micro-vortex generator family that has shown great potential in solving the adverse phenomenon. The term micro refers to the height of the device, which is smaller than the boundary layer thickness, $\delta$.

It is important to highlight the two main novelties of this investigation. Firstly, it is the first micro-ramp study conducted in the hypersonic flow regime (Mach 5) since most of the previous micro-ramp studies were only performed in subsonic, transonic and supersonic flows. Another novelty is the various experimental techniques that were used in single study for example schlieren photography, oil-dot and oil-flow visualisation and conventional pressure transducers. In addition, advanced flow diagnostic tools such as infrared thermography, pressure-sensitive paints (PSP) and particle image velocimetry (PIV) were also employed.

The flow characteristics of the micro-ramp at Mach 5 were investigated in detail using various experimental techniques. The use of both qualitative and quantitave measurements enable the visualisation of detail flow structures occurring in both upstream and downstream region of the micro-ramp. Detail information such as the structure of the primary and secondary vortices, direction of primary vortices, high and low temperature and pressure regions around the micro-ramp and also the formation of the Kelvin-Helmholtz vortices.

The role of micro-ramp in controlling SBLI was also investigated. A shock-generator was installed to create an incident shock that impinged on the boundary layer at a specified distance downstream the micro-ramp. The improvement of the

SBLI condition was observed based on a number of criteria and recorded by the various flow diagnostic tools used. The detail topology of the separation region which comprises of the separation line, reversed flow region and reattachment region were also clearly visualised using oil-flow and PSP.

The final investigation was the optimisation studies of the micro-ramp at Mach 5. Using the RSM approximation technique, a series of experiments were performed. From the results, the optimal configuration of the micro-ramp that involved three variables; height, spanwise spacing and chord length for Mach 5 was obtained. The ratios between the three variables were also calculated. The relation between the three variables with respect to the SBLI improvement were discovered and discussed.

# Declaration

No portion of the work referred to in this report has been submitted in support of an application for another degree or qualification of this or any other university or other institute of learning.

# Copyright

i. The author of this report (including any appendices and/or schedules to this thesis) owns any copyright in it (the "Copyright") and s/he has given The University of Manchester the right to use such Copyright for any administrative, promotional, educational and/or teaching purposes.

ii. Copies of this report, either in full or in extracts, may be made only in accordance with the regulations of the John Rylands University Library of Manchester. Details of these regulations may be obtained from the Librarian. This page must form part of any such copies made.

iii. The ownership of any patents, designs, trade marks and any and all other intellectual property rights except for the Copyright (the "Intellectual Property Rights") and any reproductions of copyright works, for example graphs and tables ("Reproductions"), which may be described in this thesis, may not be owned by the author and may be owned by third parties. Such Intellectual Property Rights and Reproductions cannot and must not be made available for use without the prior written permission of the owner(s) of the relevant Intellectual Property Rights and/or Reproductions.

iv. Further information on the conditions under which disclosure, publication and exploitation of this report, the Copyright and any Intellectual Property Rights and/or Reproductions described in it may take place is available from the Head of dept (or the Vice-President).

# Acknowledgements

I would like to take this opportunity to thank my supervisor Professor K. Kontis for his encouragement, inspiration and guidance throughout the duration of my studies. Besides all the technical and fundamental flow physics guidance, he has also instill the importance of efficient task planning and creativity in me.

My special thanks goes to my friends and my collegues during these years in the Aero-Physics Laboratory; especially Mr. Azam Che Idris (soon to be Dr.), who has spent a lot of his time with me in the laboratory, Dr. Hossein Zare-Behtash, Dr. Erinc Erdem, Dr. Leichao Yang, Dr. Nalleli Gongora-Orozco, Dr. Rasool Erfani, Dr. Tohid Erfani, Dr. Mark Quinn, Mr. Eric K.H. Lo, etc. for all their technical help and guidance.

I would also like to acknowledge the help and support of all the technical and administrative staff of the school of MACE of the University of Manchester, especially Mr. Michael Carroll, Mr. David Golding and Mr. Lee Paul.

I am thankful to the Ministry of Higher Education of Malaysia and Universiti Pertahanan Nasional Malaysia for their full financial support along the whole period of my studies.

I am indebted to my fellow brothers in Manchester; Shahrir, Baharin, Haidir, Sufian, Shahrin and Suriyadi, for the never-ending support and advice during the hard-times. Also to the big IKRAM UK & Eire family for all the help and encouragement.

Last but not least my deepest gratitude goes to the love and meaning of my life; my wife, Durar and my little princess, Aaliyah. Without their patience, understanding and kind motivations, this PhD would not be a dream come true. Also to both of my parents, Saad and Zuraini and my brother, Harith for the continuous help and prayers.

Thank you to everyone who at some point has contributed any means of support during the course of my PhD. I am forever in your debt.

# List of Publications

## Journal Publications

1. M.R. Saad, H. Zare-Behtash, A. Che Idris, and K. Kontis. Micro-Ramps for Hypersonic Flow Control. *Micromachines* 3, 364-378, 2012.

## Conference Publications

1. M.R. Saad, A. Che Idris, K.H. Lo and K. Kontis. Micro-Ramps Flow Characteristics at Mach 1.9 & 5. In *Proceedings of the 29th International Symposium on Shock Waves*, Madison, WI, USA, 14-19 July 2013, 2013.

2. A. Che Idris, M.R. Saad, H. Zare-Behtash, and K. Kontis. Experimental and Computational Study of Flow Interactions in a Generic Scramjet Inlet-isolator. In *Proceedings of the 29th International Symposium on Shock Waves*, Madison, WI, USA, 14-19 July 2013, 2013.

3. M.R. Saad, A. Che Idris, and K. Kontis. Experimental Studies on Micro-Vortex Generators in Hypersonic Flow. In *Proceedings of the 28th Congress of the International Council of the Aeronautical Sciences*, Brisbane Australia, 23-28 September 2012. ICAS 2012-3.5.2. 2012.

4. A. Che Idris, M.R. Saad, H. Zare-Behtash and K. Kontis. Performance Analysis of a Scramjet Inlet-Isolator using Experimental & Numerical Methods. In *Proceedings of the 28th Congress of the International Council of the Aeronautical Sciences*, Brisbane Australia, 23-28 September 2012. ICAS 2012-P4.12. 2012.

5. M.R. Saad, A. Che Idris, H. Zare-Behtash, and K. Kontis. Micro-Ramps in Mach 5 Hypersonic Flow. In *Proceedings of the 50th AIAA Aerospace*

*Sciences Meeting including the New Horizons Forum and Aerospace Exposition*, Nashville, TN, USA, 9-12 January 2012. AIAA 2012-0676, 2012.

6. M.R. Saad, E. Erdem, L. Yang, and K. Kontis. Experimental Studies on Micro-Ramps in Mach 5. In *Proceedings of the 28th International Symposium on Shock Waves*, Manchester, UK, 17-22 July 2011, 2011.

# Nomenclature

## Roman Symbols

| | |
|---|---|
| $Ap$ | micro-ramp angle of incidence [degrees] |
| $A_{sec}$ | area of nozzle exit [$m^2$] |
| $c$ | chord length [m] |
| $c_f$ | skin-friction coefficient |
| $c_m$ | thermal heat capacity of material [kJ/kg.K] |
| $c_p$ | specific heat capacity of air at constant pressure [kJ/kg.K] |
| $d$ | vortex diameter [m] |
| $d_m$ | diameter of model [m] |
| $d_m$ | wall thickness of material [m] |
| $d_p$ | diameter of particle [m] |
| $h$ | height of micro-ramp [m] |
| $h_s$ | vertical distance from shock generator to plate [m] |
| $H$ | incompressible shape factor |
| $M_\infty$ | freestream Mach number |
| $p$ | static pressure [bar] |
| $p_0$ | stagnation pressure [bar] |
| $p_{pitot}$ | pressure measured by pitot tube [bar] |
| $P$ | nozzle exit perimeter [m] |
| $\dot{q}$ | local heat flux rate [$w/m^2$] |
| $r$ | distance travelled by seeder particle [m] |
| $Re$ | Reynolds number |
| $Re_{\delta 0}$ | local Reynolds number |
| $St$ | Stanton number |
| $T_0$ | stagnation temperature [K] |
| $T_w$ | wall temperature measured by IR camera [K] |

| | |
|---|---|
| $u$ | streamwise velocity component [m/s] |
| $u_e$ | boundary layer edge velocity [m/s] |
| $u_{ref}$ | reference velocity [m/s] |
| $v$ | velocity component [m/s] |
| $v_y$ | wall normal velocity [m/s] |
| $v_z$ | spanwise velocity [m/s] |
| $W$ | mass flow [kg/s] |
| $X_c$ | spanwise centre of flat plate [m] |
| $X_L$ | streamwise distance from centre of micro-ramp to shock impingement [m] |
| $X_s$ | streamwise distance from plate leading-edge to shock impingement location [m] |
| $X_{SG}$ | streamwise distance from leading edge to shock generator [m] |
| $X_p$ | upstream location of inviscid shock impingement point [m] |
| $y$ | transverse coordinate |
| $z$ | spanwise coordinate |

## Greek Symbols

| | |
|---|---|
| $\beta$ | blockage ratio |
| $\gamma$ | specific heat ratio |
| $\delta$ | boundary layer thickness [m] |
| $\delta_0$ | boundary layer thickness at location of model [m] |
| $\delta^*$ | boundary layer displacement thickness [m] |
| $\theta$ | boundary layer momentum thickness [m] |
| $\mu$ | Mach angle [degrees], dynamic viscosity of fluid [Pa.s] |
| $\rho_m$ | material density [kg/m$^3$] |
| $\rho_\infty$ | density of freestream fluid [kg/m$^3$] |
| $\rho$ | density [kg/m$^3$] |
| $\rho_p$ | density of seeding particle [kg/m$^3$] |
| $\tau$ | time constant |
| $\tau_s$ | relaxation time of seeding particle [s] |
| $\varphi$ | flow deflection angle [degrees] |
| $\omega_x$ | streamwise vorticity [s$^{-1}$] |
| $\omega_y$ | vertical vorticity [s$^{-1}$] |
| $\omega_z$ | spanwise vorticity [s$^{-1}$] |

## Subscripts

| | |
|---|---|
| $bleed$ | bleed system |
| $max$ | maximum |
| $ref$ | reference |
| $rel$ | relative |
| $shk$ | shock impingement location |
| $supply$ | supply upstream |
| $vac$ | vacuum |
| $w$ | wall |

## Acronyms

| | |
|---|---|
| FoV | Field of View |
| HSST | High Supersonic Tunnel |
| IR | Infra-Red |
| MVG | Micro-Vortex Generator |
| PIV | Particle Image Velocimetry |
| POI | Point of Interaction |
| PSP | Pressure Sensitive Paints |
| RMS | Root Mean Square |
| RSM | Response Surface Methodology |
| SBLI | Shock Boundary Layer Interaction |
| VG | Vortex Generator |

# Chapter 1

# Introduction

## 1.1 Background

Hypersonic flight in air space is currently under the spotlight of both the military and commercial sector. However the prominent issue facing hypersonic flights is the engine limitations due to the occurrence of the shock-wave/boundary layer interactions (SBLIs) in the supersonic portion of the flow inside the supersonic engine inlets. The interactions are caused by a number of oblique and normal shock waves interacting with the boundary layer of the inlet flow consequently causing boundary layer separation and unsteady flow due to severe adverse pressure gradients.

Currently the problem of SBLIs is treated by the use of boundary layer bleed system that involves the removal of certain amount of mass of the inlet flow. The use of this system on the other hand is accompanied by several drawbacks that are undesirable for engine performance. The purpose of this study is to investigate the use of a novel type of flow control called micro-ramp which is a part of the micro-vortex generator family which is able to replace the conventional bleed system and at the same time offers similar benefits in suppressing the SBLIs as well as improving the boundary layer health at the engine intake.

### 1.1.1 Shock Boundary Layer Interactions

Shock boundary layer interactions (SBLI) is a phenomenon when a shock wave meets a boundary layer and it can be found in most of the high-speed flows. The typical case of SBLI is when a generated shock wave impinges onto a surface where the boundary layer is developing. As a result, the shock imposes a severe adverse pressure gradient towards the boundary layer causing it to eventually thicken and creates the possibility of separation. In most cases, SBLI also causes flow unsteadiness. The consequences of the phenomena are found to be detrimental especially in high speed flows. In hypersonic flows, SBLI causes intense localised heating due to high Mach numbers that can be severe enough to destroy the body of the aero-vehicle.

### 1.1.2 Micro-Ramp

The micro-ramp is a novel flow control device that is a part of the micro-vortex generator family. It has recently shown great potential in controlling the adverse phenomena. The term micro relates to the device having the height less than the boundary layer thickness, $\delta$. In most present literatures, the height range of the micro-ramp is between 30% to 90% of $\delta$. Due to the small size, the micro-ramp is embedded inside the boundary layer hence reducing the parasitic drag compared to the conventional full size vortex generator. Further advantages from the other SBLI flow control mechanisms are it is physically robust, independent of power source and also cost effective.

## 1.2 Aims & Objectives

The ultimate objective of this research is to experimentally investigate the performance of micro-ramps in controlling the SBLIs-induced separation. The main elements of the investigation are as the followings:

a. To understand the flow characteristics of the micro-ramps at specific locations such as at the leading edge, over the ramp surface, at the sides, at the rear of trailing edge and finally at the downstream region.

b. To investigate the capabilities of the micro-ramp in controlling the flow separation induced by SBLI.

c. To determine the optimal design of the micro-ramp geometries that would lead to the best improvement of the boundary layer that encountered SBLI in Mach 5 flow.

## 1.3 Report Outline

Following the introduction chapter, this thesis is divided into:

*Chapter 2* presents the background understanding on SBLIs and an extensive review on the previous studies involving micro-ramps.

*Chapter 3* provides information on the experimental facilities, the models manufactured for the present study and also the experimental techniques used in the investigations.

*Chapter 4* presents the detail findings on the flow characteristics of the micro-ramp in Mach 5 flow.

*Chapter 5* presents the results on the performance of micro-ramps in controlling SBLI using different experimental techniques.

*Chapter 6* presents the results of the micro-ramp optimisation investigation, in search of the optimal configuration of the micro-ramp design.

*Chapter 7* concludes the overall findings of the present study including the recommendation of future work.

# Chapter 2

# Literature Review

## 2.1 Shock Boundary-Layer Interactions

Before reviewing the history and evolution of the micro-vortex generators (MVG), it is best to have a clear understanding on shock boundary-layer interactions (SBLI) so that later on, the importance of MVG will be more appreciated.

SBLIs are one of the fluid dynamics phenomena that are significant to the development of the hypersonic knowledge at this age. SBLIs are prevalent in many supersonic and hypersonic applications such as supersonic and hypersonic inlets, missiles and aircraft after bodies, etc. The effects caused by SBLI are severe therefore large portions of effort are being spent in understanding the physics of the phenomena and the methods that can be applied to overcome SBLI.

### 2.1.1 SBLI: Why is it so harmful?

Let us begin by highlighting a number of events written in history that were troubled by SBLI. The U.S. Space Shuttle program that spanned its operation from 1981 to 2011 encountered two major problems during its early stage and interestingly, both of them were related to SBLI [1]. The first problem was called Shuttle Flap Anomaly and it almost caused a catastrophic failure during the space shuttle's maiden flight. A significantly larger flap deflection was needed to stabilize the shuttle than the calculated value that was determined from the ground tests. Luckily necessary control took place and the disaster was successfully avoided. Engineers came to the conclusion that the problem was caused by the failure to take into account the influence of real-gas effects on the SBLI regions since the

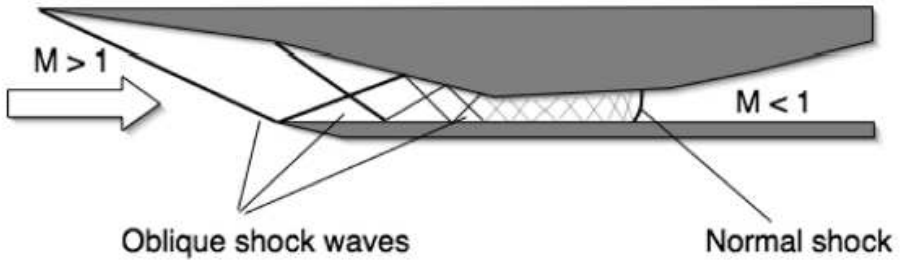


Figure 2.1: Shock wave/boundary layer interaction in mixed compression inlet [3]

ground tests were conducted in cold-flow facilities. The second problem was the structural failure of the leading-edge. The dynamic loads induced by the SBLI fractured the foam from the shuttle tank and impacted on the leading-edge. The strong dynamics loads were not predicted in the design phase and this shows that the effects of SBLI were underestimated in the early years. Another classic case is the X-15 hypersonic airplane vehicle in 1960. Due to the severe aerodynamic heating caused by shock-wave impingements on the vehicle's body, holes were burned on its pylon surface and through the vehicle's body [2].

The design of mixed compression inlets in the engine intakes in Figure 2.1 proves to enhance the performance of the propulsion system compared to the conventional pitot intake. However the generation of the shock train that travels internally towards the nozzle creates a number of issues. When the shock train reflects off the inlet walls, it interacts with the developing boundary layer and causes SBLI effects. The interactions induce adverse pressure gradients that results in boundary layer separation at several locations downstream the inlet. The thickening of the boundary layer due to the separation decreases the effective throat area and could lead to inlet unstart. Another contributing factor to the inlet unstart is the flow distortion and unsteadiness which translates to large oscillating structural loads that could also result in structural fatigue. Hence the SBLIs effects in mixed compression inlet affect not only the propulsion system but also endanger the structural strength of any aero-vehicle.

Another important location that SBLIs are occurring is in the vicinity of deflected control surfaces that are used for controlling and manoeuvring hypersonic flights such as re-entry space plane and guided missiles. As an example during re-entry the vehicle will experience very low density flow. Hence high flap angles are needed to produce the required control forces on the incoming flow. As a result of the high flap angles, flow separation will occur upstream of the control

surface due to the high adverse pressure gradients followed by generation of complex shock-wave structures. The separation region reduces the effective area of the flap, consequently minimising the manoeuvrability of the vehicle. The generated shock-waves that impinge on the vehicle's body will also increase the local heating rates. Another problem is the flow separation and unsteadiness also contribute to the rise in aerodynamic drag. When all of these effects combine with the fluctuating pressure loads, the result is severe enough to cause premature structural fatigue for hypersonic vehicles [4].

It would be unfair to disregard the positive effects that SBLI offers [1]. As an example, the fuel-air mixing are enhanced due to the increase in turbulence fluctuation level in scramjet combustion chambers. However, since the negative consequences by far exceeded the positive outcomes, SBLIs are therefore undesirable and can be considered as a threat to many other technological applications of fluid dynamics from performance of transonic inlets and diffusers to airfoil aerodynamic properties. This explains why such a huge amount of effort on research is being spent to avoid them or at least suppress the effects.

### 2.1.2 Types of SBLI in Two-Dimensional Flows

There are four basic interactions between a shock wave and a boundary layer flow as compiled by Delery and Dussauge [5]; oblique shock wave impinging on a flat plate accompanied by reflection shock waves, shock-induced compression ramp flow, normal shock in downstream choking case and pressure jump interface such as at nozzle exits. The Schlieren images of all the interactions are shown in Figure 2.2.

1. For the case on an oblique shock reflection on a flat surface (Figure 2.2a), the incoming supersonic flow faces a deflection at an angle after passing the incident shock. To ensure the downstream flow remain parallel to the wall, a reflected shock is formed all the way from the wall surface. These shock patterns are normally found inside a supersonic air-intake of the mixed-compression type as shown in Figure 2.1 previously.

2. Figure 2.2b shows the ramp flow case. The approaching flow encounters the change in wall inclination causing it to undergo a deflection at an angle which is the same as the wedge angle. This type of shocks are normally found in a supersonic air-intake compression ramp, on the external control

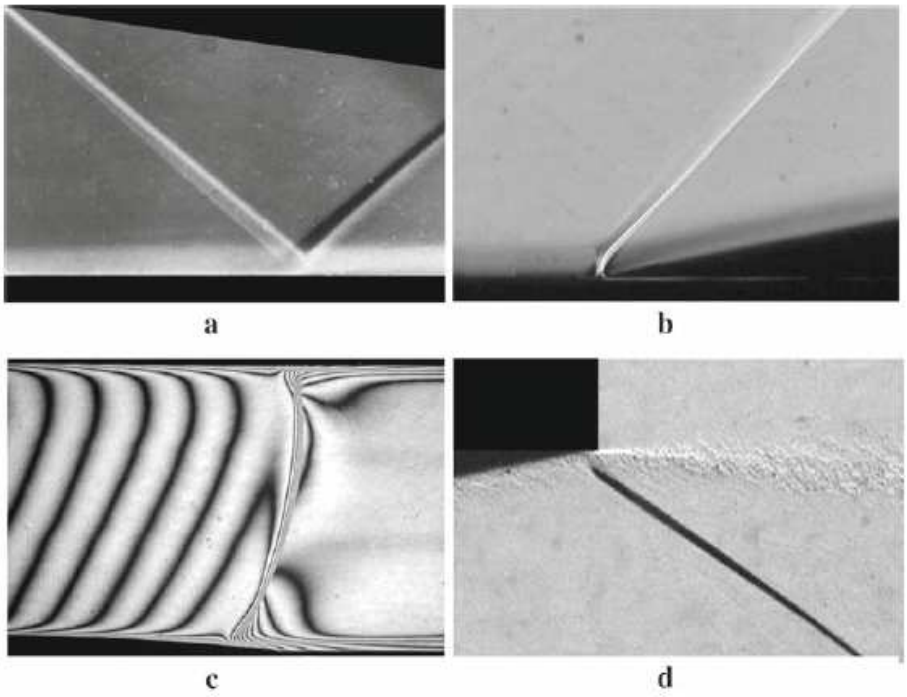


Figure 2.2: Basic shock-wave/boundary layer interactions images from Onera documents. (a) Oblique shock reflection (b) Ramp induced shock-wave (c) Normal shock wave (d) Adaptation shock at nozzle exit. [5]

surface of high-speed vehicles or possibly at any surfaces that promotes sharp change in the flow direction.

3. The third case is the normal shock created in the channel flow with two-throat system (Figure 2.2c). When a supersonic flow is forced to become subsonic by forcing back pressure, a normal shock is produced. The difference compared to the other cases is the normal shock decelerates the flow without causing any changes to the direction of the flow while achieving subsonic Mach number behind it. Normal shocks are usually found in turbomachine cascades, supersonic diffusers, shock tubes and also in air intakes.

4. The final case is the phenomenon occurring at the exit of an overexpanded nozzle. When a supersonic flow encounters a change in geometry, which in this case is the geometry of the nozzle, a change in pressure takes place and an oblique shock wave is produced as the result as illustrated in Figure 2.2d.

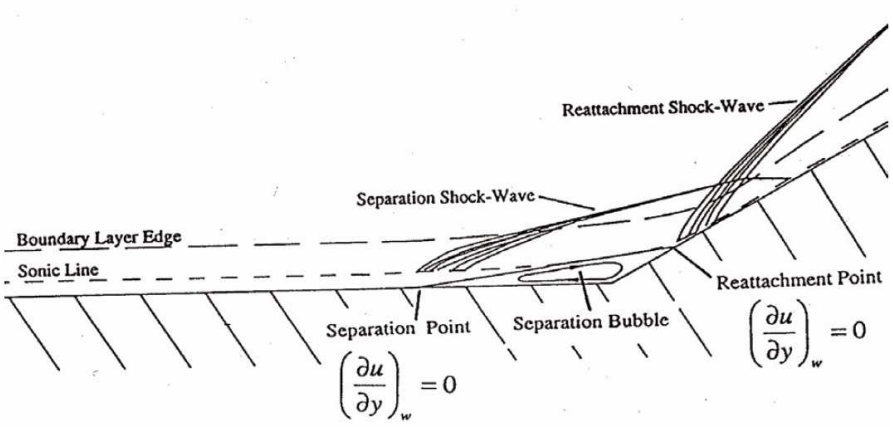


Figure 2.3: Schematic of shock-wave/boundary layer interaction at hypersonic compression ramp [6].

However only the first two cases will be covered in detail in the following subsections of this report and only the impinging shock case of SBLI will be investigated in the experiments due to the nature of facilities that are available.

### 2.1.3 Flow over a Compression Ramp

In the inviscid case of a flow over a compression ramp, a single shock discontinuity is formed at the corner of the ramp. However it is not the same case for viscous flow. Prince et al. [6] provide an extensive explanation on this topic. The developing boundary layer along the flat plate will be aware of the sudden change of its direction due to the existence of the ramp and pressure waves will be fed upstream through the subsonic portion of the boundary layer. This will give rise to the pressure upstream of the compression corner.

When the ramp is deflected at a small angle, the weak shock wave extends into the supersonic region of the boundary layer and subsequently curving down towards the surface because of the variation of Mach number. As a result the subsonic layer faces a continuous increase in pressure and causes the thickening of the boundary layer at the near-corner region. The incoming flow eventually faces an obstruction and starts deflecting away from the surface. In turn, this generates compression waves which coalesce to form the outer 'inviscid' shock wave.

As the ramp angle is increased, the compression shock becomes stronger and imposes higher pressure on the subsonic layer. The incoming boundary layer faces

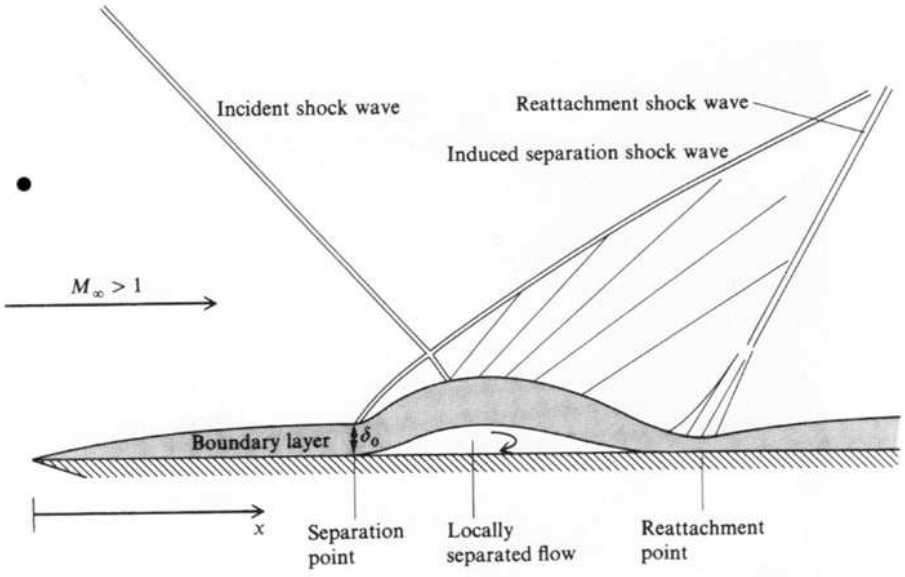


Figure 2.4: Basic schematic of the shock-wave/boundary layer interaction by Anderson [2].

a higher pressure gradient and up to a point where it can no longer overcome this, separation region is formed and this is shown in Figure 2.3 hence changing the whole structure drastically. Separation and reattachment points can be observed at locations before and after the corner.

When the ramp angle is further increased, the flow will become more separated and the recirculation bubble is formed. This is followed by the generation of compression fans upstream the hinge line and the reattachment compression fans due to the behaviour of the shear layer that starts to turn parallel to the ramp surface exactly after the reattachment point. The compression fan upstream coalesces and form the separation shock wave and this is usually observed as the equivalent 'inviscid' oblique shock wave.

### 2.1.4 Oblique Shock Wave Impinging on a Flat Plate

The generic case of an oblique shock wave impinging on a flat plate is represented by Figure 2.4. It is the case of shock impingement on a flat plate in a flow more than Mach 1. Starting from the flat plate leading edge, the boundary layer develops and becomes thicker. An incident shock-wave impinges on the boundary layer at some downstream location from the leading edge. The impingement of the shock wave causes a large pressure difference across it hence induces the boundary

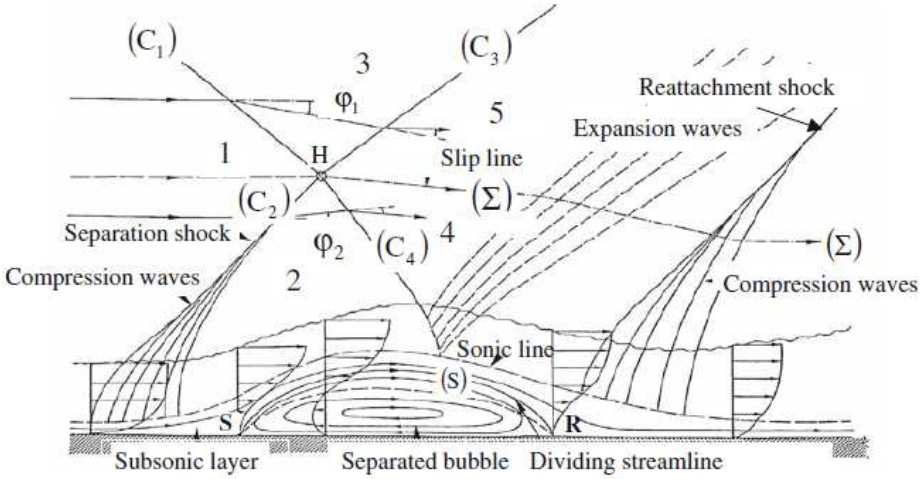


Figure 2.5: Sketch of boundary layer separation induced by oblique shock reflection [5]

layer to separate due to the consequent effect of severe adverse pressure gradient. The separation point of the boundary layer occurs slightly upstream from the shock impingement point. This is because the high pressure developed behind the shock, feeds upstream through the subsonic region of the boundary layer and perturbates the incoming flow hence causing separation.

Another shock wave is being induced by the separated boundary layer and labelled induced separation shock wave in Figure 2.4. As the separated boundary layer recovers and reattaching to the surface of the flat plate, another shock-wave is induced downstream of the separation region and called reattachment shock. The process of the boundary layer reattaching to the plate also produces expansion waves in between the induced separation shock wave and reattachment shock wave. A region of high local aerodynamic heating exists at the reattachment point since the boundary layer has become relatively thin compared to its upstream thickness and at the same time the pressure increase is rapid.

### 2.1.5 Boundary Layer Separation

Figure 2.5 shows the detail structure of the flow. The separation point is denoted by **S** and at its further downstream exists a recirculating 'bubble'. This area is bounded by a layer called dividing streamline ($S$) that separates the recirculating region from the incoming flow. The dividing streamline originates from point **S** and finishes at the reattachment point labelled **R**. Strong mixing takes place in

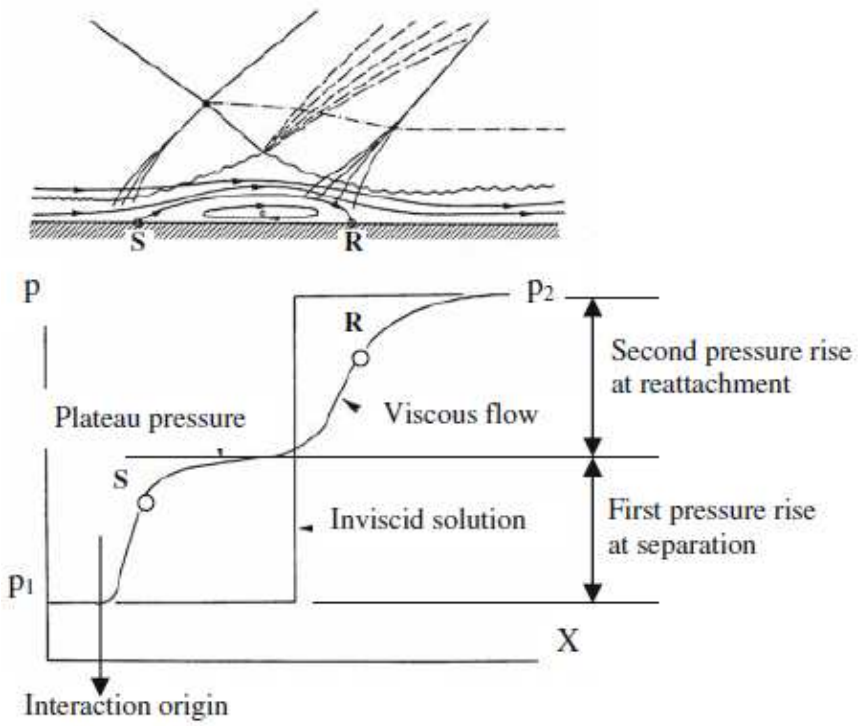


Figure 2.6: Wall pressure distribution in the case of shock reflection inducing separated flow [5]

the detached shear layer emanating from **S** and causes mechanical energy transfer to occur from outer high-speed flows into the separated region. As a result the velocity $U_D$ on the dividing streamline ($S$) increases gradually until it approaches the reattachment point (**R**) where deceleration starts.

The transmitted shock ($C_4$) which originates from the incident shock ($C_1$) penetrates into the separation region and is being reflected as an expansion wave because there is near constant pressure within the bubble. This causes the shear layer to move back against the wall after it started to deflect at **S** and finally reattaches at **R**. Following the reattachment process, a series of compression waves are generated which then coalesce to form the reattachment shock. Referring to Figure 2.6, the pressure increases dramatically until the separation point **S** and remains constant for a limited distance, indicating the separation region. Then it increases further, up to point **R** due to the reattachment process and continues to rise until reaching the value of pressure jump in the inviscid case. The pressure behaviour observed seems to differ from the purely inviscid case and therefore it is said to be a *strong viscous interaction* meaning that the effect of viscosity needs to be taken fully into account when predicting this type of flow.

### 2.1.6 SBLI Control Mechanisms

It seems almost impossible to avoid the occurrence of SBLI in any practical applications hence, this leads to the idea of developing control mechanisms by manipulating the flow either before or during the interaction itself. The objectives of the control mechanisms are to prevent shock-induced separation and also stabilising the oscillating shock [7, 8]. The momentum of the turbulent boundary layer appears to be an important factor affecting the upstream influence of the shock as well as the resistance of the boundary layer towards separation. Hence, by increasing the incoming boundary layer momentum prior to the interaction with the shock, proves to be one of the beneficial mechanisms. This can be done using several boundary layer manipulation techniques listed below [1, 9]:

- Mass injection: This is done by applying fluid injection through a porous plate or several slots positioned upstream of the shock impingement location [10, 11].
- Distributed suction: This is applied at a certain distance upstream (usually specified in scale of the boundary layer thickness, $\delta$) of the shock impingement. This will lower the shape parameter, $H_i$ and produce a fuller velocity profile and more robust boundary layer towards separation [12, 13].
- Localised suction: This type of suction is applied locally inside the interaction region or in the immediate vicinity. It is done through drilling holes perpendicularly to the surface [14, 15].
- Vortex generators: The vortex generator devices are placed upstream of the shock and produces counter-rotating vortices that transfer high momentum flow from the outer region into the low momentum flow near the wall. This will in produce a more energise boundary layer and high resistance to adverse pressure gradient [16, 17]
- Bleed System: Currently this is one of the most popular techniques due to its effectiveness. The detail are as the following.

The introduction of bleed system is aimed to suppress the boundary layer separation induced by the impinging shock wave by removing the low momentum portion of the boundary layer. This is achieved through different designs such as

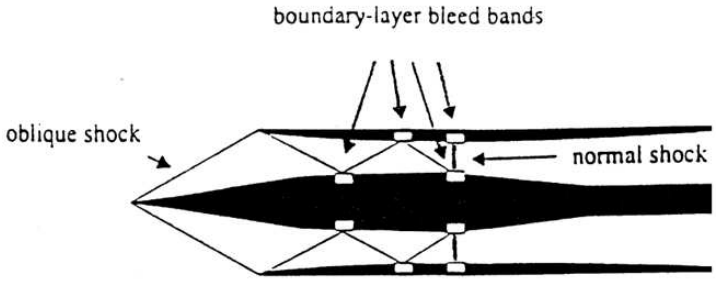


Figure 2.7: Axisymmetric mixed compression inlet with bleed bands [19].

holes, porous wall sections, slots and scoops which are distributed at designated locations predicted for boundary layer separations which SBLIs are likely to occur. The locations are along the compression ramp, cowl and sidewall of the intake [18].

Figure 2.7 displays the boundary layer bleed bands that are placed exactly at the oblique shock wave impingement location in order to control the effect of SBLIs [20]. By removing the low momentum portion of the boundary layer, this reduces the effective thickness of the boundary layer hence contributes to eliminate or reduce the severity of the separation [21]. This means that the boundary layer characteristics and size are controllable by the bleed technique. Boundary layer separation will also cause the destabilization of the terminal shock where the normal shock moves upstream and downstream and not fixed at the position required which is just downstream of the throat. By using boundary layer bleed, the separation can be suppressed and the normal shock will stabilize and therefore inlet unstart problem will be avoidable.

Despite the benefits that the bleed system brings, it also carries along a large performance penalty. The bleed mass flow is normally not reinjected into the system and therefore a significant amount of 10-20% of the captured mass flow is lost. This degrades the engine performance hence a larger nacelle is needed to have higher mass flow to compensate for the lost. However larger nacelle means there will be an increase in the friction drag consequently increasing the total drag. Structurally, the larger nacelle will increase the weight of the inlet and add up to the total weight of the aircraft. The captured mass that was not reinjected was instead vent overboard through bleed exits and this phenomenon will also result in a drag penalty.

In a trade studies conducted by Lockheed-Martin [22], the range of flights could significantly be increased up to 20% without the weight and drag penalty

from the bleed system. Boeing Phantom Works [21] also did a trade studies that proved without the bleed system, the Gross Total Over Weight (GTOW) can be reduced up to 10%. The increase in range and reduction in weight translate to large amount of savings in operational cost. Therefore there is an urgent need in minimising the amount of boundary layer bleed or develop alternative solution to solve the SBLIs problem while at the same time maintaining good aerodynamic performance.

## 2.2 Micro-Ramp

### 2.2.1 History & Evolution of Micro-Vortex Generators

Vortex generators (VGs) are known for their potential role in flow control. Conventional VGs which have the height of the boundary layer thickness, $\delta$ have been used for decades to control the separation by increasing the near-wall momentum by transferring the high momentum flow from the outer region into the lower momentum region, at the wall. This type of flow control, which is usually characterised as passive flow control are becoming more favourable despite active devices have their own attractions [9, 23, 24, 25]. They are used extensively to delay boundary-layer separation, enhance aircraft wing lift, tailor wing-buffet characteristics at transonic speeds, reduce afterbody drag of aircraft fuselages and avoid or delay separation in subsonic diffusers [26].

Conventional VGs however increase the parasitic drag on the aircraft due to their size and furthermore they are used to control a localised flow separation over a relatively short downstream distance [26]. Kuethe [27] began the effort of designing better VGs by reducing the size, when he invented a non-conventional wave-type VG with ratio of height to boundary layer thickness, $h/\delta$ of 0.27 and 0.42 that was able to use the Taylor-Goertler instability to generate streamwise vortices within the boundary layer. Following the success of the previous research, in 1980s more researches proved that the micro VGs, termed after having the height less than the boundary layer thickness, are able to outperform the performance of the conventional [28].

The first experiment conducted using the micro VGs to control the effect of SBLI was done by McCormick [17] in 1992. The design of the micro VG used was called "Wheeler's doublet" shown in Figure 2.8 named after the inventor, G.

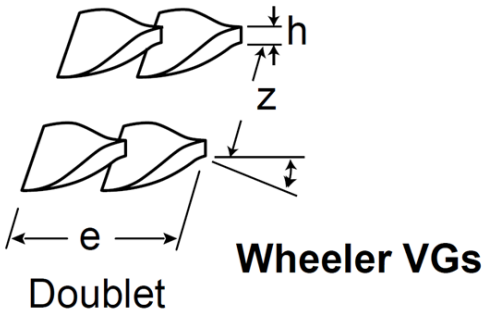


Figure 2.8: Geometry of the Wheeler's Doublet and design parameters by McCormick [17].

O. Wheeler. From his experiment, McCormick compared two different types of flow control, the micro-VG and the passive cavity. The final results showed that the separation due to SBLI was suppressed by the presence of micro-VG.

Following the success of McCormick, numerous investigations were done after that to test the capability of the micro VGs. Hence other different names were given such as submerged VGs, sub boundary-layer VGs and MEMS-scale effectors [26]. The term micro VGs was also differently characterised and are specified according to the ratio of $h/\delta$ as listed in Table 2.1. Different design geometries were also proposed and tested by Lin [26] as shown in Figure 2.9 and the results turned out to be promising.

| Height of MVG (% of $\delta$) | Author |
|---|---|
| 10-50 | Lin [26] |
| 10-40 | Blinde et. al [29] |
| 20-40 | Li & Liu [30] |
| 25-40 | Anderson et. al [31] |
| <40 | Ghosh et. al [32] |

Table 2.1: Definition of micro VG height by numerous authors

### 2.2.2 Micro-Ramp

Recent works have been focusing on a specific design of micro VGs known as micro-ramps or also called forward wedge in Lin [26] shown in Figure 2.10. This design proves to execute the role of a micro VG effectively because of the design geometry. Anderson et al. [31] were the first to investigate into depth the optimal design of the micro-ramps and the effects in controlling SBLIs. The detail

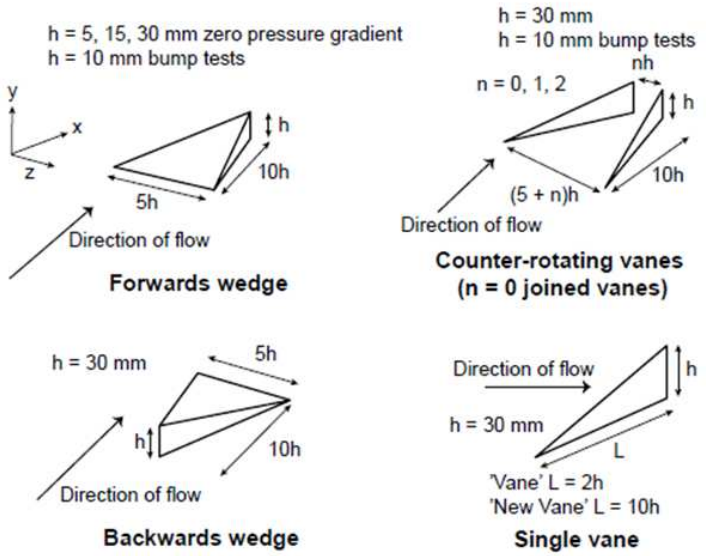


Figure 2.9: Geometries of different micro VGs tested by Lin [26].

Figure 2.10: Close-up view of a micro-ramp [33].

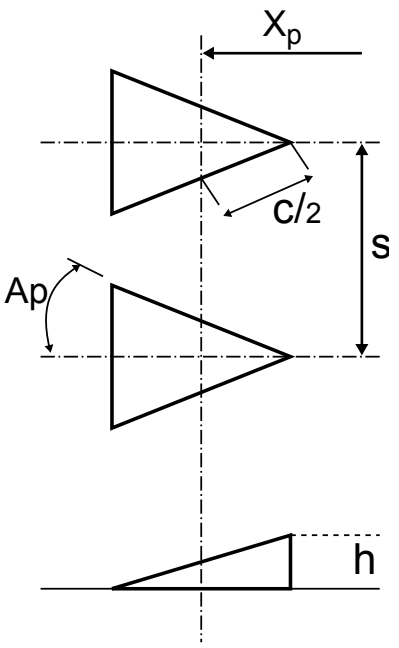


Figure 2.11: Geometry and nomenclature for standard micro-ramp. Reconstructed from Anderson et al. [31].

geometry of the micro-ramps is shown in Figure 2.11.

The SBLI suppression or the health of the boundary layer is characterised by many factors and one of them is the shape factor, $H$ [15]. Lower $H$ means less susceptible to separation and healthier boundary layer. In order to investigate the optimal design of the micro-ramp [31], the angle of incidence, Ap of the micro-ramp was varied. Results showed that $H$ decreases with the increase of the angle until reaching a minimum plateau. In contrast to the use of bleed system, in order to reach the same minimum plateau of $H$, 1.87% of the inlet capture mass flow ($W_{bleed}/W_0$) is needed and this is significant. Therefore micro-ramp flow control is very practical for use in supersonic inlets replacing the conventional bleed due to the fact that they are simple, "fail-safe", structurally robust, low-cost and no power requirements. At the same time, it also has the ability to produce benefits equivalent to the bleed system [19, 31].

### 2.2.3 Design Optimisations

The results from the well-known optimal design investigation by Anderson et al. [31] were used in most of the recent micro-ramps studies. The computational investigation covered the optimal shock control of SBLIs using 3 types of micro

VG geometries; micro-vanes, tapered micro-vane and micro-ramp placed in arrays. The purpose was to alter the properties of the supersonic boundary layer by introducing a cascade of counter-rotating vortices in the near wall region.

The design variables (refer Figure 2.11) were number of co-rotating micro VG pairs ($n$), micro VG geometric angle of incidence ($Ap$), height of the micro VG ($h$), chord length ($c$) and upstream location of the inviscid shock impingement point ($Xp$). While the variables that were kept constant were the tunnel Mach number ($M_\infty$), shock generator angle, tunnel total pressure ($P_0$) and tunnel total temperature ($T_0$). The response variables were the averaged total pressure change ($dP/P_0$), the area averaged compressible boundary layer displacement thickness at the reference plane ($\delta^*$), the area averaged compressible momentum thickness at the reference plane ($\theta$) and the area averaged boundary layer transformed form factor ($H$). Also note that the boundary layer thickness at the inviscid shock impingement location represented by $\delta_{shk}$ is the value measured without the presence of the impinging shock wave.

The Design of Experiment (DOE) for the optimisation selected was a Central-Face-Centred (CCF) which resulted in 27 unique computational fluid dynamics (CFD) cases for each of the three micro VGs devices considered for the investigation. Finally the results are presented in the form of generalised design guidelines to be applied to supersonic inlet problems and tabulated in Table 2.2.

| Parameter | Value |
|---|---|
| $s/h$ | 7.5 |
| $Ap$ | 24.0 |
| $h/\delta_{shk}$ | 0.4 |
| $c/h$ | 7.2 |
| $Xp/\delta_{shk}$ | 14.2 |

Table 2.2: Generalized optimal design guideline for micro VG [31].

Table 2.2 above outlines the generalised optimal design guidelines that can be used for all three micro VG tested including the micro-ramp array. Hence most of the micro-ramp geometries used in experiments after the year 2006 to understand the flow physics and the effect of micro-ramps on SBLIs are based on Table 2.2. It is acknowledged as a reliable optimisation investigation.

Another computational optimisation work was done by Hirt & Anderson [34]. Fifteen micro-ramp geometries with varying height, chord length and spacing

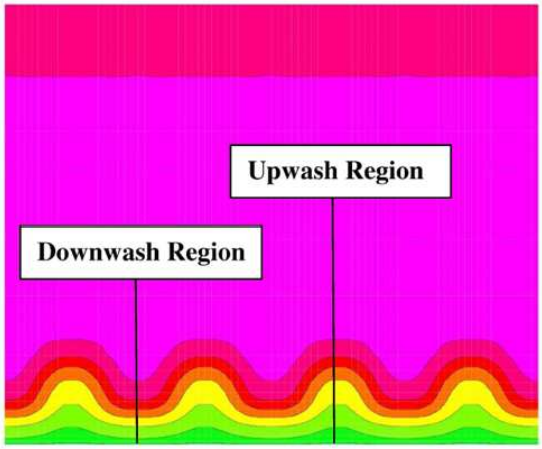


Figure 2.12: Upwash and downwash region in spanwise total pressure contours for micro-ramp array of nvg431 in [31].

between ramps were tested. The half angle of the micro-ramp was held constant at 24 degrees as suggested by Anderson et. al [31] and the range of heights tested were from 26.3% to 43.7% of the boundary layer thickness. The final findings stated that the optimum value to get the lowest $H$ according to each of the orders of DOE design occurs for micro-ramps with a large height and chord length, and a close spacing relative to the design space. Larger micro-ramps produce stronger vortices that pull more flow into the near wall region which provides a greater benefit to the near wall flow leading to the improvements in $H$.

### 2.2.4 General Flow Topology

The general idea behind the operation of micro-ramps is a micro scale device, having the height of a fraction of the boundary layer which is placed in the direction of opposing the flow and produces counter-rotating vortices. The vortices generated provide upwash and downwash motion [3, 31] that enables the exchange of the higher momentum flow from the freestream flow to the lower momentum region at the near wall which is shown in Figure 2.12.

However since the interest in micro VGs started to bloom after the success by McCormick [17], different ideas on how micro-ramps operate were presented and started to become one of the highlights in the aero-physics field. Despite the differences, all of them contributed to the overall understanding of the physics of the micro-ramps flow which now can still be considered as not yet fully understood [19] and is still developing.

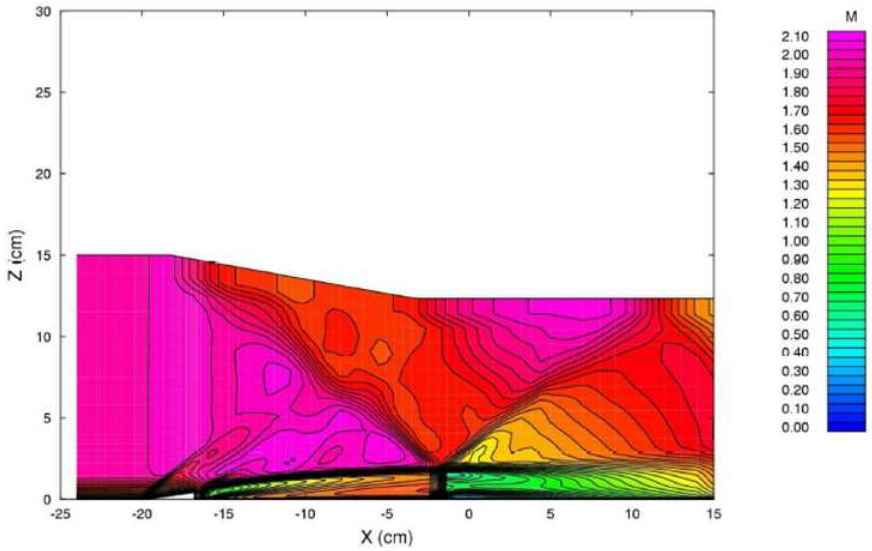


Figure 2.13: Visualisation of the 'virtual space' downstream the micro-ramp [31].

Anderson et. al [31] first introduced the concept 'virtual space' created by the micro-ramp array surrounding the wall surface. The region bounded by the virtual surface is three-dimensional and can sustain a normal shock wave structure. The region created has its own characteristics and is different from the normal supersonic boundary layer. This is shown in Figure 2.13. Therefore it is exhibited that such a region could support the effect of SBLIs that would separate a normal supersonic boundary layer.

The pioneer work in exploring the detail flow topology of the micro-ramp devices was actually done by Babinsky et al. [3]. The summary is shown in Figure 2.14. The horseshoe vortex is observed and this is generally occurring when supersonic boundary layer flows past a surface-mounted protuberance [35]. The flow passing such ramp geometry creates a single separation zone off its leading edge which creates the horseshoe vortex structure. However the horseshoe vortex is predicted to be weak since both numerical and experimental investigations were not able to capture the detail of the structure and the only evidence is available from deductions made from the surface flow visualisation [36].

The horseshoe vortices generated were classed as one of the secondary vortices. Apart from that, there are also another two pairs of secondary and a pair of primary trailing vortices exists. On the other hand, Herges et al. [37] only identified one pair of secondary vortices instead of two and this is shown from the surface flow visualisation in Figure 2.15.

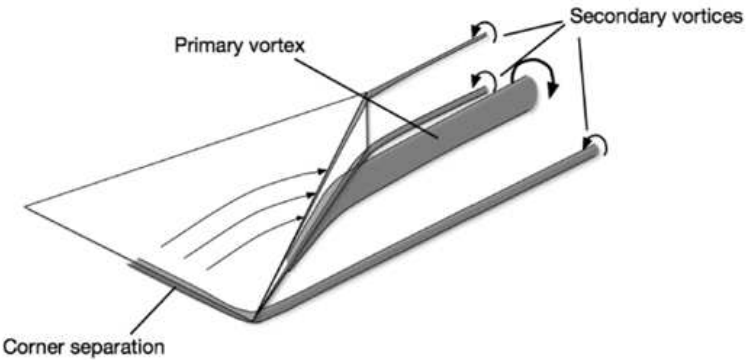


Figure 2.14: Sketch of main flow features of flow over micro-ramp [3]

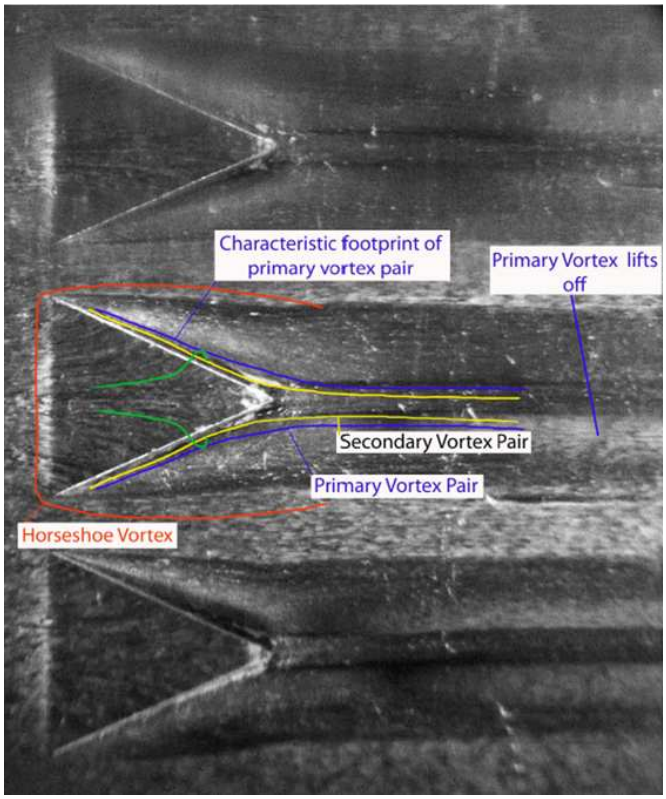


Figure 2.15: Surface flow visualisation of micro-ramp array with features marked [37]

The primary vortices which is commonly observed to exhibit the 'herringbone' pattern [3, 30, 36] originates from a small separation zone ahead of the compression zone that earlier created the horseshoe vortex. This herringbone pattern is considered to be the result of open separation [38] according to Lu et al. [36]. The open separation zone contains the primary vortex on each side of the micro-ramp and counter-rotating towards each other as shown in Figure 2.14. The two secondary vortices observed both started from two separation points on the trailing edge of the device, one at the tip and one at the bottom near to the junction of the slant sides of the micro-ramp and the wall [3, 39, 40] which will be discussed in detail later in this chapter.

The herringbone pattern and the two bright lines both representing the primary and secondary vortices respectively claimed to disappear or fade after two micro-ramp length downstream [3]. The explanation behind this is the vortices tend to lift off from the surface because of the upwash motion and a certain limit of time is binding the vortices to stay low and inside the boundary layer [37]. Therefore another characteristic to assess the performance of the effectiveness of the micro-ramp is by the time the vortices remain inside the boundary layer or the measured downstream length before they lift off.

A detail Particle Image Velocimetry (PIV) investigation was done by Blinde et al. [29] and a conceptual model of the flow topology was proposed as shown in Figure 2.16. The model tested was an array of micro-ramps instead of single configuration. The micro-ramps generated vortices that travel downstream hence inducing regions of low-speed flow while at the same time regions of high-speed were also induced at intermediate spanwise locations.

The existence of the streamwise counter-rotating vortices were claimed not apparent and thought to be reminiscent of the conditional eddies that appear to be cross-sections through hairpin vortices [41]. This is consistent with the findings that trains of hairpin vortices were created in the wake of a hemispherical roughness element in a low-speed turbulent incompressible boundary layer [42, 43] and is anticipated to be a comparable phenomenon with the downstream condition of micro-ramps. These observations however do not contradict with the downstream topology understood before on the vortices lifting off [3]. They just add to the understanding that the vortices do not lift off and disappear but instead form such a unique structure visualised as hairpin vortices [36].

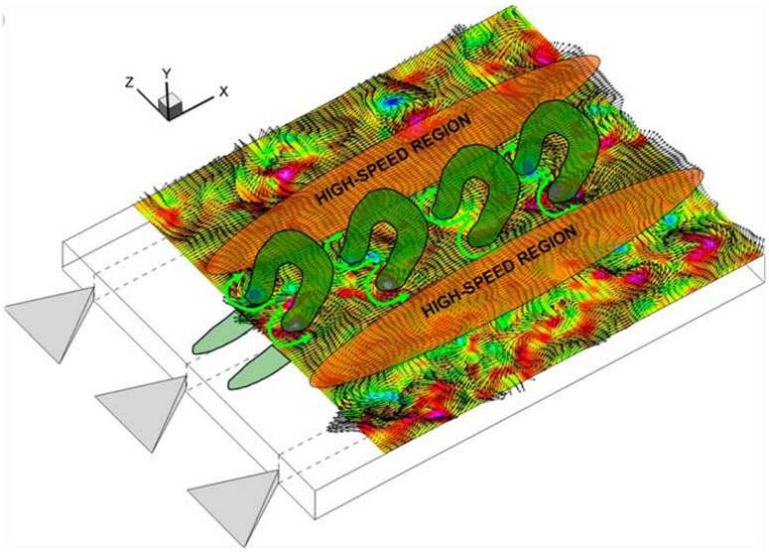


Figure 2.16: Conceptual sketch of hairpin vortices downstream of micro-ramp and high speed regions at intermediate positions [29]

### 2.2.5 Leading Edge Flow Topology

A closed separation occurred at the leading edge of the micro-ramp and this can be observed both in experimental and computational investigations. However by comparing the size, the separation bubbles in the experiments are smaller than in the computational one and this is predicted by Lu et al.[36] due to the lower Reynolds number in the computation. Figure 2.17 shows the results comparison of the flow visualisation both in experiments [44] and computations [30].

The presence of the separation region is however below the threshold of about 16-degree ramp for separation to occur. The possible reason behind the induced separation at small leading edge angle is that the effective Mach number of the flow at the leading edge has been lowered due to the micro-ramps being submerged in the boundary layer [36]. The attachment line in front of the leading edge must then curve and intersect at the leading edge tips in order for the velocity gradient to remain finite. Then the reattachment line continues downstream on the flat plate. The nature of the separations and reattachments are always explained by the presence of focus and saddle points and this can be observed in the computational results [30] in Figure 2.18 marked by Lu et. al [36]. Experiments have not yet been able to capture such detail structures due to the limitations of the flow visualisation resolution.

High-pressure regions were observed at the leading-edges of the micro-ramps

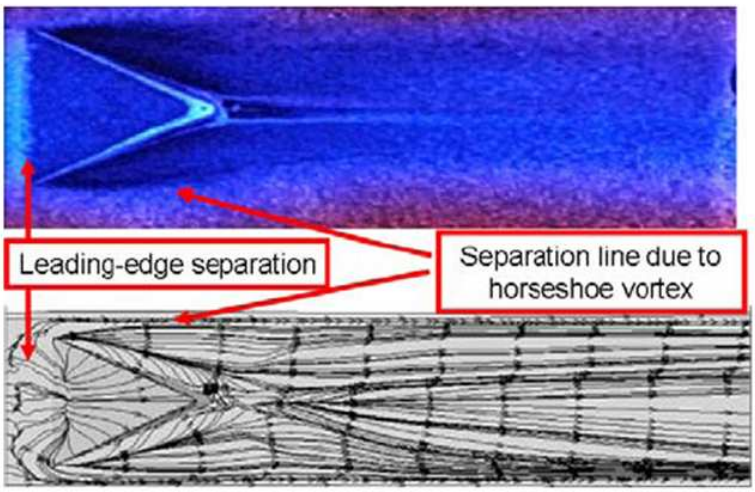


Figure 2.17: Comparison of surface flow visualisation of the top view [36].

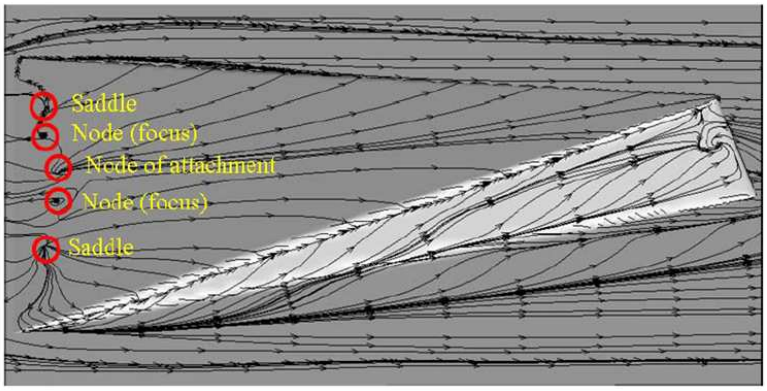


Figure 2.18: Marked focus and saddle points at micro-ramp leading edge [36].

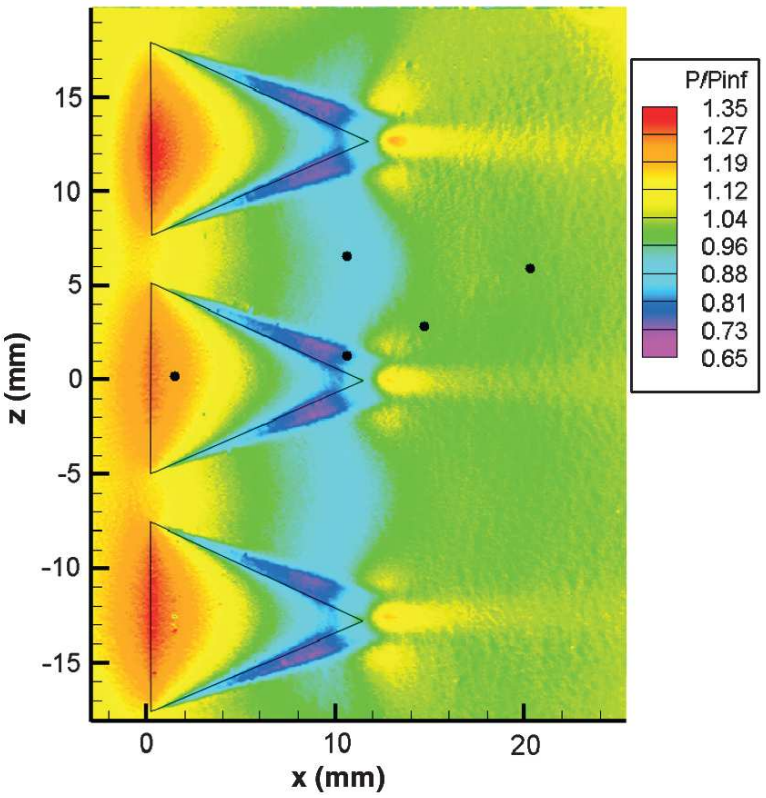


Figure 2.19: Surface pressure distribution around micro-ramp in array configuration using PSP [45].

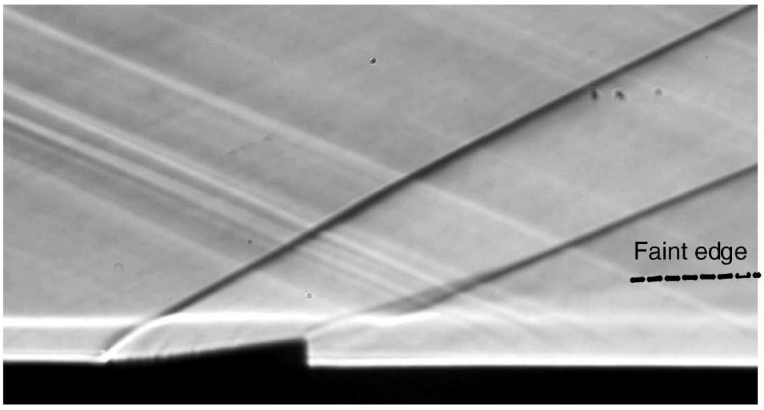


Figure 2.20: Schlieren visualisation of shock structure at leading and trailing edge of micro-ramp [3].

depicted by the red areas in the Pressure Sensitive Paint (PSP) results in Figure 2.19. According to Lu et al. [46] the high pressure regions were caused by a localised SBLI occurring at the leading-edge as explained in Section 2.1.3 of the compression ramp type. As a result an oblique shock-wave can be seen emanating from that location in the schlieren image in Figure 2.20.

### 2.2.6 Side Flow Topology

The surface streamlines over the micro-ramp seem to spill over the slant edges of the sides after a certain distance climbing up the ramp and can be visualised in Figure 2.18. The slant edges act as a separation line [36]. The flow detaching from the separation line then attaches on the flat plate and spirals downstream in a structure known before as the herringbone pattern which is recognised as the primary vortex. However as mentioned earlier, the experimental visualisations have not been able to capture the herringbone pattern.

Instead of the herringbone pattern, the oil-flow experiments show a dark region filling the sides of the micro-ramps which indicates that the pigments are being spread away by the high shear forces created due to the open separation at the slant edges as shown in Figure 2.21. This is different from the separation occurring at the leading edge which is classed as closed separation. Conversely what can be observed is that at the leading edge separation, there is a bright region of pigment, different from the separation at the sides. This reinforces the understanding of different types of separation occurring at these two locations. Referring to the PSP results in Figure 2.19, the region of low pressure were seen

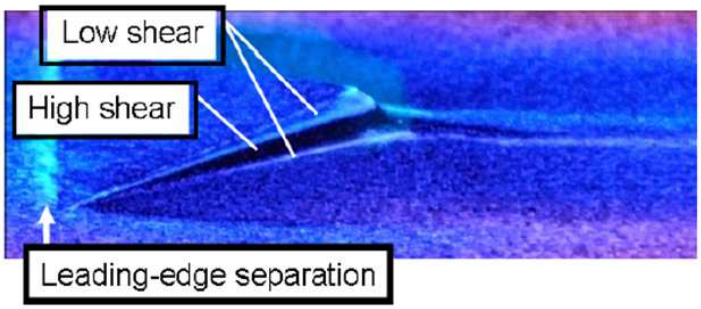


Figure 2.21: Surface flow visualisation of side view [36].

at the junction between the sides of the micro-ramps and the wall surface. This is the indicator of the existence of high-speed flow originating from the primary vortices.

There are two bright fringes observed at the edges of the micro-ramp, one at the top edge and another at the junction between the side of the micro-ramp and the wall. Bright fringes are experimentally explained due to the accumulation of the pigment that indicates flow attachment regions. So it can be deduced that the two bright lines are separation lines which can be seen also from the numerical investigation in Figure 2.18 represented by extremely thin separation lines and attachment zones. This might also be the explanation behind the existence of the herringbone pattern that could originate from the open separation at the edges of the micro-ramp. Furthermore the herringbone pattern started to become irregular and break down after moving towards the rear of the micro-ramp.

### 2.2.7 Rear Flow Topology

The experimental visualisations in Figure 2.22 show a bright smear on either side of the trailing edge. This bright region is the indicator of the location where the surface streamlines converge on a pair of spiral foci, one on each side as previously found in the numerical investigations by Li and Liu [30, 47]. These foci points act as lift off points for the surface streamlines [36]. From the experimental visualisations, the foci can be seen as an accumulation of pigment.

The detail description of the saddle and node points can be found in [36]. The role of these foci points can be connected with the disappearance of the pair of bright lines downstream about two micro-ramp lengths [3, 37, 44]. Babinsky et al. [3] and Herges et al. [37] suggested that the disappearance was due to the lift off of the primary vortices resulting from mutual upwash with each other. However

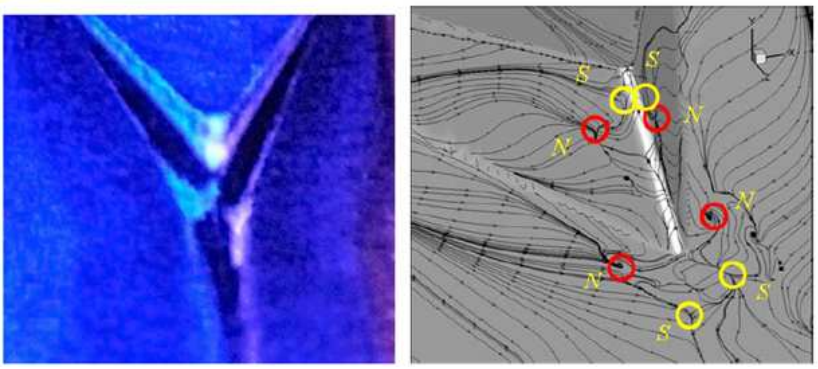


Figure 2.22: Rear view of micro-ramp (S = saddle, N = node/focus) [36].

Lu et al. [36] claimed that this explanation may be incomplete as such a lift off has to be rapid enough for the sudden disappearance. On top of that there are also other studies on the wakes of protuberances [47], where the trailing vortices were found to leave a signature for a long distance downstream that proves to be inconsistent with the concept of vortices lifting off.

A high-pressure region exist at a location not far downstream from the leading edge of the micro-ramp. This is represented by the yellow streaks from Figure 2.19. Lu et al. [46] explained that the source of the high-pressure streaks is from the recompression shocks taking place due to the change of direction of the flow. Initially the flow was moving down from the slant edges of the micro-ramp and suddenly it was required to change its direction parallel to the wall. Therefore it gave rise to the small recompression shocks on the wall surface. From the detailed analysis of computational and experimental results, Li & Liu [48] proposed an improved five-pair vortex model, comprising a pair of primary vortex, three pairs of secondary vortex and finally a pair of horseshoe vortex. This five-pair vortex model is shown in Figure 2.23.

### 2.2.8 Wake Region

There have been different thoughts earlier on the near wake behaviour of the micro-ramps. The understanding of this topic is essential since the actual mechanism in controlling the SBLIs effects is from the behaviour of the fluid downstream of the micro-ramp devices. Earlier understanding proposed that the counter-rotating vortices tend to lift off after certain downstream length such as at two micro-ramp lengths [3, 37]. This was explained by the disappearing bright lines observed in the surface flow visualisations.

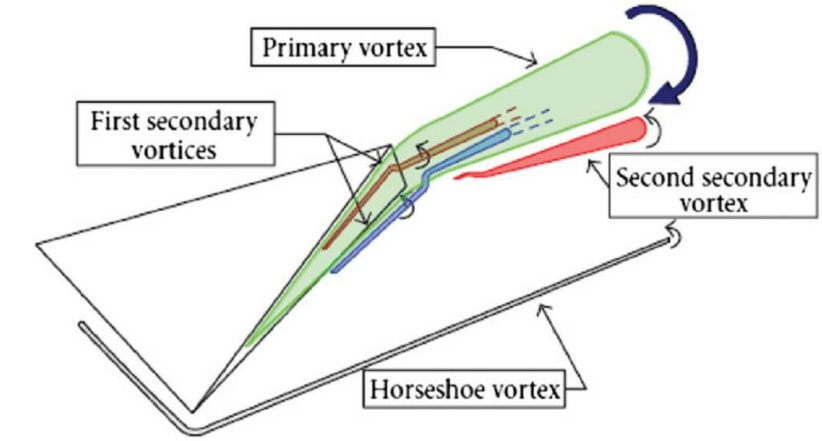


Figure 2.23: Schematic diagram of five-pair vortex structure [48].

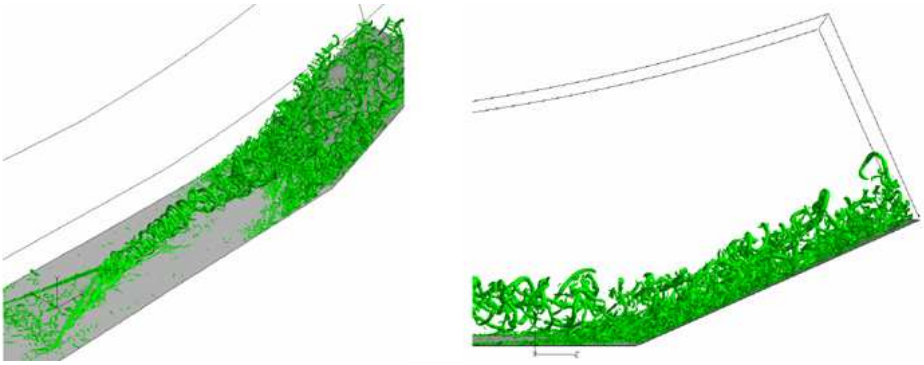

Figure 2.24: Vortex rings captured by numerical investigation [30].

However Blinde et al. [29] from a detailed Particle Image Velocimetry (PIV) mapping from Figure 2.16 suggested the existence of the hairpin vortices together with the alternating regions of high speed and low speed. The hairpin vortices were created due to the breakdown of the initial vortices sourced from the flow over the micro-ramp which is different from the lifting off vortices theory proposed earlier.

A detailed experimental investigation on the concept of vortex breakdown was done by Lu et al. [36] validating the outstanding numerical findings from Li & Liu [30, 47]. It is believed that the vortices trailing downstream from the micro-ramps experienced a symmetrical breaking due to the phenomenon close to Kelvin-Helmhotz instability [49]. The breaking vortices form large vortical structure which is identified clearly in both experimental and numerical investigations or also known as vortex rings as shown in Figure 2.24 and Figure 2.25.

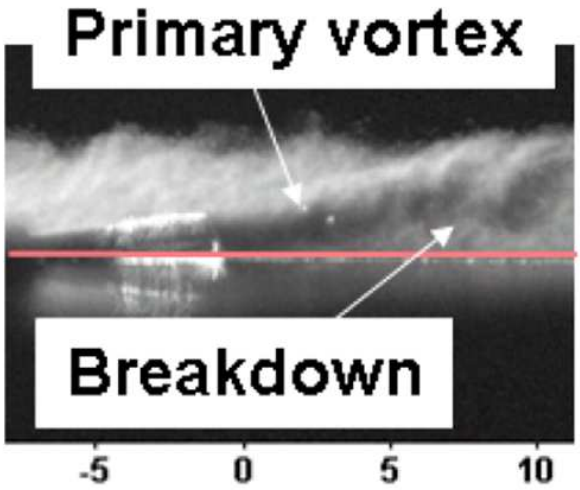


Figure 2.25: Experimental visualisation of vortex breakdown using laser lightsheet [36].

The vortex rings structure visualised are identical to the hairpin vortices theory [29]. Therefore a complete preliminary storyline on how micro-ramps are capable of controlling SBLIs are explainable as proposed by Lu et al. [36]. The counter-rotating vortices downstream the micro-ramps experience an unstable condition similar to the Kelvin-Helmholtz instability due to the complex flow condition at the rear of the micro-ramps. The instability induced a symmetrical breakdown for the vortices. Then the breaking of the vortices form vortical structures known as vortex rings or hairpin vortices.

However, a subsequent experimental study by Sun et al. [50, 51] showed that the vortex rings and the two streamwise primary vortices actually exist at the same time and are not the product of each other. The vortex rings which were also identified as the hairpin vortices were observed wrapping over the vortex pair as shown in Figure 2.26. These findings were actually discovered earlier in high-order LES investigations by Li & Liu [47, 52]. There might be a slight difference in the shape of the vortex rings in the experiments and simulations where the one in experiments resemblance an arch instead of a round vortical structure. This is due to the fact that the bottom region (near wall) is difficult to be accessed by PIV instrumentation [46]. This might also be the reason why the hairpin structure is visualised instead of vortex rings in Figure 2.16 by Blinde et al. [29]. Another experimental findings supporting this phenomenon is by Bo et al. [53] shown in Figure 2.27. The dark zone represents the cross-section of the micro-ramp's wake. Inspecting carefully inside that wake, a pair of vortex core

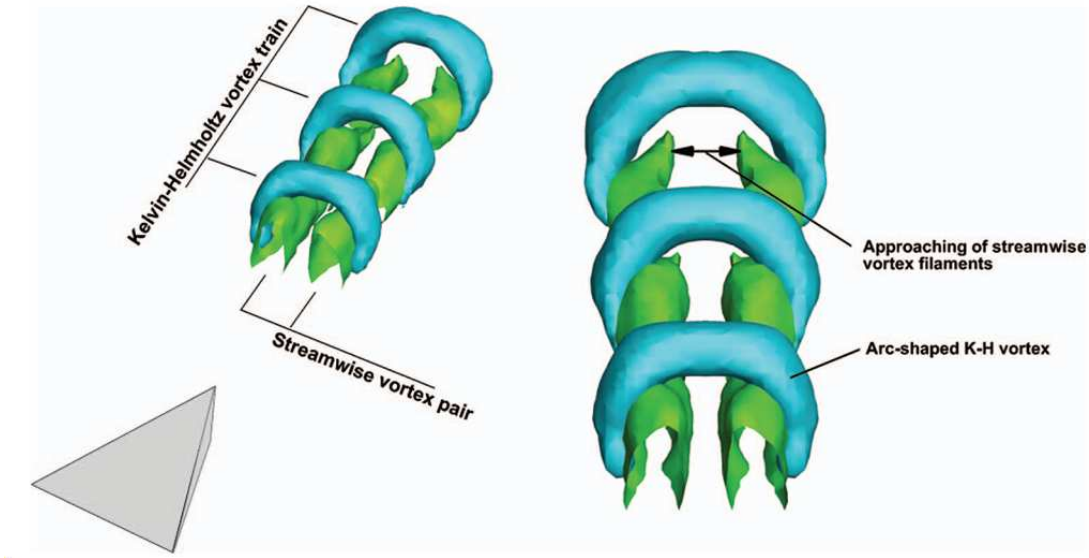


Figure 2.26: Vorticity of the iso-surfaces of the streamwise component $\omega_x$ in green and the spanwise-wall-normal component $\sqrt{{\omega_y}^2 + {\omega_z}^2}$ in light blue [51].

is visible depicted by the lower luminance structure. Hence again shows that the pair of streamwise vortices were wrapped inside the wakes flow which are most probably the vortex rings or hairpin vortices.

The high resolution PIV experiment using nanoparticle-based planar laser scattering (NPLS) technique by Bo et al. [53] revealed more information on the complex structure of the downstream wake region. In Figure 2.28a the large scale vortices were observed, similar to the 'large billowing' structures found in experiments by Lu et al. [54, 46]. Progressing downstream, the wriggling of the vortices seems to increase gradually. This can be seen when comparing both structures in region *S1* and *S2* in Figure 2.28a. Figure 2.28b shows the cross section of the vortex core at 1/6 span location. The vortex core is differentiated from the turbulent eddies by low luminescence or dark region. It is interesting to see that the vortex core gradually dissappeared after a certain distance downstream. Bo et al. [53] suggested from the NPLS images that the vortex structure were only able to sustain for a length of $4\delta$ from the micro-ramp trailing-edge before being succeeded by a new type of flow organization (labelled as region II).

It would also be interesting to investigate the behaviour of the dissappearing vortices. Sun et al. [51] showed from the top row of Figure 2.29 that the vortex structure rises as it moves further downstream at an approximately linear rate of $x = 1.63h$. This behaviour is consistent with Bo et al.'s findings where the angle

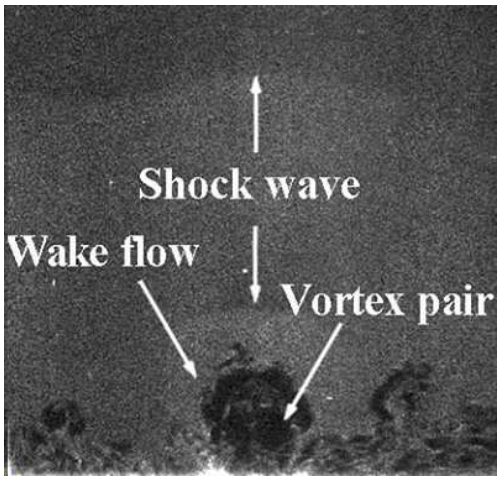


Figure 2.27: Cross-section of micro-ramp wake from nanoparticle-based planar laser-scattering technique at 20mm downstream micro-ramp trailing edge [53].

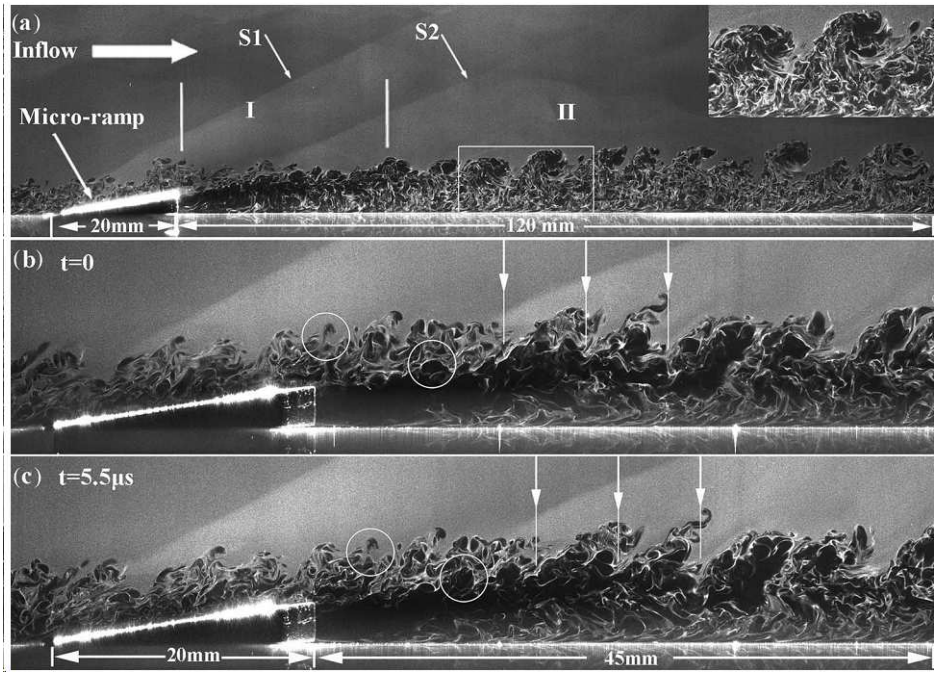


Figure 2.28: NPLS PIV instantaneous flow of micro-ramp wake (a) at median plane (b) and (c) at 1/6 span location with a delay of 5.5 $\mu s$ [53].

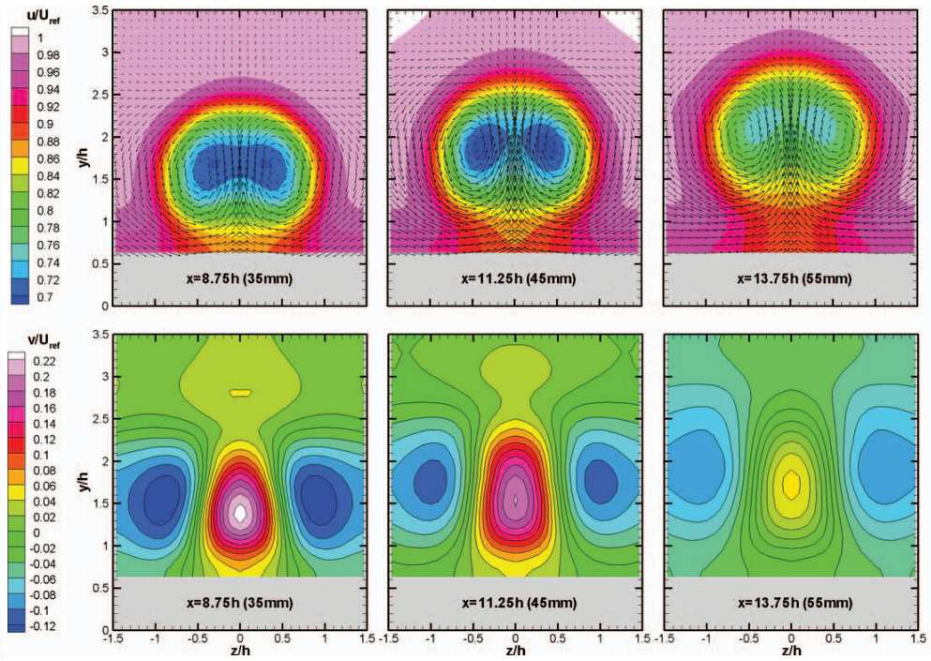


Figure 2.29: Two-dimensional cross sections of $u$ and $\nu$ contours from the mean flow field downstream micro-ramp [51].

was measured as 6.5° to the wall. The upwash motion from both of the vortices caused the whole structure to experience the increase in altitude. Conversely the spanwise distance of the two vortices remained relatively constant as it travels downstream as shown in the bottom row as depicted from both experiments in Figure 2.29 and Figure 2.30.

### 2.2.9 Effect on Shock Boundary Layer Interaction

The famous optimisation studies by Anderson et al. [31] sparked the interest in micro-ramps. The studies outlined the micro-ramp geometries based on a large test matrix. The optimisation studies were based on boundary layer health (shape factor) as the response parameter. However there are other parameters that might be useful to consider as the response parameter such as drag reduction and flow distortion which are important for internal flows [46]. A pattern can be drawn from all of the investigations on the effect of micro-ramps on SBLI. Most computational studies involved a single micro-ramp while experiments generally use array configurations of them. Also most experimental studies involve impinging shocks [3, 29] which is more prominent for internal cases.

The geometries of the micro-ramps were sized according to the results from

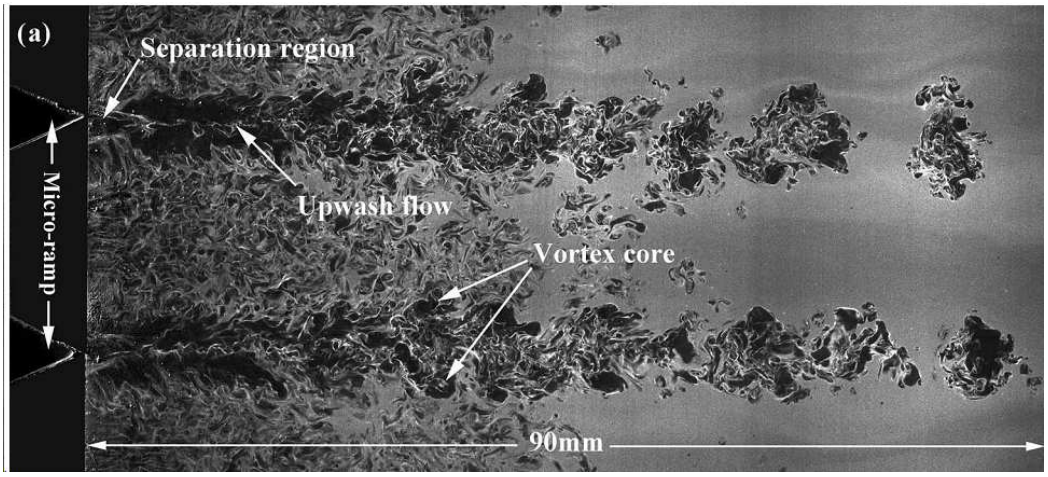


Figure 2.30: Downstream flow structure of micro-ramp. The laser-sheet was positioned at an angle of 6.5° to the wall [53].

the optimal investigation done by Anderson et al. [31]. The dimensions however are based on ratios from Table 2.2 and most of them are dependent on the height of the devices which best represents the size of the devices. Definitely the height must be scaled to the boundary layer thickness in order to fulfil the status of micro-ramps as low-profile vortex generators.

The study on the effect of the micro-ramp height was done by Babinsky et al. [3]. It was shown that the height has little effect on the fundamental flow development specifically the region downstream of the device (refer Figure 2.31). After comparing experimental results of different heights from both surface flow visualisation and pressure ratios, it can be deduced that the main flow features are almost identical. When comparing the streamwise effect, all of the micro-ramps with different heights also showed similar development in momentum exchange behaviour as shown in Figure 2.32.

The flow development although similar but still vary with height. Ashill et al. [55] also agrees with this conclusion and stated that flow by smaller devices develops and evolves more quickly than larger devices. Hence high momentum fluid is moved to the near wall regions in a shorter period of time. Therefore practically it would be beneficial to locate smaller devices at certain regions that require more flow control. On the other hand, the role played by a bigger micro-ramp is also beneficial in producing larger, more intense and further from surface type of vortices. Although this is also helpful for flow control, there is a drag penalty accompanying that would become a major concern for the industry.

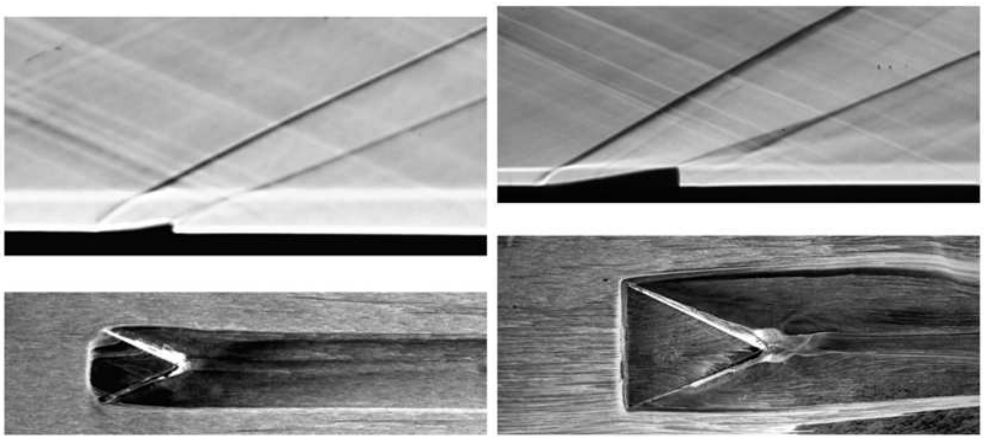

(a) 2mm micro-ramp (b) 6mm micro-ramp

Figure 2.31: Schlieren photograph and surface flow visualisation [3].

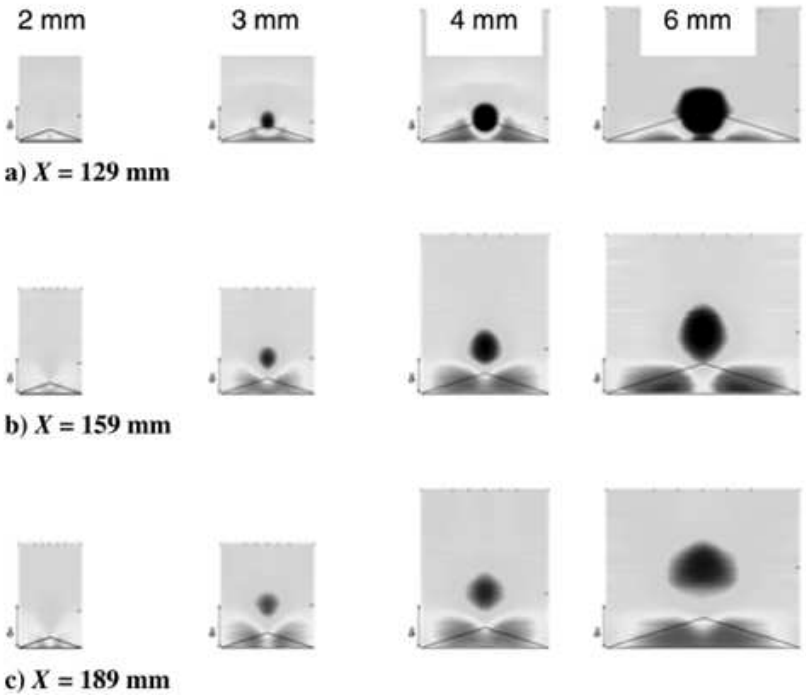


Figure 2.32: Streamwise momentum difference at various downstream locations for all micro-ramp heights [3].

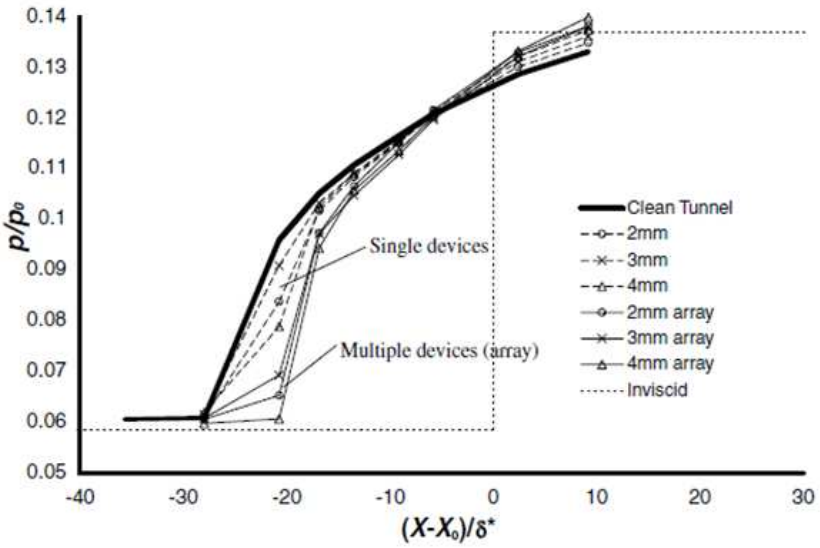


Figure 2.33: Centreline surface pressure for interaction controlled by 3mm micro-ramp for both single and array configurations [3].

In the optimal investigation done by Hirt and Anderson [34], the conclusion made was, in order to get the optimum value of $H$, the best means is to choose a micro-ramp with larger height and chord length. This is because bigger micro-ramps generate relatively big and stronger vortices that are capable in pulling more flow into the near wall region hence improving the value of $H$.

Both single and spanwise arrays of micro-ramp configuration were tested by Babinsky et al. [3] in order to investigate the effectiveness in controlling SBLIs. Both configurations proved to exhibit similar behaviour in lifting off the vortices from the surface and producing upwash motions which helped in moving the high-momentum fluid into the near wall region. Both configurations also managed to increase the pressure gradient and decrease the upstream influence that lead to the potential suppression of separation. This is shown in Figure 2.33.

The micro-ramps act to divide the separation region into multiple three-dimensional separation cells. In the event where the micro-ramps are placed in streamwise arrays, the number of separation cells increases according to the number and placement of the ramps. This can be seen from the surface flow visualisation in Figure 2.34. Both configurations were not able to eliminate the separation entirely but the reduction of the size of the separation region was observed.

From the graph in Figure 2.33, it can be seen that the use of micro-ramp arrays

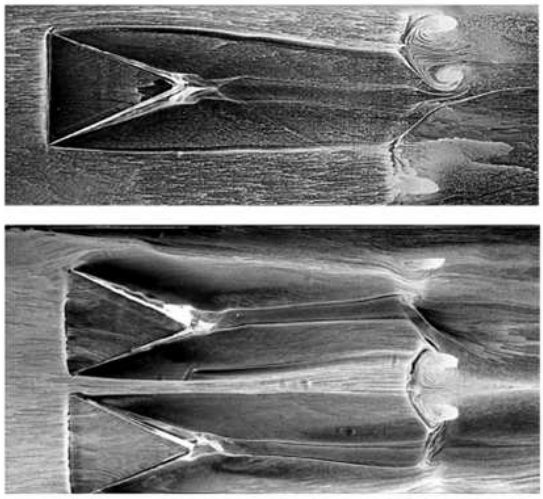

Figure 2.34: Surface flow visualisation for interaction controlled by 6mm micro-ramp for both single and array configurations [3].

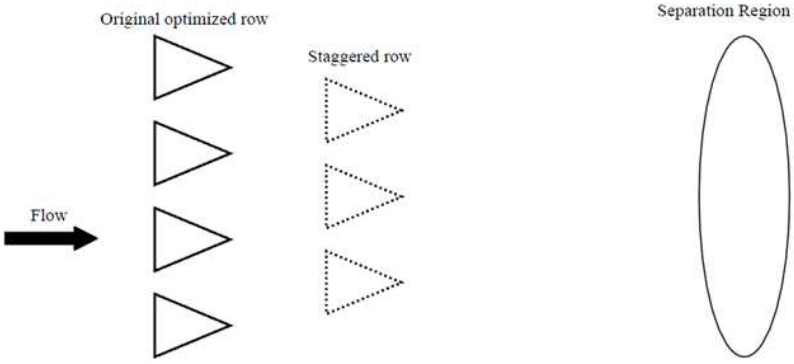


Figure 2.35: The second row micro-ramp configuration [56].

are more effective since they are able to increase the pressure gradients more than the single configuration. On the other hand in Figure 2.34, areas of undisturbed flow exist in between the micro-ramps when placed in arrays. Therefore in order to control wider regions of separation, more micro-ramps are needed to be placed in arrays.

The urgency in solving the undisturbed region problem triggered a further investigation by Galbraith et al. [56] by placing a second row of micro-ramps behind the original optimised row as shown in Figure 2.35. Anderson et al. [31] also speculated the possible benefits of a two row configuration could bring in energizing the flow in the gaps between the micro-ramps hence eliminating the remaining separated flow regions.

The results from the oil-flow numerical visualisations showed that the second

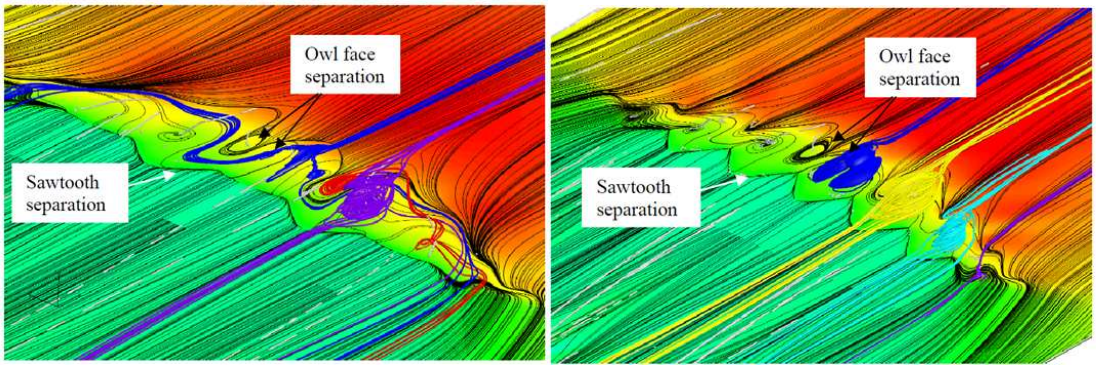


Figure 2.36: Numerical surface flow visualisation displaying the separation bubble and sawtooth structure for single row (left) and multi-row (right) [56].

row of micro-ramps has further broken up the separation region into individual cells as quoted by Babinsky et al. [3] but has not eliminated it. When the streamlines and vortex cores are visualised, it clearly showed that when one array of micro-ramp is applied, it tends to break the single separation bubble into smaller separation pockets and when the second array is placed, it is broken into smaller pockets and enhanced the saw-tooth pattern where it acts as the border for each pockets. This is shown in Figure 2.36.

However apart from the effects in breaking the separation bubble, the existence of the second row prevents the vortices generated by the first row from lifting as far from the surface as compared with the single row configuration. This is beneficial since one of the ways in SBLIs control is to keep the vortices as long as possible inside the boundary layer before lifting off. It can be seen from Figure 2.37 that in the single-row configuration, the vortex core height is much higher compared to the two-row configuration where the vortex core produced by the second row of micro-ramp managed to pull it down nearer to the surface of the separation region.

Babinsky et al. [3] revealed that the presence of micro-ramps were able to display substantial disruptions to the separated region as shown in the oil-flow image in Figure 2.34. The separation region was not entirely eliminated but small regions of attached flow are seen. This was one of the reasons why Lu et al. [46] prefer to use the word disruption instead of reduction or elimination. The most recent investigation that supported this was done by Bo et al. [53] using NPLS PIV. As can be seen from Figure 2.38, without controls (left image), the low speed region stretches in spanwise direction. However with the presence of micro-ramp,

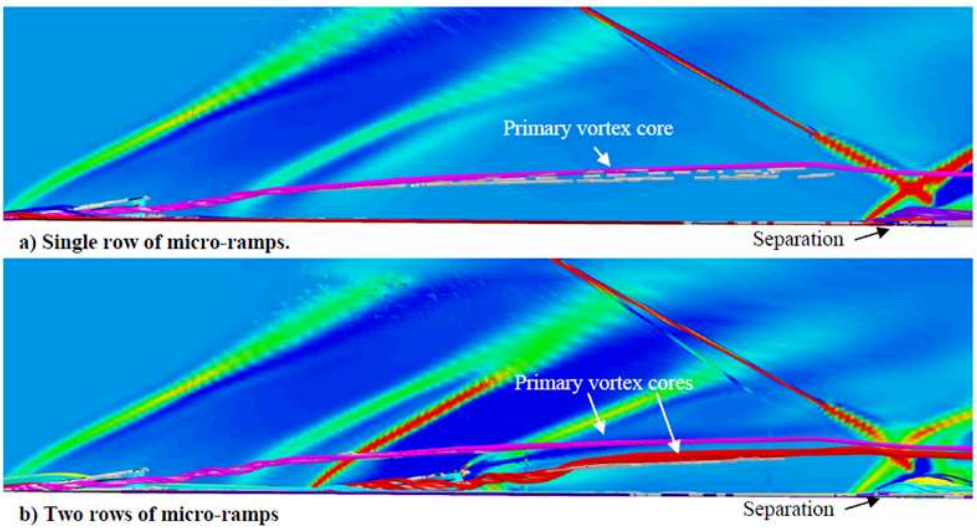


Figure 2.37: Primary vortex streamlines with contours of the centreline density gradient [56].

strips of high-speed attached flow is observable which shows that the streamwise vortices were able to penetrate through the separated flow region and disrupt the overall spanwise shape of the separation region.

Babinsky et al. [3] also suggested that using smaller micro-ramps may be better due to having lower wave drag and this was also supported by Bur et al. [57] in their transonic studies. Therefore, following the small sizes, they need to be placed at a location closer to the interaction region which is the same conclusion drawn from low speed studies [26]. Finally these two important conclusions were later agreed by Lee's et al. [58] findings through computational studies at Mach 3.

Analysing the effect of micro-ramps on SBLI from the X-Y plane, the typical velocity contour of a separated turbulent boundary layer is shown in Figure 2.39(a). The shear layer, defined as the layer dividing the interaction region from the high-speed outer region (typically $u/u_e > 0.5$) [1, 59] is observed originating from the bottom of the incoming boundary layer drawn by the red line. A region of low-speed and separated flow are also detected close to the wall. After the presence of micro-ramp, a significantly improved velocity distribution is observed in Figure 2.39(b). The reversed flow has dissappeared leaving a thin layer of low-speed region and at the same time the distortion of the boundary layer seemed to be alleviated. This can be considered as a success even though it was not able to totally eliminate the separation region.

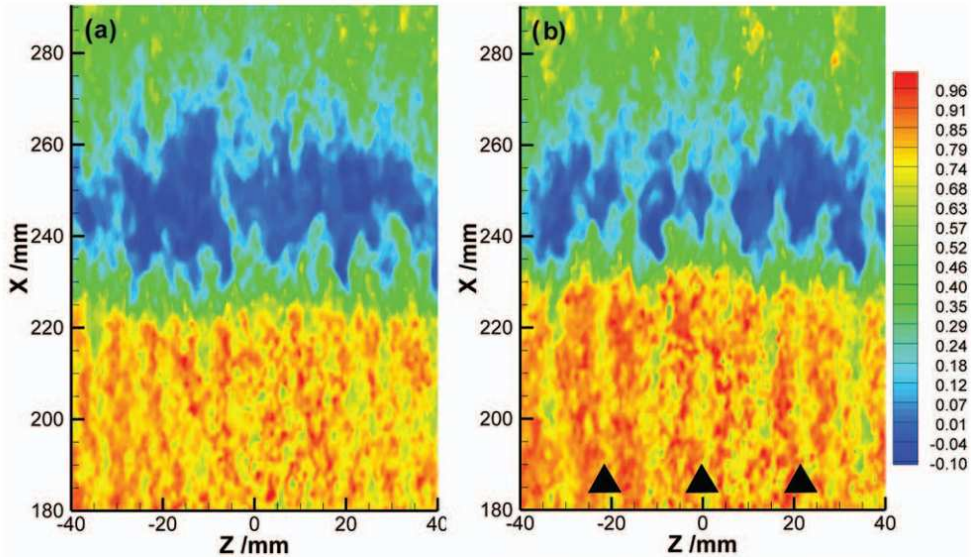


Figure 2.38: PIV results showing streamwise velocity distributions downstream micro-ramps at 1.5mm above wall [53].

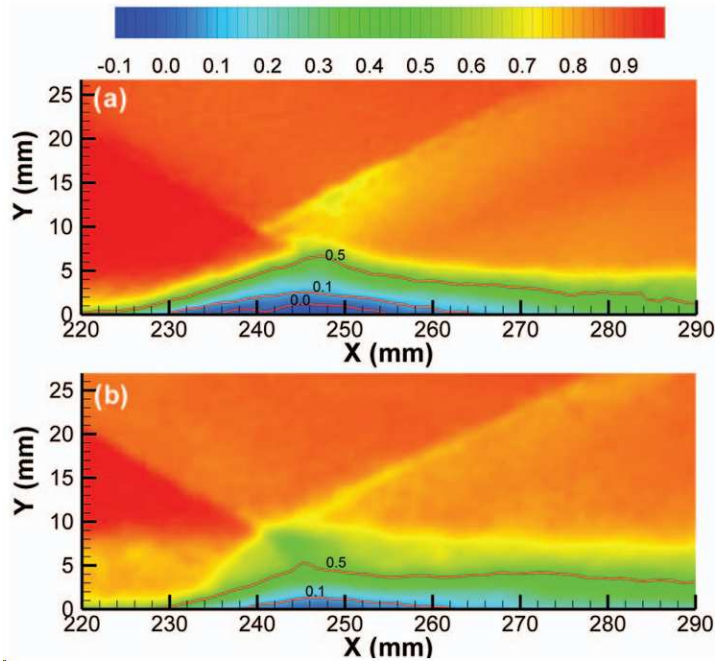


Figure 2.39: PIV results showing main velocity ($u/u_e$) distribution of micro-ramp downstream region subjected to SBLI (a) uncontrolled case (b) with control [53].

## 2.3 Conclusion

There are four main conclusions that can be made from the literature review:

1. All of the investigations using micro-ramps showed improvements in the boundary layer health compared to their baseline results. The boundary layer separations due to the shock-impingements were able to be suppressed. Yet, there are still no evidence at the moment that the micro-ramps are able to completely prevent or diminish the separations.

2. The potential of micro-ramps in improving the boundary layer health and suppressing the SBLIs have been given extensive attention by experimentalists. This can be seen from the numerous types of experimental methods conducted such as schlieren photography, Particle Image Velocimetry (PIV), oil-flow visualisation, laser Doppler anemometry (LDA) and not forgetting the conventional pressure tapings measurements.

3. Different theories on the flow structures at the near wake region of the micro-ramps are being proposed such as upwash and downwash motions, hairpin vortices and ring vortices. This leads to the different explanations on the mechanism of suppression of the boundary layer separation. It can also be concluded that the differences in the theories are due to the different experimental methods and flow visualisations used.

4. The investigations on the effect of micro-ramps are done for supersonic conditions. However, there are still no investigations being made in hypersonic flows. The geometries of micro-ramps used in the investigations are also obtained from the optimisation made in supersonic condition.

This study will involve the investigation on the micro-ramp performances and also the optimisations of the design geometries in hypersonic flow condition. It is hoped to be a stepping stone and introductory phase for micro-ramp researches in hypersonics. It will be interesting to observe if there are any differences in the flow behaviour compared to the supersonic flow.

# Chapter 3

# Experimental Methodologies

This chapter comprises of three main sections as listed below:

- *HSST Facility* - Descriptions on the wind tunnel facility that were used for all of the experiments.
- *Experiment Models & Setup* - Detail designs of the micro-ramp models showing their CAD drawings and also the experimental setup.
- *Experimental Techniques & Flow Diagnostics* - Describing the techniques used including novel and state-of-the art flow diagnostics that were used for the experiments and detail descriptions on the setup.

## 3.1 High Supersonic Tunnel (HSST)

The experiments are conducted in the University of Manchester High Supersonic Tunnel (HSST) located in the Aero-Physics Laboratory of the School of Mechanical Aerospace and Civil Engineering. The HSST is a supersonic intermittent blowdown tunnel having the capability of running experiments between Mach 4 to 6 which is achieved by using interchangeable nozzles. The working fluid used for the tunnel is dry air. The full schematic diagram of the HSST Tunnel is shown in Figure 3.1.

The gas is initially compressed up to a pressure of 17 bar and it passed through an Ecoair Series AT 15 adsorption dryer that acts as a drying unit before being stored in a high pressure vessel that is capable of storing 3.5m$^3$ of high pressure gas at 16bar. The gas then passes through an infinite variable pressure reducing

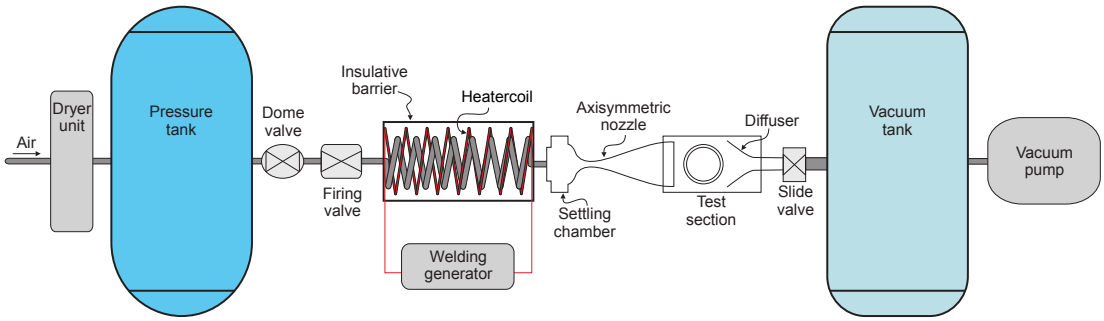


Figure 3.1: Schematic layout of the Aero-Physics Laboratory HSST Tunnel

regulator where a power dome controller Type C4 Model 208/3 is used to regulate the gas to the necessary tunnel operating pressure. The gas is maintained at the required pressure in order to achieve the required total pressure downstream of the settling chamber by using compressed air from a Compair Broomwade Type V85 compressor regulated by a pressure controller Type P.140 Model 133/140A. Next the gas passes through a pneumatically operated quick-acting ball valve, Worcester Type A45-4466-TT before entering the 24kW electric resistive heater that consists of a preheated 30m-long heater tube. The long heater tube measured 38mm inside diameter and wall thickness of 3.2mm, is formed into a coil of 16 turns of 0.6m diameter and is thermally and electrically insulated from the rest of the tunnel. The heater coil is also placed in a container filled with granules of vermiculite to reduce the heat loss to the surroundings. The heater acts in raising the temperature of the gas flow from ambient up to 700K or other temperatures that are sufficient to avoid liquefaction during the expansion through the nozzle.

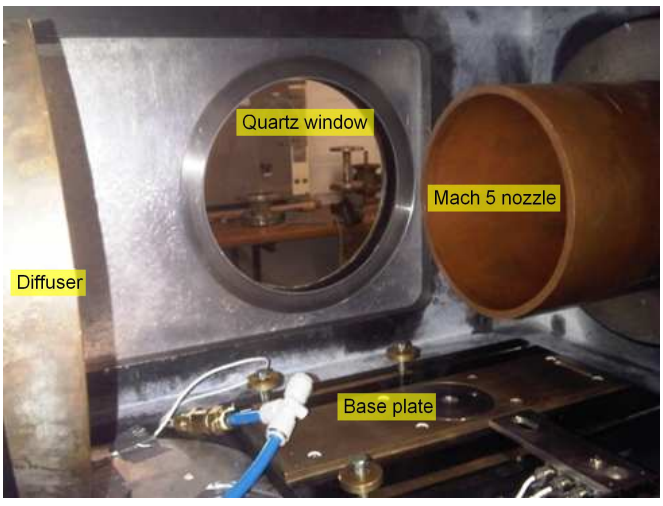


Figure 3.2: Picture of the test section with the nozzle exit and diffuser

Air is then being passed through the settling chamber consisting a flow straightener matrix that gives a uniform distribution for flow. Immediately after the settling chamber, is a contoured axisymmetric nozzle. There are three sets of 150mm exit diameter open-jet nozzles available for the tunnel with nominal Mach numbers of 4, 5 and 6. A pair of 170mm exit diameter annular-jet Mach 5 nozzles are also available consisting 51mm and 30mm diameter centre-bodies. The test section of the tunnel (refer Figure 3.2) is an enclosed free-jet design with the cross section of 325mm$^2$ and 900mm length with two interchangeable hinged access doors on either sides of the test section wall. The doors are mounted with the 195mm diameter Quartz window for optical access to the flow visualizations.

Downstream of the test section is a diffuser that has an entrance diameter of 250mm for the evacuation of the test gas from the test section to a vacuum tank which has the capacity of 32m$^3$. In order for the working section to be accessed during the depressurised process of the vacuum tank between the runs, a 200mm diameter motorised slide valve is positioned between the working section and the vacuum tank. This allows access to the vacuum tank without pressuring it so that it can be maintained at a pressure below 1.5mbar. The air is evacuated from the vacuum tanks by two rotary piston vacuum pumps, an Edwards BOC Stoke Microvac 412J and General Engineering Kinney Size GKD220 placed in series.

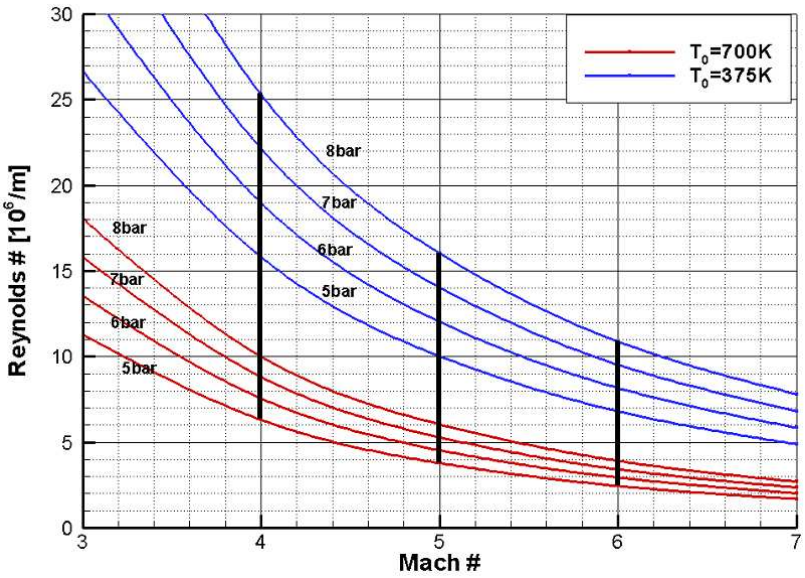


Figure 3.3: Variation of Reynolds number for different supply temperatures and pressures [60].

The variation of the Reynolds number for the tunnel operation is achieved

by varying the combination of supply pressures and heater temperatures. The typical variation of Reynolds number is between $5 \times 10^6$ m$^{-1}$ to $15.9 \times 10^6$ m$^{-1}$ for a pressure setting of 175psi and 200psi heater temperature settings between 370K and 550K. However a comprehensive envelope of the Reynolds number ranging from as low as $2.5 \times 10^6$ m$^{-1}$ to $26 \times 10^6$ m$^{-1}$ was plotted by Erdem [60] as shown in Figure 3.3. Eight curves based on stagnation pressure values of 5, 6, 7 and 8bar for two limiting values of temperature settings of 375K and 700K were drawn.

From the early HSST calibration documents [61], the heater temperature set is higher than the recorded total temperature in the freestream. This is due to the inefficiency of the heat transfer during the process. The running time of the tunnel are dependant and limited by the amount of heat that is able to be supplied by the heater and the evacuated mass flow rate by the vacuum pumps. The useful steady run times typically range between 7 to 10 seconds.

## 3.2 Calibration of HSST

This section will explain the calibration of the HSST done in detail by Erdem [60]. The main objective of the calibration is to determine the useful running time, flow uniformity and also the available space for the models to be accommodated inside the test section aft the Mach 5 non-centrebody nozzle which has a 152mm exit diameter. For this purpose, a pitot rake is specifically manufactured and is mounted on the sting of the arc system used for force balance measurements. The diagram of the pitot rake is shown in Figure 3.4. The outer diameter of the tube is 2mm while the internal diameter is 1.4mm. The pitot rake was placed at a position of 2mm (vertical distance) and 62mm (horizontal distance) from the nozzle exit. The streamwise, transverse and spanwise directions are represented by $x$, $y$ and $z$ directions, respectively. The calibration was done at a typical Reynolds number value of $13.1 \times 10^6 \text{m}^{-1}$ and the other conditions are tabulated in Table 3.1.

| $p_{supply}$ $(psi)$ | $T_{supply}$ $(K)$ | $M_\infty$ | $p_0$ $(mbar)$ | $T_0$ $(^\circ K)$ | $Re$ $(\times 10^6 m^{-1}$ |
|---|---|---|---|---|---|
| 175 | 375 | 5.0 | 6450 | 372 | 13.1 |

Table 3.1: Conditions of HSST calibration at Mach 5.

Figure 3.5 shows the time history of the stagnation pressure and temperature

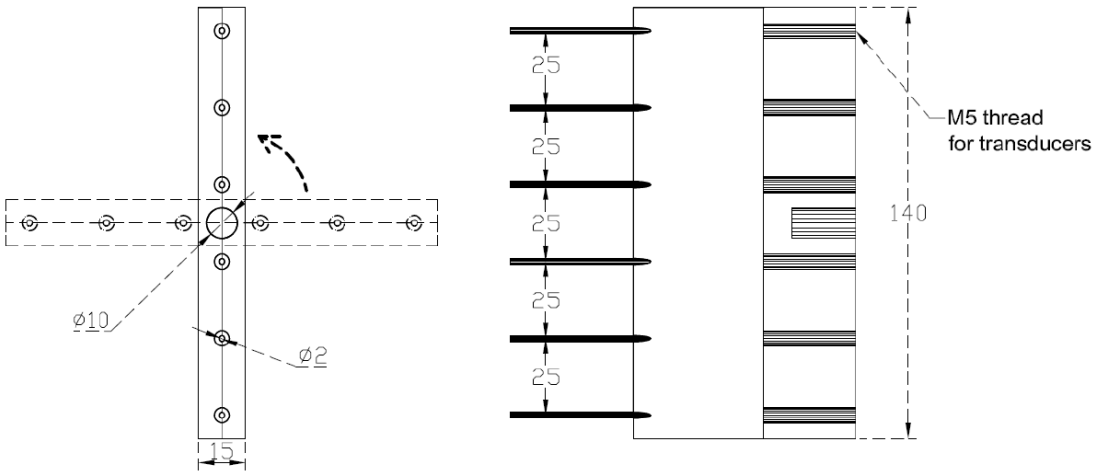


Figure 3.4: Schematic of pitot rake used in HSST calibration [60].

with pitot pressure history during the entire run. The signals were recorded at 5kHz (with 10kHz of hardware filtering). The stagnation and pitot pressure signals increased suddenly during the early stage of the run due to the initial shock propagating downstream. The initial shock passes the test section and eventually being swallowed by the diffuser. After that, a stable plateau is reached and remains for a certain duration of time. After approximately 8 seconds from the start, the pitot pressure signal recorded a sudden jump followed by severe oscillations. This corresponds to the movement of the normal shock from the diffuser to the upstream direction as a result of increased back pressure in the vacuum tanks. This denotes the termination of the useful running time. The variations during the plateau of the stagnation and pitot pressures are minor, of less than 1% and remained stable due to the stable supply of pressure by the dome valve.

By non-dimensionalising $p_{pitot}$ with $p_0$, the plateau can be seen more clearly as shown in Figure 3.6. From the divided signal, the useful running time can be determined directly as 7.5 seconds. The ratio, which is used to deduce the Mach number is very stable along the plateau line with very minor variations. Next, the Mach number is deducted using the Rayleigh's pitot tube formula as shown in Eqn. 3.1. The equation is applied based on the assumption of the specific heat ratio for air, $\gamma$ is invariable and this is true for practical purposes as long as the air temperatures of the flow are below 555K [62]. To solve the non-linear equation, MathCad© is used to conduct a root-finding routine since the left hand side of

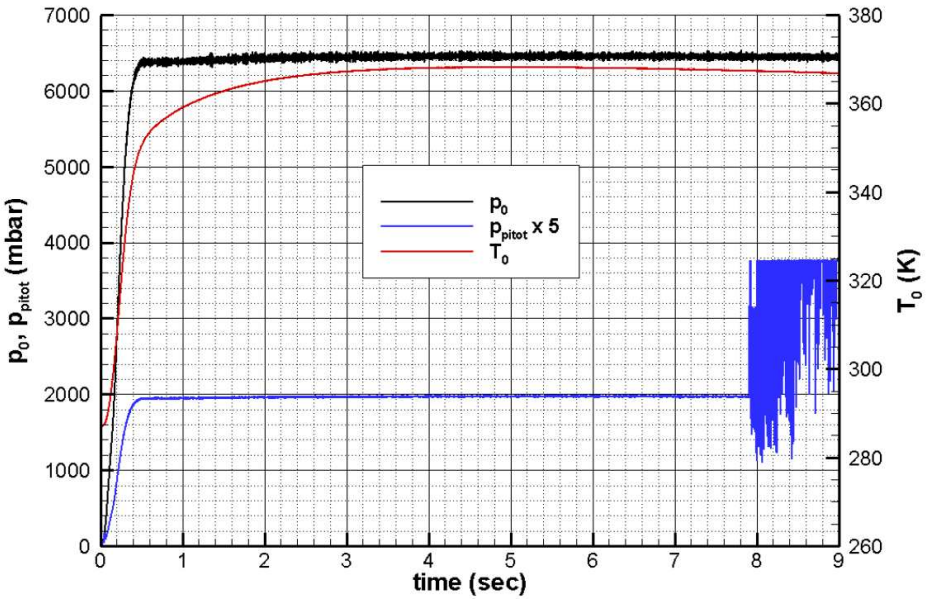


Figure 3.5: Time histories for stagnation pressure and temperature signals with a typical pitot signal. Note the right axis for stagnation temperature [60].

the equation is known.

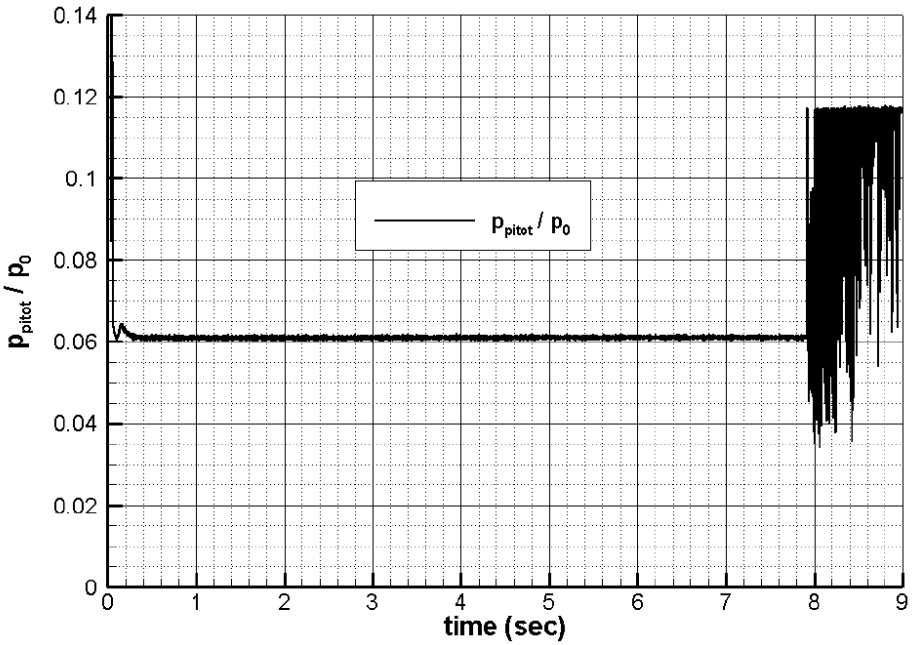


Figure 3.6: Time history of non-dimensionalised $p_{pitot}/p_0$ [60].

$$\frac{p_{pitot}}{p_0} = \left[\frac{(\gamma+1)}{2\gamma {M_\infty}^2 - (\gamma-1)}\right]^{\frac{1}{\gamma-1}} \left[\frac{(\gamma+1){M_\infty}^2}{(\gamma-1){M_\infty}^2+2}\right]^{\frac{\gamma}{\gamma-1}} \tag{3.1}$$

The frequency content of both stagnation and pitot pressure signals are also analysed as shown in Figure 3.7. The signals are clipped at both ends so that only the frequencies within the useful running time are displayed and the man values are subtracted from the instantaneous values before Fast Fourier Transform (FFT) is applied. From the graph, the highest peak in the stagnation pressure signal is seen at 200Hz. This might be caused by the harmonic component of the electronic noise. The other three peaks at 900, 1650 and 2000Hz might be sourced from the cavity frequencies, as $p_0$ is measured by a pitot tube connected to a small chamber, where the pressure transducer is fixed on the other side. All of these frequencies however are smaller than 2.5mbar in magnitude. A more spread out peak of 0.06mbar magnitude is observed at 360Hz for the case of the pitot pressure signal and no clear reason can be found. Comparing these peaks of the stagnation pressure and pitot pressure signals with the non-periodic flow signal, it can be said that they are relatively small in magnitude. Then another $p_0$ signal is recorded at 50kHz sampling rate but this time without the hardware filtering. The result is found to be considerably similar with the 5kHz case, justifying the sampling rate chosen.

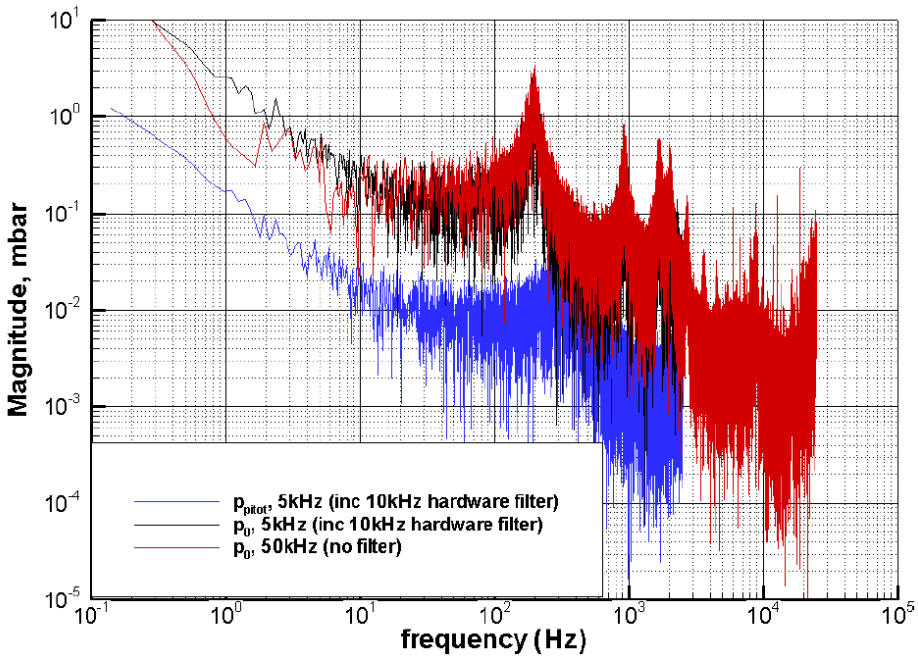


Figure 3.7: Frequency content of the pitot pressure signal [60].

For the case of stagnation temperature history, a continuous rise from the

vacuum temperature to a value close to the heater temperature (375K)is observed in Figure 3.8. Although the heater is carefully insulated, there is still a slight heat loss. The slow continuous rise of the temperature observed from the plot is due to the thermal inertia of the thermocouple. In theory, the behaviour of the thermocouple can be modelled as the solution of the first order ordinary differential equation with a time constant, $\tau$. If the theoretical values ($\tau$ is set as 0.6sec) are plotted on together with the experimental $T_0$ values, good agreement throughout the steady state value is achieved. Referring to the plot, $T_{vac}$ is taken as the initial temperature value and the final temperature value is taken as $T_{max}$ where the temperature gradient becomes practically negligible. The only difference between the experimental and the theoretical data is during the increase period where the initial increase in the experimental values is quite steep up to 0.2sec (inflection point). This might be due to the passing of the tunnel start-up shock wave. The increase is then sustained with the decreasing slope (i.e. $d^2T/dt^2$<0). The first order model started to match the physical behaviour of $T_0$ after 3sec. The steady value of 368K is taken as $T_{max}$ when the gradient becomes negligible ($dT/dt \approx 0$).

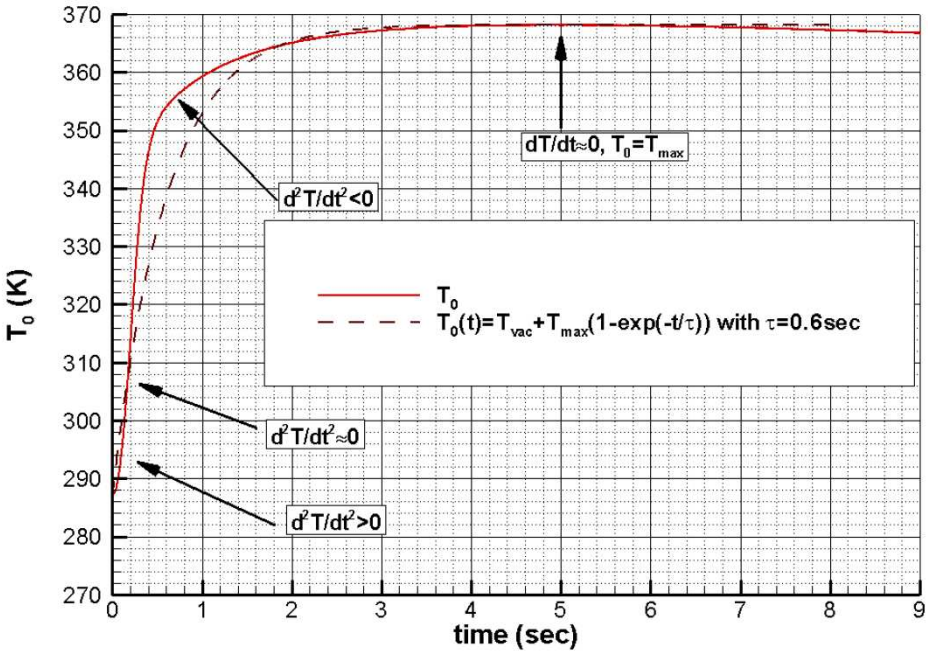


Figure 3.8: Stagnation temperature signal time history with theoretical first order estimation for a thermocouple behaviour with $\tau = 0.6$sec. [60].

The variations of the stagnation and pitot pressure signals recorded and discussed previously can be considered small and therefore the flowfield can be assumed steady for a duration of 7.5 seconds. Schlieren visualisation is later used to further verify this fact, by recording images of the flowfield spanning the entire duration of a test and the images are shown in Figure 3.9. The images shown represent the pitot rake vertical configuration at 2mm from the nozzle exit. The first image on the left corresponds to the startup phase of the flow then followed by the steady phase and the final image is the ending phase of the run. Another set of schlieren images in Figure 3.10 shows the flow over the pitot rake at two different streamwise locations; 2mm and 60mm from the nozzle exit and also at two different configurations; vertical and horizontal.

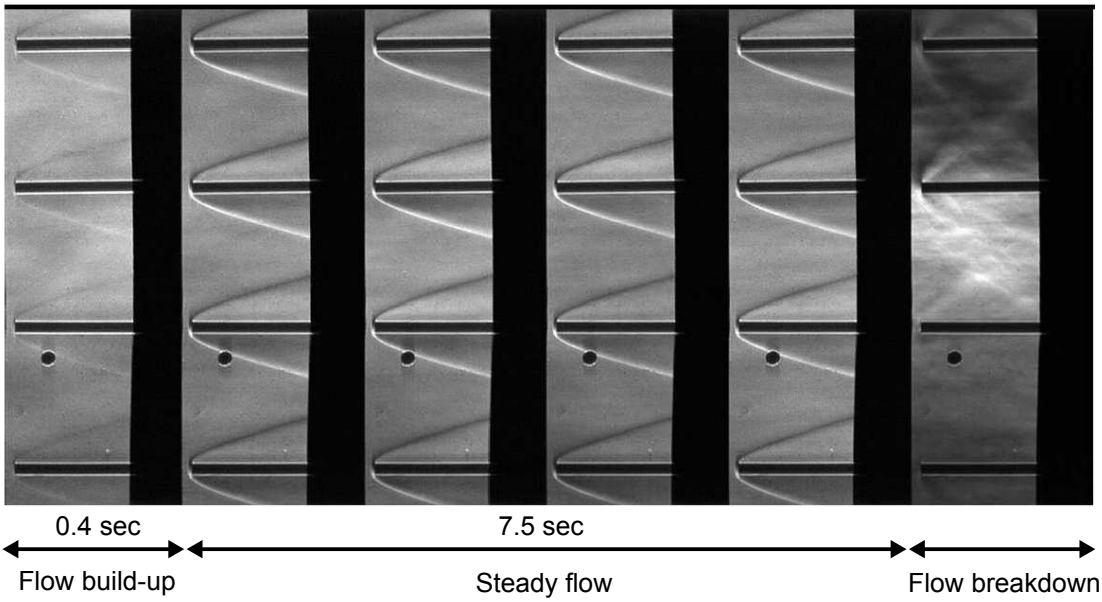


Figure 3.9: Schlieren images spanning the entire test duration. The vertical pitot rake was positioned at 2mm from the nozzle exit [60].

From the images, it can be concluded that the flowfield does not experience significant changes during the steady flow. Stable bow shock waves are seen to form clearly in front of the pitot tubes. Besides, there are Mach waves originating from the nozzle exit due to the pressure difference between the test section area and the nozzle exit. These Mach waves are not visible in the schlieren images in Figure 3.9 and 3.10. For big frontal area models like the pitot rake for instance, the weak Mach waves form a maximum angle of 20° with respect to the streamwise axis as illustrated in Figure 3.11. For models with smaller frontal area (i.e. single pitot tube), these waves propagate downstream at an angle as low as 13° from

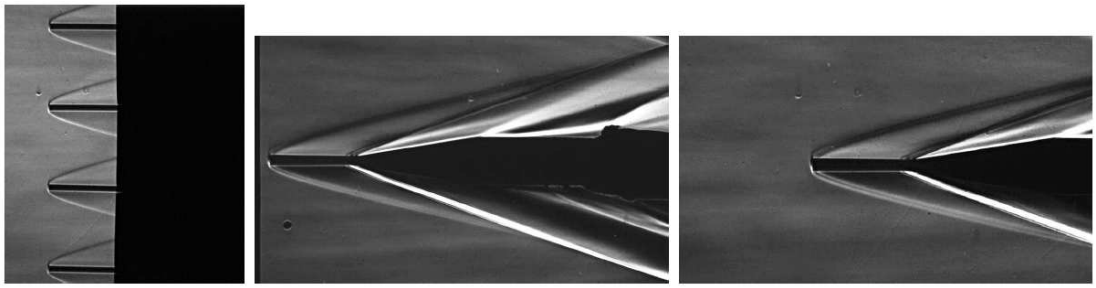

Figure 3.10: Schlieren images of pitot rake at different orientations and streamwise locations; horizontal at 2mm from nozzle exit (left), vertical at 62mm from nozzle exit (middle) and horizontal 62mm from nozzle exit (right) [60].

the horizontal axis. Therefore the designing process of each model to be tested inside HSST should take this matter into consideration. Any model should not intersect with these Mach waves to prevent wind tunnel blockage. The larger the frontal area of the model, the higher the chances of the blockage to form. The typical blockage ratio is given by Pope [62] as shown in Eqn. 3.2.

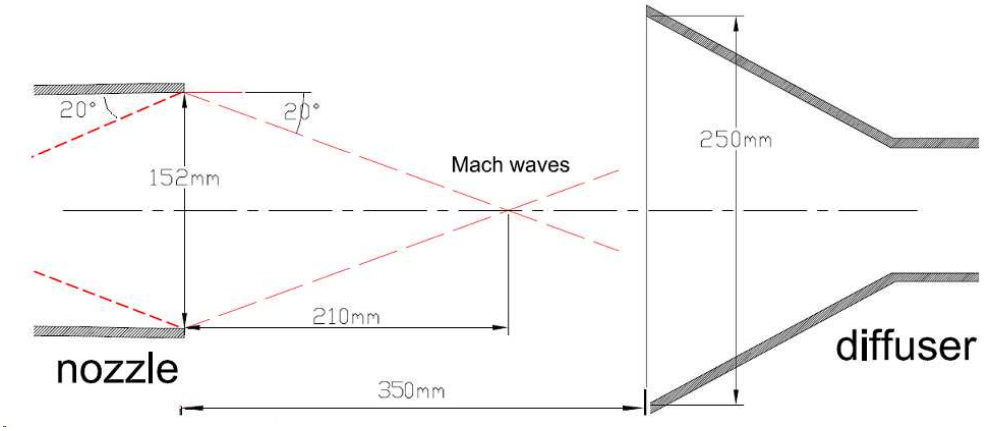


Figure 3.11: Test rhombus of HSST test section showing the minimum test section available area for models [60].

$$\beta = \frac{d_m}{\sqrt{A_{sec} - \delta^* P}} \tag{3.2}$$

where $\beta$ is the blockage ratio, $d_m$ is the diameter of the model (for blunt bodies), $A_{sec}$ is the test section area which corresponds to the nozzle exit area for HSST, $\delta^*$ is the displacement thickness and $P$ is the test section parameter which is the perimeter of the HSST nozzle exit HSST. $\beta$ for Mach 5 is 0.42 and from

this ratio, a blunt body diameter of up to 55mm is allowable for tunnel start-up. The maximum model length that can be tested inside the test section is 400mm. This is estimated based on the assumption that the symmetric Mach diamond (test rhombus) as shown in Figure 3.11 extends to a distance of 210mm upstream inside the nozzle.

| x (mm) | y (mm) | z (mm) | Mach No. | x (mm) | y (mm) | z (mm) | Mach No. |
|---|---|---|---|---|---|---|---|
| 2 | 62.5 | 0 | 4.97 | 62 | 62.5 | 0 | 4.97 |
| 2 | 37.5 | 0 | 4.98 | 62 | 37.5 | 0 | 4.98 |
| 2 | 12.5 | 0 | 5.01 | 62 | 12.5 | 0 | 5.00 |
| 2 | -12.5 | 0 | 5.01 | 62 | -12.5 | 0 | 5.00 |
| 2 | -37.5 | 0 | 4.98 | 62 | -37.5 | 0 | 4.98 |
| 2 | -62.5 | 0 | 4.97 | 62 | -62.5 | 0 | 4.97 |
| 2 | 0 | 62.5 | 4.97 | 62 | 0 | 62.5 | 4.97 |
| 2 | 0 | 37.5 | 4.98 | 62 | 0 | 37.5 | 4.98 |
| 2 | 0 | 12.5 | 5.01 | 62 | 0 | 12.5 | 5.00 |
| 2 | 0 | -12.5 | 5.01 | 62 | 0 | -12.5 | 5.00 |
| 2 | 0 | -37.5 | 4.98 | 62 | 0 | -37.5 | 4.98 |
| 2 | 0 | -62.5 | 4.97 | 62 | 0 | -62.5 | 4.97 |

Table 3.2: Complete calibration results [60].

The complete calibration results from the pitot rake measurements are tabulated in Table 3.2. The flow quality inside the test section is very reliable in terms of symmetry and the Mach number variations are very small, of only 0.4%. The values of the freestream listed in Table 3.3 were calculated using isentropic relations and the uncertainties associated with them were estimated using standard techniques based on precision and bias calculations detailed by Moffat [63]. All of the uncertainties are based on 95% confidence interval levels. The source of uncertainties are from the supply pressure set by the dome valve, supply temperature set by the heater and measured pressure from data acquisition system.

## 3.3 Experiment Models & Setup

### 3.3.1 Micro-Ramp General Study

The generic micro-ramp design is shown in Figure 3.12. All of the models were manufactured using Aluminium Grade 6082 (H30). The optimisation studies done by Anderson et al. [31] listed in Table 2.2 was taken as a guide. However a

| Freestream Properties | Value |
|---|---|
| $M$ | $5.0 \pm 0.5\%$ |
| $p_0$ $(mbar)$ | $6450 \pm 0.7\%$ |
| $Re$ $(\times 10^6)/m$ | $13.1 \pm 1.7\%$ |
| $p_{pitot}(mbar)$ | $396 \pm 1\%$ |
| $p_\infty(mbar)$ | $12.18 \pm 2.4\%$ |
| $u_\infty(m/s)$ | $790 \pm 1.0\%$ |

Table 3.3: Freestream values with uncertainties of HSST at Mach 5.

number of alterations were made in order to adapt with the wind tunnel facilities. Three different sizes of micro-ramps were manufactured and their dimensions are listed in Table 3.4.

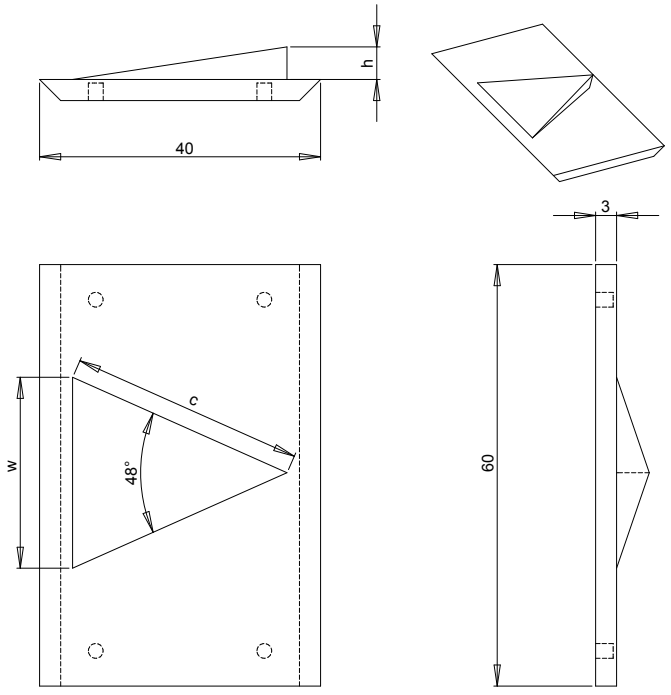


Figure 3.12: Generic dimensions of the single micro-ramp configuration.

| Dimensions (mm) | MR80 | MR60 | MR40 |
|---|---|---|---|
| Height, $h$ | 4.64 | 3.48 | 2.32 |
| Chord Length, $c$ | 33.4 | 25.1 | 16.7 |
| Width, $w$ | 27.2 | 20.4 | 13.6 |

Table 3.4: Dimensions of single micro-ramp models

As can be seen in Figure 3.12 the micro-ramps were manufactured in one piece with the aluminium strip to minimise the complication of fixing the micro-ramp onto the flat plate. Four tapped holes were drilled on the bottom surface of the strip and fixed with M2 studs and nuts were used with the studs to fasten the micro-ramp strip to the flat plate. Apart from the single configuration, array configurations were also manufactured based on the same size in Table 3.4 and this is shown in Figure 3.13. An extra dimension that needs to be considered when designing the array configuration is the spanwise distance, $s$ between the ramps. However this is limited to the width of the metal strip and therefore $s$ is not constant for all the models as listed in Table 3.5.

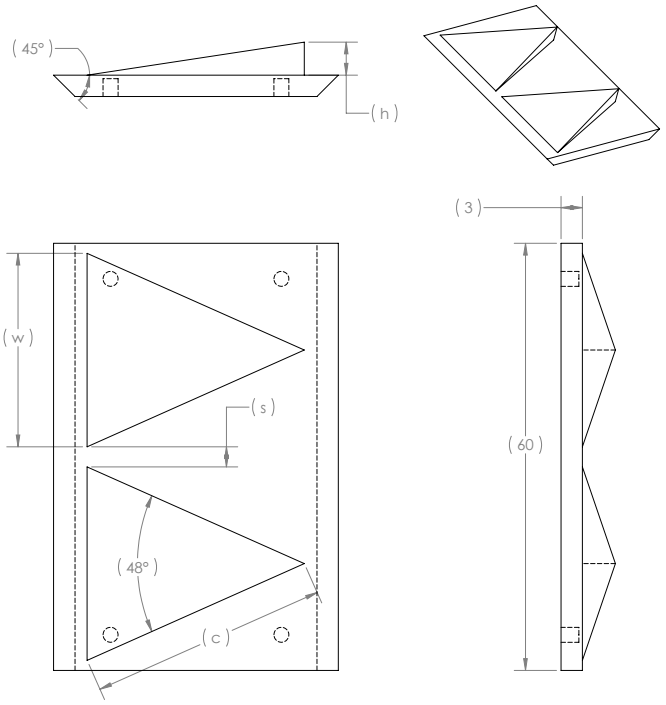


Figure 3.13: Generic dimensions of the micro-ramp array configuration.

| Dimensions (mm) | MR80 | MR60 | MR40 |
|---|---|---|---|
| Height, $h$ | 4.64 | 3.48 | 2.32 |
| Chord Length, $c$ | 33.4 | 25.1 | 16.7 |
| Width, $w$ | 27.2 | 20.4 | 13.6 |
| Spanwise spacings, $s$ | 2.8 | 2.2 | 1.5 |

Table 3.5: Dimensions of micro-ramp array models

Due to the same limitation, the number of micro-ramps on the array configurations could not be the same for all the sizes. For MR80 and MR60, there are 2 units of micro-ramps on each strip while 4 units for MR40 model. The total number of models manufactured is six, three single models and another three array models. The actual picture of them is shown in Figure 3.14.

Figure 3.14: Photo of all six models, single configuration (top) and array configuration (bottom) painted with black-matte paint.

A thin flat plate made of Aluminium 6082 grade (H30) was used for this micro-ramp general study. The micro-ramps were screwed onto a slot made on the plate. Then the flat plate was fixed to an aluminium stand. Finally the assembly was secured to the base plate on the floor of the test section (refer Figure 3.2) using eight M4 screws. As can be seen from Figure 3.15 the length of the plate is 360mm, which is relatively long compared to the previously used models in the same facility [60, 64]. This length was needed to achieve natural turbulent flow at a significant upstream distance from the location of micro-ramp.

A slot was made on the top surface of the flat plate to place the micro-ramp strip and followed by 30 pressure tappings for pressure measurements downstream the slot as shown in Figure 3.15. Note that the pressure tappings are situated only on one side of the flat plate. Stainless-steel hypodermic tubes with outer diameter of 2mm and internal diameter 1mm were used as the tappings. The final assembly of the micro-ramp (together with the strip), long flat plate and vertical stand is illustrated in Figure 3.16.

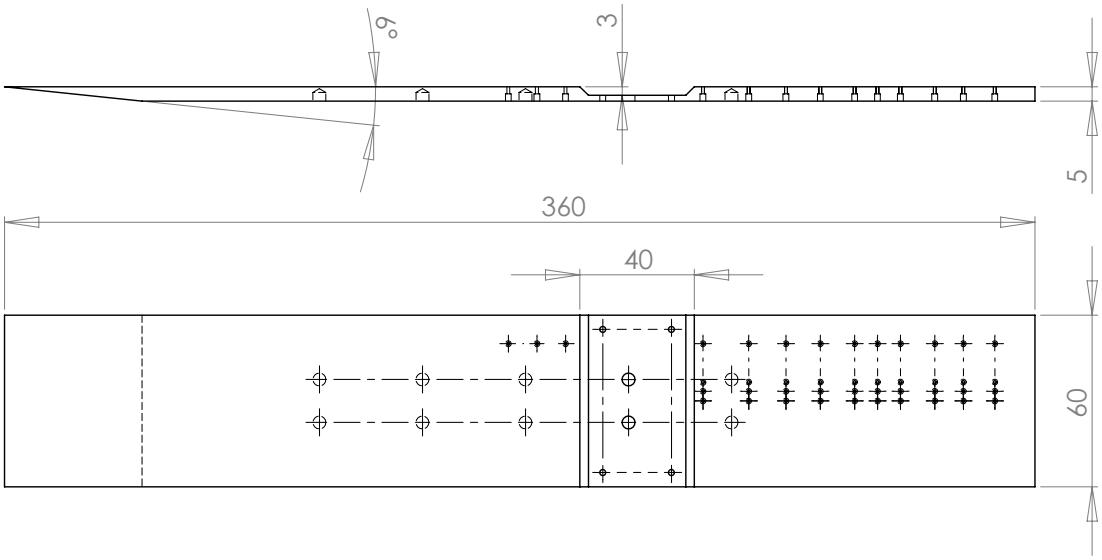


Figure 3.15: Design of the aluminium flat plate model used for general study.

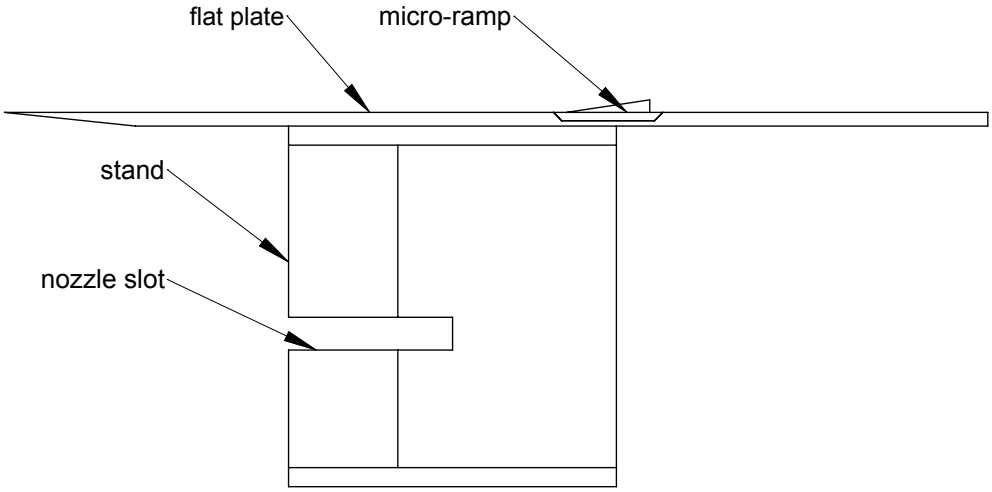


Figure 3.16: Assembly of micro-ramp, flat plate and stand. Flow direction is from left to right.

### 3.3.2 Optimisation Study

New micro-ramp models were manufactured for the purpose of the optimisation study. Three varied geometries were the height $h$, chord length $c$ and spanwise distance between micro-ramps $s$. As can be seen from Figure 3.17, the width of the strip was increased from 60mm to 90mm. This is done in order to test a range of $s$ values. This time, the number of micro-ramps per strip is fixed to three despite the sizes. This is done to eliminate external factors that might affect the optimisation studies. The length of the strip was also altered from

40mm to 44mm to allow more room for flow visualisation at surfaces close to the micro-ramp trailing-edges. The thickness of the strip was maintained the same as in the general study as shown in Figure 3.13.

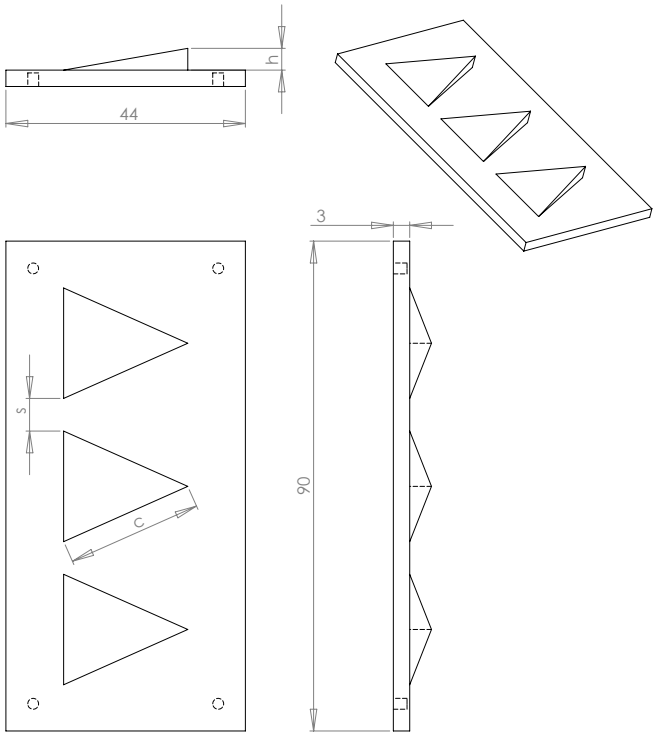


Figure 3.17: Generic geometries of the models used for the optimisation study.

A new flat plate was manufactured to conduct this study. The width of the new plate was increased to 90mm from 60mm to accommodate the new wide model strip. The number of pressure tapping holes were increased to give more resolution of the pressure and drilled only along the centreline of the plate. This was done to ensure more undisturbed surface area is available for visualisation reason. The screw holes for mounting the vertical stand were maintained at the same locations.

### 3.3.3 Mach number validation

Based on the calibration documents of the HSST wind tunnel [61], there is a maximum usable area inside the test section. The main reason for this is due to the existence of the cone-shock wave and this limits the area that the model could be placed inside the test section. The shock wave originates from inside the nozzle and is reflected at the nozzle exit. Finally this shock wave propagates

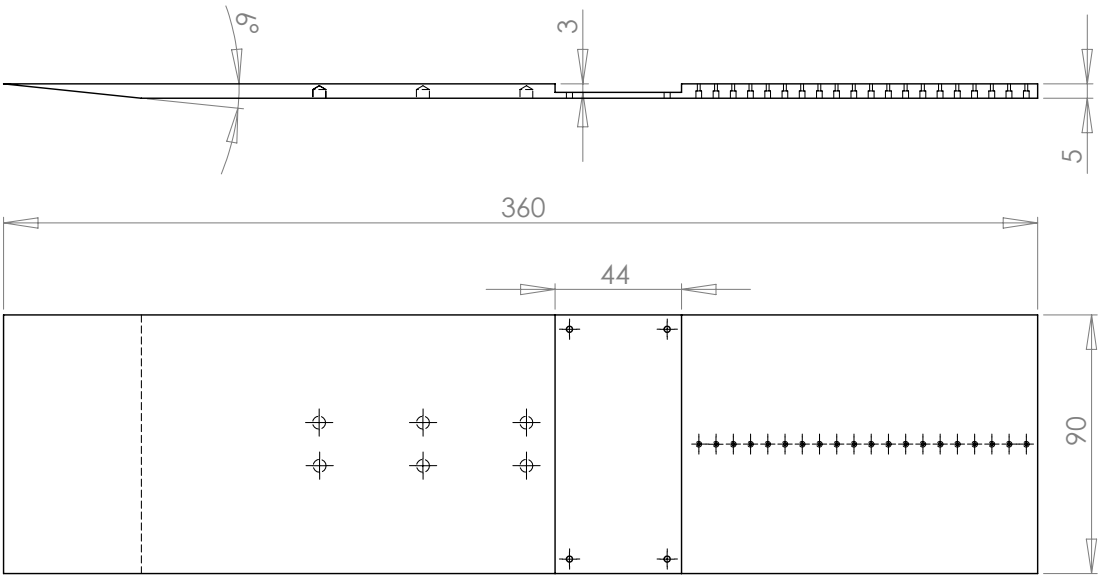


Figure 3.18: Design of the new 90mm wide aluminium flat plate used for optimisation study.

downstream to the test section area and form a cone-shape wave. The maximum model length that can be placed inside the test section is 400mm based on the assumption of the test rhombus constructed by Erdem [60] shown in Figure 3.11.

From Figure 3.15 a number of pressure tappings are located at the most downstream position on the flat plate and due to the length of the flat plate, the nozzle-shock will definitely impinge on the pressure tappings. The undesirable impingement could lead to pressure peaks during the pressure measurements. Therefore to avoid this the leading edge of the flat plate is inserted into the nozzle exit for a distance of 164mm. To achieve this the vertical stand was modified by cutting a slot to allow room for the nozzle exit as shown in Figure 3.19.

Mach number measurements in the HSST facility were done previously by Edwards and Orchard [61] but only up to a distance of 100mm inside the nozzle at the centreline. The Mach number was found to only fluctuate by less than 1%. However, there are no evidence that the Mach number would remain constant if the flat plate is being inserted for 164mm. Therefore before proceeding further with the test it is important to conduct Mach number measurement inside the nozzle. A pitot probe was mounted from the top of the test section and connected to a Kulite pressure transducer as shown in Figure 3.20. Three streamwise locations on the flat plate were tested as shown in Table 3.6 .

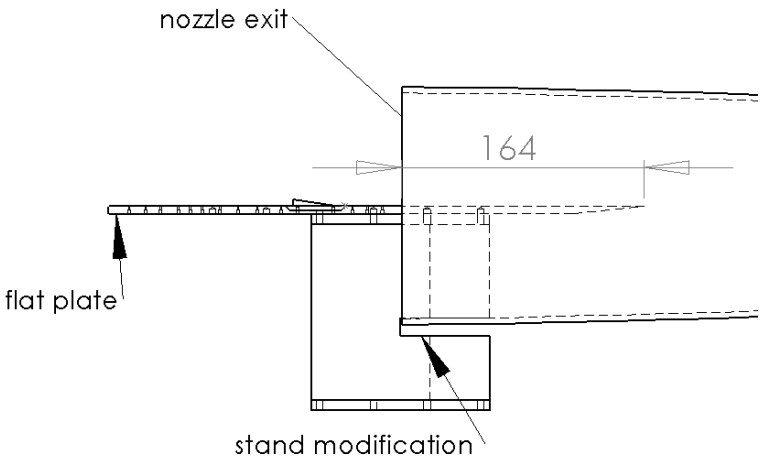


Figure 3.19: Leading edge of flat plate inserted 164mm inside the nozzle.

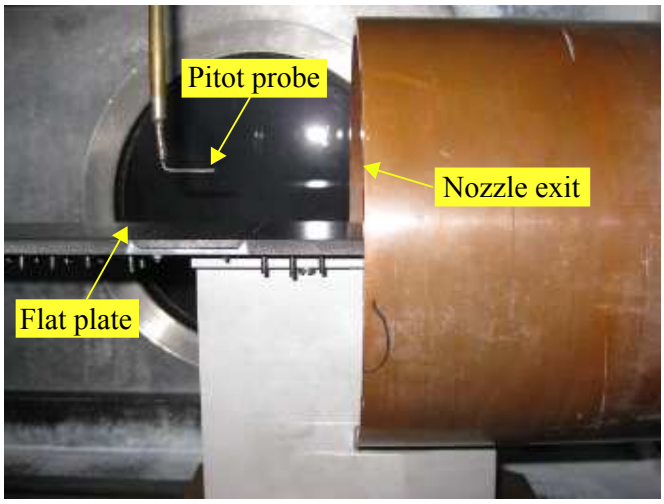


Figure 3.20: Mach number investigation inside the HSST test section using a single point pitot probe.

| Location | A | B | C |
|---|---|---|---|
| Distance from leading edge (mm) | 325 | 218 | 125 |
| Distance from wall (mm) | 20 | 20 | 5 |

Table 3.6: Streamwise locations of Mach number measurements.

The measurements were repeated three times at each location to ensure repeatability. In order to deduct the Mach number from the pressure measurements, the normal shock relations (Rayleigh Pitot tube formula) in Equation 3.1 is used with the assumption that $\gamma$ is invariable.

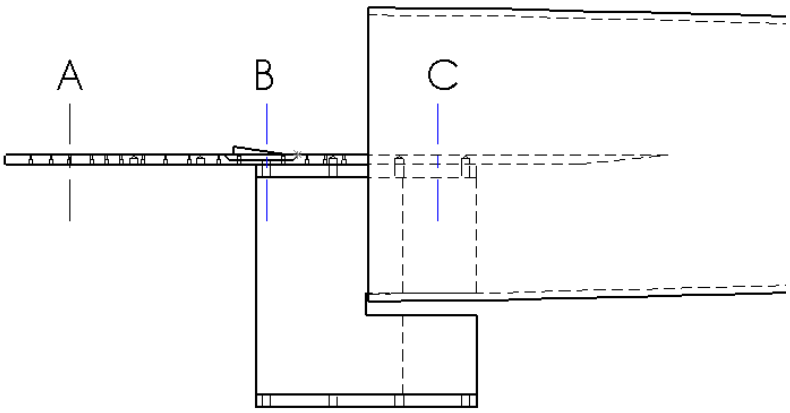


Figure 3.21: Three streamwise locations on flat plate for Mach number measurements. Z location was maintained at the centreline of the nozzle exit.

| Location | Mach Number |
|---|---|
| A | 4.96 |
| B | 4.95 |
| C | 4.95 |

Table 3.7: Results of Mach number measurements at different streamwise locations.

From the findings in Table 3.7, the standard deviation of the Mach number was calculated to be only 0.57% from the three locations. Earlier, Erdem [60] also conducted Mach number calibration at two several streamwise locations using a pitot rake and he deducted that the variations in Mach number were 0.4%, which is very small. For this case, there is an increase of 0.17% of the standard deviation.

Another method to validate the Mach number is by calculating the Mach angle of the model, which is the Mach angle produced by the leading edge of the flat plate in this case. Theoretically the Mach angle is given by the following formula:

$$\mu = \sin^{-1} \frac{1}{M} \tag{3.3}$$

Schlieren visualisation is one of the best experimental method to record the image of the shock wave produced by the leading edge. From the Schlieren image in Figure 3.22 the measured Mach angle is 11.79°. Theoretically the Mach angle

for a Mach 5 flow is calculated to be 11.54°. The error calculated between the experimental and theoretical value is 2% which can be considered low. Hence it can be concluded that after inserting the flat plate inside the nozzle for a distance of 164mm the Mach 5 flow remains constant and there are no sign of tunnel unstart or blockage. Therefore all of the results obtained from this investigation are valid for Mach 5 flow.

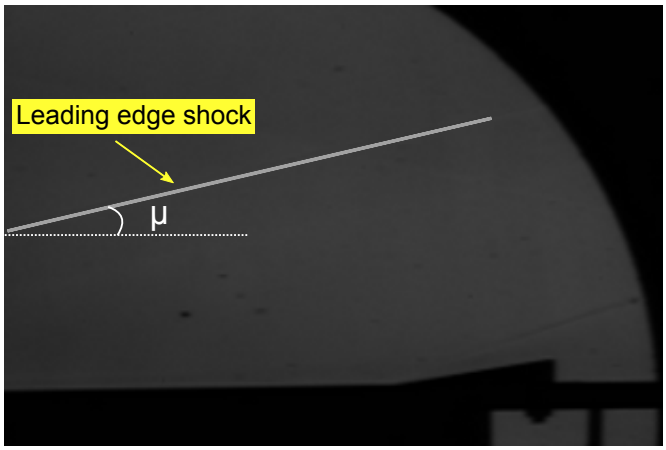


Figure 3.22: Schlieren visualisation showing the Mach angle from flat plate leading edge.

### 3.3.4 Installation of Shock-Generator

In order to investigate the effect of micro-ramp towards shock-boundary layer interaction, an oblique shock needs to be generated and it will eventually impinges on the flat plate downstream the micro-ramp location. For this reason a shock-generator is installed by mounting it to the ceiling plate of test section using an adaptor to accommodate an M8 threaded rod. The shock-generator creates a 34° oblique shock. Figure 3.23 shows the design of the shock-generator.

From Figure 3.24, there are two parameters that determines that positioning of the shock generator. $X_{SG}$ is the streamwise distance of the shock generator relative to the flat plate leading edge while $h$ is the vertical distance from the shock generator to the surface of the flat plate. These two parameters were varied in order to fix the location of the shock impingement on the flat plate according to the objectives of the experiments. Decreasing values of $X_s$ and $h$ will cause the shock to impinge at a more upstream location.

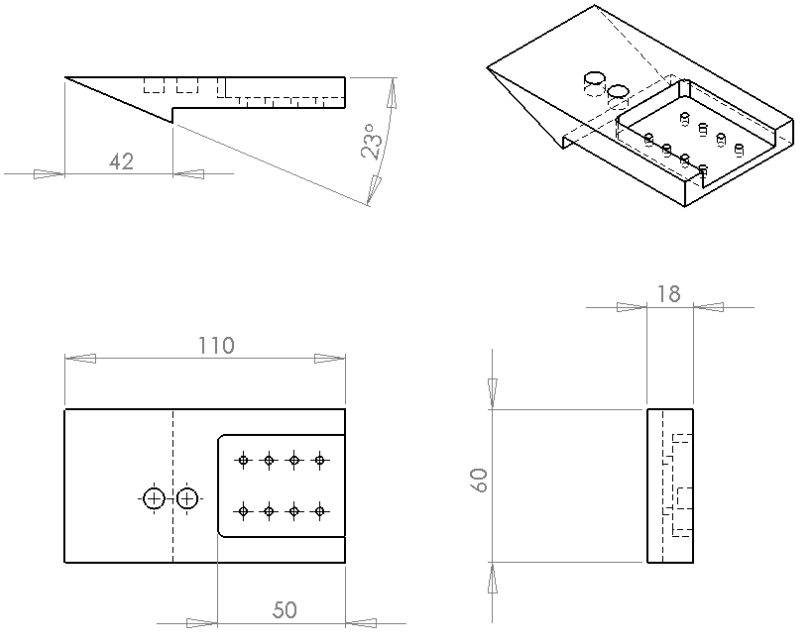


Figure 3.23: Technical drawing of the oblique shock generator.

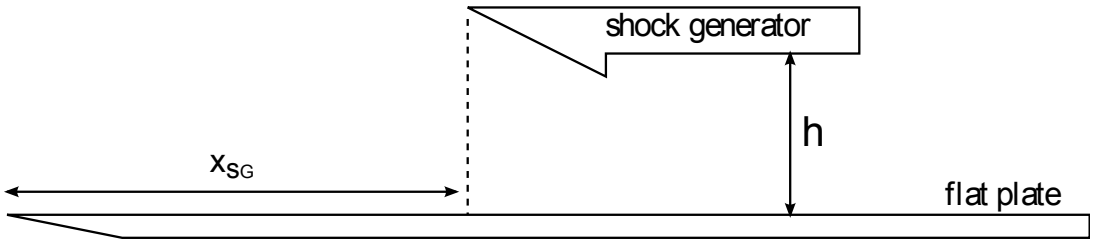


Figure 3.24: Schematic drawing of the position of the shock-generator.

## 3.4 Experimental Techniques & Flow Diagnostics

### 3.4.1 Schlieren Photography

The Aero-Physics Laboratory of the University of Manchester has the Toepler's z-type Schlieren technique [65] which consists of Palflash 501 (Pulse Photonics) continuous light source with a focusing lens and a 2mm wide slit, two 8 inches parabolic silver coating mirror of 6ft focal length, a knife-edge and a set of Hoya 49mm close-up lenses. To capture the images, a Canon digital SLR camera, EOS-450D, 12MP and a Photron APX-RS High Speed Video System is being used.

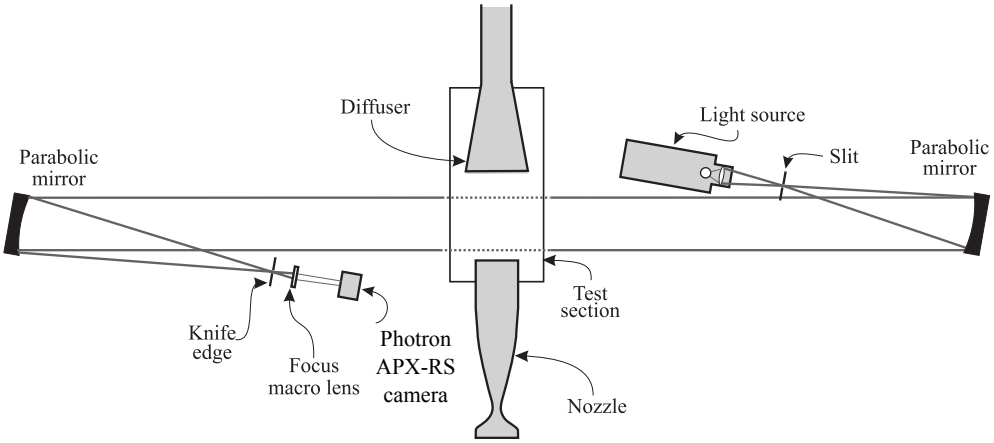


Figure 3.25: The schematic setup of high-speed Schlieren photography.

The parallel beam of light from the continuous light source travels through the test section windows before focusing on the knife edge plane which is positioned perpendicular to the flow direction. Later on, the focused beam is captured by the cameras. The Canon digital EOS-450D is capable of shooting in continuous mode which can record 3.5fps at full resolution and the shutter speed can be adjusted to maximum value of 1/4000sec with ISO400 speed to capture clear and enough detail images. On the other hand, the high speed Photron camera is used to record time-resolved Schlieren images up to 5000fps at a number of pixel resolutions and shutter speeds. Both cameras can be operated automatically from the 5V TTL trigger signal from the pressure transducer at the settling chamber.

The Schlieren technique is considered to be a qualitative measurements technique since it does not reveal any values of the flow characteristics including density. Other qualitative measurement methods need to be employed in order to get a comprehensive investigation of the flow. However, it is worth mentioning that Schlieren plays a vital role in giving an initial overview of the flow structures and determining the specific location of interest for measurements before other qualitative methods such as conventional pressure tapings can be applied.

Since Schlieren integrates the density of the whole volume of the flow, the density change can only be detected in two-dimension. This means that unsteady flows that involves three-dimensionality will not able to be captured intensively. However for two-dimensional flow structures, Schlieren would be a very helpful tool in flow diagnostics. Extra caution is needed when aligning the model and also the shock-generator so that the shock created are aligned with the plane of view. If this is not taken care of, the shock waves will be recorded as thick lines

instead of thin lines.

### 3.4.2 Oil-dot Visualisation

Oil-dot visualization is a technique that is used to visualize the flow pattern on a surface of a body. It is a representation of the behaviour at the near wall flow. Discrete dots are applied on the surface of the model and the final condition of the oil-dot deposits will indicate the flow condition such as flow separations, laminar, transitions and turbulents [66].

Grids are drawn on the model surface based on specific location of interest before applying the oil-dots. The discrete dots that are made from the combination of linseed oil, silicon 800 oil and titanium dioxide powder $TiO_2$ were applied on the matt black painted model surfaces by using a syringe in order to create 0.5mm blobs. The suggested mixture that has found to be optimum and suitable for hypersonic wind tunnels are 3g of $TiO_2$ dissolved in 12ml of linseed oil [67]. Oleic acid are introduced in order to improve the dispersion capability of the oil-dots. This is done by increasing the surface tension and size of the dot. Without the use of oleic acid, instead of the dots moving in the direction of the flow and producing oil-streak, it will tend to spread in a random manner. Silicone oil is also used to control the viscosity of the oil-dots.

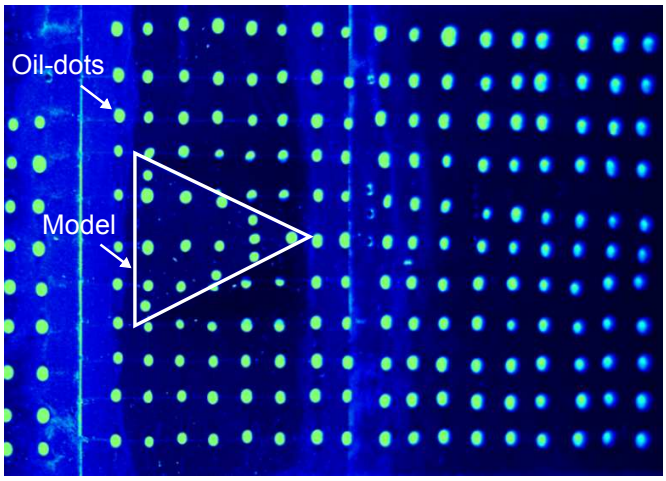


Figure 3.26: Setup of oil-dots applied on flat plate. Flow is from left to right. Distortion of the downstream region is due to image perspective correction.

The early challenge is to produce the correct recipe of the oil. The viscosity and surface tension of the oil-dots play an important role in the size of the dots produced and the dispersion abilities. Oil-dots that are too small will not react

to the flow and will not produce any movements. Large oil-dots will tend to spread instead of leaving streaks. Both of these characteristics, viscosity and surface tension depend on the quantity of oleic acid and silicone oil used. Another challenge is to determine the size of the grid for the positioning of the oil-dots. Low viscosity oil-dots will produce longer streaks. If the dots are close to each other, there are possibilities of overlapping streaks. Overlapping streaks are not favourable since they do not represent accurate behaviour of the flow. Changing the formula of the oil-mixture in order to improve the oil-dot dispersion will also require the grid spacings to be revised each time.

### 3.4.3 Oil-Flow Visualisation

The oil-flow visualisation method employed in this facility is inspired by the previous work by Pierce et al. [44]. In wind tunnel testing, the ability to reveal the complex flow features on the surface of a model is essential in having an initial insight of the flow for subsequent detailed measurements. Therefore, oil-flow seems to be the best method to be applied due to its ability to expose the footprints of the flow which later are useful to deduce the flow characteristics. This is the first time oil-flow is successfully employed in the Aero-Physics Laboratory while obtaining the correct setup and formulation for oil-flow were the hardest challenge.

The viscosity of the paint used in oil-flow plays the most important role. Having a high viscosity will cause the paint to take a longer time to move and exhibits the desired pattern, especially for the HSST facility that has 7-8 seconds of run time, this is a critical factor. On the other hand, if the viscosity is too low, the paint would simply be blown downstream straight after the tunnel started and no pattern can be visualised. Apart from the viscosity, the ability of the paint to be illuminated and produce reflections that are able to be captured by the recording devices is another important criteria.

The whole process of determining the right viscosity for a specific wind tunnel was trial and error. For this facility it is found that the mixture of paraffin, fluorescent colour powders, silicon oil and oleic acid satisfied the paint requirements. The fluorescent powder used has the size of 10$\mu$m on average. Initially, the powders were mixed with paraffin and applied ultrasonic stirring for five minutes. Later silicon oil and olec acid were added into the mixture and again ultrasonic stirring was applied but this time for a duration of 30 minutes. The recipe for

Figure 3.27: Three different fluorescent colours prepared for oil-flow visualisation.

the mixture was physically tested in the wind tunnel runs for several times. The mixture was initially too runny and to overcome this problem, more fluorescent powder was being added. This was done a number of times until the final and correct viscosity was close to a pancake syrup [44]. The exact formula for the paint is shown in Table 3.8.

| Ingredient | Quantity |
|---|---|
| Fluorescent powder | 2.63g |
| Parrafin | 9.0g |
| Silicon oil | 0.6g |
| Oleic acid | 5 drops |

Table 3.8: Paint formulation for oil-flow visualisation.

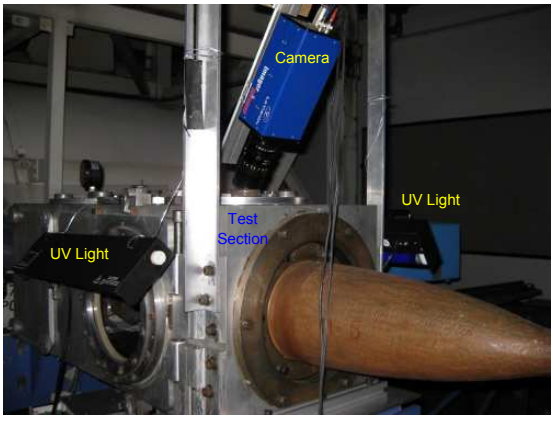


Figure 3.28: Experimental setup for oil-flow visualisation.

Three different colours were prepared for the investigation using the same

method; blue, yellow and red shown in Figure 3.27. Normally, one colour is sufficient. However, by using multiple colours, complicated flow features such as separations and mixing can be detected. Two Maplin Electronics UV light with 20W fluorescent tube of length 600mm was mounted at 45° angle on both sides of the test section windows to illuminate the mixture and this enhances the fluorescent effect. Mounting the lights on both sides of the test section provided maximum illumination with minimum direct exposure to the cameras. It also prevented shadows from occurring as a direct result from the model that would otherwise occur from using light on one side only.

A Digital SLR camera, Nikon D90 12.3 million pixels with 18-105 VR lense was used to record High-Definition videos of the run. It is capable of recording at 24fps of 1280×720 video with mono sound. Another camera that was used was the La Vision Imager Intense CCD camera that has a maximum frame rate of 5fps. The images captured by this camera were processed in DaVis 7.2® software. Both cameras were mounted on top of the test section one at a time at an angle of 20.8° from the vertical plane. Due to the design of the test section, it was impossible to position the camera normal to the model surface. This creates a perspective distortion to the images recorded. Before applying further post-processing with the images, first they are corrected using image processing software as shown in Figure 3.29 and then rotated so that the flow is seen coming from left to right.

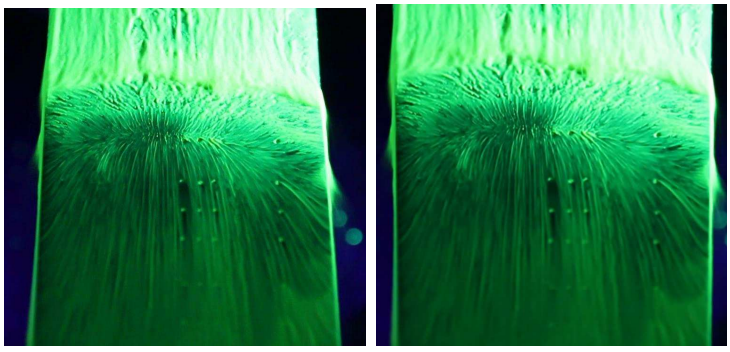

(a) Raw image (b) Corrected image

Figure 3.29: Oil-flow image captured by Nikon camera of uncontrolled interaction before and after correction.

The flat plate and the micro-ramps were both painted matte-black to increase the contrast. An area of 60mm × 60mm was drawn 30mm upstream from the micro-ramp leading edge to mark the location where the paint will be deposited.

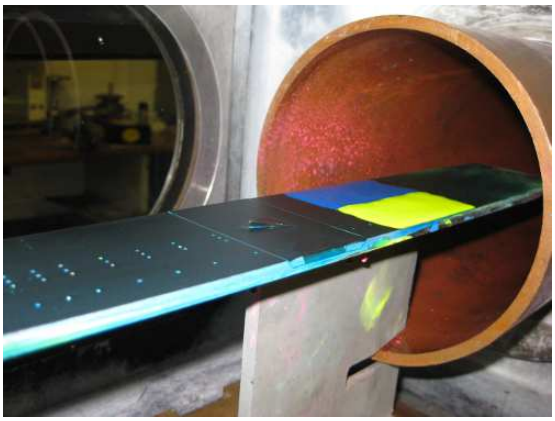

Figure 3.30: The multi-colour paint mixture is being applied upstream the model before the run.

A 5ml syringe was used to apply the paint onto the model and this was done carefully so that the paint does not spill and flow outside the dedicated boundary. The final setup before the run is shown in Figure 3.30.

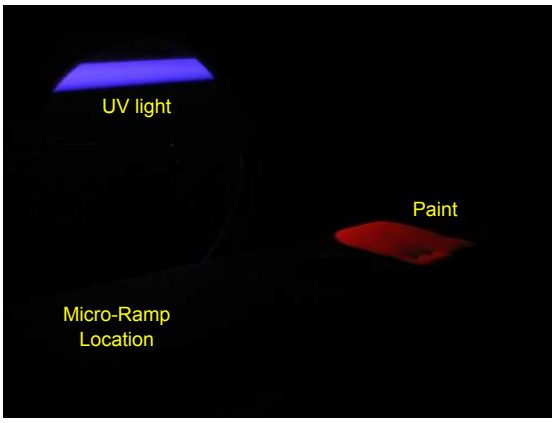


Figure 3.31: View of the 'glow in the dark' paint inside the test section.

After the paint was deposited, the valve that connects the test section and the vacuum tank was opened and this created a vacuum condition inside the test section. Hence, it is important to make sure that the paint applied upstream has constant thickness and is uniformly distributed. If not, when the test section starts to vacuum, the paint will start to smear and this is an undesirable condition prior to the testing. After the run, the model was taken out from the test section and pictures of the dried paint (due to evaporation during the run) was recorded. Finally a window cleaning solvent was used to wipe the model and a new paint was applied once again onto the surface. The time between two runs can be

estimated to be less than 20 minutes. Multi-colour paints were used for both single and multi array micro-ramp configurations.

### 3.4.4 Infrared Thermography

Infrared (IR) thermography is a state of the art diagnostic method to measure the surface convective heat transfer which is useful for many hypersonic applications such as boundary layer laminar to turbulent transition detection [68], heat transfer characteristics in a compression corner [69] and the study on blunted cone-flare model [70]. Therefore the studies on heat transfer can potentially reveal complex flow topology such as separation region and vortices that proved to be useful in the studies of micro-ramp.

The IR camera used in the Aero-Physics Laboratory for this investigation was the FLIR Thermacam® SC 3000 cooled system. It is capable of measuring temperature ranging from $-20°$C to $+1500°$C with the accuracy of $\pm 2\%$ or $\pm 2°$C. It is equipped with GaAs QWIP detector with resolution of $320 \times 240$ pixels and cooled to 70K in less than 6 minutes. The recording frequency of the camera is 50/60Hz. The camera has to be kept at ambient pressure and therefore mounted on top of the test section at an angle of $15°$ from the vertical plane. The window on top of the test section is specially made from Germanium (Ge) which is a commonly used material for infrared window. It has high index of refraction and good IR transmission. Its transmission is very temperature sensitive, becoming opaque near 100°C. The camera is connected to a dedicated PC to record and store the images. The camera was calibrated before the series of test. This is done using a calibrated dark body. The calibration must use the actual optical pieces that will be used for the experiments in order to consider all the possible errors and defects.

Another aspect is the material used for the studies. It can be both from insulating material or conductive material. However insulating material increases the temperature at a higher rate and this may affect the result. The emissivity of the model surface in an important factor and needs to be as high as possible. The normal practise in order to achieve this is by coating the surface with a thin layer of paint that has high emissivity. In this case both flat plate and micro-ramps are painted with black paint which eventually yields emissivity of 0.95.

Two main properties that were investigated using this technique were local heat flux rate $\dot{q}$ and Stanton number $St$ which is the nondimensionalised value

of $\dot{q}$. Obtaining $\dot{q}$ especially can reveal the flow characteristics at the specific location of interest while $St$ is useful for comparison with other models which are conducted at different experimental conditions. To work out $\dot{q}$, the following thin-skin technique from Schülien [71] was used:

$$\dot{q} = \rho_m c_m d_m \frac{\mathrm{d}\, T_w}{\mathrm{d}\, t} \tag{3.4}$$

for $t_{min} < t < t_{max}$. The limiting values of $t_{min}$ and $t_{max}$ were obtained from the steady run time of the HSST wind tunnel, excluding the tunnel startup and shutting down time. $T_w$ is the measured rise of the wall temperature. The thin-skin technique can be applied if the wall temperature normal to the model surface can be assumed uniform and the lateral heat conduction in the wall can be neglected. These conditions are attained if the thin-wall test model is manufactured from high thermal conductivity materials such as copper, nickel, aluminium, etc. To nondimensionalise $\dot{q}$, the following formula for $St$ was applied:

$$St = \frac{\dot{q}}{\rho_\infty U_\infty c_p (T_0 - T_w)} \tag{3.5}$$

The properties of the freestream flow conditions and material in this investigation applied in Equation 3.4 & 3.5 are listed in Table 3.10 and Table 3.9 respectively. The model surface is considered isothermal, due to the very short running time of the wind tunnel of about 7 seconds [62].

| | |
|---|---|
| Specific Heat (Air), $C_{p-air}$ | 1007.81(N.m/kg.K) |
| Static Temperature, $T$ | 62.79K |
| Static Pressure $P_\infty$ | 1354.93Pa |
| Reynolds number $Re$ | 13.3 $\times 10^6 \mathrm{m}^{-1}$ |
| Total Temperature $T_0$ | 376.74K |
| Freestream Velocity $U_\infty$ | 785.69m/s |

Table 3.9: HSST Flow condition during infrared thermography experiment.

After the acquisition of the images which were saved in .mat format, the images were loaded into Matlab for further processing, including the calculation of the Stanton number and the averaging of the steady-state images. For the case of image averaging, the initial image showing the average temperature distribution of the model is shown in Figure 3.32a. It can be seen that the pixelisation of the

| | |
|---|---|
| Material | Aluminium Alloy (Grade 6082) |
| Density $\rho_m$ | 2700kg/m$^3$ |
| Thermal Heat Capacity C$_m$ | 896J/kg.K |
| Thermal Conductivity $\lambda_m$ | 167W/m.K |

Table 3.10: Properties of the material used in the infrared thermography experiment.

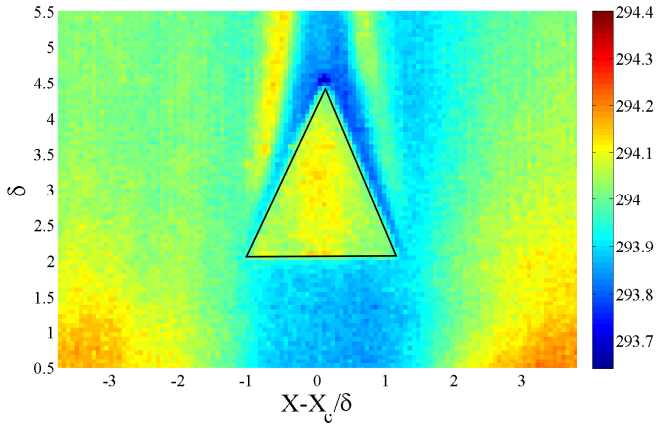


(a) Image before filtering.

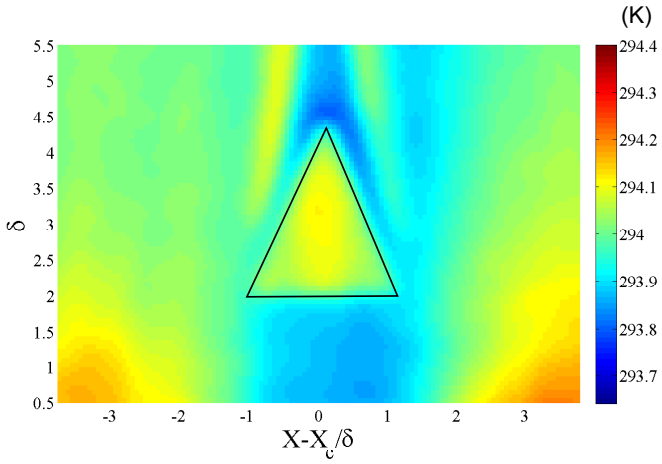


(b) Image after filtering.

Figure 3.32: Time-averaged infrared thermography images of MR40 before and after applying the filters.

temperature distribution is apparent. Therefore a series of image filtering was applied. A 3 pixel×3 pixel filter with 5 passes were used to smoothen the images and the results is shown in Figure 3.32b. The use of a larger filter such as 5 pixel×5 pixel would significantly smoothen the images but it will also eliminate detailed flow features that are desirable to be observed. Therefore using a smaller

pixel filter with multiple passes was found to be the best method to smoothen the pixelization but at the same time keeping most of the flow features visible.

### 3.4.5 Pressure Sensitive Paint

The basic operating theory of Pressure Sensitive Paint (PSP) is the illumination of the luminescent molecules that are used as probes at a specific wavelength which results in excitations. The excited molecules then emit lights of longer wavelength that are visible to the image capturing devices. The photons emitted however interact with the oxygen molecules since the polymer binder for the PSP is oxygen permeable. The interaction causes the photons to lose some energy due to the collision with oxygen in a process called oxygen quenching. When the excited luminescent molecules have returned to the ground state while at the same time the emitted photons are being quenched by the oxygen molecules, the luminescence is being decreased as a result. The change in intensity of the surface is recorded by the cameras. The schematic of the working process is illustrated in Figure 3.33.

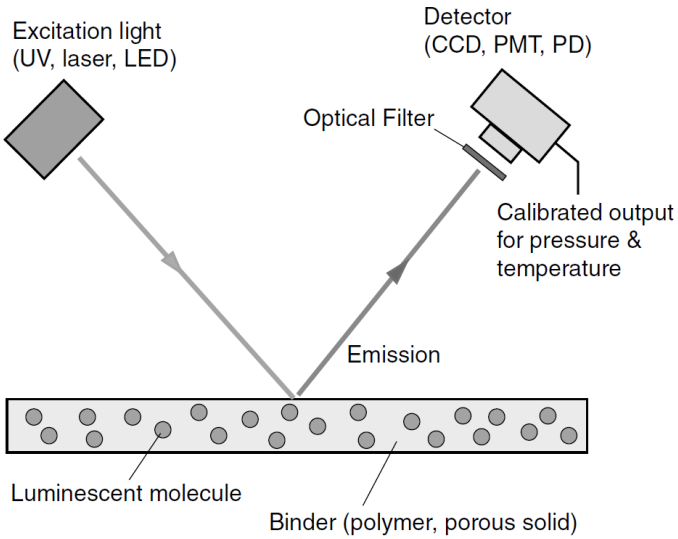


Figure 3.33: Schematic of a luminescent paint (PSP) on a surface [72].

Based on Henry's law, the concentration of the oxygen's molecules in PSP is proportional to the partial pressure of oxygen in the gas above the polymer [72]. When the pressure is increased on the surface, the concentration of oxygen molecules will be higher. Hence more quenching process of the luminescent molecules by oxygen takes place. This results in the decrease of the paint

intensity. Therefore, the higher the air pressure of the painted surface, the lower the intensity of the paint. The change in pressure is translated into the change in the paint intensity. The relation between the intensity, $I$ and the pressure, $p$ is given by the Stern-Volmer relation:

$$\frac{I_{ref}}{I} = A + B\frac{p}{p_{ref}} + C\left(\frac{p}{p_{ref}}\right)^2 + \dots \tag{3.6}$$

where $I_{ref}$ and $p_{ref}$ refers to the intensity and pressure at the reference condition, respectively. $A$, $B$ and $C$ are the Stern-Volmer temperature-dependent coefficients that are obtained experimentally from the calibration process. $I_{ref}$ is the intensity of the model that is taken when the wind-tunnel is turned off or at no flow condition and is usually called wind-off intensity while $I$ is the image recorded during the wind-on situation. So it can be seen here that the reference condition that is usually used for wind-tunnel experiments is the no-flow condition. From Equation 3.6, the ratio of intensity $I_{ref}/I$, theoretically eliminates the effect of uneven coating of the paint, non-uniform illumination and the non-homogeneous luminophore concentration in the paint. A complete system of PSP usually consists of several components; the specially formulated paint, illumination lights (lasers, ultraviolet xenon lamps, LEDs), photodetectors (CCD cameras or photomultiplier tubes) and an integrated data acquisition and processing unit.

The Aero-Physics Laboratory has developed a new PSP formulation that consists of platinum-tetrakis (pentafluorophenyl) porphyrin (PtTFPP), methy triethoxysilane (MTEOS), ethanol and hydrochloric acid (HCl). PtTFPP, which was found to be more pressure sensitive, was chosen as the luminophore replacing ruthenium tris-(bathophenanthroline) perchlorate (Ru(II)) that was used in the previous in-house formulation [73]. The METEOS solution is used as the binder, based on its high oxygen permeability property and ethanol acts as the solvent for the luminophores. Finally HCl was used as the catalyst for the reaction.

The models were cleaned completely using acetone to remove the grease and remaining paint that is left on the model surface. The cleaning is followed by the use of water to remove all the acetone that is left on the surface. Next the models were placed in an oven and left at a temperature of 100°C for an hour to completely dry the surface of the model. Then the oven was switched off and the models were left to cool down to the room temperature before the painting process could be started. The models were then sprayed with five layers of matt

white paint as the base coat. To ensure that each layer was properly dried before another layer is to be applied, a time interval of 5 minutes between layers was set. The models were then left to dry completely for 12 hours in room temperature.

The pressure sensitive paint was mixed on the same day as the spraying process. The mixing process was done in a dark environment in order to minimise the effect of photodegradation of the paint. Upon completion of the mixing process, the paint was placed inside the ultrasonic bath for 30 minutes to ensure proper mixing of the chemicals. Again this was done in a dark environment. Next the paint was removed from the ultrasonic bath and left to cool down to room temperature, as the paint was heated up during the mixing. Only then the paint was ready to be sprayed onto the models and this was done using an airbrush. For each model, a total of 120 layers of paint were applied on the model and between every 10 layers, there was a waiting time of 5 minutes. The flow rate of the airbrush was carefully ensured constant throughout the spraying process so that the result would be as uniform as possible.

Once the spraying process was done, the models were once again placed inside the oven at a temperature of 70°C to ensure all the solvent in the paint evaporated and the paint itself was dried completely. The oven was only turned on when all the models were placed inside and the temperature was increased gradually to 70°C from room temperature. This is important to avoid the sudden and rapid evaporation of the solvent due to the abrupt change of temperature experienced by the painted models if the temperature of the oven were preset beforehand. The rapid evaporation would cause the painted surface to suffer from poor surface finishes and even cracks as this has been reported in the study of Basu and Kamble [74].

During the experiments, the painted models were mounted inside the test section with two UV LEDs panels acting as the excitation light source, shining through the test section window on both sides. Each LED panel consists of 100 blue LEDs arranged in $10 \times 10$ array producing the peak wavelength of the emission of 475nm. Both LEDs panels were mounted on the tripods and the tilting angle were adjusted so that the excitation light were equally distributed amongst the entire surface of the model. The signals emitted from the painted model surface were captured by the LaVision Image Intense 12-bit CCD camera that was mounted on top of the test section. Two types of filters were used in front of the lens; 530nm long pass and an infrared cut-off filter. These filters

filtered out unwanted light signals and heat during recording. For each set of experiment, both wind-off and wind-on images were captured. Wind-off images are the images that were captured before the start of the run while wind-on images were the ones recorded during the run-time. The frame rate of the camera was set to 6 frames per second.

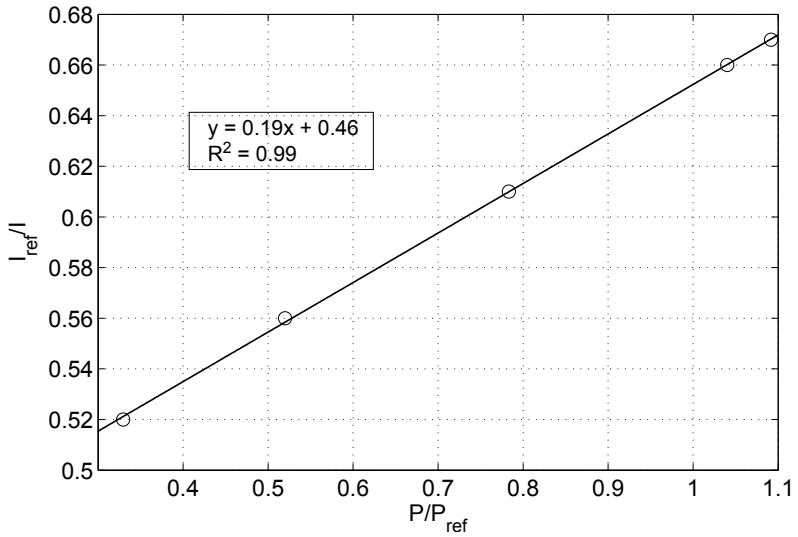


Figure 3.34: Stern-Volmer calibration graph. Data were obtained from in-situ calibration.

The images recorded were then processed in Matlab. A total of 20 images were averaged to create both the wind-on and wind-off averaged images. Next, the averaged wind-on and wind-off images were subtracted with the dark images captured from both wind-on and wind-off conditions for correction purposes. Then the corrected image of wind-on were divided by the corrected wind-off image so that another image that represents the reciprocal of the intensity ratio, $I_{ref}/I$ could be produced. After inputting the calibration constants obtained from the calibration curve based on Equation. 3.6, another image that represents the pressure ratio, $p/p_{ref}$ could be obtained.

Stern-Volmer plot in Figure 3.34 shows good agreement between pressure and intensity. The paint was responding to the pressure change in a linear behaviour. The calibration process was done *in-situ*, where both the images and the pressure signals were recorded simultaneously during the wind tunnel run. This type of calibration has its advantages compared to static calibration (*in-priori*). The actual test model were used for calibration instead of the samples, hence, the

calibrations are more accurate. Another advantage is the optical system set for the calibration and experiments are identical, and therefore the results are not affected by the setup variations. In addition, since PSP is sensitive to pressure, the emitted intensities are already corrected for temperature variations on the model.

The locations of the pressure tappings were carefully spread out in the streamwise axis so that a large pressure range can be covered. The pressure tappings were located at 244mm, 273mm, 285mm, 297mm, and 313mm from the flat plate leading-edge. When plotted, all the pressure readings gave an almost perfect linear regression, $R^2$ value of 0.99. Based on Eqn. 3.6, the A and B is given by 0.46 and 0.19, respectively. These values were then used to calibrate the $I_{ref}/I$ images into $P/P_\infty$ representation, as will be shown later in Chapter 5.

### 3.4.6 Particle Image Velocimetry

Particle Image Velocimetry (PIV) is an optical non-intrusive method of measuring the velocity of the fluid particle in just a single test. This is favourable compared to conventional measurement techniques such as pitot measurements, hot-wire anemometry, laser Doppler anemometry (LDA) which are just capable in measuring the velocity at a specific point at one time. Therefore in order to obtain the data for the whole interest area, more than one measurements are needed for the conventional techniques and this is different with PIV, where a single test can directly extract the whole velocity field. With the use of PIV, complex flow structures and instantaneous flow organization that were not able to be visualised using the traditional point methods such as turbulence, vortex shedding and shock-wave interactions are now able to be captured. PIV is considered to be an indirect method in measuring the flow velocity because it measures the velocity of the seeding particles which are assumed to be following the flow accurately instead of the flow directly like other conventional methods.

The generic PIV setup for wind tunnel experiments is shown in Figure 3.35. The basic theory behind PIV is calculating the velocity based on the displacement of the seeder particles for a known period of time. By comparing two consecutive images and assuming that the image of the same particles are captured but with slight displacements, the velocity of each particle can be computed when the delay between the two images was set earlier in the experiment. The specific area where the particles are being focused and illuminated is called the Field of View

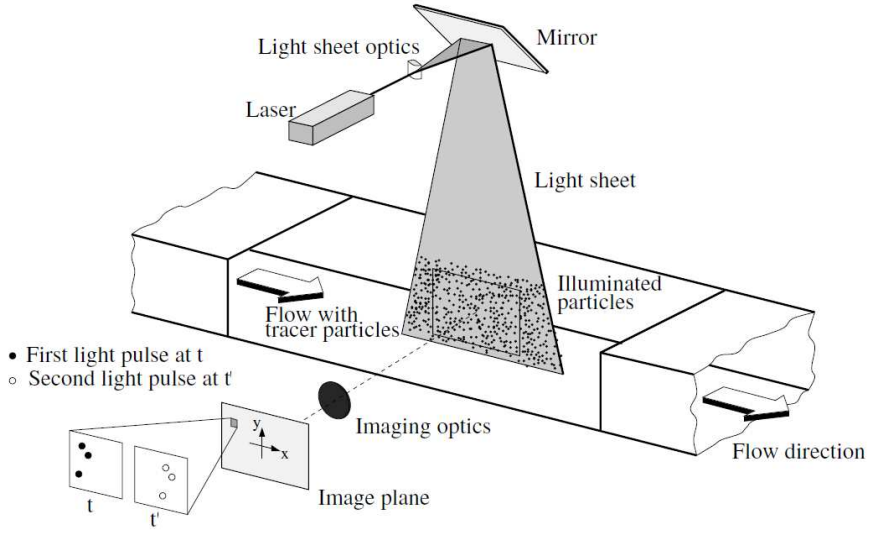


Figure 3.35: Generic experimental setup for PIV wind tunnel testing by Raffel et al.[75].

(FoV). The seeder particles introduced to the interest area are being illuminated by the laser lightsheet produced by a dedicated PIV laser in two consecutive laser pulse separated by a very short time duration. The light scattered by the particles which acted as a response towards the movements in the flow, were being recorded in sequence of frames by high quality lens or high performance optical devices such as Charge Coupled Device (CCD) sensor also in two consecutive instants.

The time elapse between the consecutive pulses produced by the laser is called separation time, denoted by $\Delta t$ and is usually in the unit of microseconds (ms). Analysing the PIV images will reveal information on distance travelled by the seeder particles, $\Delta r$ and therefore the velocity can be easily computed using the following equation:

$$\vec{V} = \frac{\vec{\Delta r}}{\Delta t} \tag{3.7}$$

In order to obtain $\Delta r$, a detail analysis on the images recorded needs to be performed using dedicated image processing softwares. Initially, the images are divided into small sub regions containing the sample of interest. This is called the interrogation windows. A comparison between the location of the seeder particles is made and subsequently the displacements of the same particles between both frames can be calculated by cross correlation. The assumption made to enable this calculation is that the particles moved uniformly and homogeneously.

Having both the particle displacements and time delay between both frames, the magnitude and direction of the velocity can be determined. The same process is repeated for other interrogation windows so that the complete velocity vector can be obtained for the whole FoV.

The seeder particles or also called tracer particles play a vital role in the PIV system because they enable the visualization of the fluid flow field and information on the velocity are extracted through their behaviour and motion. Therefore, it is extremely important to understand and satisfy the fluid mechanical properties of the particles in order to maintain the consistency between the fluid and particle motion. The seeder particles are sufficiently small so that they can follow the fluid motion accurately and at the same time attention has to be given to ensure that they do not alter the fluid properties of the flow characteristics. In order to trace and visualize their motion, they are illuminated by a thin lightsheet produced by the PIV laser. The light scattering images produced are recorded and analysed.

Basically, there are two functions of the seeder particles in PIV experiments, to follow the path of the flow as faithfully as possible and to scatter the light to the PIV recording devices. Smaller particles are favourable to follow the flow faithfully and not altering the fluid properties of the flow. On the other hand larger particles will scatter more lights and provide clearer images of the particles. There is a clear conflict between the selection of the size of particles in accomplishing both functions and therefore one of them needs to be compromised based on specific cases.

$$\tau_s = {d_p}^2 \frac{\rho_p}{18\mu} \tag{3.8}$$

Relaxation time of a particle, $\tau_s$ is defined as the time required by the particle to adjust its velocity to the change in the new environment and in this case is the velocity of the fluid. This is represented by Equation. 3.8. $d_p$ and $\rho_p$ is the diameter and density of the particle, respectively. $\mu$ is the dynamic viscosity of the fluid. $\tau_s$ acts as an indicator of the ability of the particle. From Equation. 3.8, it can be seen that $\tau_s$ is proportional to the square of the diameter of the particle. Therefore, smaller particles will have smaller relaxation time hence better ability to follow the flow well. However again, smaller particle will scatter less light and it is clear that a compromise has to be found.

The PIV setup for HSST is shown in Figure 3.36. The laboratory is equipped

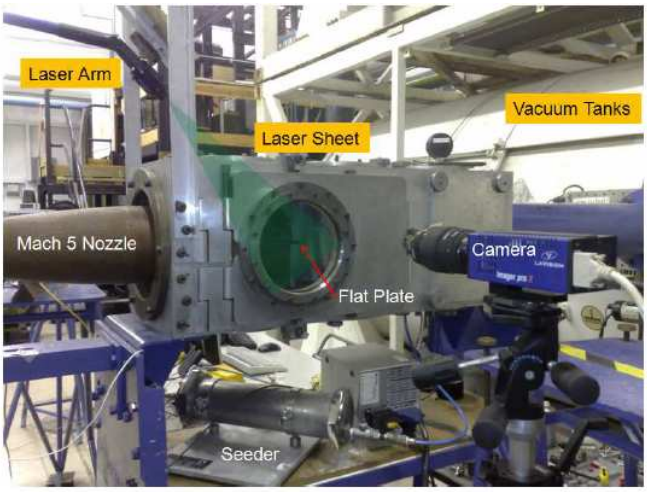


Figure 3.36: PIV setup in HSST [60].

with a PIV system that utilises a dual cavity Nd:YAG laser as the light source. The wavelength of the light produced is 532nm. The maximum energy of the laser is 200mJ per pulse and is adjustable between 0 to 200mJ using a Q-switched system. The beams are operated at 5Hz at a maximum pulsating rate of 15Hz. The pulse separation time is 1$\mu$s. The laser beam can be directed to any direction required by using the flexible laser guiding arm. To convert the laser beam into laser sheets of 0.2mm thickness to obtain the image for a specific cross-section, a cylinder lens or mirror mounted on top of the guiding arm is used. The laser sheet can be positioned at any location on the flat plate. It can be adjusted to relocate at any streamwise or spanwise positions to suit the need of the flow visualization.

De-agglomerated Aluminium Oxide ($Al_2O_3$) is chosen as the particle seeds. It has the nominal particle diameter of 300nm, bulk density of 4000kg/m3 and relaxation time of 3.2$\mu$s. The selection is based on its convenience in high-speed flows with good tracking capabilities and no risk of evaporation due to the high operating temperature of the tunnel. It is seeded at the settling chamber upstream of the flow. A single compressed gas cylinder is connected to the seeder in order to drive the seeds into the main flow. It is assumed that the seed particles move with the local flow velocity and the light scattered by the motions is recorded using a high quality camera. The photographical PIV recording is then digitised by means of scanner and the ouput from the digital sensor of the camera is stored directly to the memory [75].

There are a number of challenges involved in performing PIV experiments in hypersonics flow. One of them is choosing the tracer particles that has the ability

to follow the high-speed flow faithfully and scattering the light at very high-speed. It also means that the image recording system must be sensitive enough to record the displacements of the high-speed particles. Another challenge for this specific wind tunnel is to create the laser lightsheet in the test section and at the same time positioning the camera for recording. This will be challenging since the test section has limited viewing windows. The final challenge that could be anticipated is the limited number of images that can be captured since the run time of the HSST is just between 8-10 seconds.

### 3.4.7 Measurement Uncertainties & Challenges

This section details the measurement uncertainties and also the challenges associated with the experimental techniques employed throughout the experimental campaign. It is aimed at preparing and providing other researchers with the anticipated experimental errors that need to be taken into account and also the challenges encountered in setting up the experimental techniques.

#### Schlieren Photography

The schlieren technique is considered to be a qualitative measurement technique since it does not reveal any values of the flow characteristics including density. Other supporting quantitative measurement methods need to be employed in order to get a comprehensive result of the flow. However schlieren plays a vital role in giving a preliminary overview of the flow structures and also in identifying the specific location for quantitative measurements such as conventional pressure tappings.

Since schlieren technique integrates the density of the whole volume of the flow, the density change can only be detected in two-dimension. This means that the unsteady flows that involve three-dimensionality will not able to be captured accurately. However, for two-dimensional flow structures, schlieren proved to be a very helpful tool.

#### Oil-Dot Visualisation

The early challenge is to produce the correct mixture of the oil. The viscosity and surface tension of the oil-dots play an important role in the size of the dots produced and the dispersion abilities. Oil-dots that are too small will not react

to the flow and will not produce any movements. Instead of leaving streaks, large oil-dots tend to spread. Both of these characteristics; viscosity and surface tension depends on the quantity of oleic acid and silicone oil used.

Another challenge is to determine the size of the grid to position the oil-dots. Having in mind that low viscosity oil-dots will produce longer streaks, if the dots are closed to each other, there are possibilities of the streaks to overlap. The overlapping streaks are unfavourable since they do not represent the accurate behaviour of the flow. Altering the formula of the oil-mixture in order to improve the oil-dot dispersion will also require the grid spacings to be revised each time.

### Oil-Flow Visualisation

Similar to oil-dot visualisation, the greatest challenge is to produce the correct viscosity of the oil mixture. If the oil-mixture is less viscous, the oil will easily be blown downstream by the flow before being able to follow the flow features on the surface of model. In contrast, if the oil is too viscous, it will slowly flow downstream and cover only a short distance. During the short 7 seconds of the wind tunnel run, it will not have sufficient time to flow into the downstream region of interest.

Another challenge is to produce equal illumination on both sides of the model during the run. This is to ensure that the images captured by the DSLR camera are sufficiently bright and symmetry at the same time, so that the image processing conducted after the experiments will yield more useful information. The brightness of the surface does not only represent the presence of the oil, but also provide qualitative information on the shear stress level. Therefore an uneven illumination will cause substantial error in the final results.

### Infrared Thermography

The camera used to capture the infrared images is connected to a computer preinstalled with a dedicated software used for image acquisitions. Before starting the run, the reference temperature which refers to the temperature of the model's surface, needs to be computed. Usually, the reference temperature is set to be equivalent with the ambient temperature. This means that after each run, the surface of the model which had just encountered the high-temperature flow of approximately 100°C is left to cool down to the ambient temperature. However the ambient temperature of the laboratory gradually increases after each run due

to the frequent operation of the wind-tunnel heater. Therefore this introduced an uncertainty towards the temperature recorded on the model surface since it is dependent on the reference temperature.

The reflection on the model surface from the surroundings is perceived as high-temperature spots by the infrared camera. Hence, whenever the reflections are captured, the temperature range of the model surface are altered and flow features that have small temperature range are not visible unless the range on the recording software is altered before the run or a post-processing procedure of specifying the range is conducted later on. Another challenge includes the procedure of focusing the camera's lens onto the model surface. Since the infrared camera are only sensitive to the temperature change, the focus object used in the procedure are heated using a portable air heater before being placed inside test section. This needs to be done quickly since the temperature of the object drops to the ambient temperature in a short period of time.

### Pressure-Sensitive Paints

There are a number of sources of errors related to the measurement of pressures using the PSP method. One of them is the alignment problem of the images. Usually using the wind-on situation, the model inside the wind tunnel will experience aerodynamics loading due to the aero-elasticity effect. This will affect the position of the model with respect to the imaging devices. Most model stands in the test section could not prevent this type of motion and therefore there will be an alignment problem between the wind-on and the reference (wind-off) images. To overcome this situation, a sophisticated image registration technique is required and could be done in the post-processing.

The most dominant error in PSP measurements is the temperature-dependence of the luminophore. The corrections are usually done by performing in-situ calibration. This calibration will correlate the intensity of the paint to the pressure measured by the pressure tapings located at several positions on the test object.

### Particle Image Velocimetry

Common PIV setup uses CCD sensors as the main image recording system. CCD sensors are more inclined to record more noise compared to CMOS sensors. Therefore, most of the errors associated with the CCD sensors do apply directly to the PIV system. Apart from that, two-dimensional PIV setup is also highly exposed

to out-of-plane velocity of the tracer particles. Errors due to the compressibility effects of the flow also have been taken into account. The refractive index of the gas flow changes with the change of density and this is severe in high-speed flows. The change in the refactive index causes the image to be blurred when captured by the camera.

The performance of tracer particles are limited to the characteristics of relaxation time and Stokes number. Experiments in high-speed compressible flow require the perfect selection of tracer particles due to the compressibility effects. The velocity lag caused by the particles can cause inaccuracy in determination of the velocity vector. Therefore careful selection of the seeder particles will help to reduce this type of error.

# Chapter 4

# Micro-Ramp Flow Characteristics

This chapter presents the results on the characteristics of the flow passing the micro-ramps examined using mostly qualitative flow diagnostics techniques and also a few quantitave measurements. The objective is to provide the overall understanding of the flow manipulation with the presence of the micro-ramp that would later help in justifying its importance in hypersonic flow control.

## 4.1 Overview of flow structure

Before going into each section of the micro-ramps in detail, it would be better if the overview of the flow is presented. This includes the overall shock-system involved and also the behaviour of the incoming boundary-layer. For this purpose, schlieren visualisation proves to be one of the best technique. As displayed in detail in Chapter 3, there are two types of schlieren system employed; normal and high-speed schlieren system.

Figure 4.1 shows the high-speed and normal schlieren photographs for the largest micro-ramp, MR80. It is denoted that the rounded frame on top of both photos is the window of the test section while the three unlabelled shock waves emerging from the left hand-side are the flat-plate leading-edge shocks and the nozzle cone shock (refer to Figure 3.11). From the high-speed schlieren photo in Figure 4.1a, the incoming boundary-layer was observed. As it approaches the micro-ramp, it started to thicken and eventually moved up the surface of the

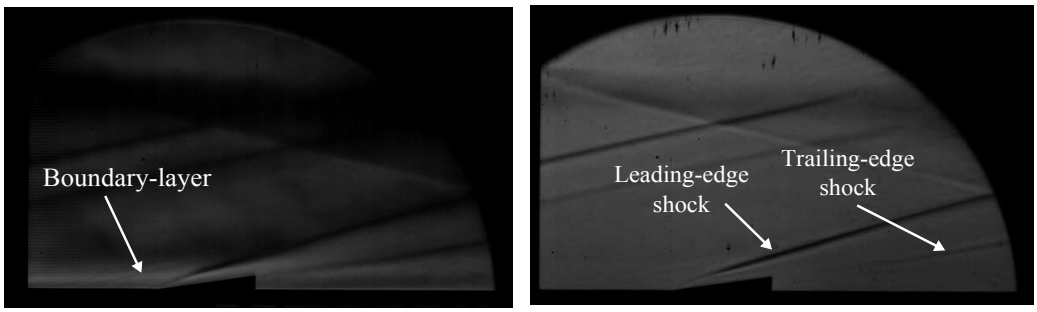


(a) High speed schlieren at 10 000 fps. (b) Normal schlieren.

Figure 4.1: Time-averaged schlieren images of model MR80 using normal and high-speed schlieren system.

micro-ramp. At the apex, it continued to move downstream leaving the micro-ramp at the same angle of the micro-ramp surface hence creating a wake region near the apex. The boundary-layer was only visible in the high-speed schlieren and was not captured in the normal schlieren due to the camera's exposure time. The exposure time of the high-speed camera was $1\mu$s compared to $250\mu$s for the DSLR camera. From the photograph, it can also be seen that the micro-ramp was submerged inside the boundary-layer and this satisfies the criterion of micro-vortex generator discussed in Section 2.2.1. Analysing the shock-waves emanating from the micro-ramps, a strong shock wave is easily visible originating from the micro-ramp leading-edge while the weaker shock wave is seen at its trailing-edge. The same features were also observed in the high-speed image yet a better contrast is seen in normal schlieren shown in Figure 4.1b.

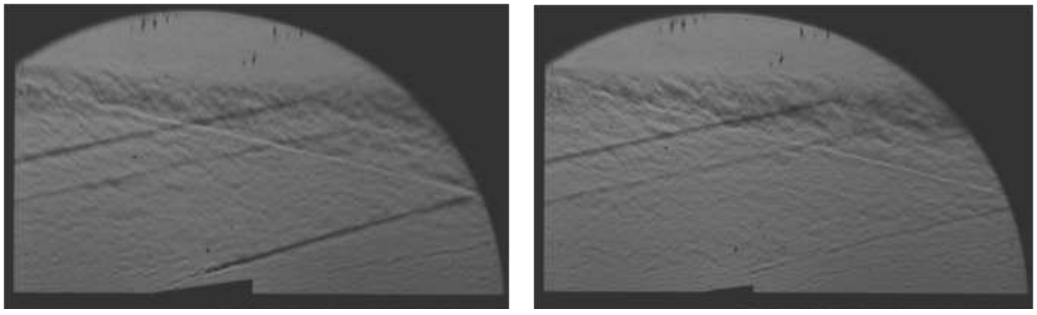

(a) MR80 (b) MR40

Figure 4.2: Instantaneous schlieren images of 2 models for comparison.

When the instantaneous normal schlieren photographs of models MR80 and MR40 were compared in Figure 4.2, the overall shock-system appeared to be

similar. However comparing the shock strength produced by the leading-edge of the models, MR80 turns out to produce a stronger shock. This can be observed from the thicker and blacker shock line originating from the leading-edge in Figure 4.2a. This is due to the significant difference in the size of the models. A bigger model deflects more flow because of the larger surface area hence a stronger shock is needed. Comparing the trailing-edge shock, MR80 again produced a slightly stronger shock whereas for MR40, the shock is very weak and is barely visible.

## 4.2 Flow Development

The images of MR80 in chronological order of the oil-flow visualisation experiment are shown in Figure 4.3. Blue oil was applied around the model for clarity as well as to observe the flow behaviour at that particular location. The green oil which was deposited upstream, initially blanketed the entire surface of the model before the flow is properly established as shown in Figure 4.3a. Once established, the actual flow features started to form. In Figure 4.3d, heavy accumulation of oil is observed at the leading-edge of the micro-ramp due to flow separation. Next the flow continued to climb the top surface of the micro-ramp and then moved towards the swept edges on both sides.

Upon flowing down from the edges in a rotational manner, the flow eventually formed the large vortices called primary vortices, seen on both sides of the model. Downstream of the model are two wide areas that are not covered with oil and this is known to be the trail of the primary vortices. The rotating motion of the vortices that touched the surface of the wall creates a region of high-shear which then prevented the oil from accumulating. The footprints of the primary vortices started to appear on the trail in Figure 4.3f, after approximately 5s of established flow. Earlier, another pair of smaller vortices are observed wrapping around the model by the thin oil streak starting from the leading-edge extending to the downstream region. These vortices which are known as the horseshoe vortices are only distinguishable from the main flow starting from Figure 4.3d.

Another feature that is present earlier is the thick band of oil which can be seen exactly at the centreline, aligning with the apex of the model in Figure 4.3c. The thick band of oil began to divide into half, creating two small tube-like structures of oil that travelled downstream as seen in Figure 4.3d. The separation is seen clearly a few seconds later in Figure 4.3f. These structures are called

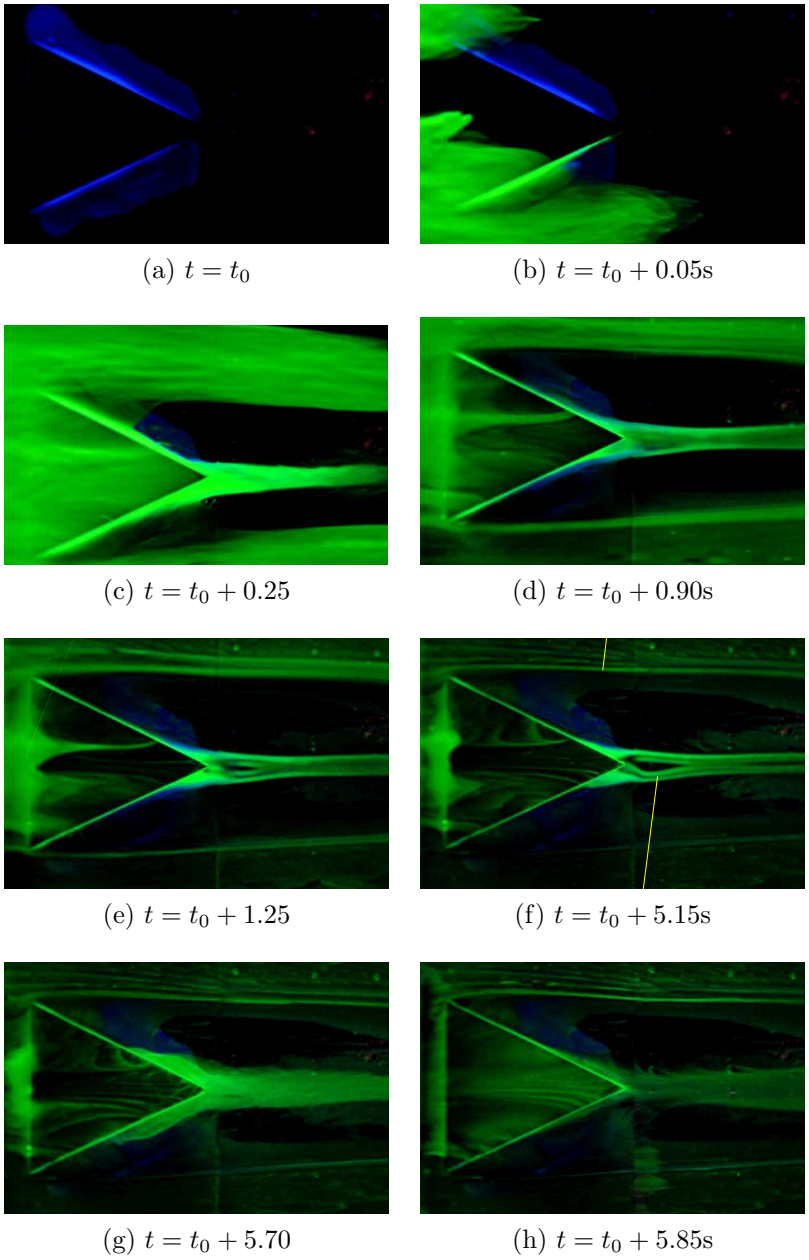

(a) $t = t_0$ (b) $t = t_0 + 0.05$s

(c) $t = t_0 + 0.25$ (d) $t = t_0 + 0.90$s

(e) $t = t_0 + 1.25$ (f) $t = t_0 + 5.15$s

(g) $t = t_0 + 5.70$ (h) $t = t_0 + 5.85$s

Figure 4.3: Chronological order of flow over MR80 using oil-flow visualisation technique.

the secondary vortices, due to the smaller size compared to the primary vortices. Finally, Figure 4.3g portrays the oil being smeared by the wind tunnel terminating shock and the final condition of the oil displayed by Figure 4.3h, which revealed no information about the flow features apart from the pattern on top of the model surface. Therefore it is essential to employ a live-time recording devices in order to obtain as much information as possible on the flow characteristics at each stage

of the flow.

## 4.3 Leading-edge topology

The first region which the incoming turbulent boundary-layer encounters is the leading-edge of the micro-ramp. From a flat surface where the boundary-layer develops it suddenly needs to face a surface inclined at a certain angle hence forcing itself to deflect. Eventually, this leads to the formation of the leading-edge shock-wave that was previously observed in the schlieren images. The angle of the leading-edge for both models MR80 and MR40 was set to 8.6° as depicted in Figure 4.4. The angle is constant for both models regardless of height, $h$ and chord length, $c$.

From the data compilation available for the case of a wedge-compression corner [76], the current condition of this investigation (Mach 5, Reynolds number $13.2 \times 10^6$), incipient separation would only occur at an angle of 23°. The angle of the leading-edge would seem to be significantly small to trigger flow separation in this case. However, as discussed by Lu et al. [36], the effective Mach number at the leading-edge is lower due to the micro-ramp being submerged in the boundary layer. Therefore the separation can be triggered at a much lower angle such as at 8.6° for this case. Similar case was found for the majority of the investigations done in supersonic flow [3, 36, 45].

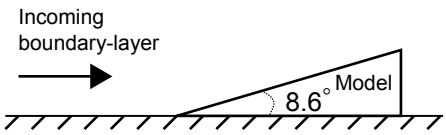


Figure 4.4: The side-view of the incoming turbulent boundary layer encountering leading-edge of micro-ramp at 8.6° of angle that created the leading-edge shock wave.

The formation of the shock-wave eventually leads to flow separation just ahead of the leading-edge, creating a localised shock-boundary layer interaction, at a smaller scale. This phenomenon was observed in most of the previous micro-ramp studies both experimental and numerical. Multiple flow diagnostics were used in order to prove the existence of the separation region including oil-dot visualisation, oil-flow visualisation and infrared (IR) thermography.

The undisturbed oil-dots before the run is shown in Figure 4.5a and during the steady-state of the run (approximately at $t = t_0 + 6s$), just before the terminating

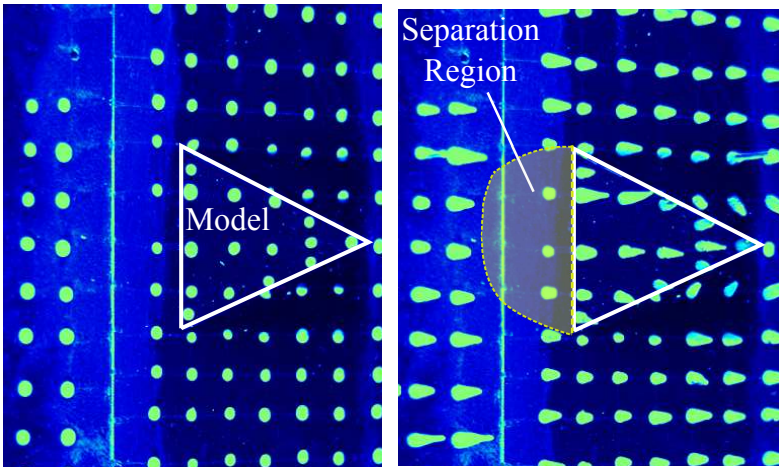


(a) Before test @ $t = t_0$ (b) Steady state @ $t = t_0 + 6s$

Figure 4.5: Oil-dot visualisation images of model MR80 recorded inside the test section during the run.

shock that leads to the smearing of the oil-dots in Figure 4.5b. For clarity, the model is drawn with the white line and the flow is from left to right. From Figure 4.5b, the separation region is indicated by the static oil-dots ahead of the leading-edge. Theoretically, separation regions have lower skin friction coefficient and therefore oil-dots are less disturbed and remained as close as its initial state. Thus instead of moving downstream and producing streaks, the dots remained in their initial condition. It can also be seen clearly that the other oil-dots in the spanwise location moved, producing long streaks. This also proved that the separation region was really originating from the localised SBLI and not induced by the gaps between the model and the flat-plate which is just ahead of the model indicated by the straight bright line in Figure 4.5.

Figure 4.6 shows the oil-flow visualisation results of MR40 and MR80. Green fluorescent dye was used in the experiment to enhance the contrast of the image captured by the camera. The accumulation of oil was observed at the upstream location of the leading-edge, precisely at the location where the separation region was observed previously in the oil-dot visualisation results. It would be beneficial to understand why oil accumulates in the case of flow separation. The oil was deposited at an upstream location from the micro-ramp. Once the flow was initiated, the oil was carried downstream by the incoming flow, covering the whole surface of the flat plate including the micro-ramp. After a certain period of time, the flow separation started to form at the leading-edge due to the localised SBLI.

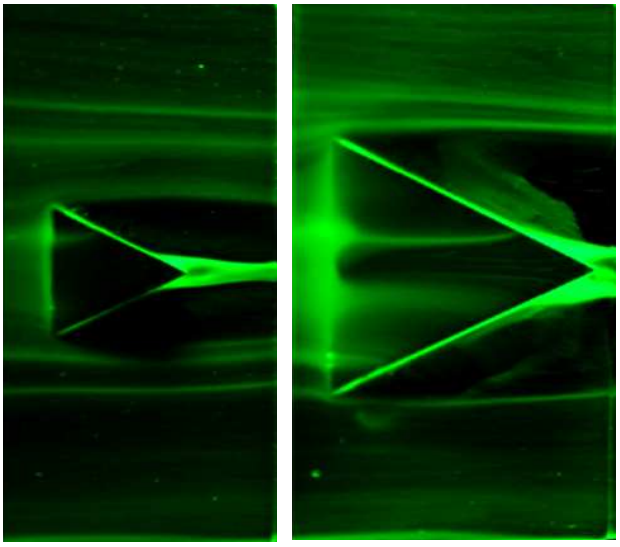

(a) MR40 (b) MR80

Figure 4.6: Oil-flow visualisation of both models showing oil accumulation at leading-edge

However at that moment, oil was already in the region. So after the formation of the separation region, the flow was not able to enter the separation region hence the oil was not able to be carried downstream. This resulted in the oil accumulation inside the separation region. Since oil-flow is a surface visualisation technique, the size of the separation region observed (by the oil-accumulation) only represents the size on the wall surface. The vertical extent of the separation region is yet to be discovered using this technique.

The time-averaged IR images mapping the surface temperature of the flat plate and models are shown in Figure 4.7. The results are being non-dimensionalised by $X_c$, the spanwise location of the centre of the micro-ramp and $\delta_0$, the boundary layer thickness at micro-ramp location. The position of the models are denoted by the black line and the flow is from bottom to top. Relatively low temperature regions were observed ahead of the leading-edge for both of the models. The low temperature regions were created due to the high-temperature flow not able to be transferred to the surface of the flat plate because of the separated flow. In the case of MR80 in Figure 4.7b, the separation region even extended beyond the leading-edge and up onto the surface of the micro-ramp while for MR40, the separation region was limited and bounded by the leading-edge. This difference was caused by the significant difference of the both models

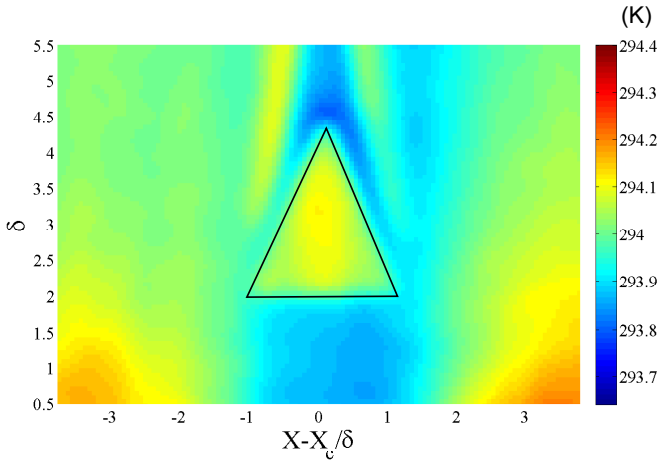


(a) MR40

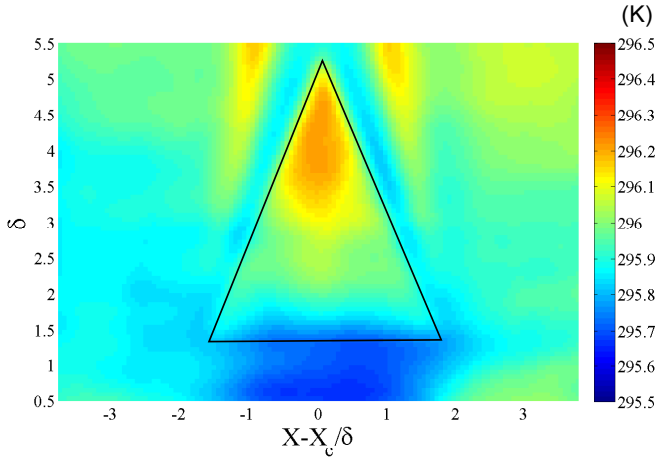


(b) MR80

Figure 4.7: Time-averaged infrared thermography images of both models showing low temperature region at leading-edge of micro-ramp.

consequently producing different size of the separation region. Because of the high sensitivity of the IR camera, the flow features were able to be captured since the temperature difference were only as small as ±0.1K. This enabled not only the separation region to be observed, but other features such as the primary and secondary vortices, that will be discussed in detail later on.

The Stanton number plot along a profile line $0.9\delta_0$ (5.44mm) ahead of MR40 leading-edge in the infrared investigation is shown in Figure 4.8. A cubic fitting is drawn on the data distribution to visualise the overall data trend. The profile line is spanned across the entire width of the plate, where $x = 30$mm is the centreline. Near the centreline, the Stanton number begins to drop to the lowest value, occurring at the centreline. Passing the centreline, it begins to increase

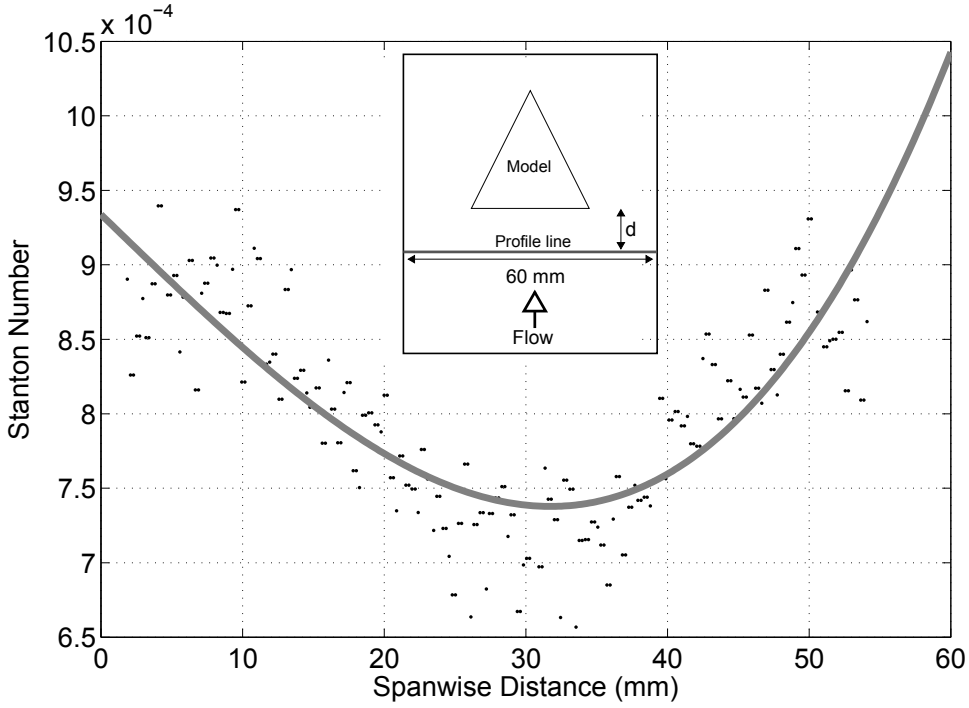


Figure 4.8: Stanton number plot along a profile line, $d = 0.9\delta_0$ ahead of the micro-ramp leading edge for model MR40. Note that the scale of the schematic is exaggerated for clarity.

forming an almost symmetrical data distribution. Due to the flow separation, the heat transfer rate dropped gradually hence creating such distribution of Stanton number.

## 4.4 Top surface topology

After passing the leading-edge, the flow continues to climb on the top surface of the micro-ramp moving towards the apex. The oil-dot results of the top surface is shown in Figure 4.9a. The streaks produced by the oil-dots were observed moving towards the slant edges on both sides of the model. Only the dots at the centreline of the model moved in a straight line towards the apex. The raw image of the oil-flow is shown in Figure 4.9b. However not too much information can be extracted from the image especially in terms of the direction of the flow. After undergoing post-processing in Davis, the image in Figure 4.9c clearly reveals the streamlines of the flow on the top surface of the model. The flow can be seen clearly moving towards the slant edges on both sides, in agreement with the

oil-dot results.

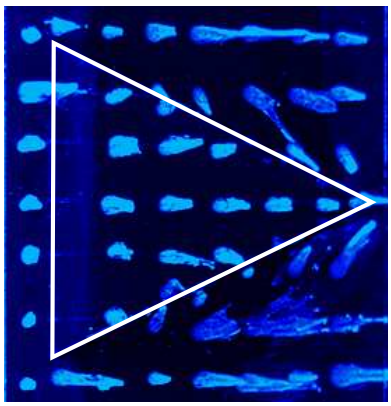

(a) Oil-dot

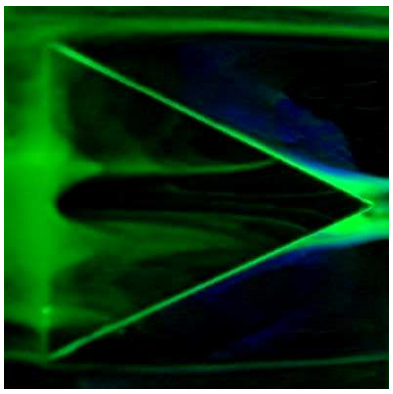

(b) Oil-flow raw image

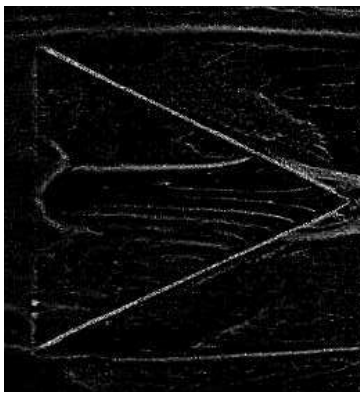

(c) Oil-flow image after filter

Figure 4.9: Image of MR80 top surface captured using oil-dot (top) and oil-flow visualisation (bottom).

The type of non-linear filters used in Davis [77] for post-processing were *concentration* and *sliding average*. The *concentration* filter concentrates intensities on the local maximum pixel. The filter works by searching for pixels which have the intensity of the local maximum. After finding the local maximum pixel, it will move the intensities of the surrounding pixels toward the center to concentrate all intensities in the middle. Next the *sliding average* is used. The filter computes a local average over a specified scale (in this case 3 pixels were chosen). The average were computed according to the specific equation built in Davis. The final image is actually the product of the image after the first filter subtracting the image after the second filter.

## 4.5 Downstream region

After the flow passes the micro-ramp, more complex flow features are seen at the downstream region. The capabilities of the micro-ramps in controlling SBLI actually relies on this region. For further clarification, this section is divided into two subsections based on the independent flow features observed; primary vortices and secondary vortices.

### 4.5.1 Primary Vortices

The flow then moves down the slant edges in a rotational manner, due to the angle of the edges subsequently forming large vortical structures on both sides, referred to as the primary vortices. The evident of the flow moving down in a rotational manner is from the herringbone structure found in numerical investigations [30, 47]. Figure 4.10b shows the instantaneous oil-flow visualisation image of MR80. The raw image was manipulated in image processing software to emphasize the existence of the primary vortices. Instead of a herringbone pattern, the experimental visualisation shows two dark regions downstream the model as the representation of the primary vortices. This indicates that the oil containing the green dye was scoured away by the high-shear forces of the travelling primary vortices. This is in contrast of the case of the leading-edge separation where the oil accumulates due to the low-shear force region in the separation zone. Further downstream, the traces of oil began to appear in the dark region after a certain time but still leaving the middle section dark. This is a clear representation of the primary vortices depositing the small amount of oil that it was carrying together with it downstream to both of its left and right side.

If careful observation is made on Figure 4.10b, a region of smeared blue oil can be seen at the trailing edge of the model, on both sides. Before the experiment, a small amount of blue-coloured oil was deposited near the trailing-edge while the green-coloured oil was deposited upstream the model as shown in Figure 4.10a. The model is bounded by the white line for clearer representation in the figure. The objective was to investigate the flow behaviour at that specific location. In due course, the result shows that the blue-oil was partially touched by the flow and the oil was not entirely swept downstream by the flow. This indicates low-shear stress in that particular region which eventually leads to the theory that the primary vortices were fully developed after a certain distance downstream

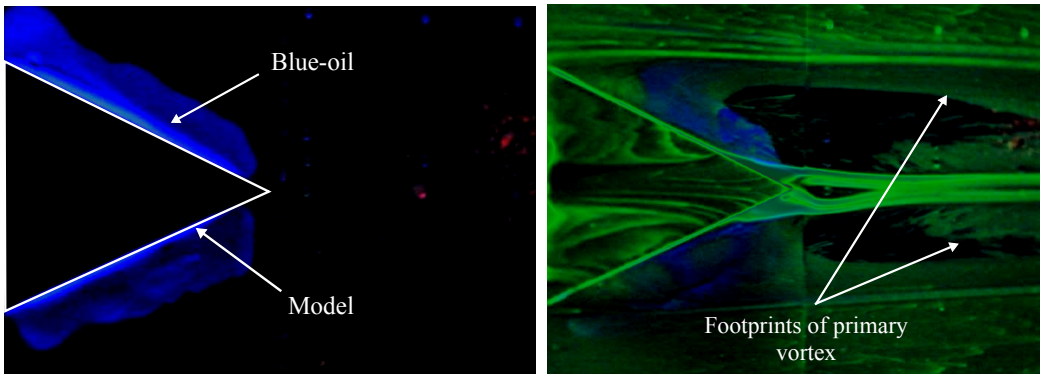


(a) Before run $t = t_0$ (b) Steady time at $t = t_0 + 6s$

Figure 4.10: Oil-flow visualisation of MR80 showing footprints of primary vortices.

before coming in contact with the wall surface which is denoted by the starting of the no-oil area in the figure.

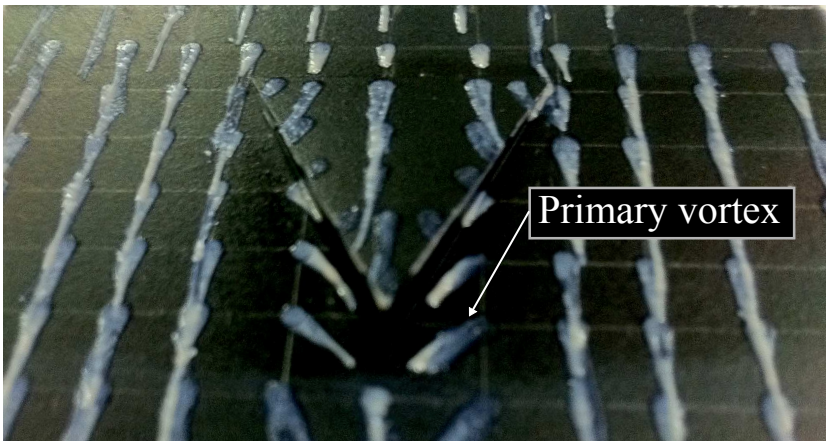


Figure 4.11: View from downstream of the micro-ramp showing evidence of the primary vortices.

So far, the evidence of the existence of the primary vortices are clear. However one question which is still unknown is in which direction do the vortices rotate along the downstream axis. Hence, the best technique to reveal the flow direction would be the oil-dot visualisation and the view from the downstream of the model is shown in Figure 4.11. The oil-dots downstream the slant edges on both sides were observed to move towards the centreline of the model, aligning with the apex. This shows that the oil-dots on the surface were swept by the vortices towards the centreline hence producing such pattern. On the other hand, if the oil-dots streaks observed moved away from the centreline then the direction of the

vortices would be the opposite. The directions of the vortices can be described as counter-rotating and is this shown in the vortex model in Figure 4.12.

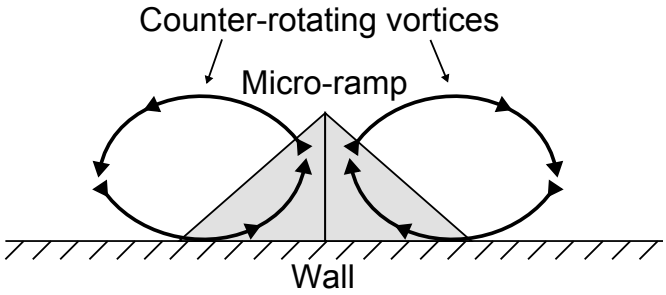


Figure 4.12: Schematic diagram of the counter-rotating vortices from downstream view.

From the image of the oil-flow in steady condition shown in Figure 4.10b, it can be seen that the vortices started to touch the wall at full strength at a distance of approximately $3.5\delta_0$ from the micro-ramp leading-edge by sweeping all the oil on the surface. This is observed on both left and right sides of the model. The traces of oil near the centreline only begin to appear at a distance approximately $6.7\delta_0$ from the leading-edge which is almost twice the distance of the first location where the vortices started to touch the wall. It is speculated that the traces of oil appeared as a result of the partial lift-off of the primary vortices from the wall surface. The vortices are no longer in full contact with the wall hence allowing small amounts of oil from the adjacent region to settle.

Another method to analyse the behaviour of the primary vortices is by referring to the temperature distribution of the downstream region, shown in the IR image in Figure 4.13. Three streamwise locations are labelled as A, B and C. A is the point where the primary vortices started to form, denoted by the sudden increase in temperature on both sides of the model. After a further distance downstream, another step in temperature rise is observed at point B. This is the point where the vortices are fully developed and are in full contact with the wall hence transferring the high temperature flow to the wall surface causing the rise in temperature. The vortices continued to travel downstream until a point where the temperature started to decrease steadily and this point is labelled as C. C is the point where the vortices started to lift-off from the surface and reducing their contacts with the wall. From the locations of all the points, a few findings can be deduced. The primary vortices started to form at a distance of $1.38\delta_0$ from the leading-edge, which can be considered quite a distance upstream of the apex of the model. After travelling $1.88\delta_0$, the vortices started to be fully developed

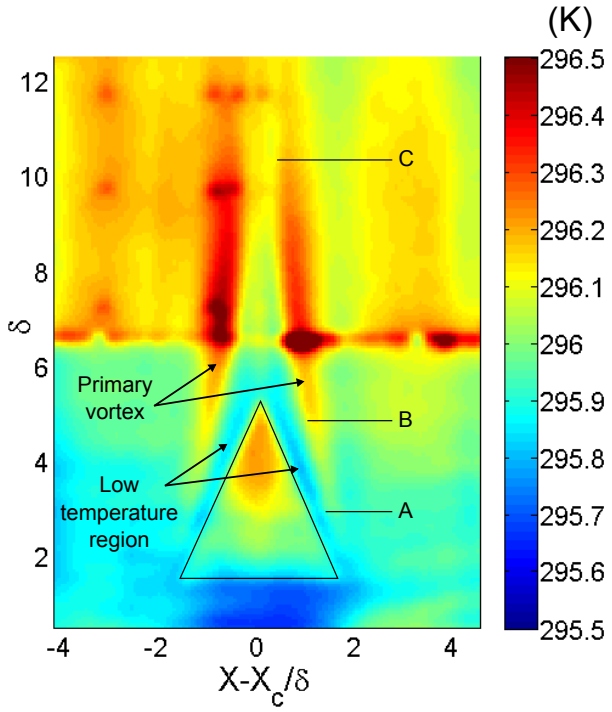


Figure 4.13: Time-averaged infrared images showing temperature distribution at full downstream length. Flow is from bottom to top.

and in full contact with the wall, at a distance $0.39\delta_0$ upstream the apex. Then they travel for $5.39\delta_0$ before lifting-off at a position approximately $5.0\delta_0$ from the apex.

Low temperature strips are observed near the location where the primary vortices started to form (Point A). The strips stretched along the side edges of the micro-ramp until the apex. Low temperature means the high-temperature flow is not transferred to the wall and this means that the regions have low shear stress. This supports the previous findings in oil-flow (refer Figure 4.10b) where the oil deposited in the region was not smeared completely by the incoming flow. This also indicates that the primary vortices are formed at a quite upstream region based on the evidence from the IR image and at a location little further away from the side edges of the micro-ramp, adjacent to the low-shear region.

Figure 4.14 shows the plot of Stanton number at a profile line located $0.5\delta_0$ (2.95mm) downstream the micro-ramp apex for two models, MR40 and MR80 for comparison. The average Stanton number for both models are actually almost equal, with only a small difference of approximately $0.4 \times 10^{-3}$. The scales in the plots are purposely amplified in order to observe the overall behaviour

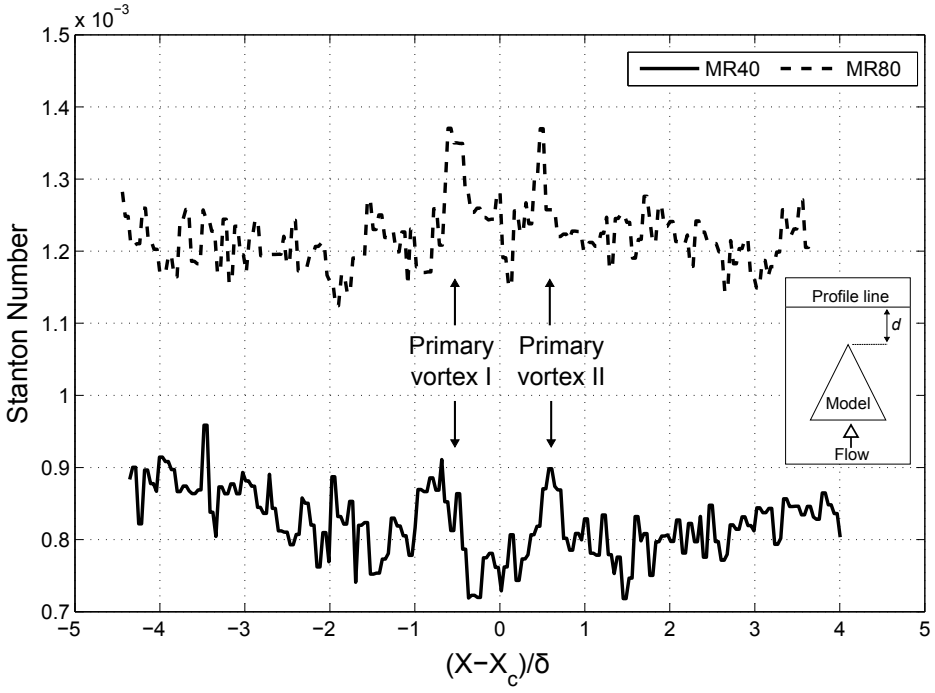


Figure 4.14: Stanton number plot along a profile line, $d = 0.5\delta_0$ downstream the micro-ramp apex for model MR40 and MR80. Note that the scale of the schematic is exaggerated for clarity.

of both readings. There are two peaks identified for each plot, almost at the same locations; $(X - X_c)/\delta_0 = -0.5$ and 0.5. These two peaks represent the two primary vortices generated by the micro-ramps as were seen previously in Figure 4.13 as high-temperature streaks. It can also be seen from the plot that they are symmetrical at the centreline.

### 4.5.2 Secondary Vortices

The first secondary vortices pair is also called the horseshoe vortices as shown in Figure 4.15. The horseshoe vortices are created when a boundary-layer flow encounters a bluff body protruding from a surface. As a result, a complex three-dimensional flow field area is created at the junction area. Upon approaching a bluff body, the boundary layer will experience flow reversal hence creating a separation region as observed in Section 4.3. The impinging boundary layer then destabilises and eventually form vortex structures in the spanwise direction. Due to the cross-stream pressure gradient imposed by the body, the vortex tend to divert symmetrically around the body and the legs of the vortices continue to

extend downstream forming the horseshoe-shape [78].

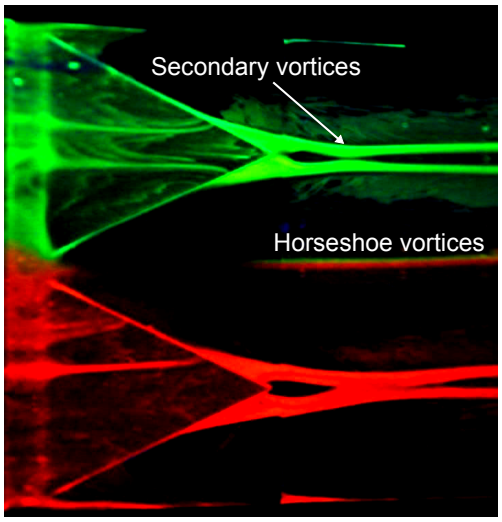


Figure 4.15: Oil-flow result of MR80 array configuration using two-coloured oil.

Generally, horseshoe vortices are formed when boundary layer flows encounter surface-mounted protuberance. However, the micro-ramp only acts as a small protuberance to the flow and therefore weaker horseshoe vortices are created [36] and were barely visible in the raw images, especially images of smaller micro-ramps. These weak horseshoe vortices are not seen to affect the downstream flow. They just created a separation envelope [79] that isolated the flow downstream the micro-ramp from its adjacent region including the neighbouring micro-ramp in the case of array configurations [46]. Evidence is seen from Figure 4.15 where two distinct vortex line are seen propagating downstream in parallel at the centreline and mixing between the two regions did not occur.

In between the two large primary vortices is a pair of smaller vortices known as the secondary vortices. These vortices are seen as two small tube-like structures of oil travelling downstream as shown in Figure 4.10b. Because of the small size, the oil is wrapped together with them forming the particular shape. Notice the difference in the sizes of the secondary vortices of both models shown in Figure 4.16. Larger vortex tubes are seen in MR80 compared to MR40. Hence there are possibilities that the size of the vortex tube might be influenced by the size of the micro-ramp. To confirm these hypotheses, the diameter of the vortex tubes of both model are measured and the chord lengths, $c$ of each micro-ramp are used as a reference parameter.

From Table 4.1, the ratio calculated for both models are almost the same,

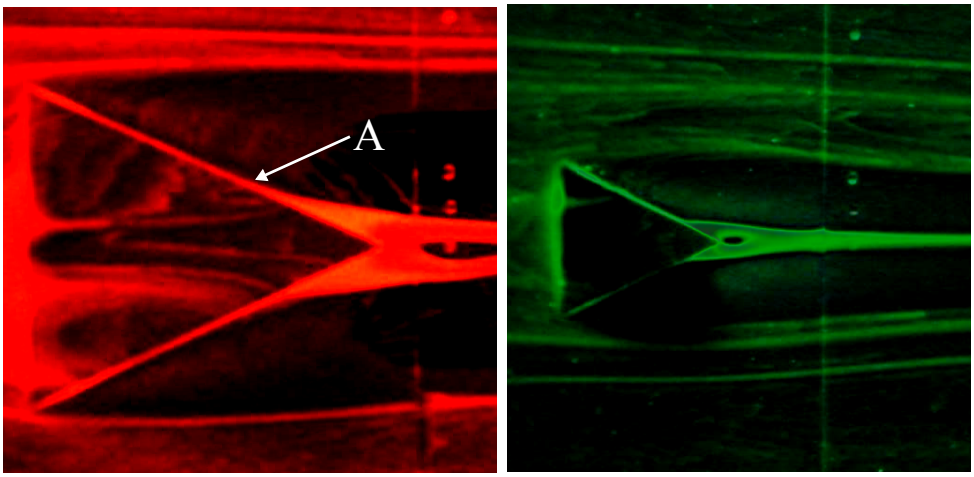


(a) MR80 (b) MR40

Figure 4.16: Comparison of the size of the secondary vortices for both models at steady condition, $t = t_0 + 6s$.

| Model | Chord length, $c$ (mm) | Vortex diameter, $d$ (mm) | Ratio |
|---|---|---|---|
| MR80 | 33.40 | 1.86 | 0.056 |
| MR40 | 16.70 | 0.90 | 0.054 |

Table 4.1: Ratio of diameter of vortex with chord length.

0.056 and 0.054 for MR80 and MR40, respectively. This revealed an interesting finding that the diameter of the secondary vortex will always be proportionate to the chord length of the micro-ramp. The larger the model, the larger the size of the secondary vortices and the ratio of $d/c$ is approximately 0.05.

Referring to the temperature distribution downstream the micro-ramp in Figure 4.13, the secondary vortices at the centreline are visible even with a mere increase in temperature is observed only after a distance downstream the micro-ramp apex. On the other hand, the horseshoe vortices (including the horseshoe vortices) are not able to be captured. This proves that the horseshoe vortices are too weak and might be too small to be captured by the IR camera. A different case is observed for the stronger primary vortices where the temperature rise is very significant. Therefore the weak secondary vortices are not hoped to contribute in controlling the SBLI compared to the primary vortices, but only as one of the flow features present.

After undergoing post-processing, the oil-flow results of MR80 is shown in Figure 4.17. The thick labelled lines represent the vortices. From the raw images,

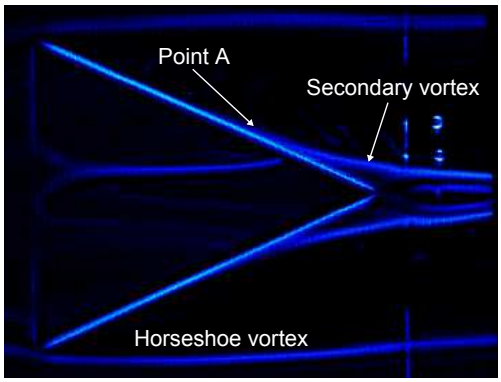


Figure 4.17: Time-averaged oil-flow result of MR80 after post-processing.

the secondary vortices at the centreline is seen to originate from the swept edges of the micro-ramps as early as at the leading-edge and continued to propagate downstream parallel with the edges. Until point A as labelled in Figure 4.17, the vortex separated itself from the edges and moved downstream parallel to the flow axis. The exact location of point A from the time-averaged image is calculated. Point A is found to be $1.69\delta_0$ upstream of the micro-ramp tip. With reference to the chord length, point A is approximately 2/3 length from the leading-edge tip. This means that rather than continuing to travel the remaining 1/3 length to the apex location, the vortex suddenly changed its path.

## 4.6 Pressure Sensitive Paints

The flow characteristics of the micro-ramps are also investigated using this novel flow diagnostics method, the Pressure Sensitive Paints (PSP). The PSP image of all the models are shown in Figure 4.18. Note that for the array configuration results shown in Figure 4.18b and 4.18c, regions of high pressure are observed in between the models as indicated by $S$ are in the figures. Initially the high-pressure regions were thought to originate from the flow physics taking place at that specific location. However after considering that the high-pressure region only existed for the array configurations, a later conclusion was made that this was actually the effect of the shadows from the illumination. Since the windows are at the same height of the model, it was not possible for the UV LED to be fixed at a higher position to avoid the shadows occurrence. Hence the region in between the models suffered from the shadow created by the illumination on both sides of the windows.

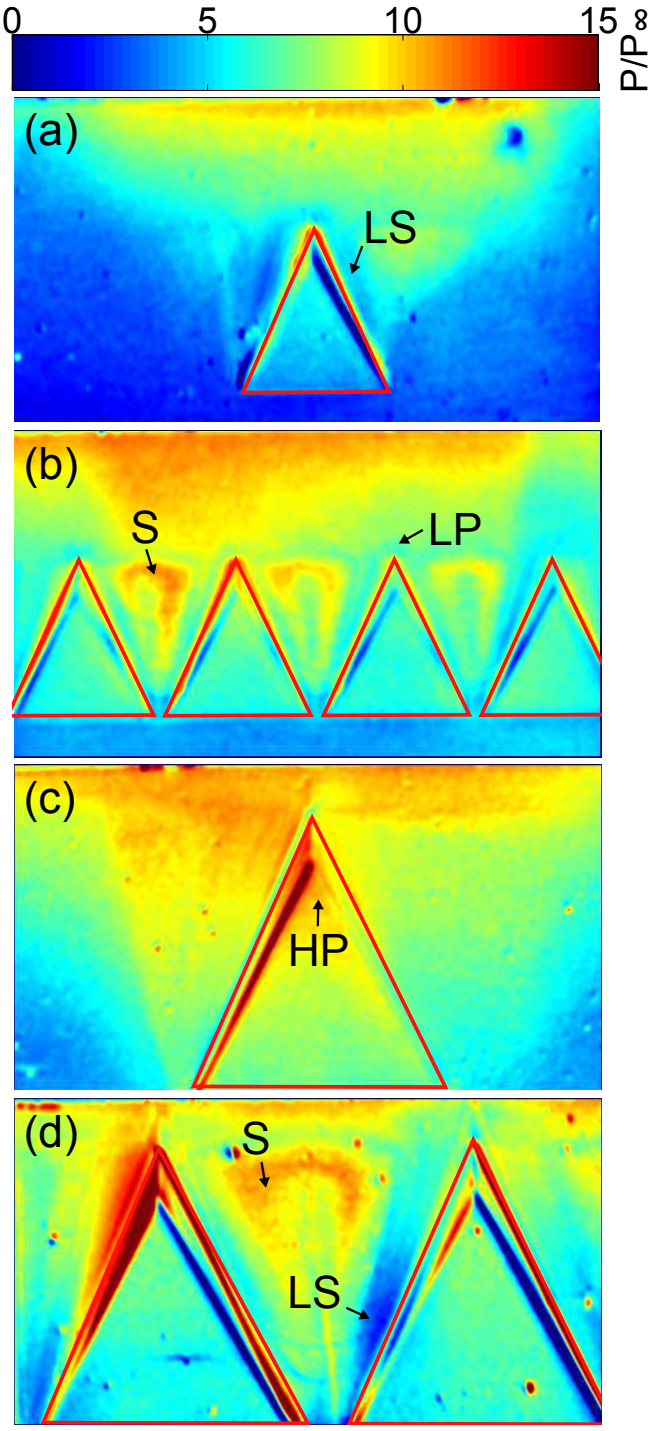


Figure 4.18: Pressure sensitive paints results of all the models. (a) MR40 single (b) MR40 array (c) MR80 single (d) MR80 array. The flow is indicated from bottom to top.

Regions of low-pressure can be seen near the junction between the model and the floor. They are clearly shown from MR40 single and MR80 array PSP

images shown and marked *LS* in Figure 4.18a and 4.18d, respectively. These low-pressure regions are caused by the low-shear stress at the particular region. The flow from the top surface of the micro-ramps moves down the slant edges in a rotational manner and eventually formed the primary vortices and touches the wall surface at a certain distance away from the wall-floor junction. The region where the wall was not touched by the flow experienced low-shear stress and hence forming the low-pressure region. This was previously evident in the oil-flow images shown and explained in Section 4.5.1.

At the small region just after the micro-ramp apex, a relatively low pressure spot can be observed. This is indicated by *LP* in Figure 4.18b. Based on the numerical studies done by Li et al. [80] shown in Figure 4.19, a nodal point (NP) exists halfway between the apex and the floor on the centre plane causing high-pressure region at that particular region. As the flow moves down, the half saddle point (HSDP1) forms at the wall surface. Opposite to the nodal point, this region is indicated by the presence of a relatively lower-pressure spot. From an experimental perspective, the region can be observed as a recirculation and dead water region.

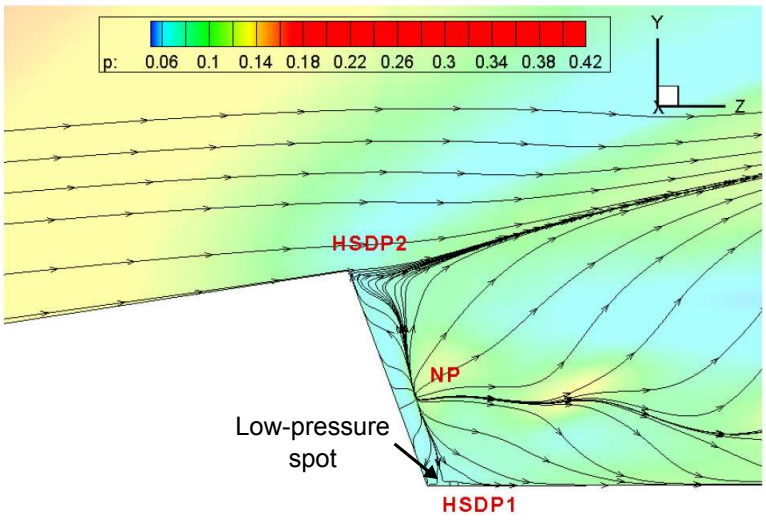


Figure 4.19: Separation pattern at the centre plane of the micro-ramp near the apex [80].

Due to the angle between the micro-ramp surface and the wall, the region near the apex of the micro-ramp suffers from high-pressure caused by the incoming flow. This can be seen from Figure 4.18c labelled as HP. Since the height of MR80 is 80% of the boundary layer, the incoming flow is nearly equivalent to

the freestream velocity. Moreover, due to the head-on collision with the flow, the shear between the surface and the flow eventually forms the high-pressure spot on the surface. This was not clearly seen in the MR40 models. Due to the small sizes, they are more embedded inside the boundary layer compared to MR80 and encounter less shear with the high-speed flow.

## 4.7 Particle Image Velocimetry

Particle Image Velocimetry (PIV) experiments were conducted using the largest model MR80 in single configuration. The objective of the experiment was to visualise the mean and the instantaneous flow organisation behind the micro-ramp both quantitatively and qualitatively.

The streamwise mean velocity distribution, $U$ with respect to the freestream velocity, $U_{ref}$ is shown in Figure 4.20. The boundary-layer developing on top of the micro-ramp surface can be seen clearly. A small region of stationary flow can be observed at the immediate downstream area from the micro-ramp apex. This is consistent with the discovery of the low-pressure region from the PSP image in Figure 4.18b. The flow field initially can be considered well organise, until about 30mm downstream the trailing-edge, a more chaotic structure of the wake began to take place. This is consistent with the PIV results of Bo et al. [53] where he divided the downstream wake region into two regions. The first region is considered relatively steady zone while more unsteadiness can be observed in the second region. In the experiments conducted by Lu et al. [54], large 'billowing' structures were found in the region.

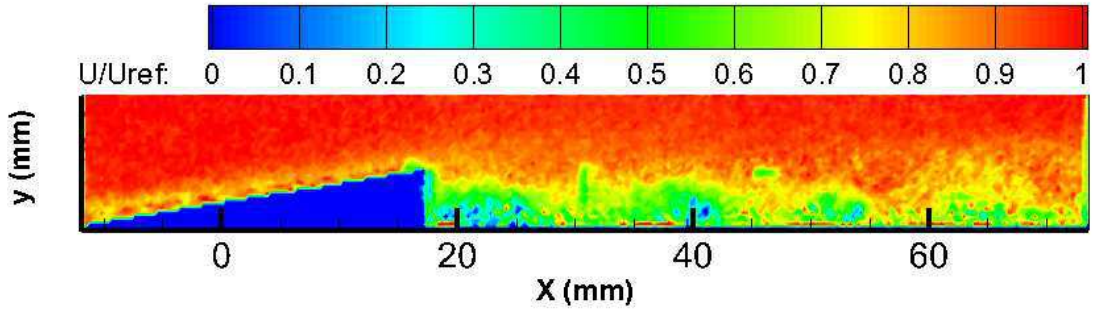


Figure 4.20: Streamwise mean velocity distribution, $U/U_{ref}$ on the median plane.

Figure 4.21 shows the wall-normal mean velocity distribution, $V_y$ on the median plane. The flow region on top of the micro-ramp surface shows that the

flow follows the angled path, climbing on top of the ramp towards the apex. After the apex, the flow continues to fly off the ramp in the same direction before readjusting to the streamwise flow axis. This was also evident in the high-speed schlieren images shown in the earlier section. The upwash motion of the wake region can be seen clearly at the region 30mm downstream the micro-ramp apex. This coincides with the steady region as shown previously in Figure 4.20. This motion can be related to the generation of two streamwise primary vortices generated by the micro-ramp. The two streamwise vortices propagate downstream in a counter-rotating manner hence producing the upwash motion at the centreline.

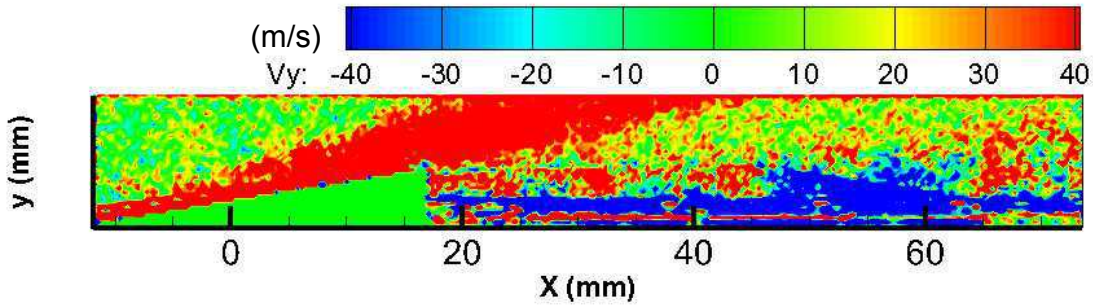


Figure 4.21: Wall-normal mean velocity distribution, $Vy$ (m/s) on the median plane.

To further investigate on the streamwise vortices, an instantaneous velocity distribution, $V_y$ of the median plane is shown in Figure 4.22. The primary vortices, that are represented by the upwash velocity are seen to limit their height to the same height of the micro-ramp. However after approximately 30mm from the leading-edge, the vortices dramatically increased their heights of up to 1.5 times the height of the micro-ramp. Towards the end of the viewing window, the structure continue to increase its height while at the same time the freestream flow started to come in place. The interaction between the vortices with the freestream flow induces the formation of vortical ring structures at the shear layer due to Kelvin-Helmholtz (K-H) instabilities.

Alternate regions of spanwise velocities can be observed from the spanwise mean velocity distribution, $V_z$ shown in Figure 4.23. The measurement plane, which was parallel to the wall was located at $y = h$ where $h$ is the height of the micro-ramp. These alternate regions are a clear indication of the arc-shaped K-H vortices as previously found by Sun et al. [51]. Moving further downstream, the K-H vortices started to decrease in width and dissipate. However evidence from Bo et al. [53] suggests that the vortices were not dissipating, but lifting-off

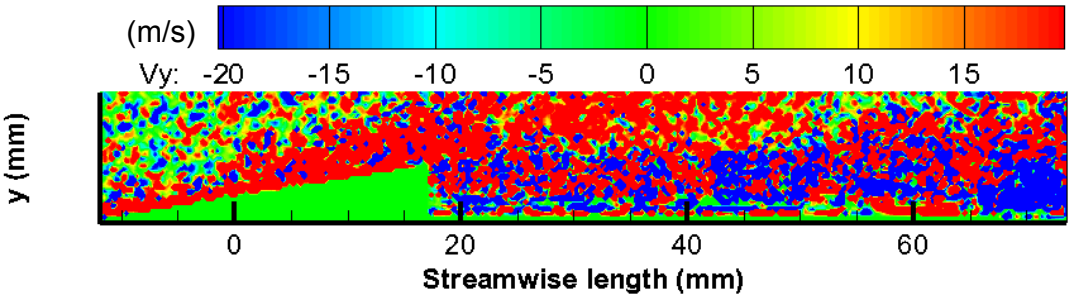


Figure 4.22: Wall-normal instantaneous velocity distribution, $Vy$ (m/s) on the median plane.

the surface at an angle instead. Note that the structures visualised on the right hand side of the figure are not the K-H vortices. They are unknown structures that were thought to be generated due to the edge-plate effects. As a conclusion, from the PIV measurements in both plane configurations, the complex vortical structures were able to be visualised. This includes the two streamwise counter-rotating vortices and also the K-H vortical structure, wrapping the two relatively smaller vortices.

## 4.8 Summary

The findings of this chapter can be summarised as the following:

- There are two shock waves produced by the micro-ramp when encountering the flow; leading-edge and trailing-edge shock waves.
- The micro-ramp were submerged inside the boundary layer of the incoming flow hence satisfying the criterion of micro-vortex generator.
- Flow separation occurred at the leading-edge of the micro-ramp as a result of a localised shock boundary layer interaction.
- Micro-ramp produced a pair of primary vortices accompanied by two pairs of secondary vortices including the horseshoe vortices.
- The ratio of the diameter of the secondary vortices to the micro-ramp chord length ($d/c$) is approximately 0.05.

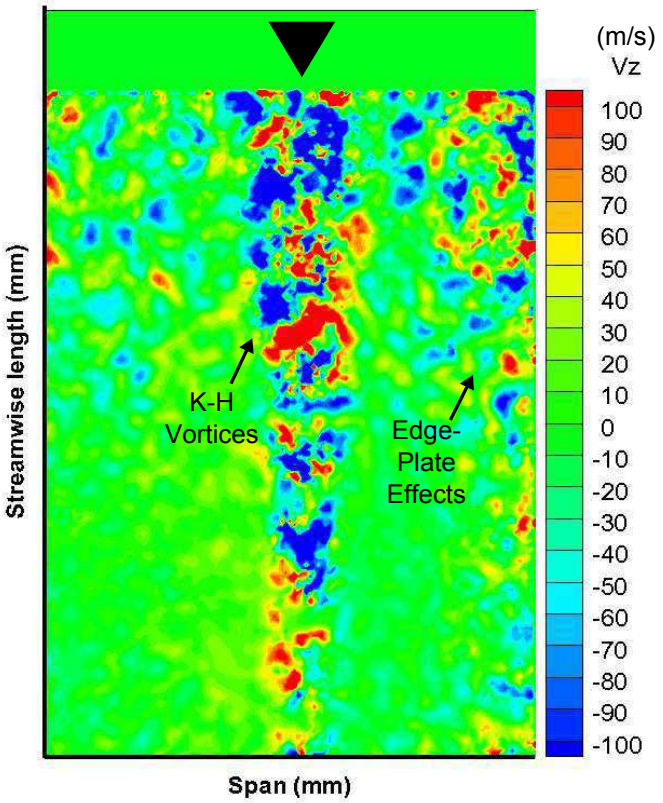


Figure 4.23: Spanwise mean velocity distribution, $Vz$ (m/s) on $y = h$ plane parallel to wall. Black triangle indicates the location of the micro-ramp in upstream position.

- The pair counter-rotating primary vortices produced upwash and downwash motion that enable the transfer of high momentum flow from the outer region to the wall.
- The K-H vortices were observed from the alternating spanwise velocities along the streamwise axis.

# Chapter 5

# Micro-Ramp for SBLI Control

The interest in micro-ramp, initiated from the idea of the existence of conventional passive vortex generators (VG) with the device height, $h$ having the order of the boundary layer thickness, $\delta$. These VG were used to control flow separation since the late 1940s [81]. Then in the early 1970s, a non-conventional wave-type VGs were developed by Kuethe [27] with $h/\delta$ of 0.27 and 0.42 to generate streamwise vortices within the boundary layer. Starting from that, the researches on low-profile or submerged VGs bloomed due to the much lower parasitic drag and the applications proved the effectiveness on flow-separation control at low speed and supersonic flows. The interest was then brought to the use of micro-ramp in controlling SBLI in high-speed flows involving transonic and supersonic flows. More knowledge on the flow physics and effectiveness of the micro-ramp started to develop. Different theories on the capabilities of the micro-ramp in controlling SBLI were presented. However none of these were investigated in hypersonics condition. This chapter describes the effectiveness of the micro-ramps in controlling SBLI in Mach 5 hypersonic flow.

## 5.1 SBLI setup in HSST

SBLI is created in HSST by a shock-generator, mounted to the ceiling plate of the test section. The shock-generator created a 34° obllique shock that impinged on the hypersonic boundary layer developing on the flat plate. The detail setup and dimensions of the shock-generator were explained in Section 3.3.4. The two variables that are used to fix the location of the shock impingement location ($X_s$) on the flat plate are the streamwise distance from the plate leading-edge

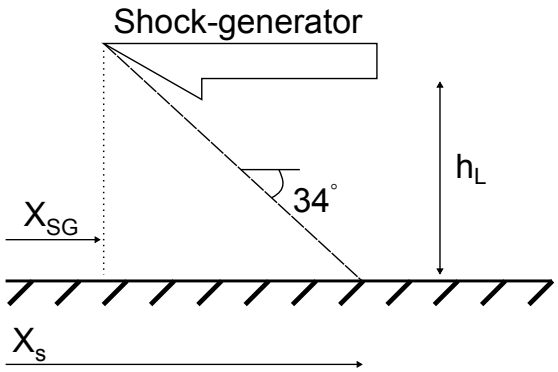


Figure 5.1: Variables related to the location of the shock-impingement location, $X_S$ on the flat plate.

to the tip of shock-generator, $X_{SG}$ and the vertical distance from the body of shock-generator to the wall, $h_L$ as shown in Figure 5.1. Note that $X_s$ is the distance from the leading-edge of the plate to the shock-impingement location. $X_s$ is varied depending on the experimental techniques employed.

To simplify the setup, for all experiments, $X_{SG}$ is kept constant at $30.6\delta$. Only $h_L$ is varied to get different values of $X_s$. The outcome of 5 combinations of $h_L - X_s$ is plotted in Figure 5.2. The values are obtained from schlieren visualisation images. Note that $X_s$ is the inviscid shock-impingement location. Since the oblique shock are refracted along the way by the leading-edge shock and separation shock, the exact location of impingement on the boundary layer is difficult to be determined. Therefore in the schlieren image, a line is drawn from the leading-edge of the shock-generator along the shock line and extrapolated straight to the flat plate as illustrated in Figure 5.1. The point where the line intersects the plate surface is selected as $X_s$.

From the plot, the line of best fit is drawn and yields Eqn. 5.1. From the equation, $X_s$ can be easily calculated for all experiments conducted in Mach 5, with 34° shock-generator and fixed value of $X_{SG} = 30.6\delta_0$. For all the locations used in the experiments, this equation is used and schlieren images are still conducted for verification.

$$X_s = 1.21h_L + 38.58\delta_0 \tag{5.1}$$

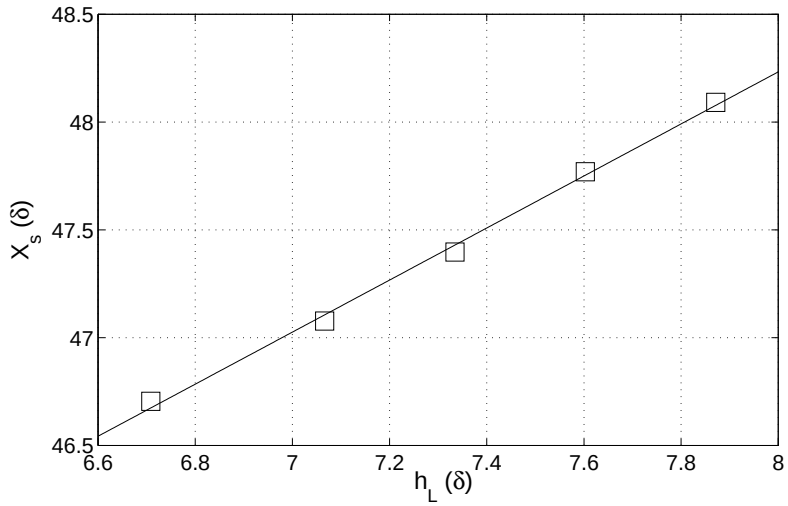


Figure 5.2: Plot of $h_L$ versus $X_s$ with constant $X_{SG} = 30.6\delta_0$.

## 5.2 Effect of local Reynolds number

Viscosity plays a vital role in influencing the overall size of the separation region. The extent of the separated region is dependent on the shear layer ability (that originates from the separation point) to overcome the increased pressure at reattachment point. This in turn is the function of the momentum available during the start of the reattachment process. Therefore to overcome the pressure rise, an increase in the shear-layer strength is needed to obtain a greater transfer of momentum from the outer flow and this pushes the origin of the shear layer, corresponding to the separation point to move further upstream.

Delery [82] proposed the relationship of the interaction extent $L$ is of the form in Eqn. 5.2 based on the free-interaction theory. $L$ is taken as the streamwise scale given by $L = x_s - x_0$ which is the distance between the start of the interaction (where pressure rise is observed) and the location of the separation point. ${\delta_0}^*$ is the boundary layer displacement thickness at the interaction onset, while $C_{f0}$ is the skin-friction coefficient and $M_0$ refers to the local Mach number. This equation suggests that $L$ is only dependent on the flow properties at the interaction onset and not on the downstream conditions. One of the important properties that affects $L$ in the equation is $C_{f0}$ which is also related to the local Reynolds number, $Re_{\delta 0}$ given by $C_{f0} \propto {Re_{\delta 0}}^{-1/5}$. Therefore the effect of viscosity on the interaction decreases as the Reynolds number increases. In simpler words, for lower $Re_{\delta 0}$ where viscosity is dominant, $L$ is expected to increase accompanied

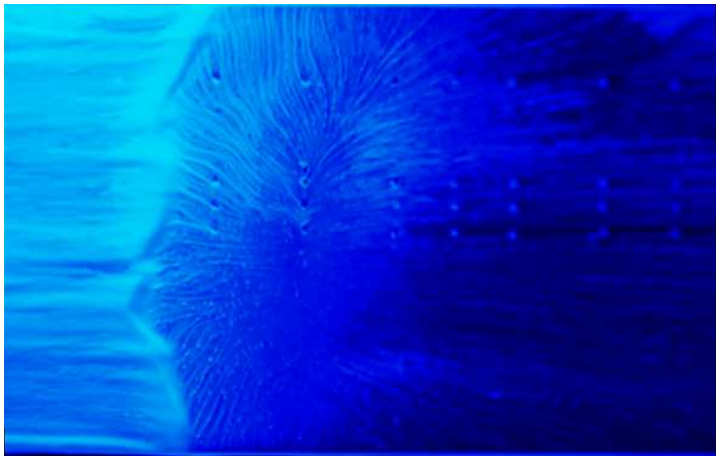

(a) $Re = 3.7 \times 10^6, X_S = 50.7\delta_0$

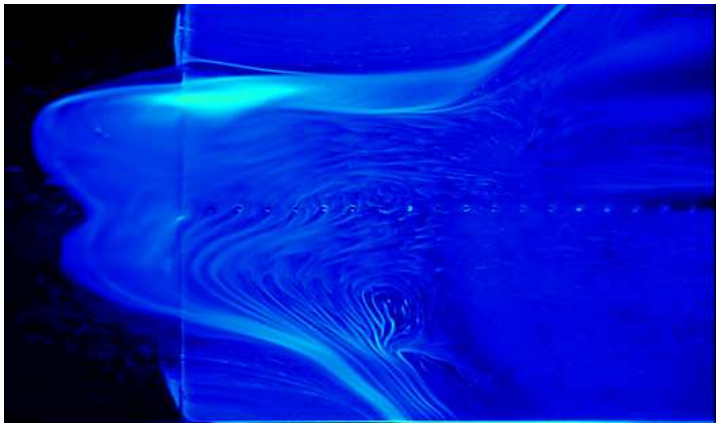

(b) $Re = 4.1 \times 10^6, X_S = 55.2\delta_0$

Figure 5.3: Interaction at two different streamwise location.

with a lower peak pressure at reattachment. On the other hand, for higher $Re_{\delta 0}$ where viscosity is less dominant, the opposite is expected.

$$L \propto {\delta_0}^* (C_{f0})^{-1/2} \left({M_0}^2 - 1\right)^{-1/4} \tag{5.2}$$

As for the case of $Re_{\delta 0} = 3.7 \times 10^6$ in Figure 5.3a, the distance between the reattachment line to the separation line is calculated as only $2.6\delta_0$. However, for the case of a higher Reynolds number, as shown by $Re_{\delta 0} = 4.1 \times 10^6$ in Figure 5.3b, the separation region extended further upstream which can be seen from the location of the separation line. The pattern of the separation region also changed significantly as observed. The distance between the reattachment line to the separation line at the centreline now is calculated to be $18.2\delta_0$. This is almost

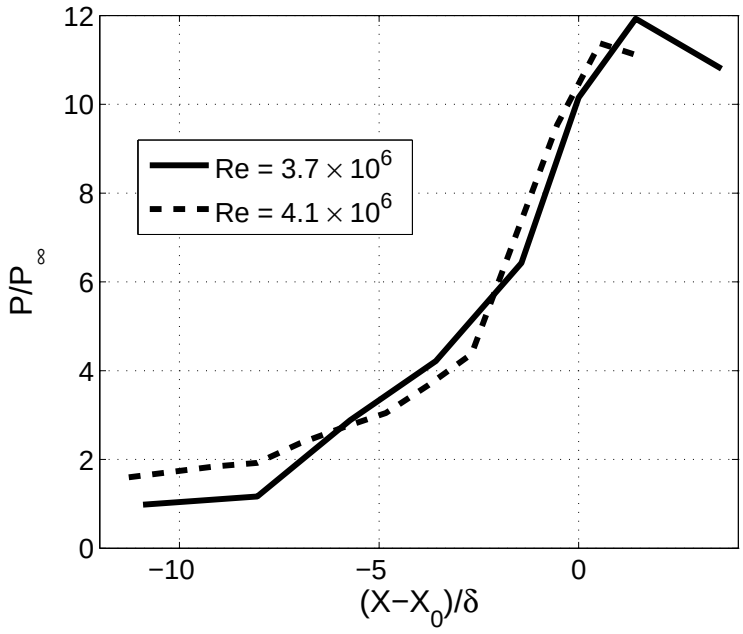


Figure 5.4: Surface pressure distribution of uncontrolled interaction at two different Reynolds number at centreline.

7 times more upstream. Since the separation line was pushed further upstream, which also means that $x_0$ is also located more upstream, proportionate to the separation line position. This is evident from the surface pressure distribution shown in Figure 5.4. The origin of the pressure rise for $Re_{\delta 0} = 3.7 \times 10^6$ is observed at $x = -8$ while at the same position, the pressure had already increased for $Re_{\delta 0} = 4.1 \times 10^6$. Thus from the plot, $x_0$ for $Re_{\delta 0} = 4.1 \times 10^6$ is predicted to occur at a more further upstream location.

Another point observed in the plot in Figure 5.4 is the peak pressure measured for both $Re_{\delta 0}$. It is clear that the peak pressure for $Re_{\delta 0} = 4.1 \times 10^6$ is lower than $Re_{\delta 0} = 3.7 \times 10^6$. Delery [82] also stressed that this behaviour is confirmed through the experimental investigations for both laminar and turbulent flows as long as $Re_{\delta 0}$ is less than about $10^5$. Above that, the tendency is reversed where the increased in $Re_{\delta 0}$ will be accompanied by the contraction of the separation region and the increase of the peak pressure. However in this study it is demonstrated that for $Re_{\delta 0}$ of the order of $10^6$, this relation is still relevant.

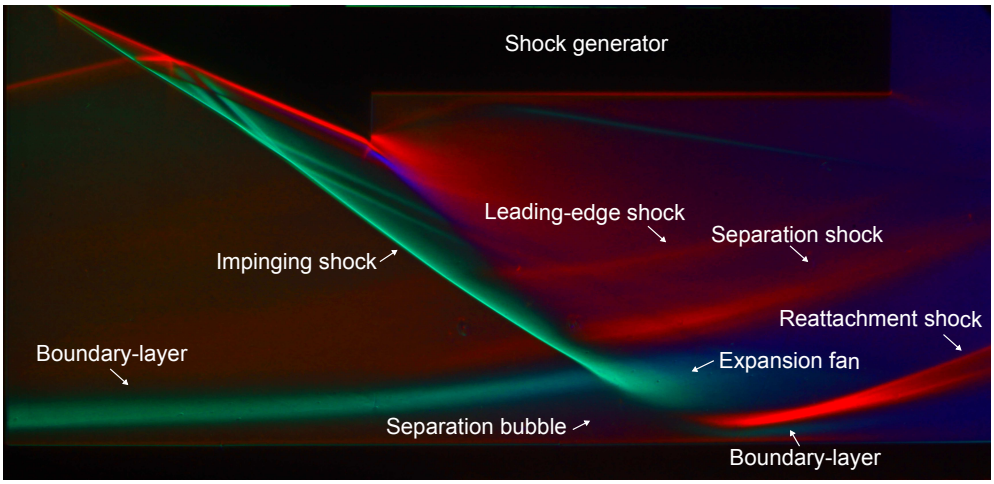


Figure 5.5: Colour schlieren image of shock-boundary layer interaction in HSST with no control (clean tunnel) [$X_s = 44.6\delta_0$, $h_L = 5.0\delta_0$].

## 5.3 Schlieren visualisation

The overall view of the shock wave system resulting from the SBLI will be presented in this section. Features of typical SBLI shock products such as separation shock, reattachment shock, separation bubble, expansion fan are captured by schlieren visualisation. First, the case of uncontrolled SBLI (clean tunnel) where no control is employed is presented followed by the case where the micro-ramps are used for control.

Figure 5.5 displays the image of colour schlieren for SBLI case in HSST in the case of clean tunnel where no boundary-layer control is applied. The result acts as the baseline case and source of comparison for the later experimental results with the presence of micro-ramps. Starting from the flat plate leading-edge (far left in the image and not seen), the boundary layer developed and gradually became thicker. The edge of boundary layer is seen clearly in the figure. Then an oblique shock impinged on the boundary-layer causing a large pressure difference across it and consequently induced boundary-layer separation. At the location where the shock impinged, a separation bubble is formed, acting as a virtual bump which caused a form of flow obstruction forcing the boundary layer on top to climb over it.

Due to the flow deflection, a separation shock wave is induced. The intersection of the separation shock with the flat plate is identified as the separation point, where the boundary layer began to separate and shall have absolutely no

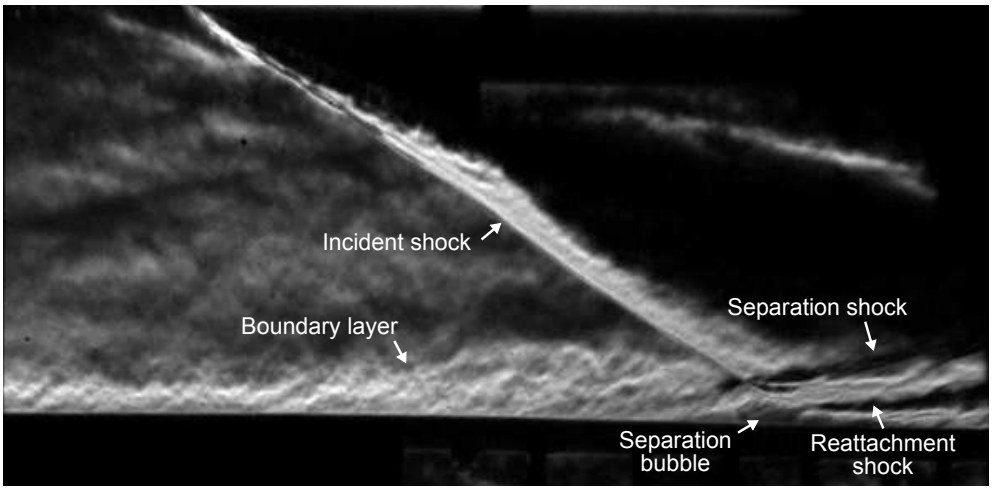


Figure 5.6: High-speed schlieren instantaneous image of shock-boundary layer interaction in HSST with no control (clean tunnel). Image recorded at 5000fps [$X_s = 50.7\delta_0$, $h_L = 10\delta_0$].

contact with the wall. This is also identified as the point where the boundary layer suddenly experienced rapid thickening of about double of its previous thickness. This point occurred slightly upstream from the shock-impingement point. This is because the initial high pressure caused by the shock impingement, is feeded upstream through the subsonic region of the boundary layer and perturbated the incoming flow hence causing separation. The impinging shock that penetrated into the separation region is reflected as a series of expansion waves due to the near constant pressure within the separated region. This would cause the flow to move back against the wall and finally reattach itself at a point named reattachment point. Following the reattachment process, compression waves are generated due to the change of direction of the flow, which moved towards the reattachment point. At the exact reattachment point, the flow once again changed its direction to move parallel with the wall and this induces another shock wave called the reattachment shock. The boundary layer started to redevelop after the reattachment point and this was captured in the schlieren image.

The high-speed schlieren instantaneous image of the clean tunnel is shown in Figure 5.6. The image is captured at 5000fps and $1\mu s$ exposure time. High-speed schlieren is used to observe the unsteadiness occuring in the flow. The eddies of the incoming turbulent flow are seen in the figure. Upon approaching the separation region, the thicknening of the boundary-layer became obvious, almost doubling its size and more eddy structures appeared. In the figure, the separation

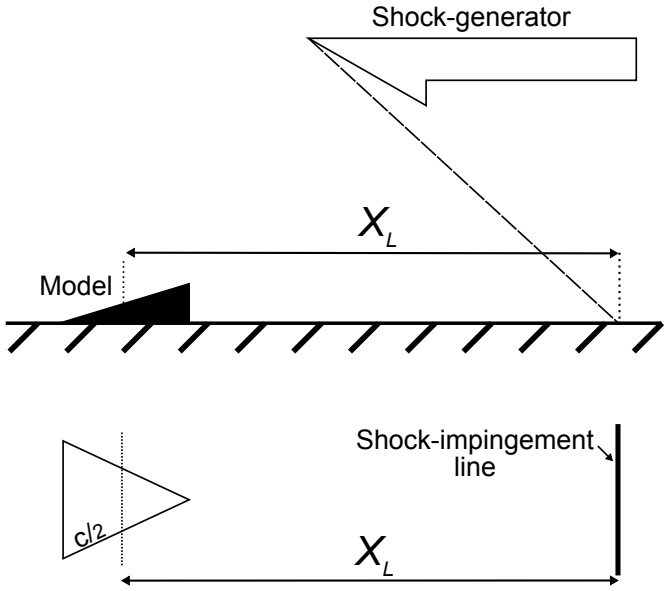


Figure 5.7: Schematic diagram of $X_L$, the distance between micro-ramp centreline with the shock-impingement location.

and reattachment shock are also clearly visible represented by the two dark thick lines in the downstream region. If careful observation is made on the surface of the flat plate (represented by the dark line at the bottom of the image), an inclination at the downstream region is noticeable. This is caused by the effect of the shock impingement on the plate. The flat plate is mounted on top of a vertical stand as shown in Figure 3.16. Because of the loading exerted by the strong shock, the rear section of the flat plate oscillated during the duration of the run. This proved that SBLI could cause serious structural loading problem on aero-vehicles hence lead to catastrophic failure if no control measures are taken. This another smaller stand was manufactured to provide an extra support at the rear of the flat plate to eliminate the oscillations and to ensure high accuracy in the data collection.

A new variable is introduced to have a clearer view on the location of the micro-ramps relative to the shock-impingement location. $X_L$ is the upstream distance of the location of the micro-ramp centreline ($c/2$) with respect to the shock-impingement line as shown in Figure 5.7.

Figure 5.8 and Figure 5.9 show the high-speed schlieren image of the SBLI condition when flow control is employed using MR80 and MR40, respectively. The turbulent eddies of the incoming boundary-layer are seen in both images and the micro-ramps are submerged in them. The separation bubble still existed

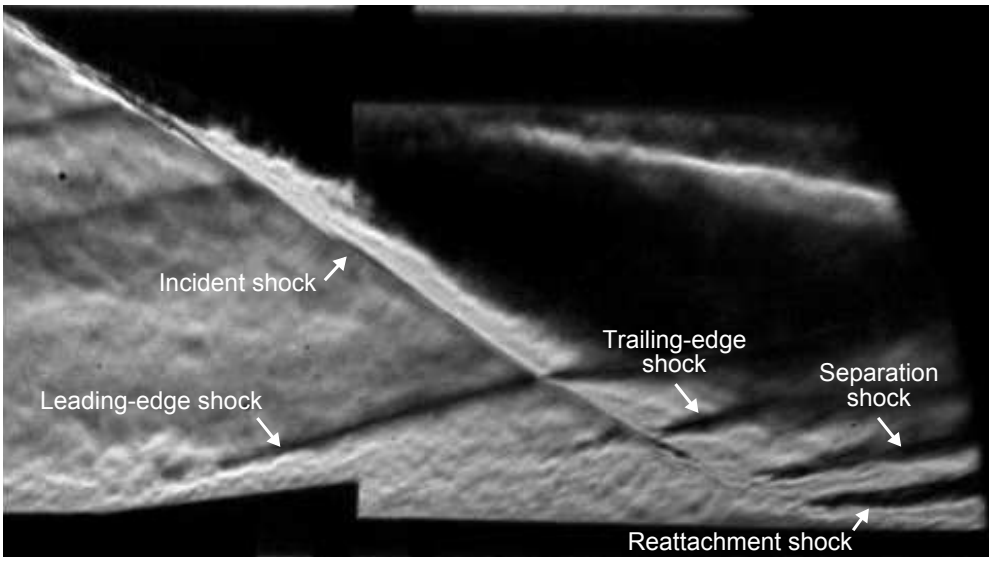


Figure 5.8: High-speed schlieren instantaneous image of shock-boundary layer interaction in HSST with MR80 control. Image recorded at 20,000fps [$X_s = 50.7\delta_0$, $h_L = 10\delta_0$, $X_L = 7.8\delta_0$].

even after the flow control. Even though the size of the separation bubble is not clearly visible in the high-speed schlieren images, the separation bubble still exists and this can be deduced from the shocks that appeared in the downstream region. If the separation region is totally eliminated, only one shock is seen reflecting from the surface of the plate and that will be considered as the shock-boundary layer interaction without separation. However for these cases, two shock waves corresponding to separation and reattachment shocks are seen and this is a clear indication that the separation region still exist. This is consistent with the results from other literatures [3, 29, 53] which suggested the separation regions are not totally eliminated with the presence of micro-ramps, but they are instead distorted or broken into multiple segments as will be discussed in the coming sections. The results from oil-flow visualisation will provide a better understanding. Apart from that, the incident shock wave is seen to meet the strong leading-edge shock from MR80 in Figure 5.8 producing a type I shock-shock interference. However this is not observed for the case of MR40 in Figure 5.9 due to a weaker shock because of the smaller model size.

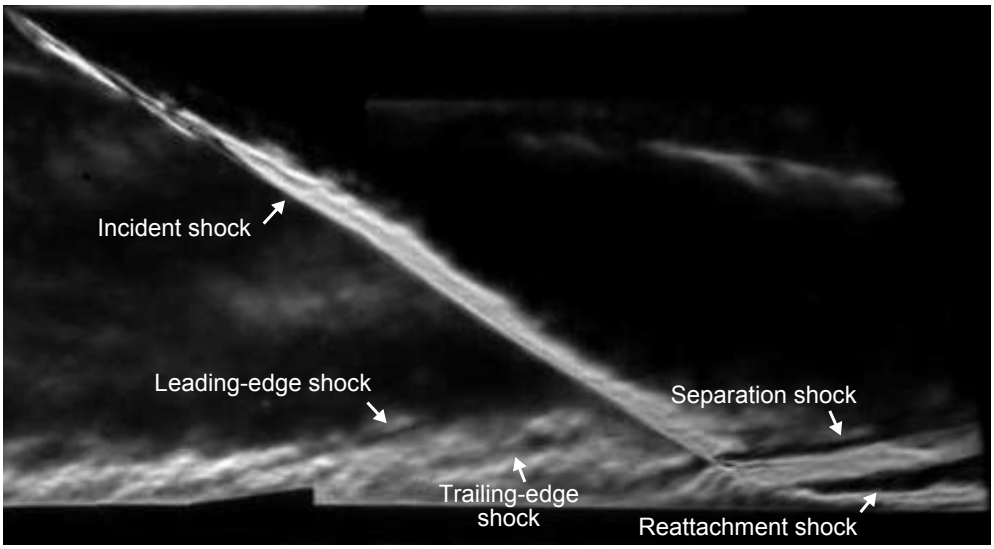


Figure 5.9: High-speed schlieren instantaneous image of shock-boundary layer interaction in HSST with MR40 control. Image recorded at 16,000fps [$X_s = 50.7\delta_0$, $h_L = 10\delta_0$, $X_L = 7.8\delta_0$].

## 5.4 Kulite pressure measurements

The upstream interaction influence which is only possible in the viscous environment, causes the upstream pressure distribution over a boundary layer thickness to rise compared to the purely inviscid case where a pressure jump is obtained. Figure 5.10 shows the surface pressure distribution for uncontrolled baseline interaction (clean tunnel) at different spanwise positions including at the centreline. Note that $X_0$ is the location of shock impingement in the inviscid environment. It can be seen that even the pressure rise across the interaction is almost uniform and a three-dimensional effect of the interaction region across the spanwise distance is observed. The most affected region is at the centreline. The pressure rise is observed at a distance as upstream as $8\delta_0$ from the shock impingement location. The pressure rise at the offcentre locations are seen at $6\delta_0$ upstream. Therefore for the upcoming results that will be discussed in this chapter, the improvements brought by the micro-ramps will only be focused based on the pressure distribution at the centreline, since it was found to be the worse region affected by the SBLI.

For well separated case, the two inflexion points in the surface pressure distribution where the maximum pressure gradients occur, are usually the representation of the separation and reattachment points [6]. From the centreline plot,

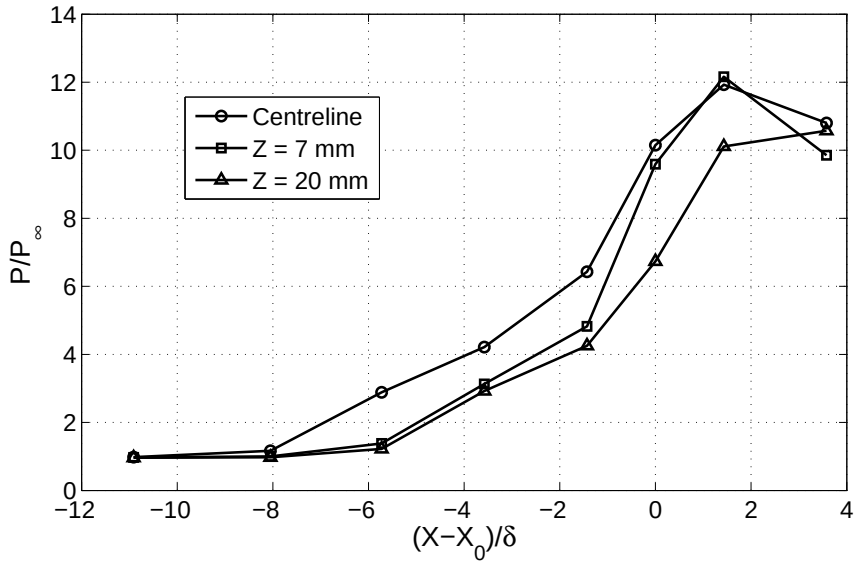


Figure 5.10: Surface pressure distribution through uncontrolled baseline interaction along centreline and offcenter locations [$X_s = 54.6\delta_0$].

the maximum pressure gradients between two points are observed at two regions; $x = -1.4$ to 0 and $x = 0$ to 1.4. The peak pressure are usually associated with the necking motion of the shear layer at the reattachment line. Elfstrom [76] relates the peak pressure in hypersonic SBLI as the pressure overshoot aft the reattachment point. This is due to the intersection of the separation and reattachment shock taking place close to the surface. However this is only presence in the case of SBLI on a compression ramp and not in an oblique shock impingement case due to the angle of the second ramp. In this case, the separation and reattachment shocks are found not to intersect each other based on the evidence from the schlieren images. Therefore the peak pressure at $x = 1.4$ can be directly related to the reattachment line. Following the peak pressure, the pressure then experiences relaxation to the inviscid pressure level.

Conversely the direct determination of the separation point is not as easy as the reattachment point. Hence there is a need in flow visualisation on the surface of the interaction region as shown by the oil-flow image in Figure 5.11. The separation line is represented by the location of oil accumulation upstream the reattachment line. The centreline distance from the reattachment line to the separation line is measured to be $2.6\delta_0$. If the peak pressure on the plot in Figure 5.10 is assumed to be the exact location of the reattachment point, the separation point can be estimated to occur at $x = -1.2$. This agrees with the

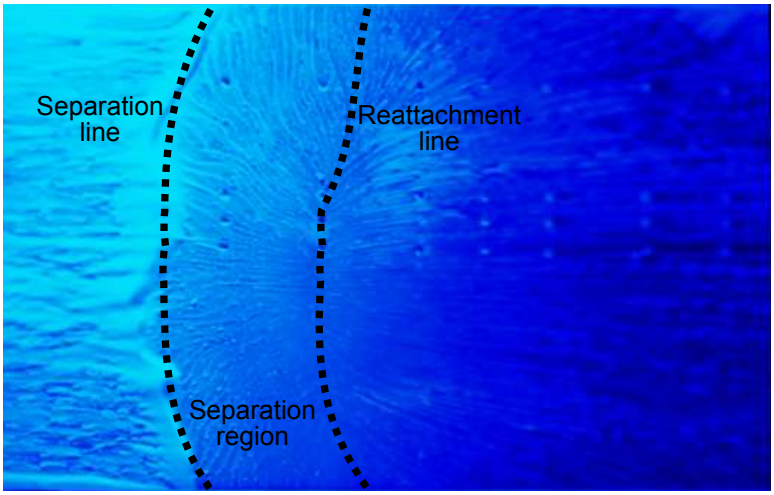


Figure 5.11: Oil-flow visualisation of the separation region in the uncontrolled baseline interaction [$X_s = 50.7\delta_0$].

first region of maximum pressure gradient in pressure plot. The pressure rise is observed to start at a position as early as $x = -8$ although the separation point is estimated to start only at $x = -1.2$. This implies that the upstream interaction influence in this SBLI case is significantly large. The upstream influence length parameter $L_0$, which is defined as the distance from the location of the start of the pressure rise to the invscid shock impingement location, is calculated at approximately $6.8\delta_0$.

The centreline pressure distribution with single micro-ramp control is compared with the baseline case in Figure 5.12. Both MR80 and MR40 are tested. Each micro-ramp are placed at the centre of the flat plate with the apex alligned at the centreline at a distance of $7.8\delta_0$ upstream of the inviscid shock-impingement location. The presence of the micro-ramps successfully delayed the pressure increase upstream hence reducing the upstream influence compared to the uncontrolled case. Referring to the region at the separation point at $x = -1.4$, a slight increase in the pressure gradient is observed and this is an indication of a reduction of separation [3]. In terms of size, the greater size micro-ramp, MR80 proved to be slightly more effective especially in delaying the pressure rise.

The micro-ramp array configuration are then tested with the same experimental setup and the results of the centreline pressure distribution are shown in Figure 5.13 in comparison with the single configuration and the uncontrolled interaction. The number of micro-ramps in an array are dependent on their size. For MR80, two models were placed side by side and for the MR40, four models

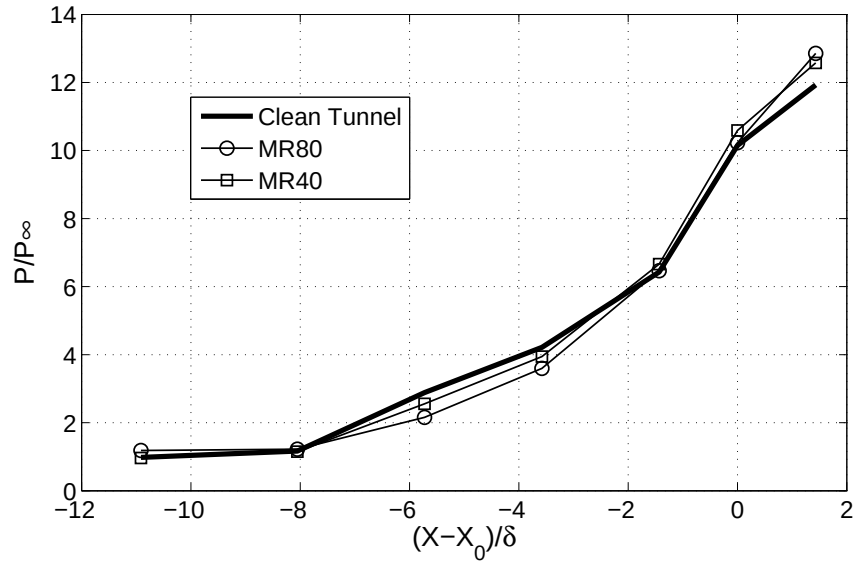


Figure 5.12: Centreline surface pressure distribution of interaction for uncontrolled and with single micro-ramp control case [$X_s = 54.6\delta_0$, $X_{SG} = 15\delta_0$].

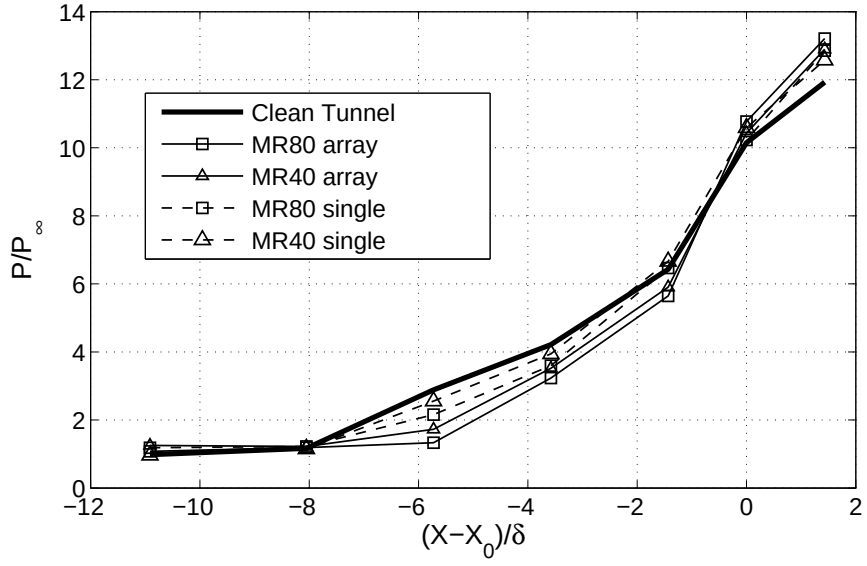


Figure 5.13: Centreline surface pressure distribution of interaction for uncontrolled, single and array micro-ramp control case [$X_s = 54.6\delta_0$, $X_{SG} = 15\delta_0$].

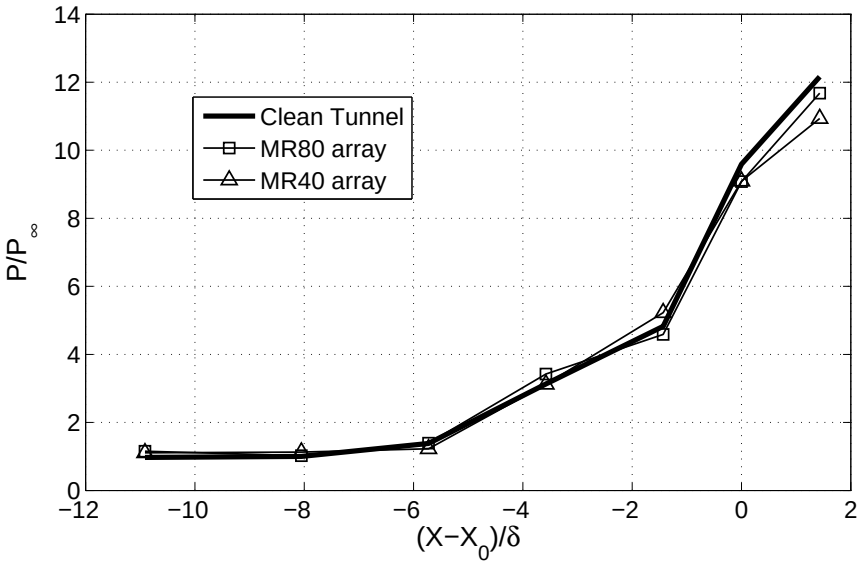


Figure 5.14: Surface pressure distribution at $Z = 20$ mm of interaction for uncontrolled and micro-ramp control case [$X_s = 54.6\delta_0$, $X_{SG} = 15\delta_0$].

made up the array. From the plot, the pressure rise only started at $x = -6$ for MR80 array configuration and a slight rise after $x = -8$ for MR40. Near the separation point, the pressure gradient was the maximum for the array configurations that also exhibits the maximum peak pressure. Comparing the single and array configurations, without a doubt, the results shows that the array configurations perform far better than the single configuration for all the sizes of the micro-ramps. The improvements brought by the array configurations, based on MR80 data is significant. $L_0$ was reduced from approximately $8\delta_0$ for the uncontrolled case to $6\delta_0$, a large difference of $2\delta_0$.

The effective array configurations are then tested at a different spanwise location, $z = 7$ mm to see how they could improve the upstream interaction influence. Previously in Figure 5.10 it was found that at $z = 7$ mm, the region is lightly affected by the SBLI. Therefore there might be a possibility that the presence of the micro-ramp array would totally improve the situation. However from the plot in Figure 5.14, the pressure distribution of the controlled environment does not portray any significant difference with the uncontrolled case. The pressure rise occurred at the same location while no significant change in the pressure gradient at the separation region. Another comparison is brought in Figure 5.15 for the case at $z = 20$ mm, which is almost at the maximum spanwise location. No clear improvements can be observed for the case with micro-ramp control unlike at

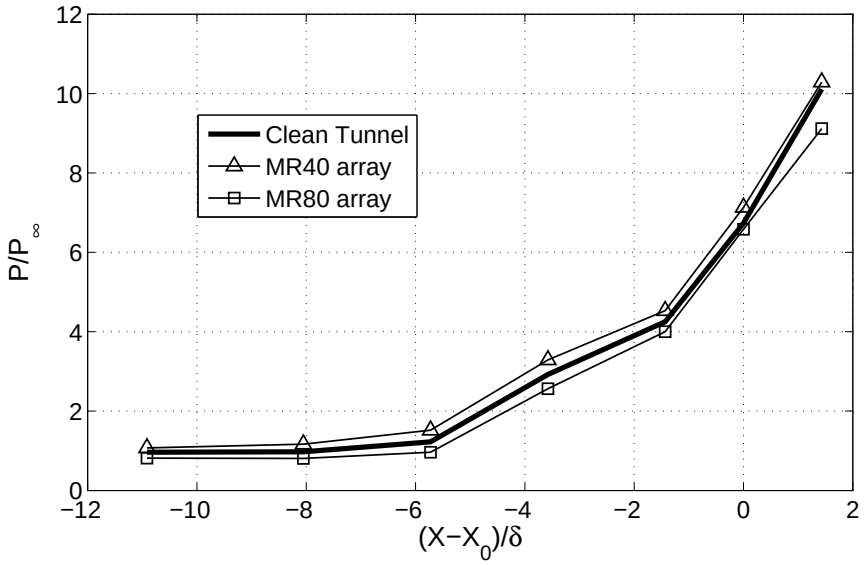


Figure 5.15: Surface pressure distribution at $z = 20$ mm of interaction for uncontrolled and micro-ramp control case [$X_s = 54.6\delta_0$, $X_{SG} = 15\delta_0$].

the centreline region. Hence it shows that the micro-ramps proved to be most effective in controlling the SBLI at the centreline region.

## 5.5 Oil-flow visualisation

The formation of the separation region in chronological order for the uncontrolled case is shown by the oil-flow images in Figure 5.16. Grayscale colour was applied to the images for clarity. The actual oil colour used in the experiments was green which can be seen in the raw images shown in Figure 3.29 in Chapter 3. The holes seen on the surface of the plate in Figure 5.16a are the pressure tappings. To visualise the oil pattern in the separation region, the oil was applied at a larger area and more downstream location compared to the oil-flow results in Chapter 4. The area was $119 \times 60$ mm and starting at 20 mm downstream the micro-ramp centre. The shock impingement distance from the leading-edge ($X_s$) was set as $50.7\delta_0$. The blobs of oil seen were caused by the reaction of the thin oil layer after the test section was vacuumed.

After the flow started, the reattachment line at the middle of the image started to form as shown in Figure 5.16c. To the left side (upstream) of the reattachment line, the flow is observed to move upstream, the opposing the direction of

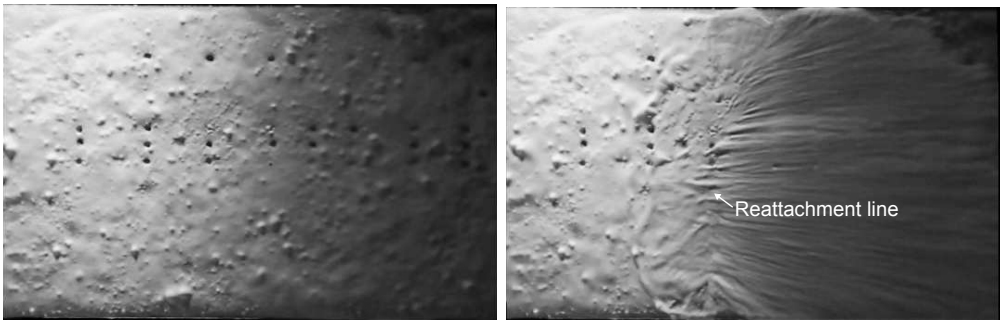

(a) $t = t_0$




(b) $t = t_0 + 0.2s$

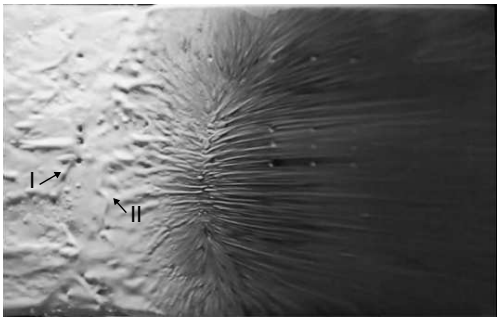


(c) $t = t_0 + 0.3s$

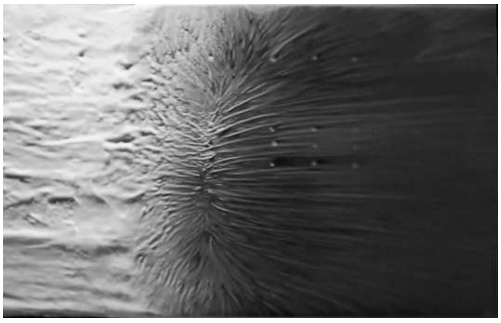

(d) $t = t_0 + 0.4s$

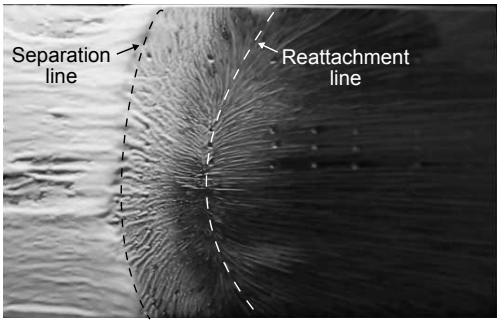


(e) $t = t_0 + 0.5s$

(f) $t = t_0 + 2.4s$

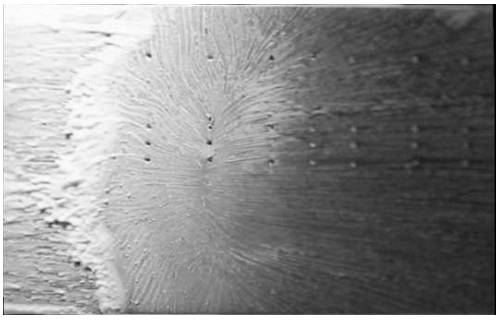

(g) $t = t_0 + 7.6s$

(h) $t = t_0 + 8.0s$

Figure 5.16: Oil-flow visualisation images in chronological order of uncontrolled interaction. Flow is from left to right [$X_s = 50.7\delta_0$].

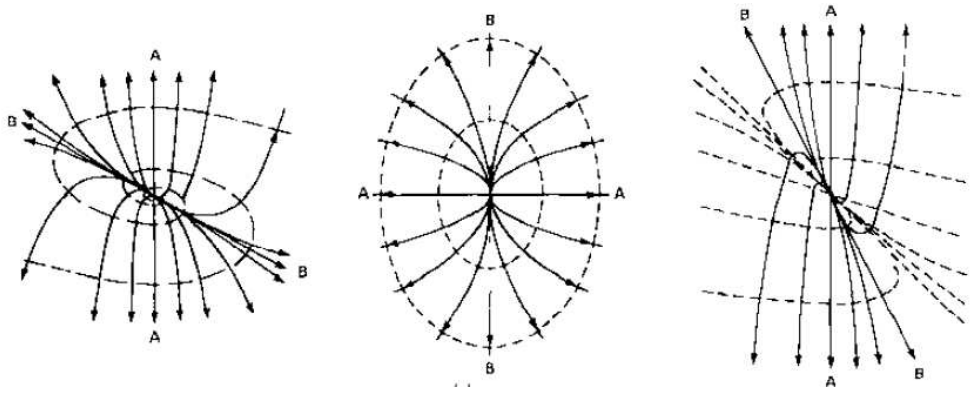


Figure 5.17: Types of singular nodal points found in three-dimensional separated flows by Tobak & Peake [79].

the flow. This is called the reversed flow. On the other hand, on the right hand side (downstream) of the line, the flow continued to move downstream. The reversed flow pushed the oil upstream forming a line of accumulated oil labelled II in Figure 5.16c. Another line of accumulated oil (labelled I) from the upstream region is seen moving towards II. After a short period of time (approximately 0.1s), the two oil lines meet each other and merged into a single line as can be seen in Figure 5.16d. The line then became more steady and this is known as the separation line as labelled in Figure 5.16e. As measured before in Section 5.4, the distance between the separation and the reattachment line is $2.6\delta_0$. After approximately 2s in the run, no movements of the oil streaks are seen in Figure 5.16f as the oil begins to dry due to the high-temperature flow. Approaching towards the end of the run, the terminating shock from the nozzle impinged on the flat plate and travelled upstream, causing the oil accumulation at the separation line to spread a small distance upstream as seen in Figure 5.16g. Finally in Figure 5.16h, after the disappearance of the terminating shock, the flow stopped and the accumulated oil smeared downstream into the previously called separation region as this time it is no longer stopped by the reversed flow.

The topology of the separation region seen in the oil-flow results is similar with the three-dimensional separation patterns outlined by Tobak & Peake [79] in Figure 5.17. The separation and reattachment lines are representation of infinite singular nodal points of separation and reattachment, respectively. A nodal point is defined as the point of common for an infinite number of skin-friction lines, as for this case is the thin oil-streaks that formed the pattern seen in the separation region. For a nodal point of separation, all of the skin-friction lines are observed to

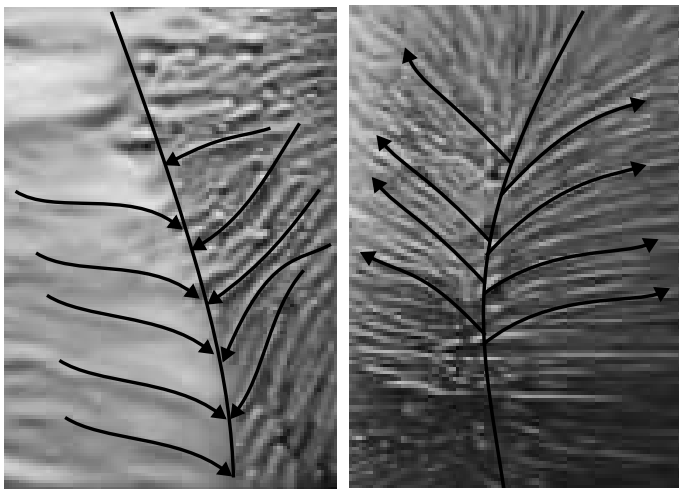

(a) Separation line (b) Reattachment line

Figure 5.18: Nodal points along the separation and reattachment lines observed in the separation region.

be directed inward toward the node while for nodal point of attachment, all of the skin-friction lines are directed outward from the node. This is excatly the pattern observed in the separation region for both separation and reattachment lines as shown in Figure 5.18. The arrows indicate the direction of the oil movements.

The results of the oil-flow images for the controlled interactions are shown in Figure 5.19. The images are the sum of 100 images during the steady flow phase. Figure 5.19a shows the interaction region controlled by a single MR40 model. The flow is from left to right and the shock impingement location is the same as the baseline case, $X_s = 50.7\delta_0$. The two thin lines at the centre on the left of the image correspond to the secondary vortices originating from the centre of the model. The global position of the separation and reattachment lines did not change with respect to the uncontrolled case. The measured distance between the two lines is still $2.6\delta_0$. The separation line where the oil accumulates and form a thick oil band near the centreline is observed to be slightly distorted towards downstream direction forming a kink. This matter might be caused by the primary vortices produced by the MR40 that entrained onto the separation line. However the primary vortex pair are not sufficiently strong to break up the separation region. When MR40 are placed in arrays, 4 pairs of secondary vortices is seen originating from the upstream region as shown in Figure 5.19b. This time the separation line is distorted at various locations according to the

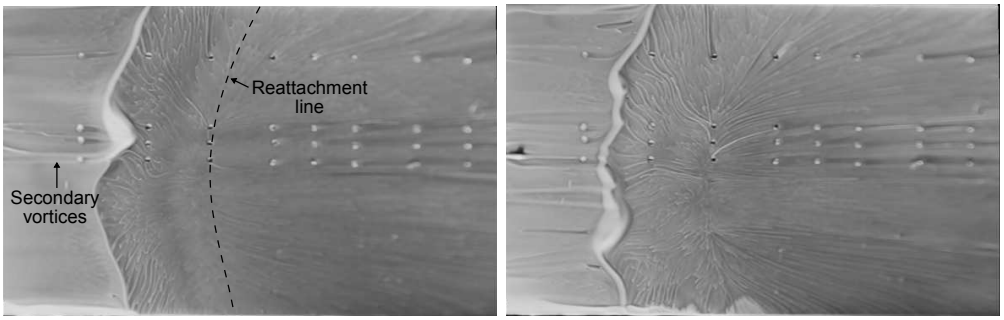


(a) MR40 single (b) MR40 array

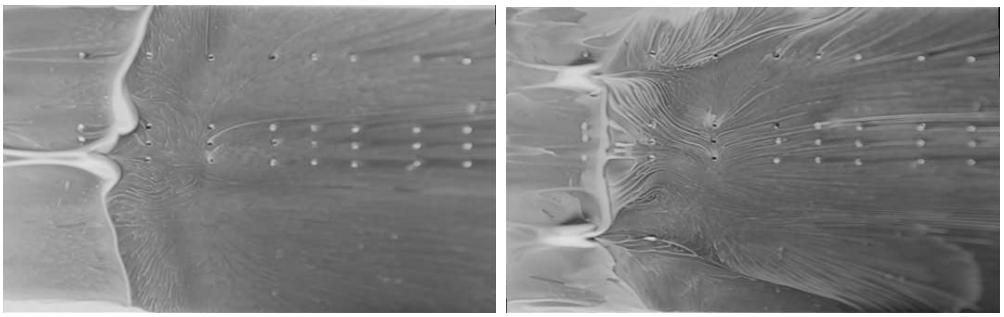

(c) MR80 single (d) MR80 array

Figure 5.19: Oil-flow visualisation images of controlled interaction using various micro-ramp sizes [$X_s = 50.7\delta_0$, $X_{SG} = 11.2\delta_0$].

entrainment of the secondary vortices, hence multiple kinks on the separation line can be observed.

When a larger single micro-ramp is used for control, a thicker oil band is seen entraining into the separation line shown in Figure 5.19c. A more severe distortion of the separation line is seen occurring near the centreline. The position which was affected the worst is not actually at the exact centreline, but a little distance on both sides, where the separation line is seen to moved into the separation region. Again this is caused by the strong primary vortices generated by MR80 upstream. Two kinks on the separation line can be seen adjacent to the centreline. So far all the micro-ramps in single and array configuration tested are not able to bring major distortion to the shape of the separation region. All of them are only able to affect the geometry of the separation line. No changes whatsoever were observed inside the separation region and at the reattachment line. Turning on to the MR80 positioned in array in Figure 5.19d, a drastic change towards the topology of the separation region is observed. A different pattern of the separation line and a more complex separation pattern at downstream can be seen. The

development of such a pattern is shown by the images shown in chronological order in Figure 5.20.

The initial state of the oil before the start of the flow is depicted in Figure 5.20a. After $0.3s$ of the flow, the first feature to appear is the reattachment line. A curved line is seen to form along the span of the plate and the oil on both of its sides are seen to move in opposite direction, just like in the baseline case in Figure 5.16. Then upstream of the reattachment line, two thick bands of oil (labelled I and II in the figure) are seen to move towards each other in Figure 5.20d. At the same time other flow features started to develop. It is not until 2.4s, the other features became more clear and distinctive as shown in Figure 5.20e. The two pairs of large oil tube travelling from upstream are the primary vortices of MR80 while the small vivid oil tubes at the centre from upstream are the horseshoe vortices. The separation line at the centre region is seen to have been straightened by the large primary vortices. Towards the end on both sides (refer to the top and bottom region in the image) starting from the location of the interaction between the primary vortices and the separation line, the separation line is seen to be deflected towards the downstream region.

Interestingly, regions of attached flow are seen in the separation region, originating from the location where the primary vortices impacted on the separation line. Two small channels of attached flow are observed in Figure 5.20e, starting at the location aligned with the micro-ramp centrelines, and deflecting towards the plate side edges as they travelled further downstream. The long separation region stretching in spanwise direction as previously observed in the uncontrolled case in Figure 5.16 is now broken up, leaving the fully affected separated region only in the middle. A similar feature of the separation region is also observed in the oil-flow experiments of Babinsky et al. [3] shown in Figure 5.21. The channels of attached flow are seen to allign with the centre of the micro-ramps. The region which was affected the worst is the area in between the two micro-ramps, where the horseshoe vortices are seen. This is indicated by the owl-face separation pattern in the middle of the image. The oil began to dry in the steady condition in Figure 5.20e and no movements of oil are detected. The features of the attached flow, reattachment and separation line are clear from the dried traces of oil. Finally, at the end of the run in Figure 5.20f, the terminating shock smeared the oil accumulated at the point of interaction between the secondary vortices and the separation line and also within the separation line itself.

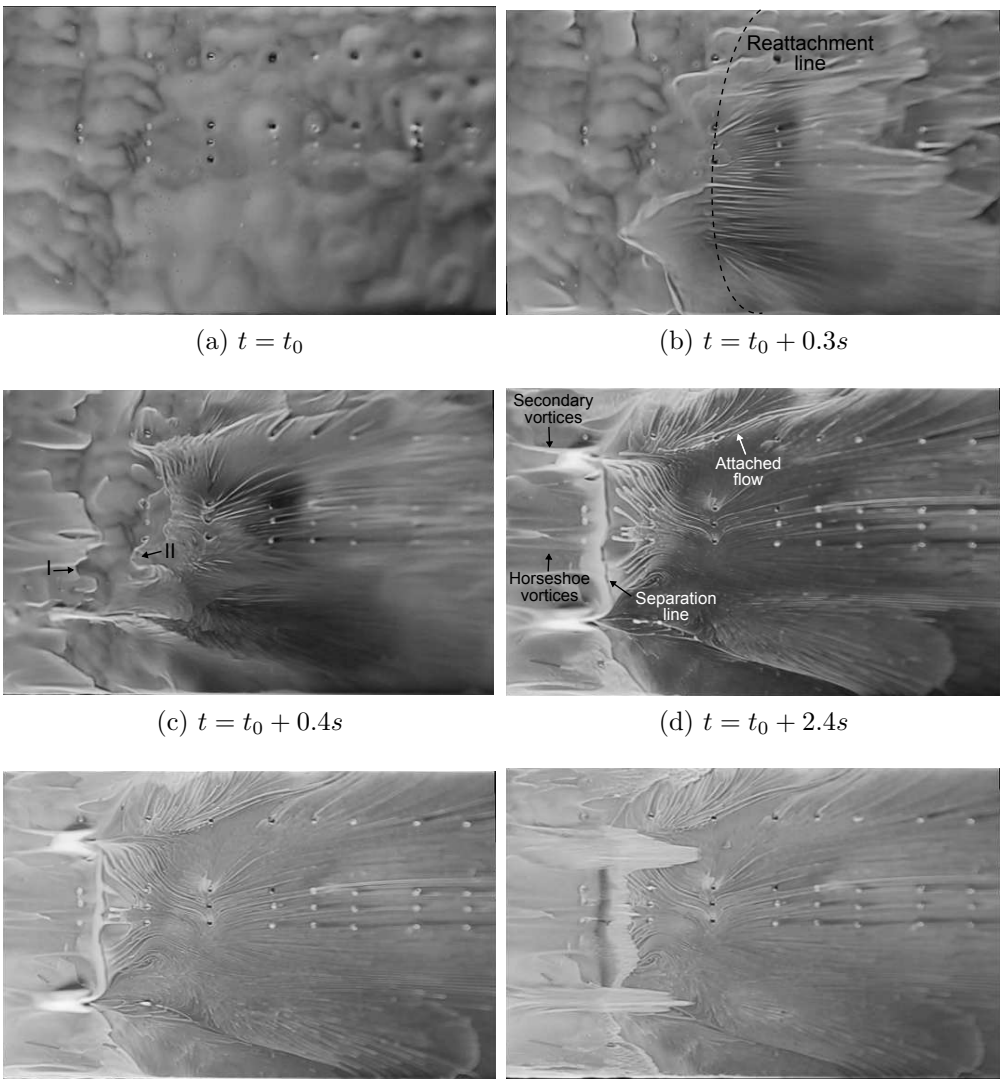


(a) $t = t_0$ (b) $t = t_0 + 0.3s$

(c) $t = t_0 + 0.4s$ (d) $t = t_0 + 2.4s$

(e) $t = t_0 + 5.6s$ (f) $t = t_0 + 8.0s$

Figure 5.20: Oil-flow visualisation images in chronological order of MR80 array controlled interaction [$X_s = 50.7\delta_0$, $X_L = 11.2\delta_0$].

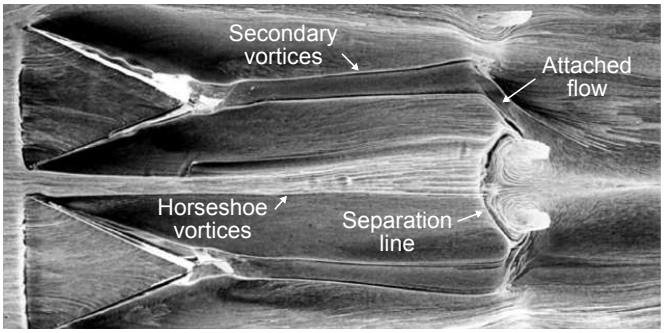


Figure 5.21: Detail characteristics of the controlled interaction region using oil-flow visualisation by Babinsky et al. [3].

## 5.6 Pressure Sensitive Paints

The Pressure Sensitive Paints (PSP) resulted from the uncontrolled interaction (baseline) is shown in Figure 5.22. Note that the black dots represent the location of the pressure tappings utilised for *in-situ* calibration. The high-pressure region observed in between $x = 2$ to $x = 6$ is caused by the oblique shock-impingement. The alternate streaks of high and low pressure inside the high pressure region are caused by the imperfect surface finish during the paint spraying process. As an example between $y = 3$ to $y = 5$, a relatively low pressure area can be seen while the opposite is observed in the area between $y = 2$ to $y = 5$. However, since the pressure readings (shown later) are taken along the centreline ($y = 0$), these imperfections do not affect the results.

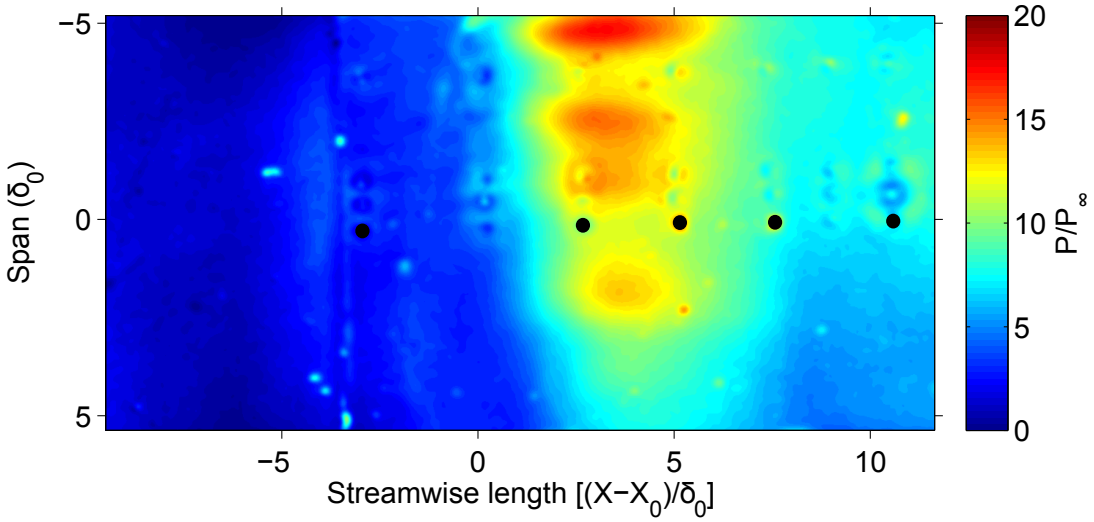


Figure 5.22: PSP: Uncontrolled interaction (baseline).

A clearer view of the pressure distribution along the flat plate under SBLI is given by the pressure contour in Figure 5.23. The first contour seen in the upstream region refers to the upstream pressure rise due to the phenomenon called the upstream interaction influence. The pressure rise is recorded at a distance of approximately $5\delta_0$ upstream of the inviscid shock impingement location ($x = 0$). Then another small pressure step is observed in Figure 5.22 which corresponds to the separation line. Since the step is so small, it is not visible in the contour plot in Figure 5.23. The next contour line represents the start of the reattachment process. A rapid increase of pressure is observed from the contours until reaching the peak pressure. Finally the pressure decreases gradually towards the

downstream region of the flat plate. The contour plot was proved informative in providing the locations where pressure jumps occurred, which separated the different regions along the flat plate.

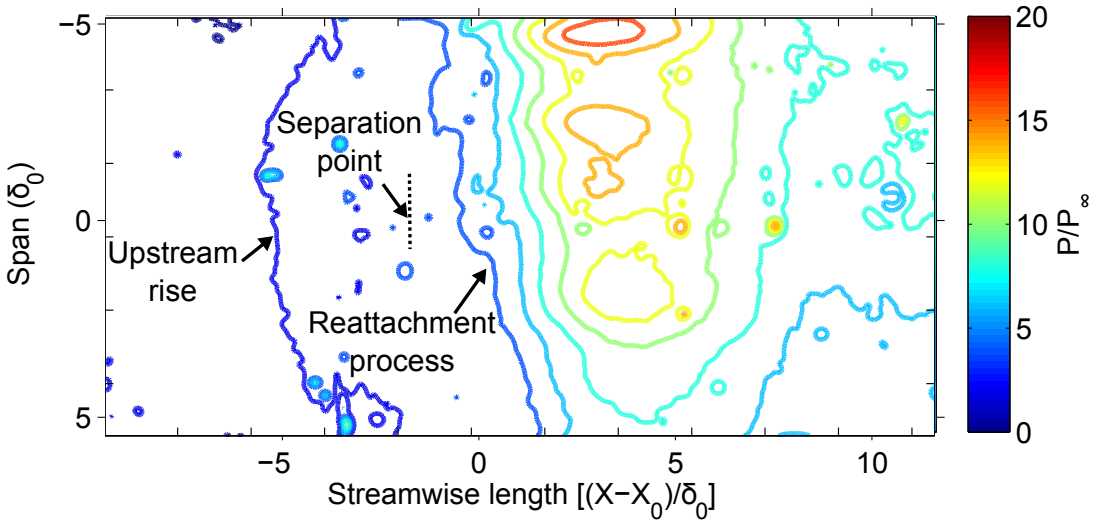


Figure 5.23: PSP: Pressure contour along the flat plate.

The surface pressure distribution along the centreline of the flat plate ($z = 0$) is plotted in Figure 5.24. The upstream pressure, which was recorded approximately the same pressure of the freestream, $P_\infty$, suddenly experienced an increase in pressure at location $x = -6$ which is caused by the upstream interaction influence. This is followed by a number of peaks that correspond to the pressure fluctuation at the region around the gap between the model and flat plate. Next, a small pressure jump is observed near $x = -2$ and followed by a pressure plateau for a distance of $\delta_0$. This type of pressure behaviour (small jump and plateau) is a clear indication of the separation point [82]. After the plateau, another rapid increase in pressure is recorded until it reached a pressure peak at $x = 3$. This region of pressure increase is associated with the reattachment process of the boundary-layer. After the peak, the pressure drops gradually and undergoes relaxation to the inviscid pressure level.

Figure 5.25 illustrates the surface pressure measurements along the centreline, comparing the uncontrolled and micro-ramp controlled cases. Both single and array configurations of MR40 and MR80 were tested and the surface pressure of the flat plate were measured. The initial pressure spikes between $x = -3$ and $x = -4$ are due to the gap existing between the models and the flat plate. The highest pressure spikes in the plot originated from MR40 array and MR80

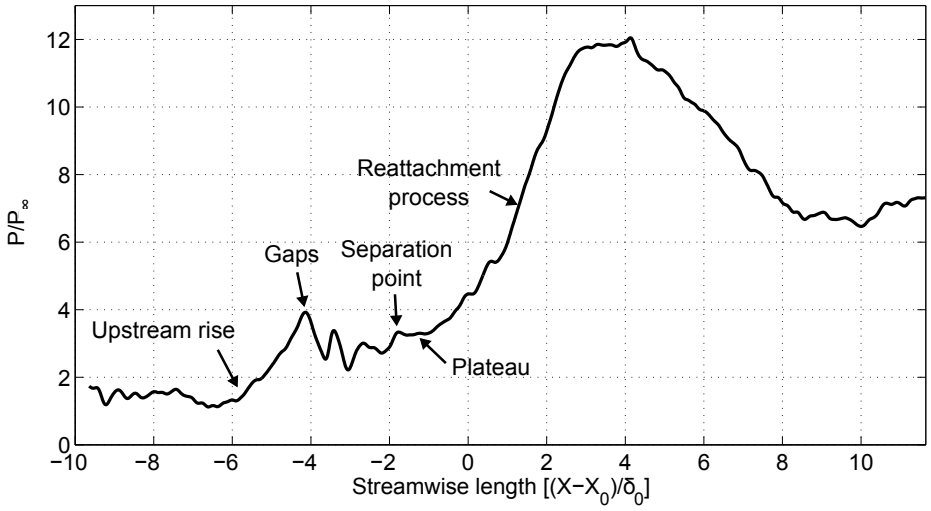


Figure 5.24: Surface pressure measurements along centreline ($z$ = 0mm) for uncontrolled interaction from PSP.

single which is clearly seen in the PSP image of both models in Figure 5.26b and 5.27a. Due to the undesirable high-pressure region caused by the gap, the initial upstream pressure of MR40 array and MR80 single exceeded the uncontrolled case, which in theory should not be the case.

At $x = -1.8$, a small pressure jump followed by a plateau can be observed for most of the models including the baseline case. However the pressure jump was unclear for MR80 and MR40 single configuration. For single configurations, the centreline of the flat plate aligns with the secondary vortices produced by the models. It is thought that the existence of the vortices may affect the pressure distribution hence making the small jump unobservable. The pressure jump occured at almost the same location for all the models including the baseline which is at $x = -1.8$. This leads to the assumption that the separation points for all the models occurred almost at the same location as the baseline case. Therefore in terms of upstream interaction length perspective, the models did not impose a significant improvement.

However, another aspect of SBLI improvement is the gradient of the pressure rise due to reattachment, that follows after the pressure plateau. For all models, the pressure gradients are significantly higher compared to the baseline case. This is a sign of the improvement of SBLI-caused separation [3]. Finally, the peak pressure of all controlled case exceeded the peak pressure of the baseline, which is another sign of improvement. The PSP images of all the SBLI controlled case

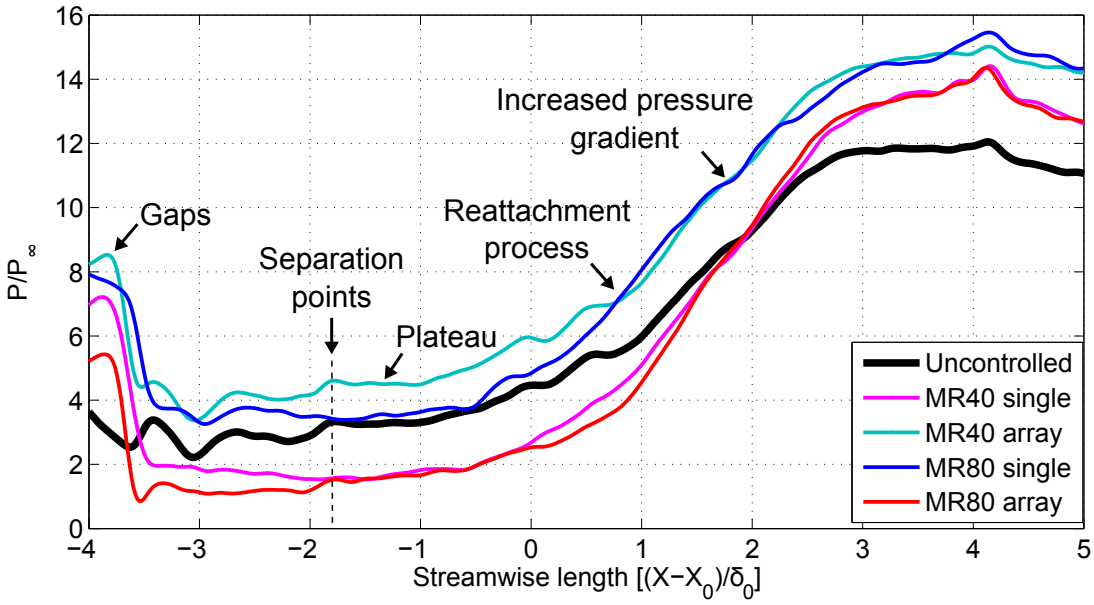


Figure 5.25: Surface pressure measurements along centreline ($z$ = 0mm) for uncontrolled and controlled interaction from PSP.

are shown in Figure 5.26 and 5.27. In agreement to the pressure plot, the location of the separation lines for all the cases are nearly consistent, between $x = -1.5$ and $x = -2$. The high pressure region are seen to be more highlighted in MR40 array and MR80 single PSP images in Figure 5.26b and 5.27a, respectively. This correspond to the two highest pressure peaks obtained in Figure 5.25.

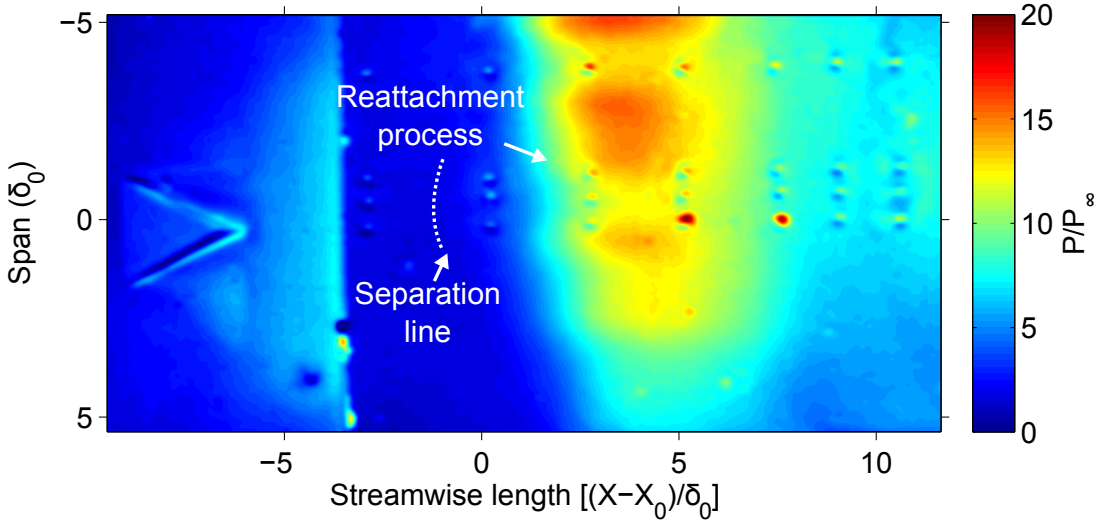


(a) MR40 single

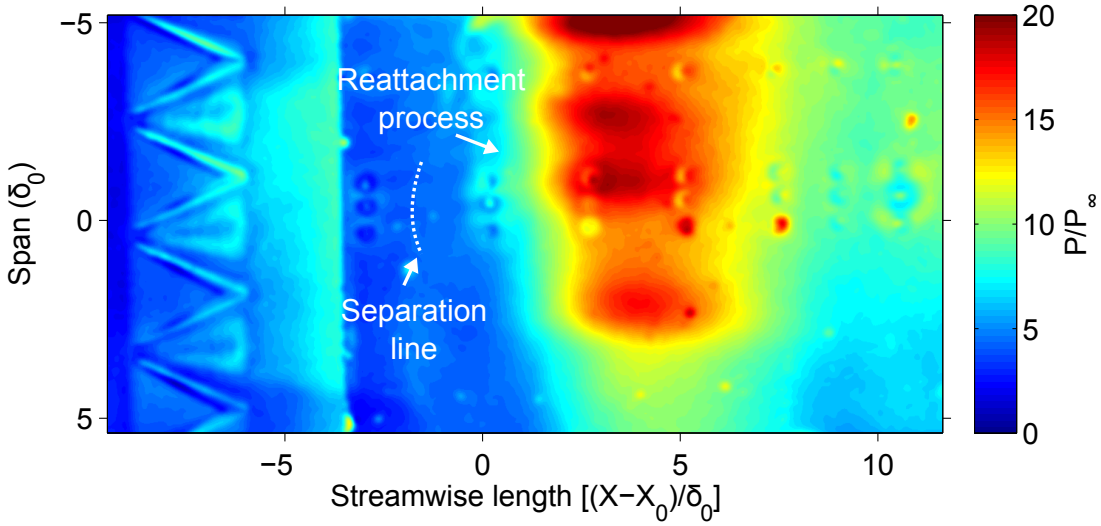


(b) MR40 array

Figure 5.26: PSP image of SBLI controlled by MR40 model in single and array configuration.

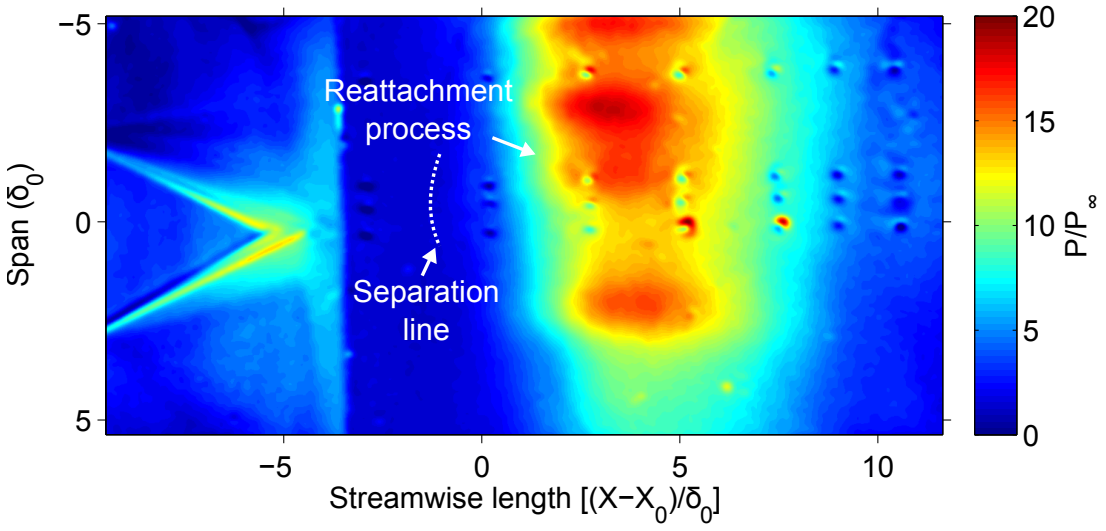


(a) MR80 single

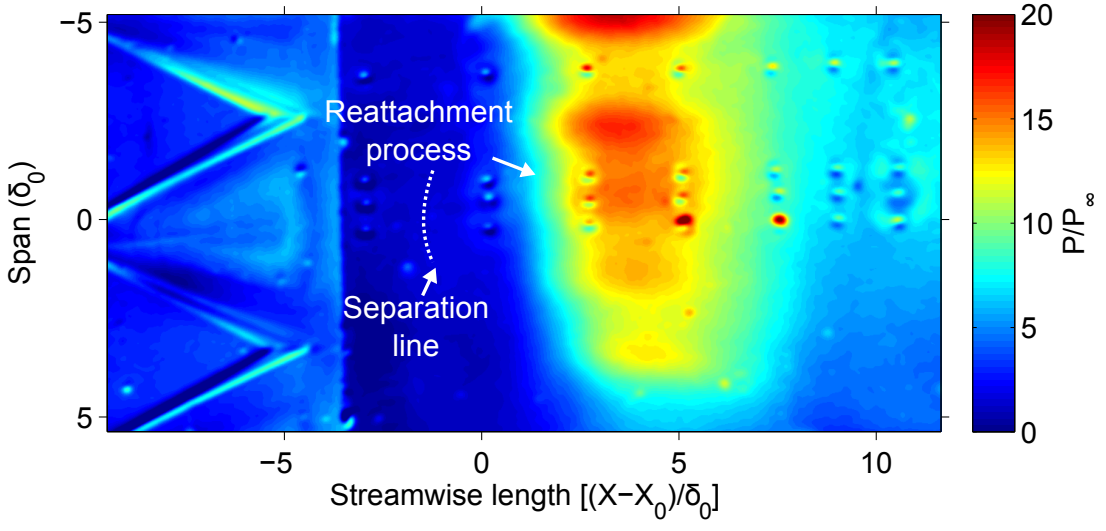


(b) MR80 array

Figure 5.27: PSP image of SBLI controlled by MR80 model in single and array configuration.

## 5.7 Summary

The findings of this chapter can be summarised as the following:

- The local Reynolds number plays an important role in the severity of the upstream influence interaction. For lower $Re_{\delta 0}$ where viscosity is dominant, the upstream length is longer.
- A separated boundary layer induced by SBLI produces a separation shock, expansion fans and a reattachment shock.
- A large separation bubble can be observed in between the separation and reattachment shock.
- The most affected region by SBLI is at the centreline.
- Micro-ramps successfully delayed the upstream pressure rise significantly.
- Micro-ramps increased the pressure gradient of the reattachment process, a sign of the suppression of boundary layer separation.
- Micro-ramps decreased the streamwise length of the separation region.
- Micro-ramps in array configuration are more effective compared to single configuration.
- Separation line, reversed flow region and reattachment line are clearly observed in the separation region.

# Chapter 6

# Micro-Ramp Optimisation

## 6.1 Motivation

One of the most cited literatures in the micro-ramp field apart from the pioneer investigation of micro-ramp in high-speed flow by Babinsky et al. [3], is the optimisation study of the micro-ramp geometries by Anderson et al. [31] conducted at Mach 2.0. The literature was reviewed briefly in Section 2.2.3. The majority of the micro-ramp investigations in high-speed flows after the year 2006 have utilised this design guidelines including the present study at Mach 5. Since the hypersonic flow regime itself is different from supersonic, it would be an interesting investigation to see the output of the micro-ramp optimisation in a hypersonic flow.

Following the investigation by Anderson et al. [31], Hirt & Anderson [34] conducted another optimisation study on the micro-ramp geometries. This time a more comprehensive campaign was performed by comparing results from four different optimisation method. The outcome from the investigation was the optimum value for shape factor (which was chosen as the response variable) occurred for the micro-ramps with large height, $h$ and chord length, $c$ and small spanwise spacing, $s$ between each other. Another optimisation study was performed by Vyas et al. [83] for hybrid flow control combining micro-ramps with micro-jets. A similar conclusion on the height of the micro-ramp was presented, in which the largest ramp height produces a better control of the flow. Interestingly, the authors found that the smallest micro-ramp spacing would produce weaker and smaller vortices which are undesirable in the control of SBLI and this contradicts the finding of Hirt & Anderson. An early conclusion that can be made is

that, larger micro-ramp height and the chord length are much better but for the spanwise spacings, the effect on the performance is still unclear.

Reviewing the flow characteristics of the micro-ramps at Mach 5 as presented in Chapter 4, there are clear evidences that the larger micro-ramp, MR80 produced larger and stronger vortices that are beneficial for the interaction control. When assessing the effectiveness in SBLI control in Chapter 5, from the surface pressure measurements, separation region pattern and relative boundary layer thickness, again MR80 showed significant control of the SBLI region. However no conclusion can yet be made on the effect of spanwise spacings as for both MR40 and MR80 array configurations, the models were machined at the constant $s/h$ ratio of 0.6. Anderson et al. [31] selected $s = 7.5h$ where $s$ is defined as the distance between the apexes of two micro-ramps while $s$ in this study is the distance between the leading-edge tips of two micro-ramps. An interesting point to note is that the separation region was most affected by the presence of the micro-ramp at the region aligned with its centre and remain separated at the region aligned to the gaps between the two of them. From these results it can be anticipated that the closer the micro-ramps, the more control they might bring towards the separation region. Therefore it would be essential to conduct a clear investigation on the optimisation of the micro-ramp geometries specific for the hypersonic flow, to really understand the effect of each geometries on the control capabilities and most importantly, it has not been done before and will serve as a guidance for all future hypersonic micro-ramp investigations.

## 6.2 Relative boundary layer thickness method

The measure of the effectiveness of the micro-ramps is conducted by evaluating the thickness of the separation bubble created by the SBLI in uncontrolled case and compare it with the controlled conditions. Since it would be difficult to determine the actual thickness of the separation bubble and it would also need a more sophisticated tool such as PIV, a relatively simpler method is conducted. This is done by determining the proportionate value of the separation bubble thickness which is the boundary layer thickness at the impingement location. The relative boundary layer thickness, $\delta_{rel}$ is the ratio of the boundary layer thickness with micro-ramp control, $\delta_{mr}$ with the boundary layer thickness at reference condition (uncontrolled interaction), $\delta_{ref}$ is calculated. The formula is

given in Eqn. 6.1.

$$\delta_{rel} = \frac{\delta_{mr}}{\delta_{ref}} \tag{6.1}$$

The boundary layer thicknesses were obtained from the schlieren photographs. Similar method was used by Schulte et al. [84] to evaluate the effectiveness of bleed in reducing the separation caused by SBLI. The investigation was done at Mach 6 with an oblique shock impinging on a hypersonic boundary layer developing on a flat plate, similar to the present case. Prince et al. [6] also used this method to estimate $\delta$ at the hinge line for the case of a hypersonic SBLI on a compression ramp at Mach 8.2. Knowing the fact that $\delta$ cannot be measured directly from the schlieren images due to the density gradient asymptotes to zero at the edge of the boundary layer, this method serves as a relative estimation towards the effectiveness of the micro-ramp control.

$$\left(\frac{\Delta\delta_{rel}}{\delta_{rel}}\right)^2 = \left(\frac{\Delta\delta_{mr}}{\delta_{mr}}\right)^2 + \left(\frac{\Delta\delta_{ref}}{\delta_{ref}}\right)^2 \tag{6.2}$$

$$\Delta\delta_{rel} = \delta_{rel}\sqrt{\left(\frac{\Delta\delta_{mr}}{\delta_{mr}}\right)^2 + \left(\frac{\Delta\delta_{ref}}{\delta_{ref}}\right)^2} \tag{6.3}$$

The error analysis for this approach is given by Eqn. 6.2 from Taylor [85]. $\Delta\delta_{mr}$ and $\Delta\delta_{ref}$ which is the error in determining the boundary layer thickness is sourced from the uncertainty in locating the upper edge of the boundary layer in the image processing software for both the controlled and reference cases, respectively. The edge of the boundary layer can be estimated to be located within 2 pixels at most. Therefore, the maximum value of both $\Delta\delta_{mr}$ and $\Delta\delta_{ref}$ predicted is 2 pixels equivalent to 0.1mm after being calibrated. Hence the value of $\Delta\delta_{rel}$ as in Equation. 6.3 is calculated as 0.009mm and the mean percentage of $\Delta\delta_{rel}/\delta_{rel}$ is 1% which can be considered as to be at the very minimal.

The relative thickness of the separation bubble is estimated from the thickness of the boundary layer at exactly the point of interaction (POI) between the incident shock and the hypersonic boundary layer. This is because the thickness of the boundary layer is seen to be at the maximum at the POI based on the

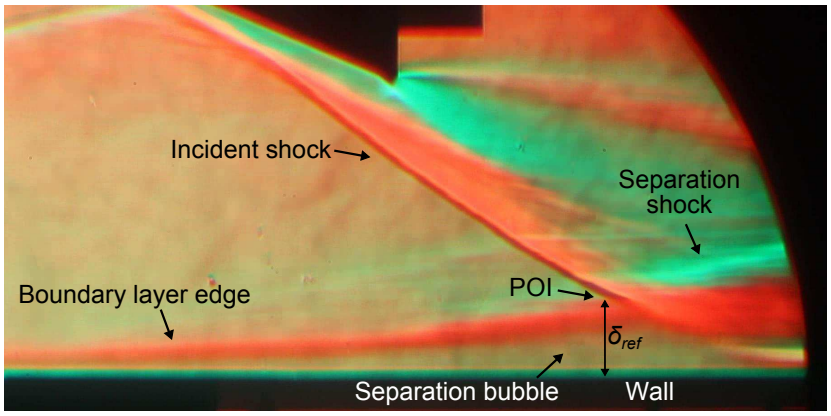


(a) Raw image

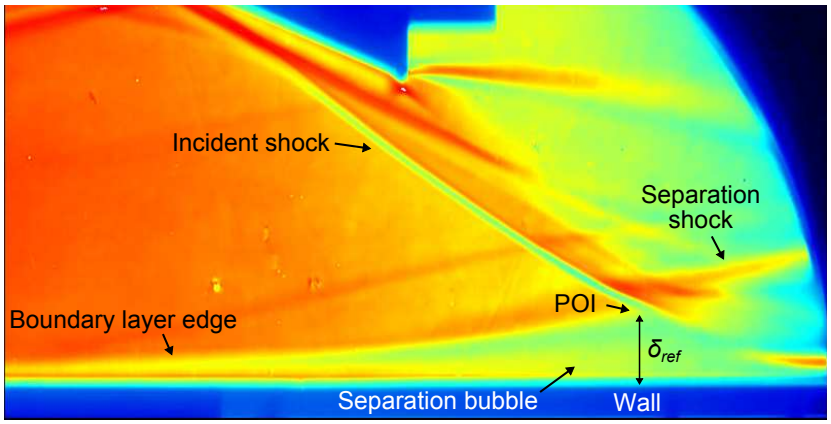


(b) Sum of 200 images

Figure 6.1: Colour schlieren image of uncontrolled interaction (baseline) used in estimating the separation bubble thickness [$X_s = 55.2\delta$].

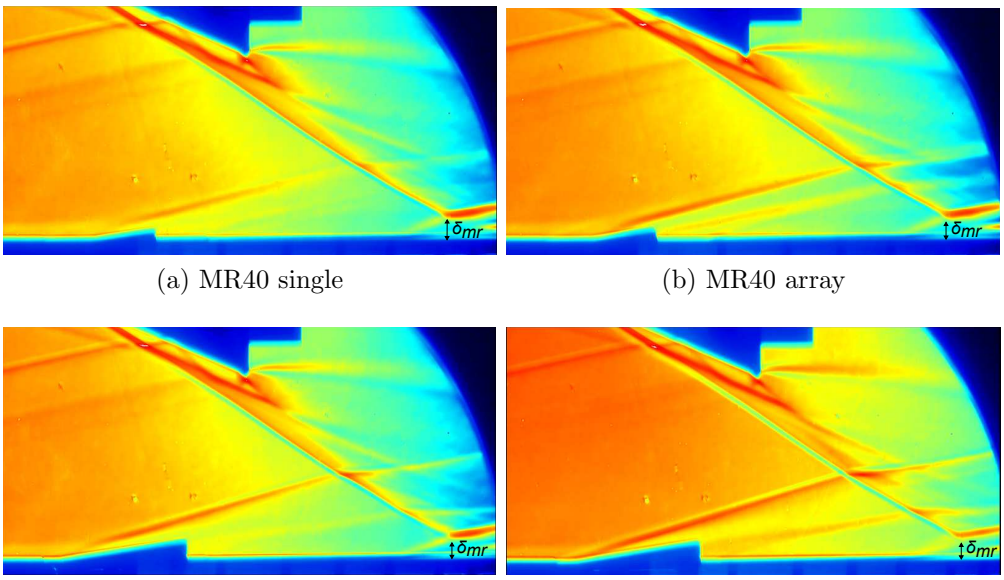


(a) MR40 single (b) MR40 array

(c) MR80 single (d) MR80 array

Figure 6.2: Summed images of colour schlieren for various ramp sizes interaction control $[X_s = 55.2\delta,\ X_L = 15.7\delta]$.

previous schlieren images and therefore is measured from the POI to the wall as highlighted in Figure 6.1a. Three types of schlieren were used throughout the entire study; conventional normal black and white schlieren (Figure 4.2), high-speed schlieren (Figure 5.8) and colour schlieren (Figure 5.5). When comparing all three methods, each of them has their own advantages and disadvantages and they are found to be useful in revealing certain information at different conditions. However, the colour schlieren was found to be the best method based on its capability in capturing the edge of the boundary layer in good contrast with the background which is proven based on the image seen in Figure 5.5 and Figure 6.1a. The images were then imported into Davis and 200 images during steady run were summed. This enhanced the colour of the images so that a better contrast was obtained as shown in Figure 6.1b. The location of the POI was clear enough to be identified and later on used to calculate $\delta_{ref}$.

The effect of summing is that it alters the colours of the original image. As an example the red boundary layer edge seen in the original image in Figure 6.1a was converted into a light blue colour. On the other hand, the light green line of the separation shock changed into the intense thick red line in Figure 6.1b. Therefore, this helped to make the process of estimating $\delta_{ref}$ and $\delta_{mr}$ easier. The POI which was identified as the point where the incident shock meets the boundary layer

edge, now can also be recognised as the point where the incident shock meets the separation shock since the separation shock became more distinct in the summed images compared to the raw images. However, not all of the colourmap in Davis were able to highlight the distinct features. Therefore a careful selection of the type of colourmap is needed.

Figure 6.2 shows the summed images for all the models tested in the previous chapter using other experimental techniques. A plain eye comparison between the uncontrolled case in Figure 6.1 with the controlled case regardless of the size of the models, shows that a massive reduction of the height of the separation bubble can be seen. To further quantify the reduction, the pixels between the POI and the wall can be counted and calibrated with the thickness of the flat plate. Therefore, this shows that this technique is able to perform both qualitative and quantitative investigations on the SBLI reduction.

## 6.3 Problem definition

As mentioned earlier, the purpose of this investigation is to outline a systematic methodology to find the best configuration of the micro-ramps for the best SBLI control. In Chapter 5, the results showed that the array configurations were far better than the single. Therefore, only the array configuration will be chosen for this optimisation task. There are three main variables to be considered in designing the micro-ramps; height ($h$), chord length ($c$) and spanwise spacing ($s$). These variables are illustrated in Figure 6.3.

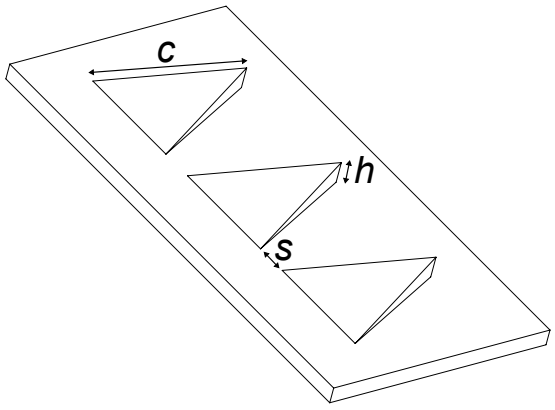


Figure 6.3: Geometries of the micro-ramps used in optimisation studies.

These three geometries are taken as the model parameters. To measure the

effectiveness of the SBLI control, the method of separation bubble thickness estimation is used. The detail explanation on the method can be found in Section 6.2. Finding the best possible configuration by changing the three parameters to get the smallest value of $\delta_{ref}$ which is the ratio of $\delta_{mr}/\delta_{ref}$ is an expensive and exhaustive job. However to make this possible, the problem can be formulated using the following optimisation task:

$$\begin{aligned} &\textit{Minimise } \delta_{rel} \textit{ subject to}: \\ &15 \leq c \leq 25\text{mm} \\ &4 \leq h \leq 8\text{mm} \\ &2 \leq s \leq 6\text{mm} \end{aligned} \tag{6.4}$$

$c$ and $s$ depend on the width of the flat plate while $h$ depends on $\delta_0$. Note that the range of $h$ selected in Equation. 6.4 is equivalent to $0.7 \leq h/\delta_0 \leq 1.4$. Even though the agreed definition on micro vortex generators is having $h$ smaller than $\delta_0$, based on the results in previous chapters, it was observed that larger $h$ value was more effective and more successful in the hypersonic flow. Therefore, in this optimisation investigation, the top range of $h$ is tested. Without neglecting the effect of parasitic drag due to having the larger model size, the focus in this investigation remains in the performance of SBLI control. The design variables derived from Equation. 6.4 are listed in Table 6.1. It should be noted that such intervals were selected so that all low, medium and top range values are included and this will also make future comparisons possible.

| Name | $c$ (mm) | $h$ (mm) | $s$ (mm) |
|---|---|---|---|
| Level | $\{15, 20, 25\}$ | $\{4, 6, 8\}$ | $\{2, 4, 6\}$ |

Table 6.1: Design variable ranges.

## 6.4 Experimental setup

From the information in Table 6.1, 10 micro-ramp models were manufactured based on the resource limitations (financial) and configuration constraints (wind tunnel setup) mentioned earlier. All of the models were named according to the

following order; the first digit represents $h$, the second two digits are $c$ and the final digit is $s$. For an example, referring to the model 8152, it tells that the height of the micro-ramp is 8mm, the chord length is 15mm while 2mm is the spanwise spacing between each other. The full dimensions of the 10 models manufactured are listed in Table 6.2 and the geometries are shown in Figure 6.4. Note the three variables $w$, $L$ and $d$ are calculated from the three independent variables $c$, $h$ and $s$. The geometric angle of incidence, $Ap$ is set constant at 24° for all the models while the distance from the centre of the micro-ramp to the shock impingement location, $X_L$ is also kept constant at $15.7\delta_0$.

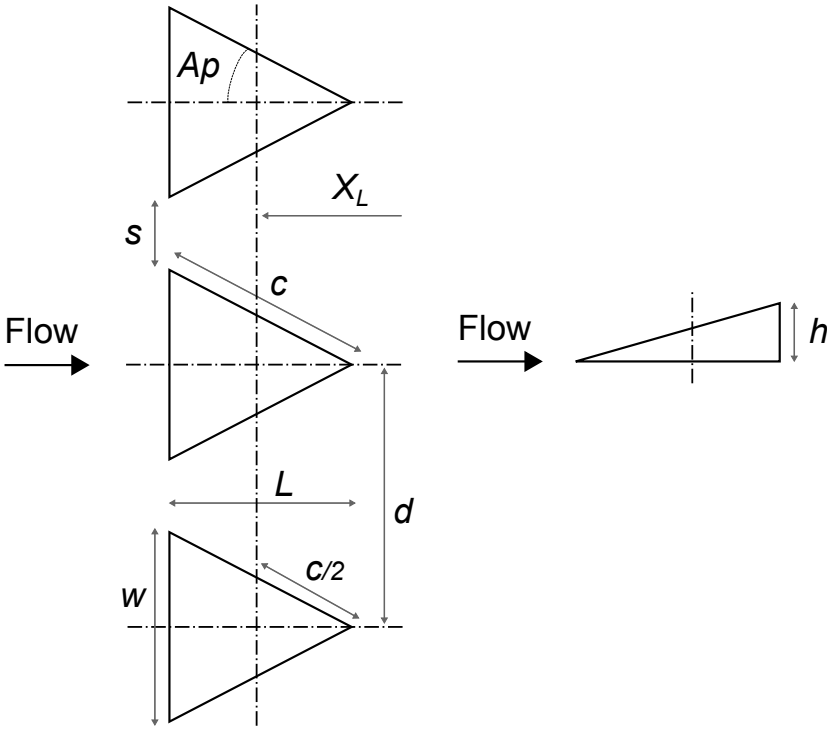


Figure 6.4: Top and side view of micro-ramp geometry used in optimisation investigation.

The relative boundary layer thickness, $\delta_{rel}$ is calculated as the ratio of $\delta_{mr}/\delta_{ref}$. Colour schlieren setup was used as the method to visualise and measure the boundary layer thicknesses. 200 images of 0.02s intervals acquired during the steady run time were imported into Davis and summed. The location of the POI was then identified and later on was used to calculate $\delta$ for each case. The previous shock-generator, which was only 60mm wide, was not suitable for the 90mm wide optimisation flat plate. Hence a new shock-generator was manufactured specifically for this optimisation study. The diagram of the new shock-generator

| No. | Model | $h$ | $c$ | $s$ | $w$ | $L$ | $d$ |
|---|---|---|---|---|---|---|---|
| 1 | 8152 | 8.0 | 15.0 | 2.0 | 12.2 | 13.7 | 14.2 |
| 2 | 4202 | 4.0 | 20.0 | 2.0 | 16.32 | 18.3 | 18.3 |
| 3 | 4256 | 4.0 | 25.0 | 6.0 | 20.3 | 22.8 | 26.3 |
| 4 | 8156 | 8.0 | 15.0 | 6.0 | 12.2 | 13.7 | 18.2 |
| 5 | 8256 | 8.0 | 25.0 | 6.0 | 20.3 | 22.8 | 26.3 |
| 6 | 4154 | 5.0 | 15.0 | 4.0 | 12.2 | 13.7 | 16.2 |
| 7 | 6206 | 6.0 | 20.0 | 6.0 | 16.3 | 18.3 | 22.3 |
| 8 | 6254 | 6.0 | 25.0 | 4.0 | 20.3 | 22.8 | 24.3 |
| 9 | 8204 | 8.0 | 20.0 | 4.0 | 16.3 | 18.3 | 20.3 |
| 10 | 8252 | 8.0 | 25.0 | 2.0 | 20.3 | 22.8 | 22.3 |

Table 6.2: Complete geometries of 10 models manufactured for optimisation. All units are in mm.

is the same as in Figure 3.23 except for the width which was changed from 60mm to 90mm.

## 6.5 Results

The colour schlieren results for all 10 models are shown in Figure 6.5. $\delta_{ref}$ for the uncontrolled case which is used to calculate $\delta_{rel}$ was measured at 17.58mm. From the images, the location of the POI were carefully identified in every images and the distances from POI to the model were measured as $\delta_{mr}$. The values are listed in Table 6.3 together with the calculated value of $\delta_{rel}$.

| No. | Model | $\delta_{mr}$ (mm) | $\delta_{rel}$ |
|---|---|---|---|
| 1 | 8152 | 12.66 | 0.72 |
| 2 | 4202 | 14.77 | 0.84 |
| 3 | 4256 | 17.22 | 0.98 |
| 4 | 8156 | 12.48 | 0.71 |
| 5 | 8256 | 13.36 | 0.76 |
| 6 | 4154 | 14.94 | 0.85 |
| 7 | 6206 | 13.71 | 0.78 |
| 8 | 6254 | 15.12 | 0.86 |
| 9 | 8204 | 12.83 | 0.73 |
| 10 | 8252 | 12.83 | 0.73 |

Table 6.3: Relative boundary layer thickness, $\delta_{rel}$ (response) from the sample data.

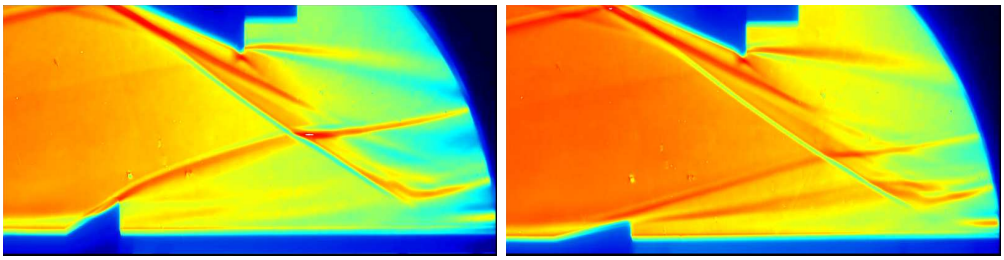

(a) 8152 (b) 4202

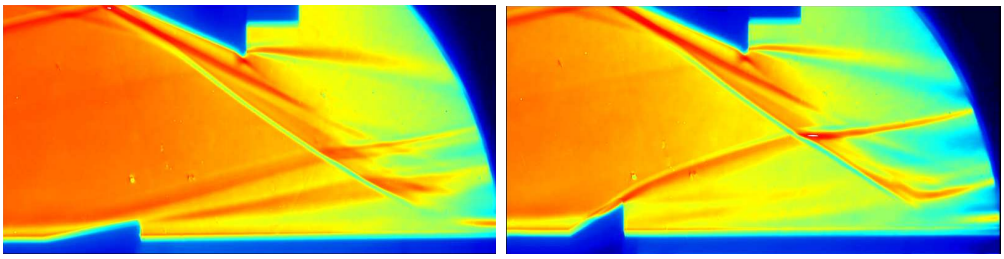

(c) 4256 (d) 8156

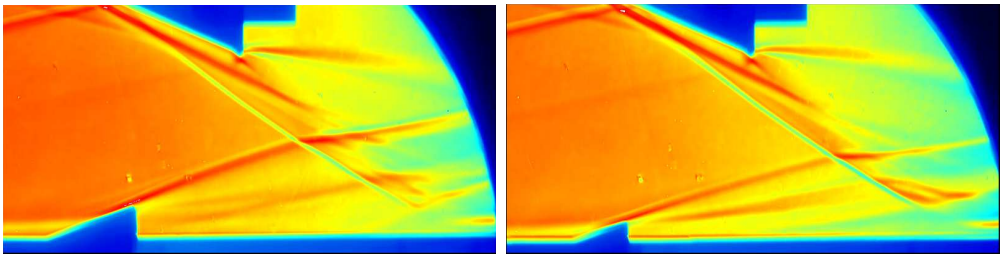

(e) 8256 (f) 4154

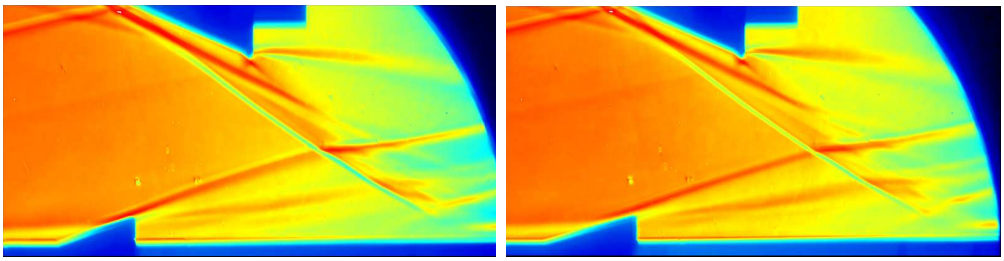

(g) 6206 (h) 6254

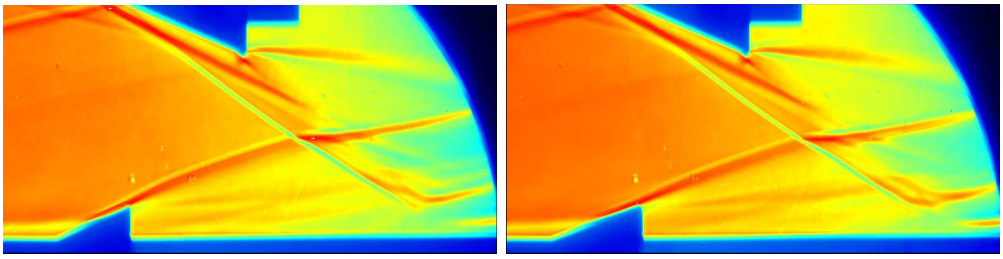

(i) 8204 (j) 8252

Figure 6.5: Experimental results for all 10 models [$X_s = 55.2\delta$, $X_L = 15.7\delta$].

From the results shown in Table 6.3, the best measurements was demonstrated by model 8156 and the worst is shown by model 4256. The amount of improvement brought by 8156 is almost 30% with respect to the uncontrolled case while the presence of model 4256 almost did not bring any significant change, with the result of improving by only 2%.

It is important to note that the schlieren technique integrates the density of the whole spanwise volume of the flow and the density change that represents the flow features (which in this case is the size of the separation bubble) can only be detected in two-dimension. Evident from the surface-flow visualisation, with the presence of the micro-ramp, the separation region was broken into individual cells comprising separated and also attached flow. Therefore, looking from the schlieren perspective, the measured $\delta_{rel}$ truly represents the thickness of the boundary layer at the separated region.

From the results tabulated in Table 6.3, it can be observed that the highest model ($h$ = 8mm) performed relatively better compared to the other model heights of 6mm and 8mm. All of them; 8152, 8156, 8256, 8204 and 8252 yielded at least 25% of improvement from the uncontrolled case with 8156 showing the most significant improvement of almost 30%. Conversely, the models with the lowest height of 4mm did not perform well. The largest improvement recorded was only 16% by 4202. This outcome is consistent with the findings from Chapter 5 where the larger the height of micro-ramp, the more improvement it brings in controlling SBLI. This early conclusion is true only for the case of Mach 5 since the results from the lower Mach number studies found in the literatures showed that the best height is approximately 40% of the boundary layer thickness.

Unlike the height factor, the chord length, $c$ and the spanwise spacings, $s$ do not exhibit a traceable trend from the tabulated data. As an example for $s$, by looking at the results of model 8152 and 8156, the values of 2mm and 6mm which is the minimum and maximum $s$, respectively both produced almost 30% improvement. Similarly, $c$ exhibits the same behaviour. By referring to the results of 8152 and 8252 where the $h$ and $s$ are constant, both values of $c$ show significant improvement of almost 30%. Again, the trend is unpredictable. Therefore, this highlights the importance of the numerical modelling in order to obtain the optimal values of all of the variables.

The optimal combination of $h$, $c$ and $s$ were determined and are listed in Table 6.4. The optimal configuration approximated the value of $\delta_{rel}$ to be 0.67,

| $h$ | $c$ | $s$ | Optimum response, $\delta_{rel}$ |
|---|---|---|---|
| 7.45 | 19.58 | 2.00 | 0.67 |

Table 6.4: Final optimal configuration setting.

with the improvement of 33% from the uncontrolled case which can be considered significant. From the final result, the optimal value of $h$ is 7.45mm, which is 1.3 times the height of the boundary layer. In the previous optimisation investigation by Anderson et al. [31] in supersonic flow, the optimal height found was 40% from $\delta$ but for hypersonic flow, this was found to be a different case. In hypersonic flow, the incident shock impinging on the boundary layer is relatively stronger hence causing a more severe flow separation. In order to overcome the separation, stronger streamwise vortices are in need. This is only possible if a larger micro-ramp is in place and this explains why a micro-ramp having the height of $1.3\delta$ is necessary. However, having the height larger than $\delta$ means that the device is no longer sub-boundary layer and this would introduce significant drag penalties. Hence, for future application, the effect of parasitic drag of the device needs to be taken into account.

The optimal value for $c$ is 19.58mm, which is 2.6 times the height of the micro-ramp. This is to ensure that the angle of the ramp inclination is not too steep nor too shallow for the incoming flow so that the vortices could be generated efficiently. Focusing on the optimal value of $s$, the result shows that the smallest spacing produces the best performance. From the oil-flow results discussed in Chapter 5, the attached flow region existed downstream the apex of each micro-ramp. This means that the closer the micro-ramps with each other, the more micro-ramps could be placed hence more attached flow region can be created. It was also observed from the oil-flow results that the region in between the two micro-ramps suffered the most from the flow separation. Therefore by having the micro-ramps as close together, this problem could be minimised.

The ratios of the optimal variables are listed in Table 6.5. These ratios will serve as a guideline for designing the micro-ramps for investigations conducted in hypersonic flow regime. Comparing the calculated ratios in this case with the supersonic investigation by Anderson et al. [31], a significant difference between the values could be observed. Therefore, this proves that the optimal dimensions of the micro-ramps in hypersonic flow are unique and different from the supersonic

| Ratio | Value |
|---|---|
| $h/\delta_0$ | 1.33 |
| $s/h$ | 0.27 |
| $c/h$ | 2.63 |

Table 6.5: Final optimal ratio for micro-ramp design at Mach 5.

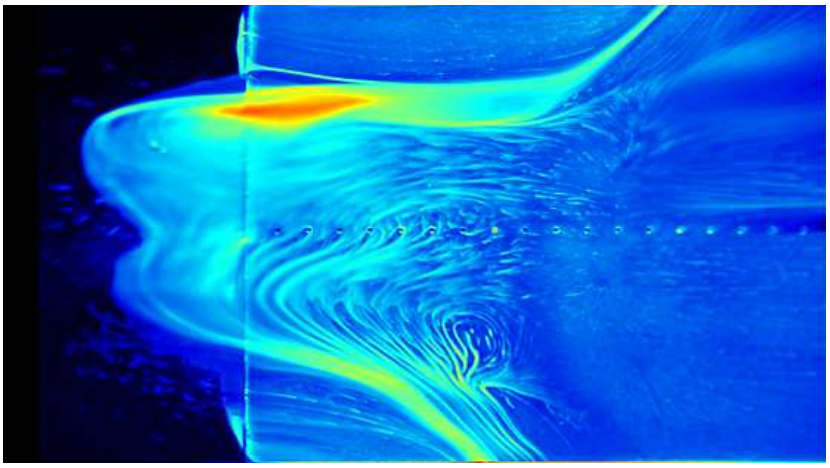

Figure 6.6: Oil-flow visualisation results for uncontrolled interaction [$X_s = 55.2\delta$, $X_L = 15.7\delta$].

case. This also shows that this optimisation study is essential for future numerical and experimental investigation in hypersonics.

## 6.6 Supporting Experimental Results

Additional experimental techniques were employed in order to support the findings of this optimisation studies. Oil-flow visualisation were conducted to visualise the improvements brought by the models by observing the upstream extent of the separation region and also the region of attached flow due to the presence of the micro-ramp. Next, PSP is used to observe the flow features appearing around the micro-ramp.

The oil-flow visualisation results for the baseline case in this optimisation study are shown in Figure 6.6. It can be seen clearly that the separation region extended to a far distance upstream from the impingement point. The distance between the separation and the reattachment line is calculated to be $18.2\delta_0$. This actually exceeds the upstream location where the micro-ramps will be placed

since $X_L$ is only $15.7\delta$. The flow separation is severe and this can be observed from the reversed flow region occurring symmetrically in the interaction region. The thick oil band at the separation line is due to the heavy oil accumulation caused by the severe flow separation.

The oil-flow results for all 10 optimisation models are presented in Figure 6.7. All the models with $h = 8$ managed to reduce the upstream extend of the separation region. However for the other heights, $h = 4$ and 6mm, the separation region can be seen still extending even up to the location of the micro-ramps. Regions of attach flow can be observed from a number of the models such as 4256, 8256, 4154, 6206 and 8252. These are evident from the disrupted separation lines which are represented by the thick oil band stretching in spanwise direction. The locations where the separation line discontinue, are identified as the attached flow regions. From all of the images, the secondary vortices, represented by the thin line propagating in the downstream region are clearly seen regardless of the size of the micro-ramps.

From Table 6.4, the best model is 8156. Referring to the oil flow result of 8156 (Figure 6.7d), a symmetrical separation pattern is observed. Apart from that, the size of the separation region, which is measured as the distance from the reattachment line to the separation line is also the smallest relative to the other 9 models. However no attached flow region can be observed from the result, compared to the others. Therefore it can be deduced that if the separation region is broken into multiple cells of separated and attached flow, the average thickness of the separation bubble will increase. On the contrary, for the worst model, 4256, the upstream extend of the separation region is severe. Oil accumulation can even be spotted at the sides of the micro-ramps. This is clearly understood since one of the signs of severe SBLI is the upstream interaction length, as discussed previously in Chapter 5.

Figure 6.8 and 6.9 display the result of PSP for all the models. Before discussing the findings, it is important to note that the high pressure region (marked $S$) detected in between the models are caused by the shadow. Apart from that, some areas are also affected by the uneven paint surface causing incorrect readings of the surface pressure. These regions are marked with $P$ for clarity. For the majority of the models, the low pressure region at the immediate downstream position of the micro-ramp apex can be observed, labelled as $LP$. The existence of these regions were explained previously in Section 4.6. The low shear regions

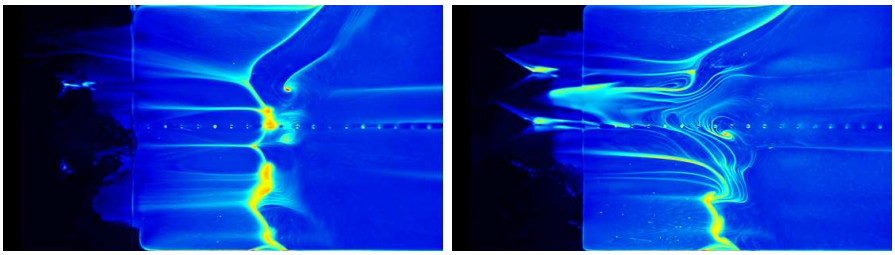

(a) 8152 (b) 4202

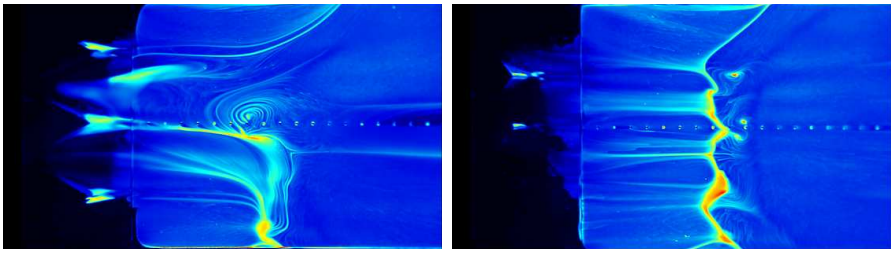

(c) 4256 (d) 8156

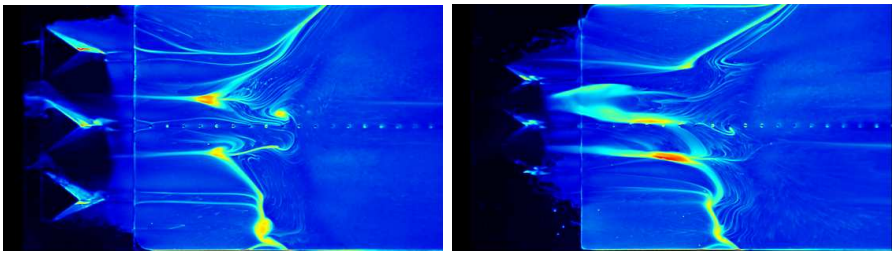

(e) 8256 (f) 4154

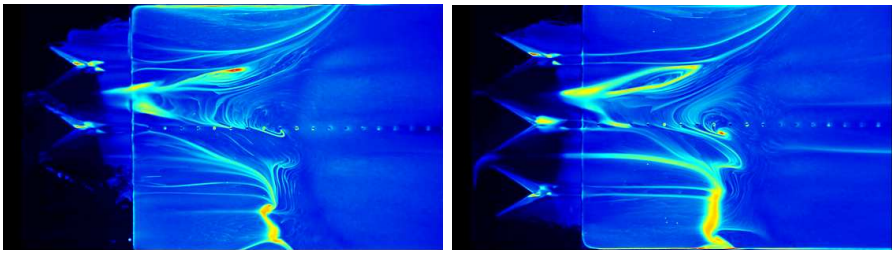

(g) 6206 (h) 6254

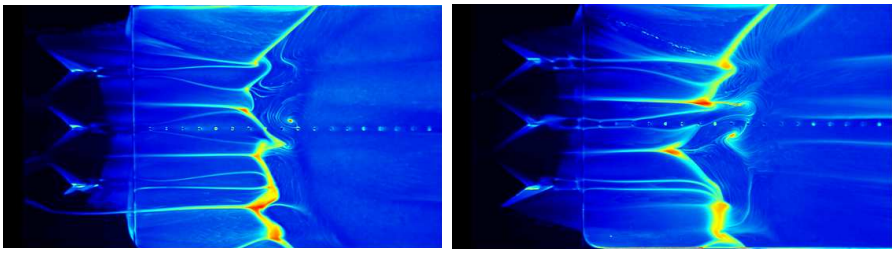

(i) 8204 (j) 8252

Figure 6.7: Oil-flow visualisation results for all 10 models [$X_s = 55.2\delta$, $X_L = 15.7\delta$].

at the sides of the micro-ramps are also observed and this is represented by the low pressure region labelled *LS*.

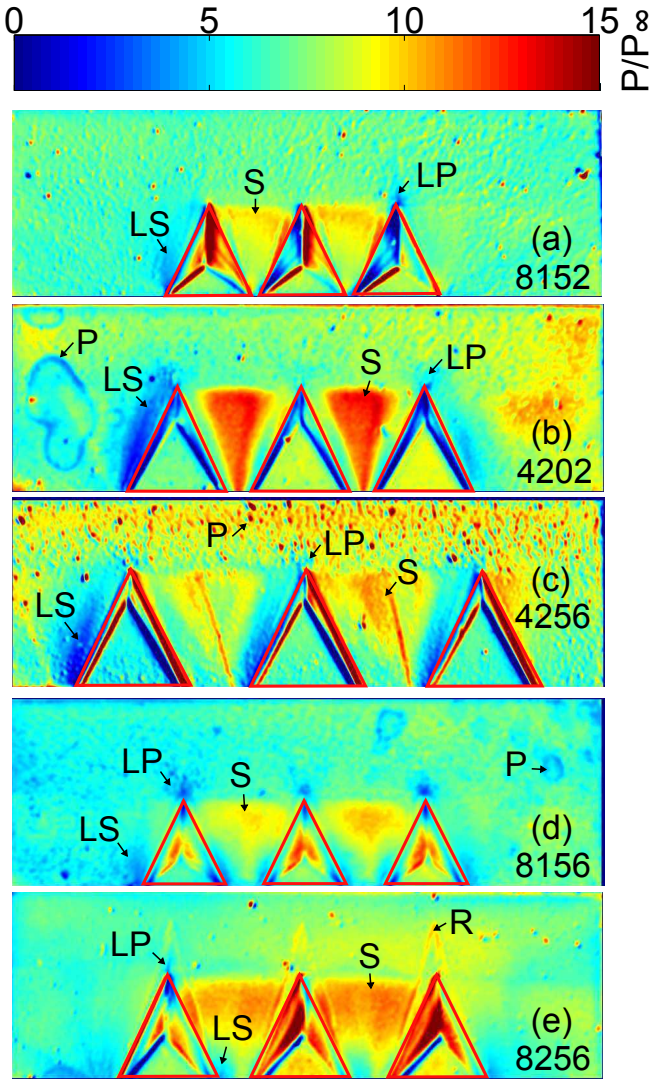


Figure 6.8: Pressure sensitive paints results of first 5 optimisation models. Flow is from bottom to top.

For most of the models that have the height as 4mm, the upstream pressure rise can be observed at the area downstream the micro-ramp apex as visible in Figure 6.8b and 6.8c. The only model that was not significantly affected by the upstream pressure rise is 8156, which was also the best model picked previously and is shown in Figure 6.8d. Constant low pressure region in the whole area downstream of the model can be observed. On the other hand, for the worst model 4256 shown in Figure 6.8c, high pressure regions can be seen downstream

the model. These high pressure regions are not only caused by the uneven surface of the paint, but they are also believed to originate from the upstream high pressure influence of SBLI.

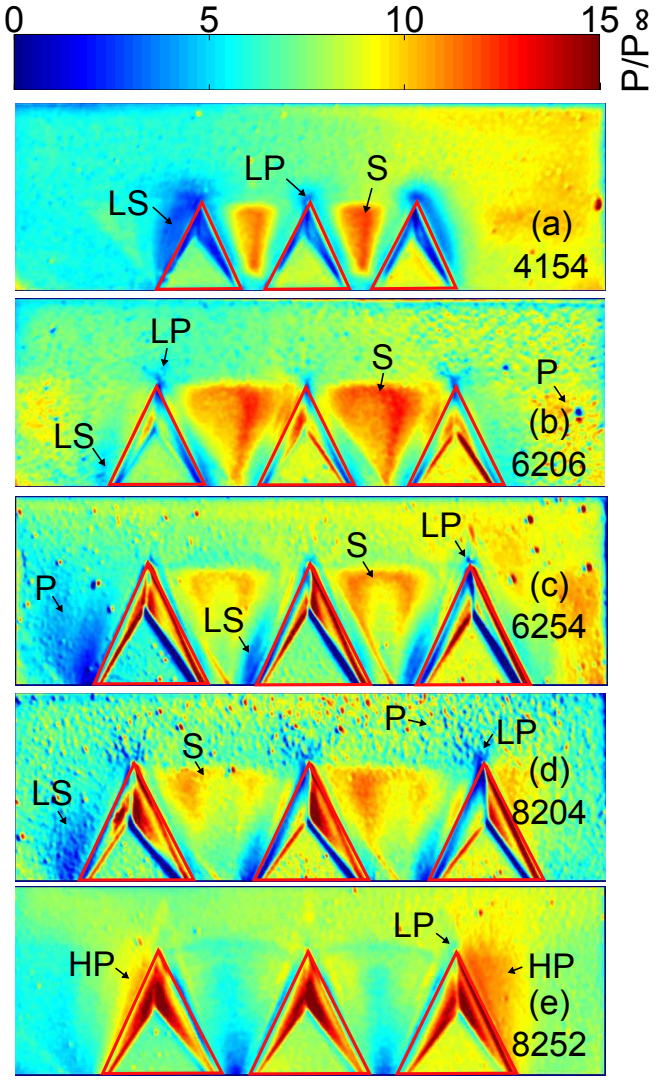


Figure 6.9: Pressure sensitive paints results of final 5 optimisation models. Flow is from bottom to top.

## 6.7 Summary

The findings of this chapter can be summarised as the following:

- 10 models with various geometries were tested as a part of the optimisation investigation of micro-ramps at Mach 5.
- The best model was 8156 that yielded 30% improvement of the SBLI condition.
- The worst model was 4256, which only brought a negligible 2% improvement.
- The optimal configuration setting are as the following; $h = 7.45$mm, $c = 19.58$mm and $s = 2.00$mm which results in $\delta_{rel} = 0.67$.
- The final optimal ratios for micro-ramp design at Mach 5 are as the following; $h/\delta_0 = 1.33$, $s/h = 0.27$ and $c/h = 2.63$.
- The optimal dimensions of the micro-ramps in hypersonic flow obtained from this investigation are unique and different from the supersonic case.
- Micro-ramps with larger height, median chord length and smallest spanwise spacings turned out to be the best combination for hypersonic SBLI control.

# Chapter 7

# Conclusion & Future Recommendations

## 7.1 Conclusion

The findings of the overall investigation can be summarised into the following three sections:

### 7.1.1 Micro-Ramp Flow Characteristics

The flow characteristics of the micro-ramp were investigated in detail using various flow diagnostics method. This covers the region upstream, represented by the area ahead of the micro-ramp leading-edge, on the top surface of micro-ramp and also the most important region that is the downstream wake. The use of different flow diagnostics tool enables for the detail flow characteristics to be captured and certainly relying only on a limited number of methods will not be sufficient in constructing a comprehensive understanding of the complex flow physics especially in the downstream region.

The use of qualitative techniques for example the oil-flow and oil-dot visualisation enabled the visualisation of the detail structures and sizes of the vortices that were created by the micro-ramps. This includes the primary vortices and also the other three pairs of the secondary vortices. Oil-dot technique revealed the information on the directions of the flow which helped to obtain the direction of motion of the counter-rotating vortices. The PSP images recorded the high and low pressure regions on the surface of the micro-ramps that are associated

with the flow physics happening on the model.

Both qualitative and quantitative results were obtained from the infrared thermography technique. The trajectory of the primary vortices was identified from the high temperature streaks in the downstream region. Finally, from the PIV results, the flow organisation in the downstream region was able to be understood. Results revealed the existence of the streamwise primary vortices and also the formation of the K-H vortices. This proves to be a good validation of the previous experimental and numerical investigations conducted by other researchers.

### 7.1.2 Micro-Ramp for SBLI Control

The results focused on the potential of micro-ramps in controlling SBLI and also the effects of different micro-ramp sizes and configurations. There are a number of parameters of improvements there were investigated as a whole. The first was the upstream pressure influence. The location where the pressure rise begins in the upstream of the shock impingement location were identified using various experimental flow diagnostics. From Kulite surface pressure measurements, the controlled case clearly shows a delay in the starting location of the pressure rise in comparison with the uncontrolled interaction. However this parameter was not clearly visible from the PSP surface pressure measurements due to the minor experimental error as explained previously. The second parameter that was investigated was the pressure gradient during the reattachment process. From both the Kulite and PSP surface pressure measurements, the increased in the pressure gradients for the controlled case were substantial compared to the baseline case. This was followed by higher pressure peaks in the pressure signals. These factors again are clear indications of significant improvements of the separation region induced by SBLI phenomenon.

The topology of the separation region also was investigated as a part of the study. In the baseline case, a totally separated flow was observed, with clear structures of the separation line, reversed flow region and also the reattachment line. The typical topology of the separation region (nodal points) was also successfully captured in the oil-flow experiments. With the presence of the micro-ramps, a significant alteration of the separation region was observed in the case of MR80 array (the largest micro-ramp). Narrow regions of attached flow can be observed passing through the separated region. The region of reversed flow was also minimise. Although the other models did not show any major alterations towards

the separation region, however, distortions of the separation line could be clearly visualised.

Although from the results it can be seen that the separation region caused by SBLI was not able to be eliminated entirely, however these findings are essential not only moving towards a better control method, but also in contributing the understanding of the physics of the separated boundary layer caused by SBLI. The improvements carried out by micro-ramps were significant compared to the baseline case.

### 7.1.3 Micro-Ramp Optimisation

The outcome from the optimisation studies of micro-ramp at Mach 5 is presented. The main experimental technique used in this study is colour schlieren. Nevertheless, the results of other experimental techniques such as oil-flow visualisation and pressure sensitive paints are also included as the supporting results.

The final optimal ratio of the micro-ramp design configuration are as the followings; $h/\delta_0 = 1.33, s/h = 0.27$ and $c/h = 2.63$. From this optimal configuration, the optimum response approximated ($\delta_{rel}$) from the RSM modelling is 0.67. which results in a substantial improvement of 33% compared to the uncontrolled case. For $\delta_0$, the individual optimised values of the variables $h, c$ and $s$ are 7.45, 19.58 and 2.00mm, respectively.

From the 3-D plot of the data scatter, the influence of each variables on the overall performance can be observed. Larger height, median chord length and smallest spanwise spacings are proved to be the best combination that should be considered in designing micro-ramps for hypersonic SBLI control.

## 7.2 Future Recommendations

Future work and recommendations include the following:

### 7.2.1 Micro-Ramp Flow Characteristics

1. Use a material with a much lower thermal conductivity such as Polyether ether ketone (PEEK) for infrared experiments. The thermal conductivity of PEEK is 0.25W/m.K so that more detail information of the flow characteristics especially the smaller secondary vortices could be revealed.

2. Conduct experiments with stereo PIV to obtain the cross-section profile of the vortex structures travelling downstream.

3. Conduct experiments with tomographic PIV system to obtain detail 3D information of the vortex structures generated by the micro-ramp in the downstream region.

4. Conduct PIV experiments with the laser sheet parallel to the wall at an elevated angle to obtain the lift-off angle of the K-H vortices.

### 7.2.2 Micro-Ramp for SBLI Control

1. Conduct investigation of various experimental techniques with a constant distance between the micro-ramp and the shock impingement location, $X_L$.

2. Conduct PIV experiments for the shock-impingement case to measure the accurate thickness of the separation bubble and also its upstream extent.

3. Conduct experiments with liquid crystal technique for the measurement of skin friction coefficient so that more information on the separation region could be obtained.

### 7.2.3 Micro-Ramp Optimisation

1. The parasitic drag of each model should be included as another output variable so that the optimal configuration takes into consideration the drag induced by each model.

2. Another reliable technique to estimate the thickness of the separation bubble for the optimisation study is by using PIV. The lasersheet should be positioned normal to the streamwise axis.

# Bibliography


[1] H. Babinsky and J.K. Harvey. *Shock Wave-Boundary-Layer Interactions*. Cambridge University Press, 2011.

[2] J. D. Anderson. *Hypersonic and High-Temperature Gas Dynamics*. McGraw-Hills New York, 2006.

[3] H. Babinsky, Y. Li, and C.W. Pitt Ford. Microramp Control of Supersonic Oblique Shock-Wave/Boundary-Layer Interactions. *AIAA*, 47(3):668–675, 2009.

[4] A.J. Smits and J.P. Dussauge. Turbulent Shear Layers in Supersonic Flow. 2nd ed. *Springer, Berlin*, 2006.

[5] J.M. Delery and J.P. Dussauge. Some Physical Aspects of Shock-Wave/Boundary Layer Interactions. *Shock Waves*, 19:453–468, 2009.

[6] S.A. Prince, M. Vannahme, and J.L. Stollery. Experiments on the hypersonic turbulent shock-wave/boundary layer interaction and the effects of surface roughness. *The Aeronautical Journal*, pages 177–184, 2005.

[7] J.C. Robinet and G. Casalis. Shock oscillations in a diffuser modelled by a selective noise amplification. *AIAA Journal*, 4:1–8, 1999.

[8] F.E.C. Culick and T. Rogers. The response of normal shocks in diffusers. *AIAA Journal*, 10:1382–90, 1983.

[9] J.M. Delery. Shock/Wave/Turbulent Boundary Layer Interaction and its Control. *Progr. Aerosp. Sci*, pages 209–280, 1985.

[10] L.C. Squire. Further experimental investigations of compressible turbulent boundar layers with air injection. R&M No. 3627, Aeronautical Research Council, 1970.

[11] G.D. Thomas. Compressible turbulent boundary layers with combined air injection and pressure gradient. R&M No. 3779, Aeronautical Research Council, 1976.

[12] G.R. Inger. Transonic shock/turbulent boundary layer interaction with suction or blowing. AIAA Paper No. 72-74.

[13] G.R. Inger and S. Zee. Transonic shock-wave/turbulent boundary layer interaction with suction or blowing. *J. Aircr.*, 15(11):750–754, 1978.

[14] D.C. Mathews. *Shock-wave/boundary layer interactions in two-dimensional and axially-symmetric flows including the influence of suction.* PhD thesis, Univ. of Washington, 1969.

[15] M.K. Fukuda, W.G. Hingst, and E. Reshotko. Control of shock wave-boundary layer interactions by bleed in supersonic mixed compression inlet. Technical Report CR-2595, NASA, 1975.

[16] C. Donaldson. Investigation of a simple device for preventing separation due to shock and boundary layer interaction. RM L 50 B 02a, NACA, 1950.

[17] D.C. McCormick. Shock/boundary-layer interaction control with vortex generators and passive cavity. *AIAA Journal*, 31:91–96, 1993.

[18] A. Hamed and J.S. Shang. Survey and assessment of validation data base for shock-wave boundary layer interactions in supersonic inlets. *AIAA*, (89-2939), 1989.

[19] S. Lee. *Large Eddy Simulation of Shock Boundary Layer Interaction Control Using Micro-Vortex Generators.* PhD thesis, University of Illinois at Urbana -Champaign, 2009.

[20] T.J. Benson, W.J. Chyu, M.J Rimlinger, T.I-P Shih, and B.P. Willis. Structure of shock wave/boundary-layer interactions with bleed though rows of circular holes. *AIAA*, (97-0508), 1997.

[21] J.P. Bodner, D.O. Davis, I. Greber, and W.R. Hingst. Experimental investigation of the effect of a single bleed hole on a supersonic turbulent boundary-layer. *AIAA*, (96-2797), 1996.

[22] E. Loth. Smart mesoflaps for control of shock boundary layer interactions. AIAA Paper 2000-2476, 2000.

[23] S. Ragunathan. Passive control of shock-boundary layer interaction. *Progress in Aerospace Sciences*, 25(3):271–96, 1988.

[24] S.S. Collis, R.D. Joslin, A. Seifert, and V. Theofilis. Issues in active flow control:theory, control, simulation, and experiment. *Progress in Aerospace Sciences*, 40(4-5):237–89, 2004.

[25] P.R. Ashill, J.L. Fulker, and K.C. Hackett. A review of recent developments in flow control. *Aeronautical Journal*, 109(1095):205–32, 2005.

[26] J.C. Lin. Review of research on low-profile vortex generators to control boundary layer separation. *Progress in Aerospace Science 38*, pages 389–420, 2002.

[27] A.M. Kuethe. Effect of streamwise vortices on wake properties associated with sound generation. *J. of Aircraft*, 9(10 715-9), 1972.

[28] D.M. Rao and T.T. Kariya. Boundary-layer submerged vortex generators for separation control-an exploratory study. *AIAA*, (88-3546), 1988.

[29] P.L. Blinde, R.A. Humble, B.W. van Oudheusden, and F. Scarano. Effects of micro-ramps on a shock wave/turbulent boundary layer interaction. *Shock Waves*, 19(6):507–520, 2009.

[30] Q. Li and C. Liu. Les for supersonic ramp control flow using mvg at m = 2.5 and $re_\theta = 1440$. Number AIAA 2010-0592, 2010.

[31] B.H. Anderson, J. Tinapple, and L. Surber. Optimal control of shock wave turbulent boundary layer interactions using micro-array actuation. *AIAA*, (2006-3197), 2006.

[32] S. Ghosh, J. Choi, and J.R. Edwards. Numerical simulations of effects of micro vortex generators using immersed-boundary methods. *AIAA*, 48(1):92–103, 2010.

[33] M.D. Atkinson. Numerical investigation of a super-sonic inlet using bleed and micro-ramps to control shock-wave/boundary layer interactions. Number AIAA 2007-24, 2007.

[34] S.M. Hirt and B.H. Anderson. Experimental investigation of the application of microramp flow control to an oblique shock interaction. AIAA Paper 2009-919, 2009.

[35] R. Sedney. A survey of the effects of small protuberances on boundary-layer flows. *AIAA Journal*, 11(6):782–792, 1973.

[36] F. K. Lu, A.J. Pierce, Y. Shih, C. Liu, and Q. Li. Experimental and numerical study of flow topology past micro vortex generators. Number AIAA 2010-4463, 2010.

[37] T. Herges, E. Kroeker, G. Elliott, and C. Dutton. Micro-ramp flow control of normal shock/boundary layer interactions. Number AIAA 2009-920, 2009.

[38] K.C. Wang. Boundary layer over a blunt body at high incidence with an open-type of separation. *Proc. R. Soc. Lond. A*, 340:33–55, 1974.

[39] H. Holden and H. Babinsky. Effect of microvortex generators on separated normal shock/boundary layer interactions. *Journal of Aircraft*, 44(1):170–174, January-February 2007.

[40] H. Babinsky and H. Ogawa. Sbli control for wings and inlets. *AIAA Journal*, 18(2):89–96, 2008.

[41] C.D. Tomkins and R.J. Adrian. Spanwise structure and scale growth in turbulent boundary layers. *Journal of Fluid Mechanics*, 490:37–74, 2003.

[42] H.M Tufo, P.F. Fischer, M.E. Papka, and M. Szymansky. Hairpin vortex formation, a case study for unsteady visualization. In *41st CUG Conference, Minneapolis, MN*, 1999.

[43] M.S. Acerlar and C.R. Smith. A study of hairpin vortices in a laminar boundary layer. part 1. hairpin vortices generated by a hemisphere protuberance. *Journal of Fluid Mechanics*, 175:1–41, 1987.

[44] A.J. Pierce, F.K. Lu, D.S. Bryant, and Y. Shih. New developments in surface oil flow visualization. AIAA Paper 2010-4353, 2010.

[45] T. Herges, E. Kroeker, G. Elliott, and C. Dutton. Microramp flow control of normal shock/boundary-layer interactions. *AIAA Journal*, 48(11):2529–42, 2010.

[46] F.K. Lu, Q. Li, and C. Liu. Microvortex generators in high-speed flow. *Progress in Aerospace Sciences*, 53:30–45, 2012.

[47] Q. Li and C. Liu. Numerical investigations on the effects of the declining angle of the trailing-edge of mvg. Number AIAA 2010-0714, 2010.

[48] Q. Li and C. Liu. Implicit les for supersonic microramp vortex generator: new discoveries and new mechanisms. *Modelling and Simulation in Engineering*, (934982), 2011.

[49] T.T. Lim. On the role of kelvin-helmholtz-like instability in the formation of turbulent vortex rings. *Fluid Dynamics Research*, 21:47–56, 1996.

[50] Z. Sun, F.F.J. Schrijer, F. Scarano, and B.W. van Oudheusden. Piv investigation of the 3d instantaneous flow organisation behind a micro-ramp in a supersonic boundary layer. In *International Symposium on Shock Waves 28*, July 2011.

[51] Z. Sun, F.F.J. Schrijer, F. Scarano, and B.W. van Oudheusden. The three-dimensional flow organization past a micro-ramp in a supersonic boundary layer. *Phys. Fluids*, 24(055105), 2012.

[52] Q. Li and C. Liu. Declining angle effects of the trailing edge of a microramp vortex generator. *Journal of Aircraft*, 47(6):2086–95, 2010.

[53] W. Bo, L. Weidong, Z. Yuxin, F. Xiaoqiang, and W. Chao. Experimental investigation of the micro-ramp based shock wave and turbulent boundary layer interaction control. *Phys. Fluids*, 24(055110), 2012.

[54] F.K. Lu, A.J. Pierce, and Y. Shih. Experimental study of near wake of micro vortex generators in supersonic flow. Number 2010-4623. AIAA, 2010.

[55] P.R. Ashill, J.L. Fulker, and K.C. Hackett. Research at dera on sub-boundary layer vortex-generators (sbvgs). AIAA Paper 2001-0887, 2001.

[56] M.C. Galbraith, P.D. Orkwis, and J.A. Benek. Multi-row micro-ramp actuators for shock wave boundary-layer interaction control. AIAA Paper 2009-321, 2009.

[57] R. Bur, D. Coponet, and Y. Carpels. Separation control by vortex generator devices in a transonic channel flow. *Shock Waves*, 19:521–530, 2009.

[58] S. Lee, M.K. Goettke, E. Loth, J. Tinapple, and J. Benek. Microramps upstream of an oblique-shock/boundary-layer interaction. *AIAA Journal*, 48:104–118, 2010.

[59] R.A. Humble, F. Scarano, and B.W. van Oudheusden. Particle image velocimetry measurements of a shock wave/turbulent boundary layer interaction. *Exp. Fluids*, 43:173–183, 2007.

[60] E. Erdem. *Active flow control studies at Mach 5: measurement and computation.* PhD thesis, University of Manchester, 2011.

[61] J.A. Edwards and D.M. Orchard. Calibration of the dera hsst mach 5 nozzle with centre body. AIAA Paper 2000-0294, 2000.

[62] A. Pope. *High-Speed Wind Tunnel Testing.* John Wiley & Sons, 1978.

[63] J.R. Moffat. Describing the uncertainties in experimental results. *Exp. Thermal Fluid Sci.*, 1(1):3–17, 1988.

[64] L. Yang. *Flow control using energy deposition at Mach 5.* PhD thesis, University of Manchester, 2012.

[65] E. Erdem. *Active Flow Control Studies in Hypersonic Flows, 2nd Year PhD Progress Report.* University of Manchester, 2009.

[66] L.C. Squire. The motion of a thin oil sheet under the boundary layer on a body. Technical report, AGARDograph, AGARD AG-70, 1962.

[67] L. Yang. *Experimental Studies of Energy Deposition Effect on the Hypersonic Flow Structure. First Year PhD Progress Report.* University of Manchester, 2009.

[68] F.F.F. Schrijer, F. Scarano, W. Pudheusden, and W.J. Bannink. Experiments on hypersonic roughness induced transition by means of infrared thermography. In *Proceedings of the Fifth European Symposium on Aerothermodynamics for Space Vehicles, Cologne, Germany*, pages 255–260, 2005.

[69] V. M. Bazovkin, A. P. Kovchavtsev, G. L. Kuryshev, A. A. Maslov, S. G. Mironov, D. V. Khotyanovsky, A. V. Tsarenko, and I.S. Tsyryulnikov. Effect

of streamwise structures on heat transfer in a hypersonic flow in a compression corner. *Journal of Applied Mechanics and Technical Physics*, 50(4):638–645, 2009.

[70] F.F. Schrijer, F. Scarano, and B.W. van Oudheusden. Transient heat transfer measurements on a blunted cone-flare model in a short duration hypersonic facility using quantitative infrared thermography. In *7th Int Symp on Fluid Control, Measurement and Visualization*, 2004.

[71] E. Schulein. Skin-friction and heat flux measurements in shock/boundary-layer interaction flows. *AIAA Journal*, 44:1732–1741, 2006.

[72] T. Liu and J.P. Sullivan. *Pressure and Temperature Sensitive Paints*. Springer-Verlag Berlin Heidelberg, 2005.

[73] H. Zare-Behtash, N. Gongora-Orozco, K. Kontis, and S.J. Holder. Application of novel pressure-sensitive paint formulations for the surface flow mapping of high-speed jets. *J. Experimental Thermal and Fluid Science*, 33(5):852–864, 2009.

[74] B.J. Basu and J. Kamble. Studies on oxygen sensitivity and microstructure of sol-gel based organic-inorganic hybrid coatings doped with platinum porphyrin dye. *J. Sol-Gel Sci Technol*, 52:24–30, 2009.

[75] M. Raffel, C.E. Willert, and K. Kompenhans. *Particle Image Velocimetry: A Practival Guide*. Springer, Berlin, 2007.

[76] G.M. Elfstrom. Turbulent hypersonic flow at a wedge-compression corner. *J. Fluid Mech.*, 53:113–127, 1972.

[77] LaVision. *DaVis 7.2 Software Product-Manual*, 2008.

[78] C.V. Seal, C.R. Smith, O. Akin, and D. Rockwell. Quantitave characteristics of a laminar, unsteady necklace vortex system at a rectangular block-flat plate juncture. *J. Fluid Mech.*, 286:117–135, 1995.

[79] M. Tobak and D.J. Peake. Topology of three-dimensional separated flows. *Annual Review of Fluid Mechanics*, 14:61–85, 1982.

[80] Q. Li, Y. Yan, P. Lu, A. Pierce, C. Liu, and F. Lu. Numerical and experimental studies on the separation topology of the mvg controlled flow at m=2.5. AIAA Paper 2011-72, 2011.

[81] H.D. Taylor. The elimination of diffuser separation by vortex generators. Technical Report No. R-4012-3, United Aircraft Corporation Report, June 1947.

[82] J. Delery. *Shock Wave-Boundary-Layer Interactions*, chapter Physical Introduction, pages 5–86. Cambridge University Press, 2011.

[83] M.A. Vyas, S.M. Hirt, and B.H. Anderson. Experimental investigation of normal shock boundary-layer interaction with hybrid flow control. AIAA Paper 2012-0048, 2012.

[84] D. Schulte, A. Henckels, and U. Wepler. Reduction of shock induced boundary layer separation in hypersonic inlets using bleed. *Aerospace Science and Technology*, (4):231–239, 1998.

[85] J.R. Taylor. *An introduction to error analysis: The study of uncertainties in physical measurements*. University Science Books, 2nd edition, 1939.

[86] R.J. Monaghan. The use of pitot-tubes in the measurement of laminar boundary layers in supersonic flow. 3056, Aeronautical Research Council Reports and Memoranda, 1957.

# Appendices

# Appendix A

# Pitot Rake Design

A micro pitot rake which has the capability of measuring the flow velocity inside the boundary layer was designed and manufactured in the Aero-Physics Laboratory. The main purpose of the rake was to investigate the boundary layer profile of the flow on the flat plate, downstream the micro-ramp. The term 'micro' was introduced due to the fact that the arrays of pitot probes are embedded inside the boundary layer. Definitely the challenge of designing the micro pitot rake comes from the small size of each components that needs to be designed. One of the most important parameter in designing the pitot rake is the ratio $d/\delta$ where $d$ is the outer diameter of the pitot tube and $\delta$ is the boundary layer thickness. Referring to experimental results reviewed by Monaghan [86], if the ratio of $d/\delta$ were less than 0.1, it would give maximum value of 2% error and this is the minimum.

For the current investigation in the HSST tunnel, $\delta$ is 5.89mm at the location of interest. Therefore based on this design requirement, the outer diameter of the probe must be smaller than 0.59mm. It is also decided that the pitot rake will also be used for different models in the HSST and consequently having different $\delta$. So the height of the rake will be extended from just 5.89mm (for the interest of current investigation) up to 28.2mm to accommodate other models. Two different

| Gauge No | 22G | 24G |
|---|---|---|
| Outer Diameter OD (mm) | 0.71 | 0.56 |
| Inner Diameter ID (mm) | 0.41 | 0.30 |
| Wall Thickness (mm) | 0.15 | 0.13 |

Table A.1: Characteristics of stainless steel pitot probe used in the micro pitot rake.

pitot tube sizes were used for this purpose and the characteristics are listed in Table A.1. The rake can be divided into two segments, the lower half (housing 12 22G probes) and the upper half (housing 9 24G probes) as shown in Figure A.1.

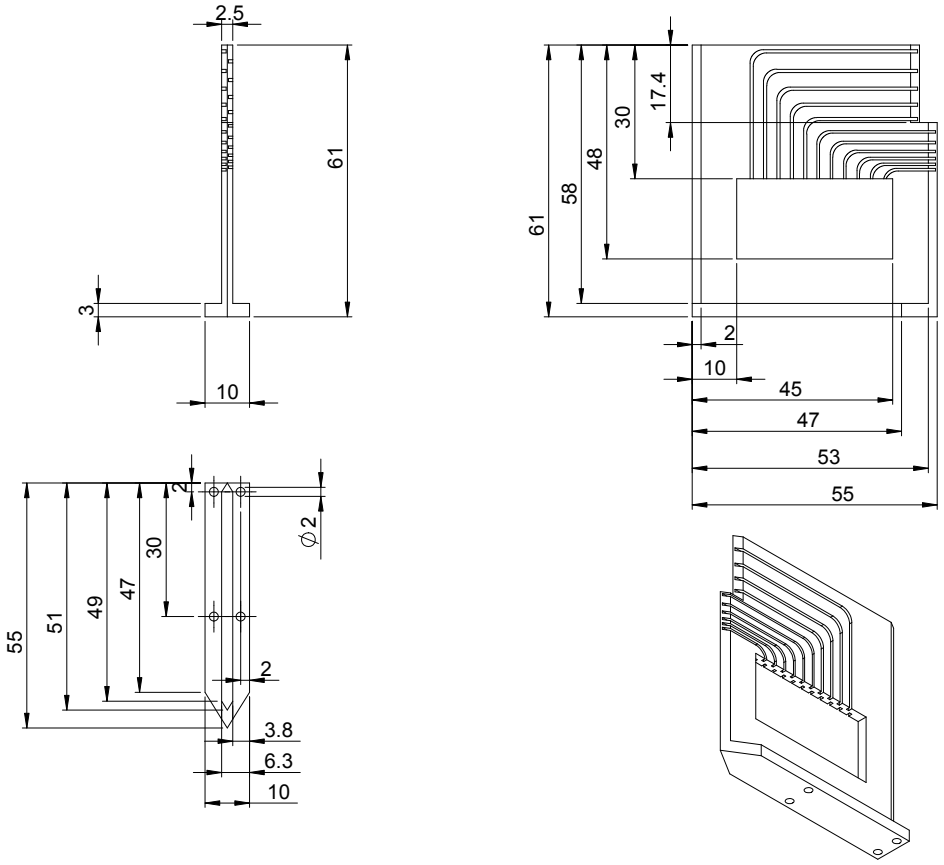


Figure A.1: Technical drawing of the micro pitot rake main body.

A square area was removed from the mid-part of the body to allow access to the bottom end of the pitot probes. The pitot probes will be connected to Kulite pressure transducers using Tygon® Masterflex® tubes. There are two types of tubes used (to fit into two types of pitot probe as in Table A.1) and the characteristics are listed in Table A.2. The assembly of the pitot rake will ensure that the lowest probe is exactly at the wall of the flat plate. The position of the other probes with respect to the wall is listed in Table A.3.

The micro pitot rake is mounted on several rails that enable 3-directional movements; streamwise, spanwise and vertical. The design of the rails is shown in Figure A.2. The streamwise rail is screwed to the base of the wind tunnel, at the rear of the flat plate mounts. The positioning of the micro pitot rake inside

| Tygon® Serial No | EW-95609-18 | EW-95609-24 |
|---|---|---|
| Outer Diameter OD (mm) | 2.69 | 2.44 |
| Inner Diameter ID (mm) | 0.76 | 0.51 |

Table A.2: Characteristics of Tygon® Masterflex® tubes used in the micro pitot rake.

| Probe | Pitot Size | Wall Distance (mm) |
|---|---|---|
| 1 | 24G | 0.0 |
| 2 | 24G | 2.3 |
| 3 | 24G | 3.0 |
| 4 | 24G | 3.6 |
| 5 | 24G | 4.2 |
| 6 | 24G | 5.0 |
| 7 | 24G | 5.8 |
| 8 | 24G | 6.8 |
| 9 | 24G | 7.8 |
| 10 | 24G | 9.0 |
| 11 | 24G | 10.2 |
| 12 | 24G | 11.6 |
| 13 | 22G | 13.0 |
| 14 | 22G | 14.6 |
| 15 | 22G | 16.2 |
| 16 | 22G | 18.0 |
| 17 | 22G | 19.8 |
| 18 | 22G | 21.8 |
| 19 | 22G | 23.8 |
| 20 | 22G | 26.0 |
| 21 | 22G | 28.2 |

Table A.3: Distance of pitot tubes from the wall.

the test section can be visualised from the final assembly shown in Figure A.3.

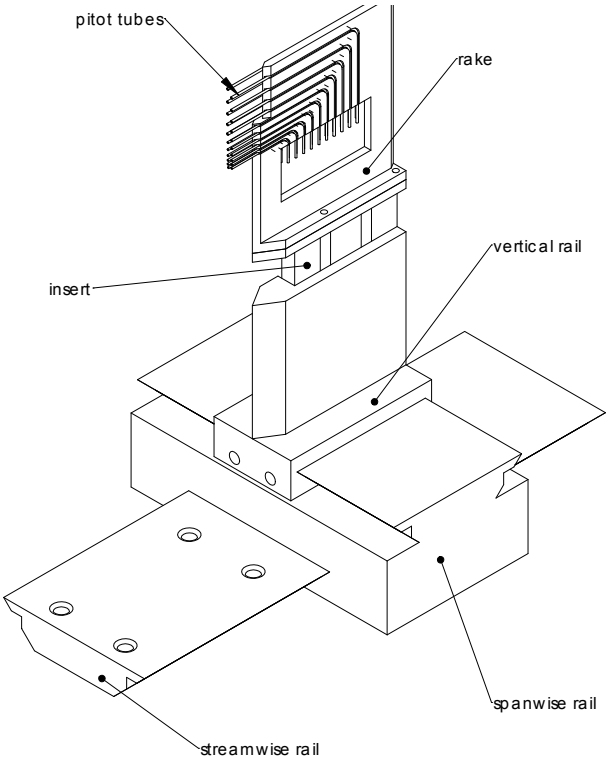


Figure A.2: CAD drawing of the assembly of the micro pitot rake together with rails.

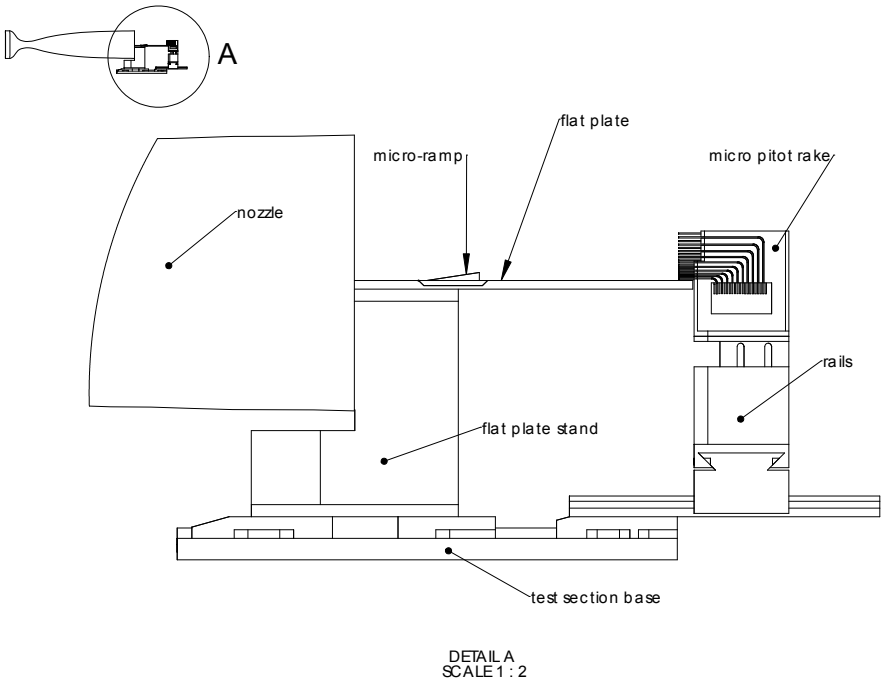


Figure A.3: CAD drawing of the final assembly of micro pitot rake with model inside the test section.

# Appendix B

# Various Designs

This section provides the designs of the various models and setups manufactured throughout the current study.

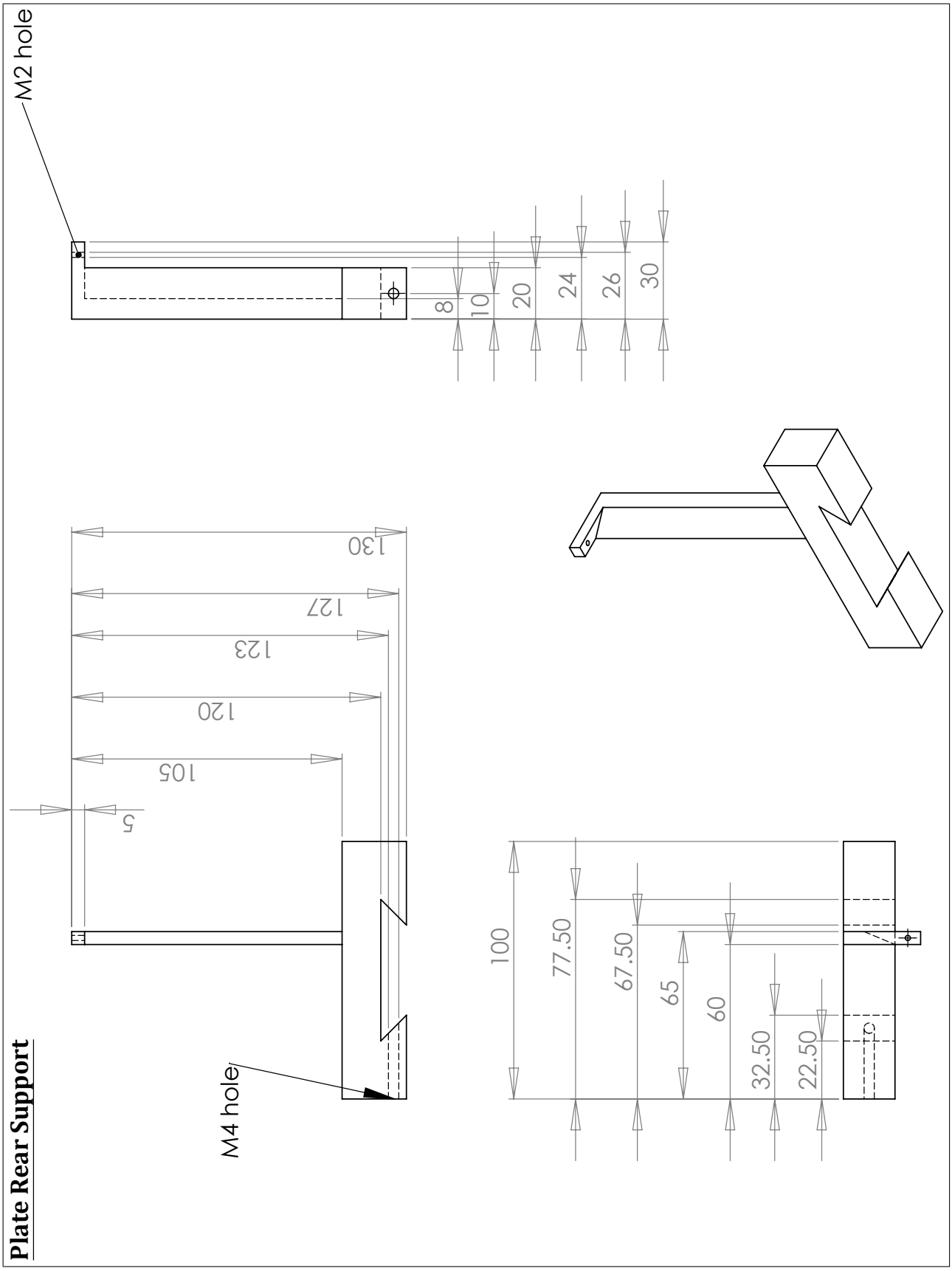


Figure B.1: CAD drawing of flat plate rear support.

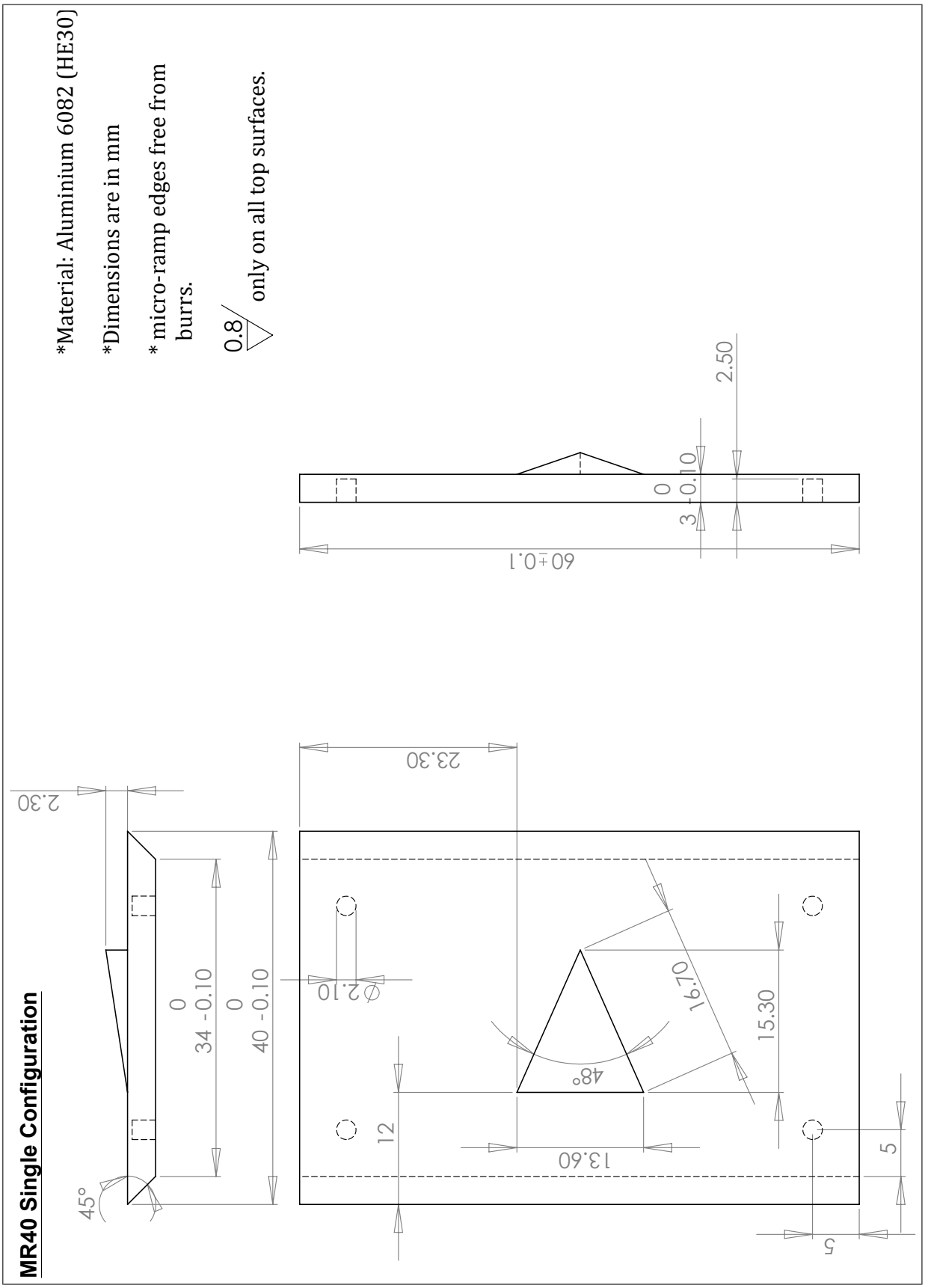


Figure B.2: CAD drawing of MR40 single configuration.

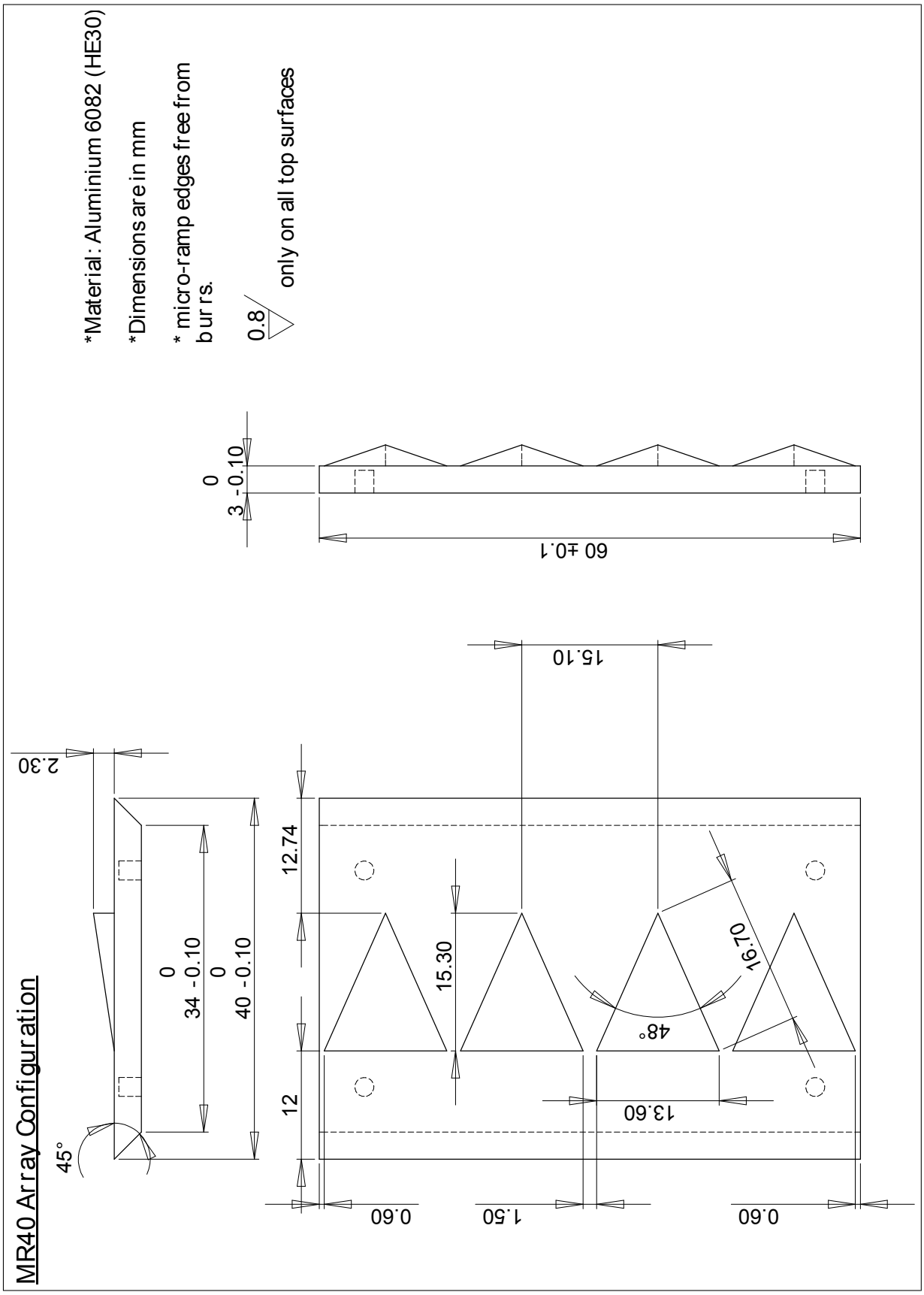


Figure B.3: CAD drawing of MR40 array configuration.

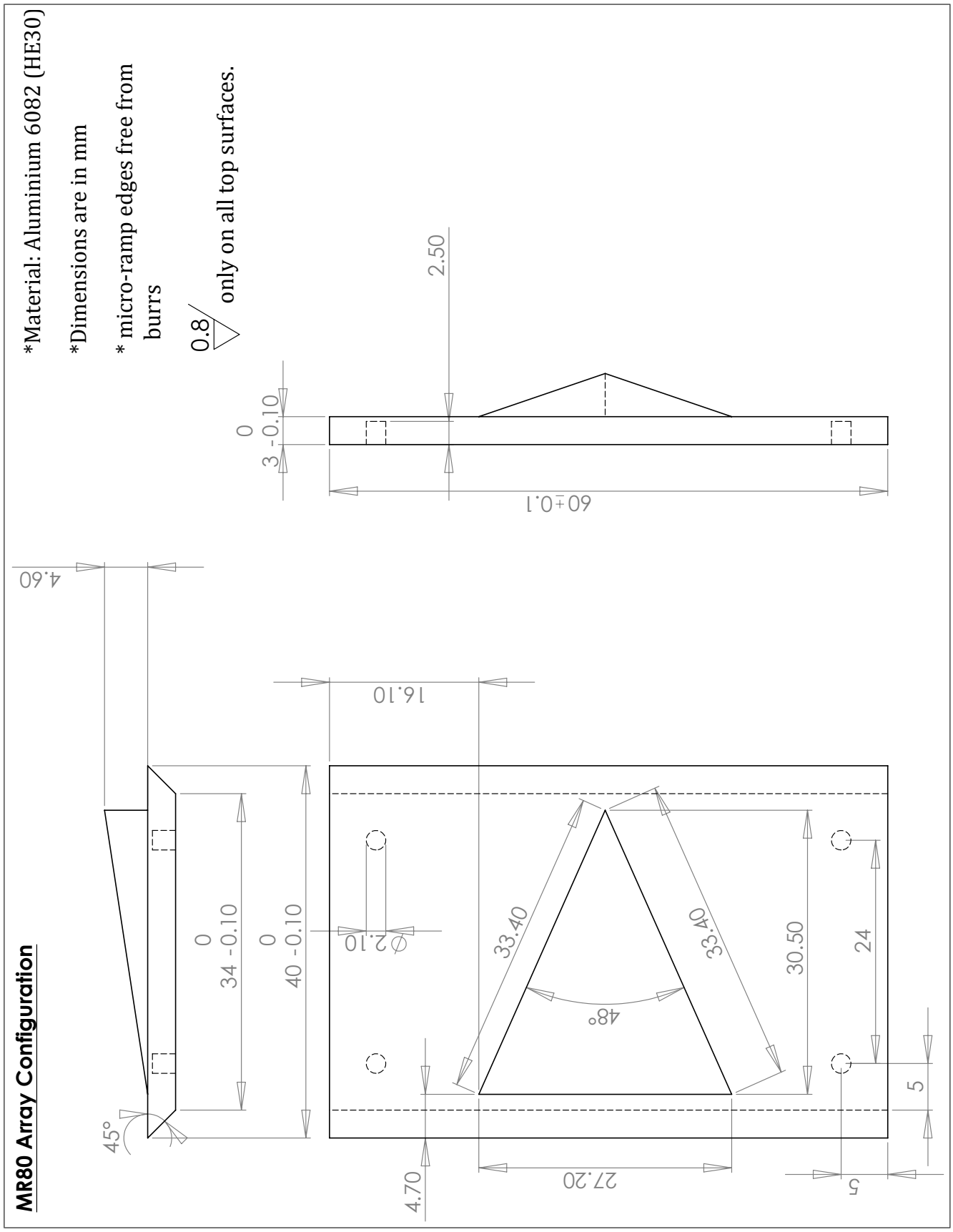


Figure B.4: CAD drawing of MR80 single configuration.

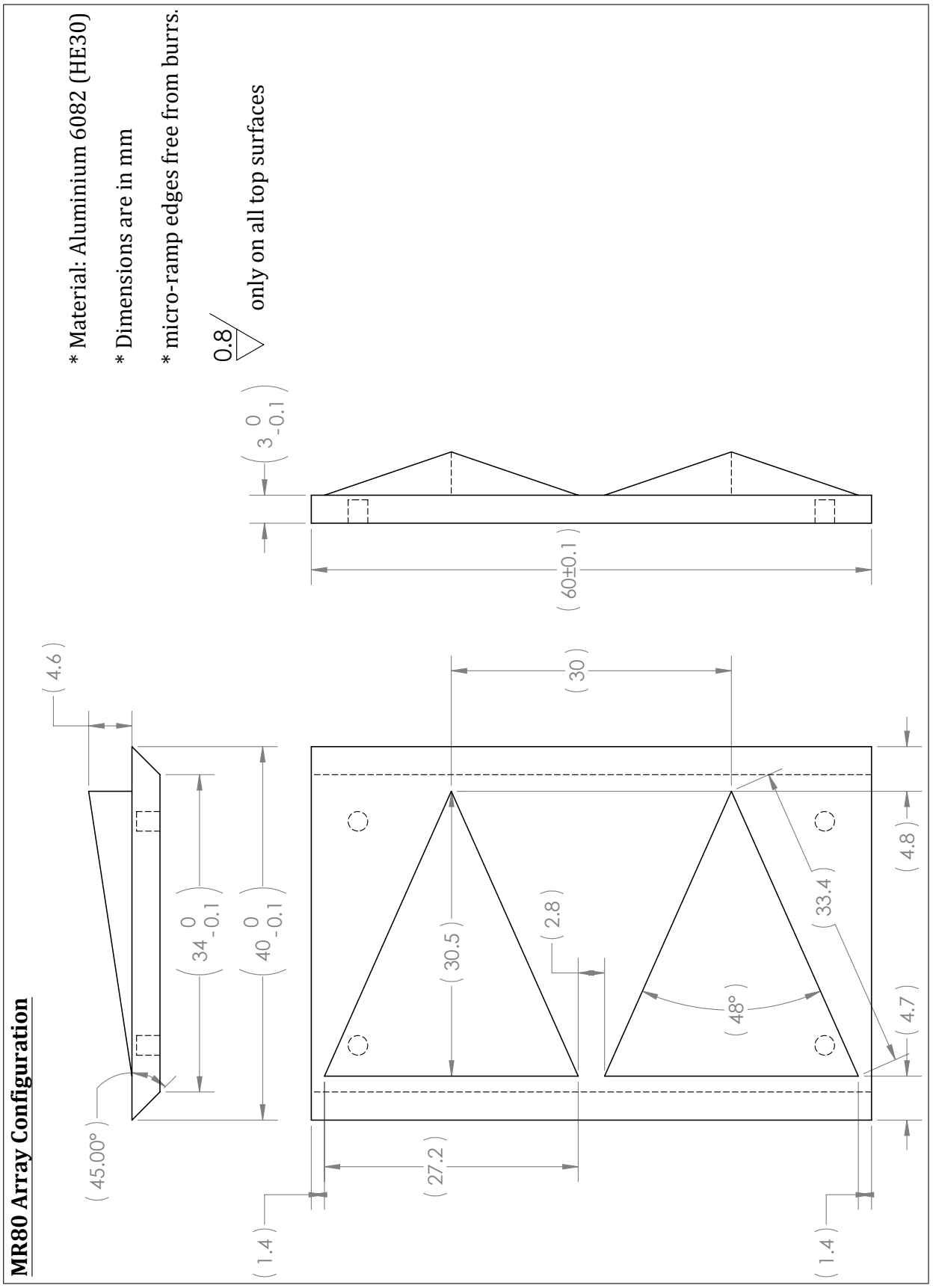


Figure B.5: CAD drawing of MR80 array configuration.

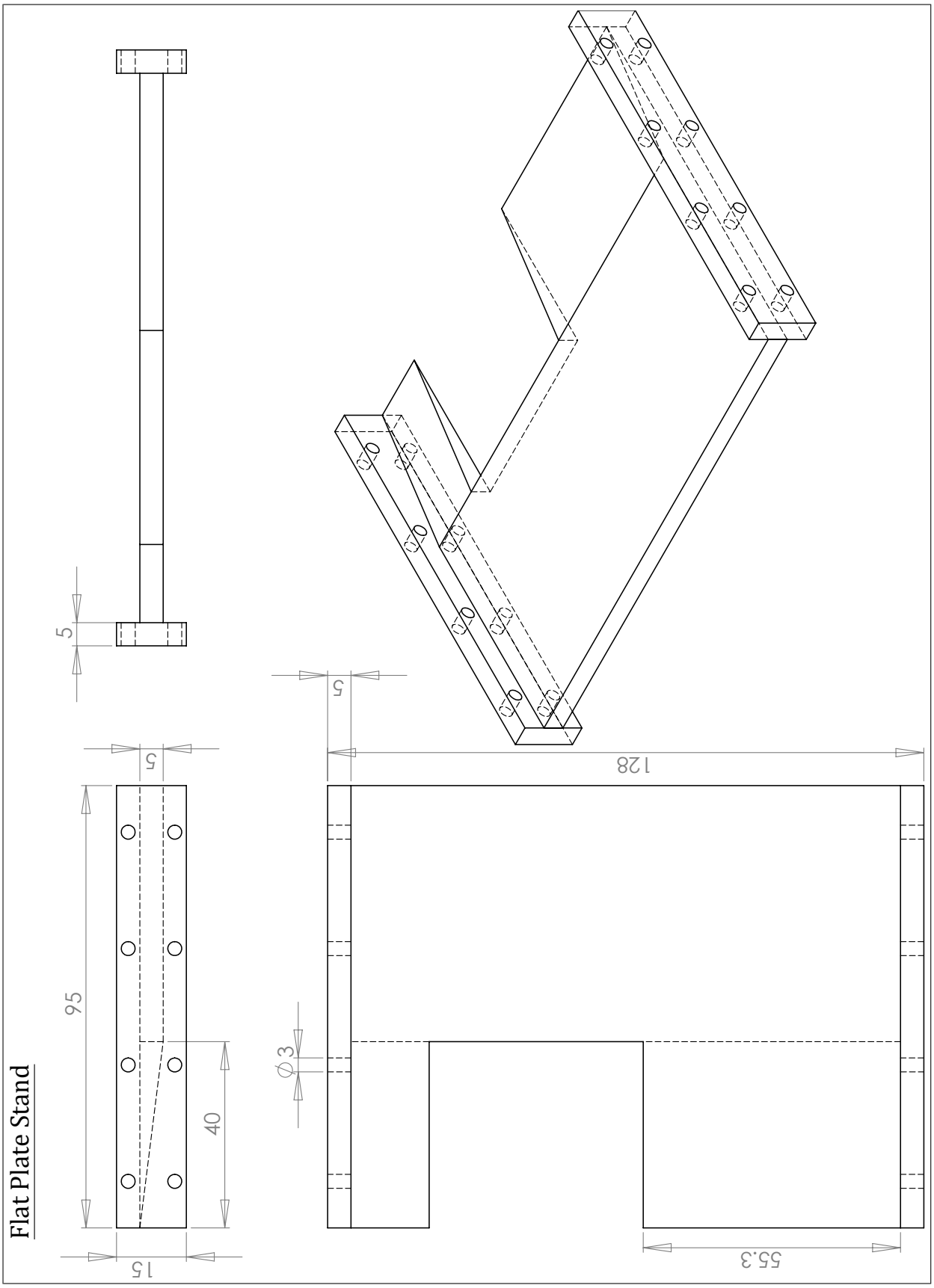


Figure B.6: CAD drawing of vertical stand for flat plate mounted inside test section.

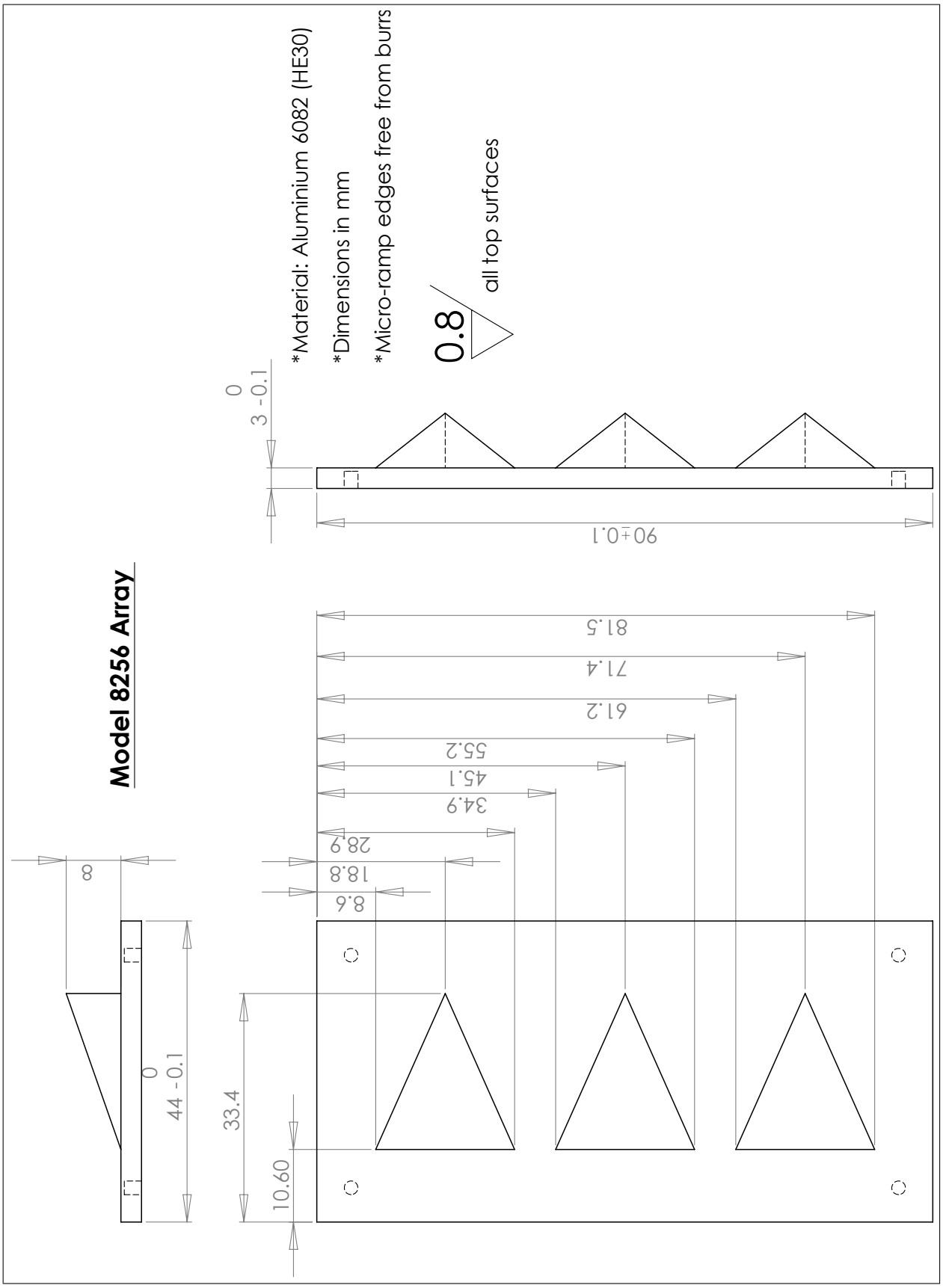


Figure B.7: CAD drawing of optimisation model 8256.

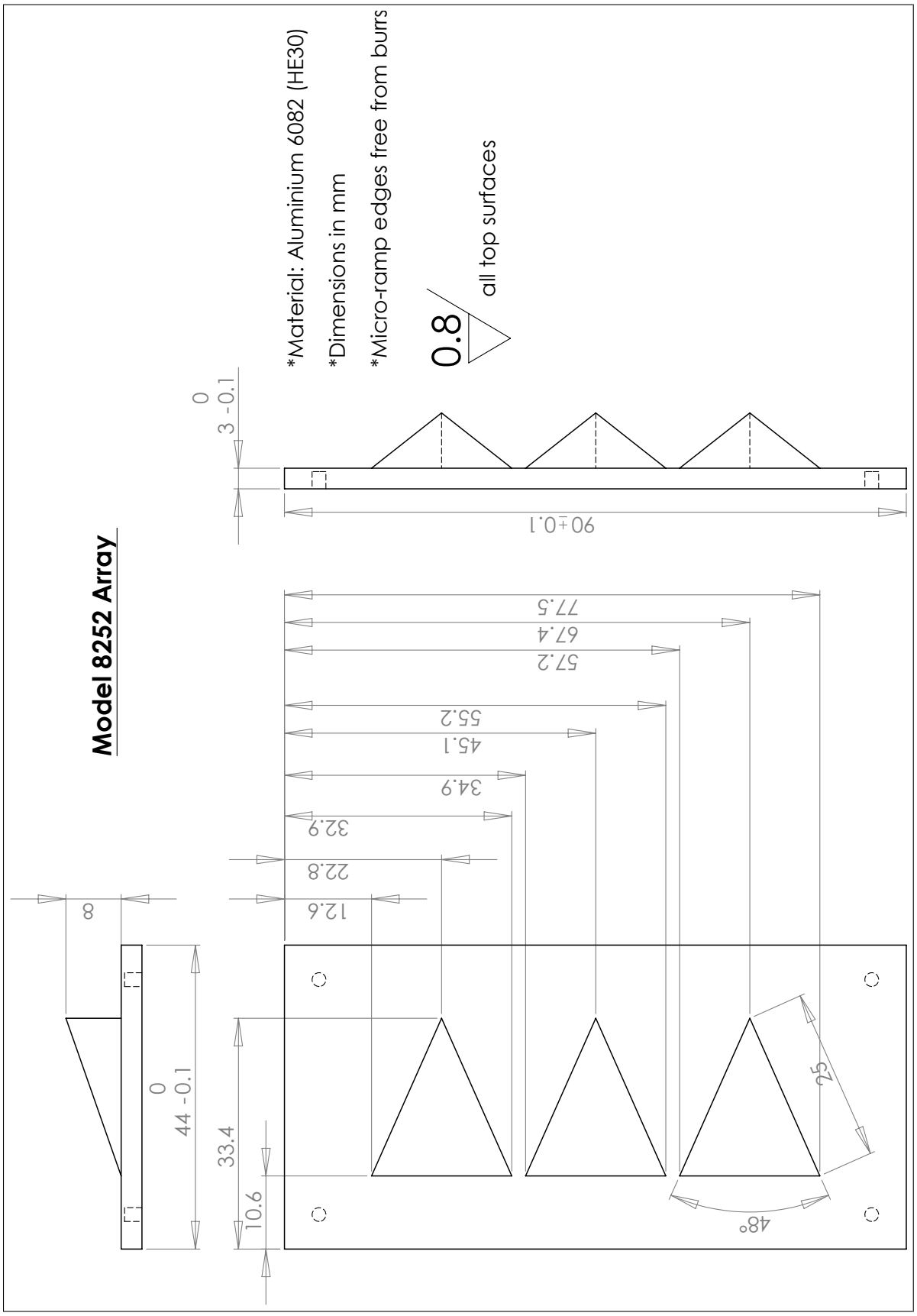


Figure B.8: CAD drawing of optimisation model 8252.

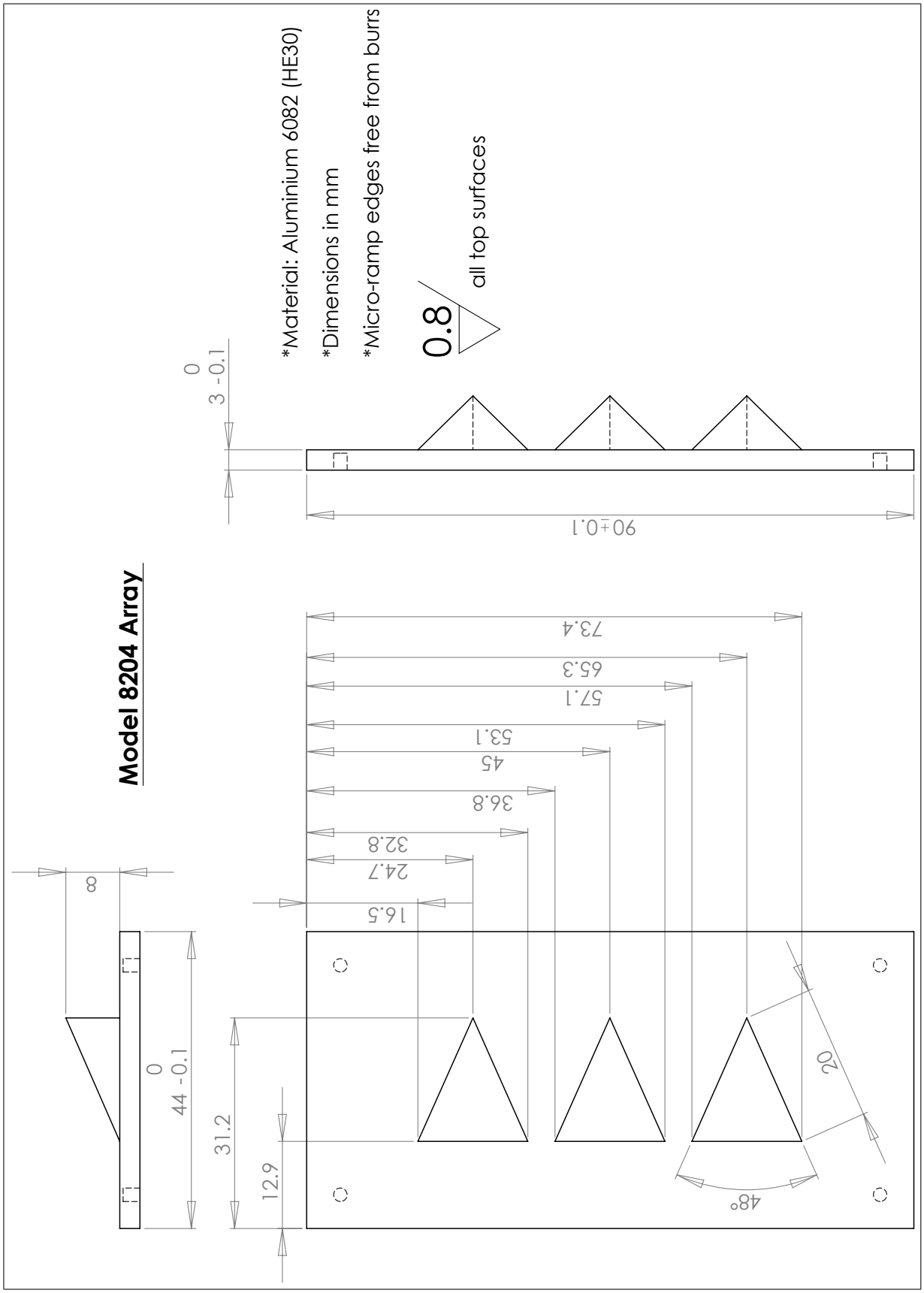


Figure B.9: CAD drawing of optimisation model 8204.

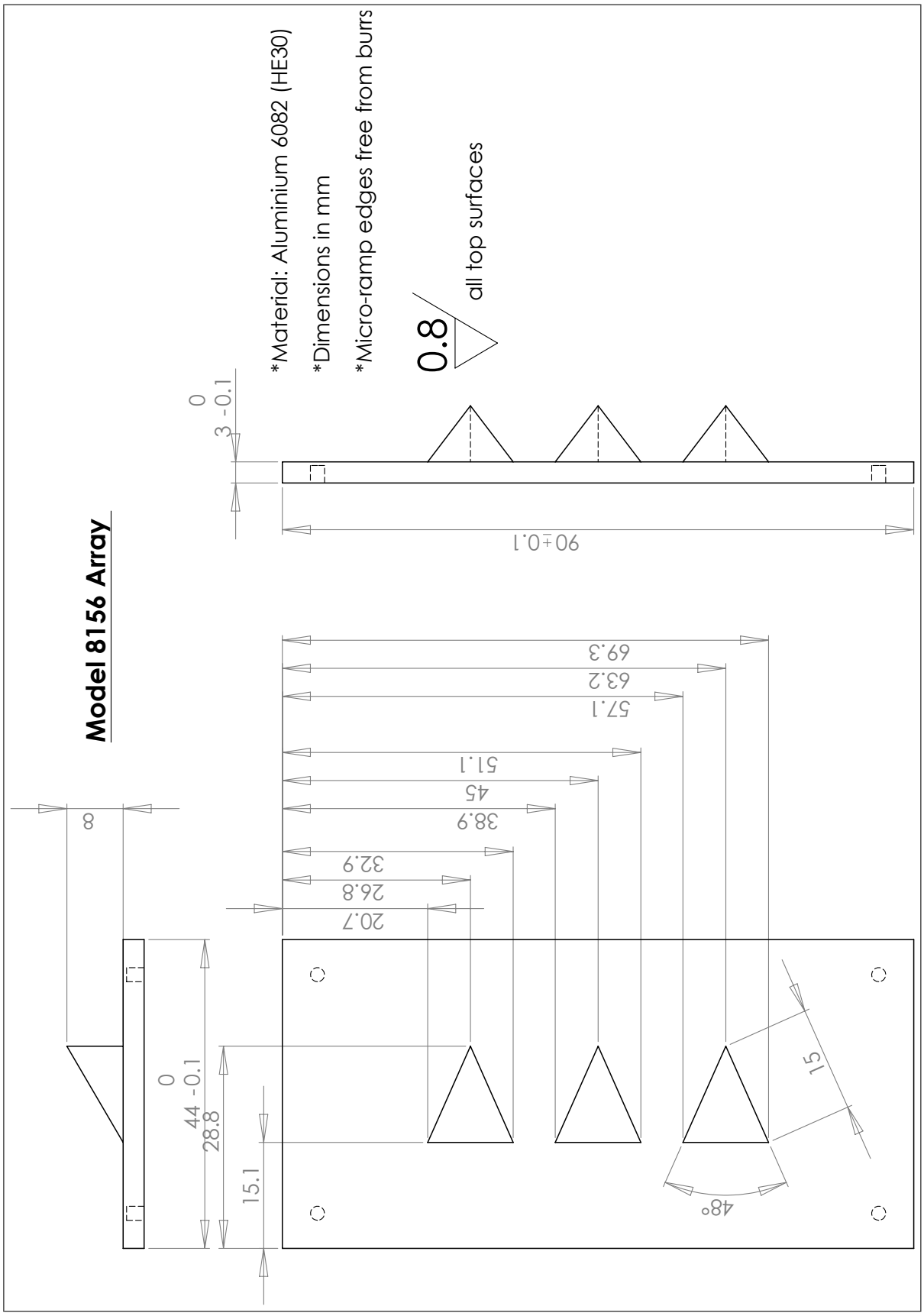


Figure B.10: CAD drawing of optimisation model 8156.

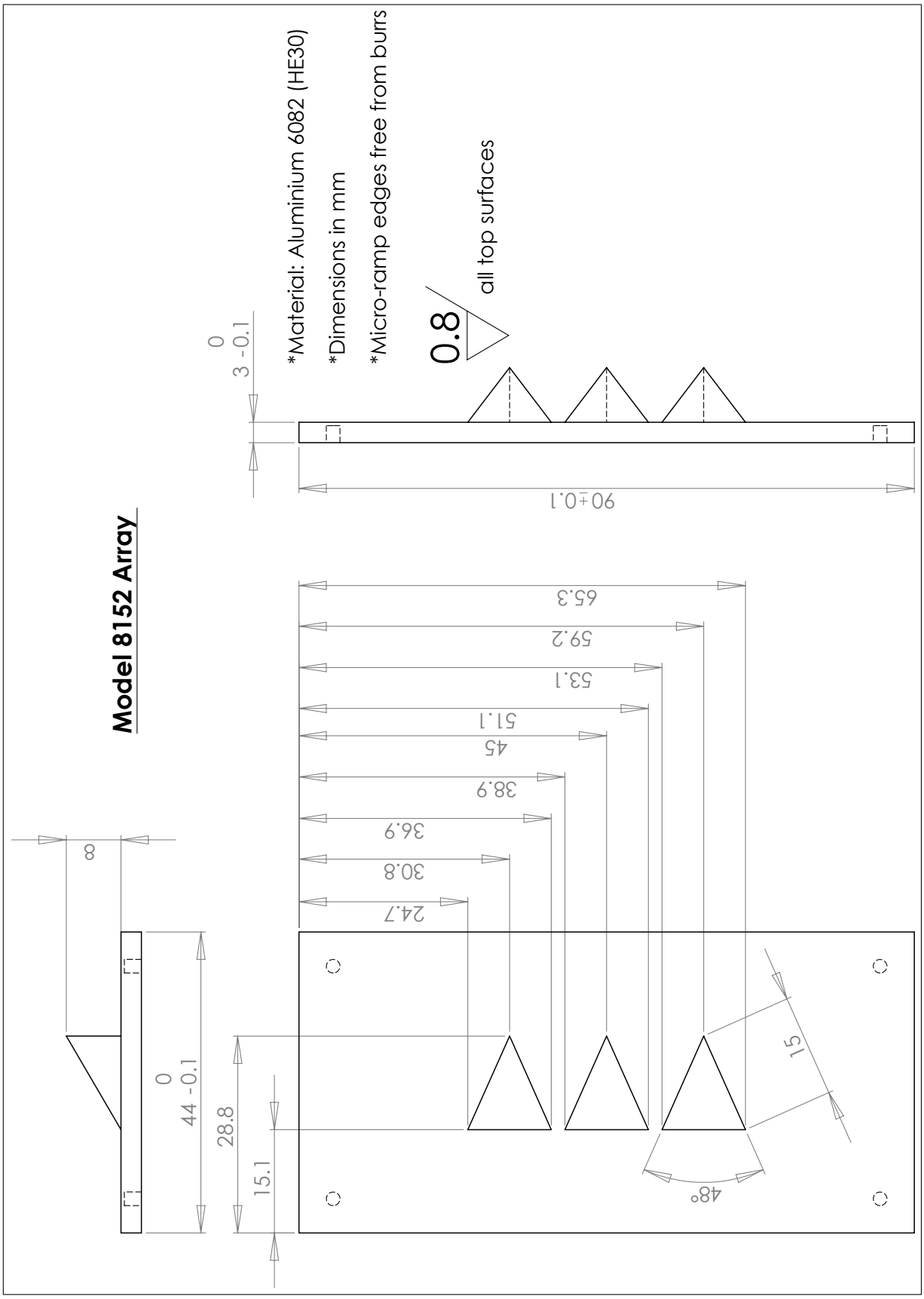


Figure B.11: CAD drawing of optimisation model 8152.

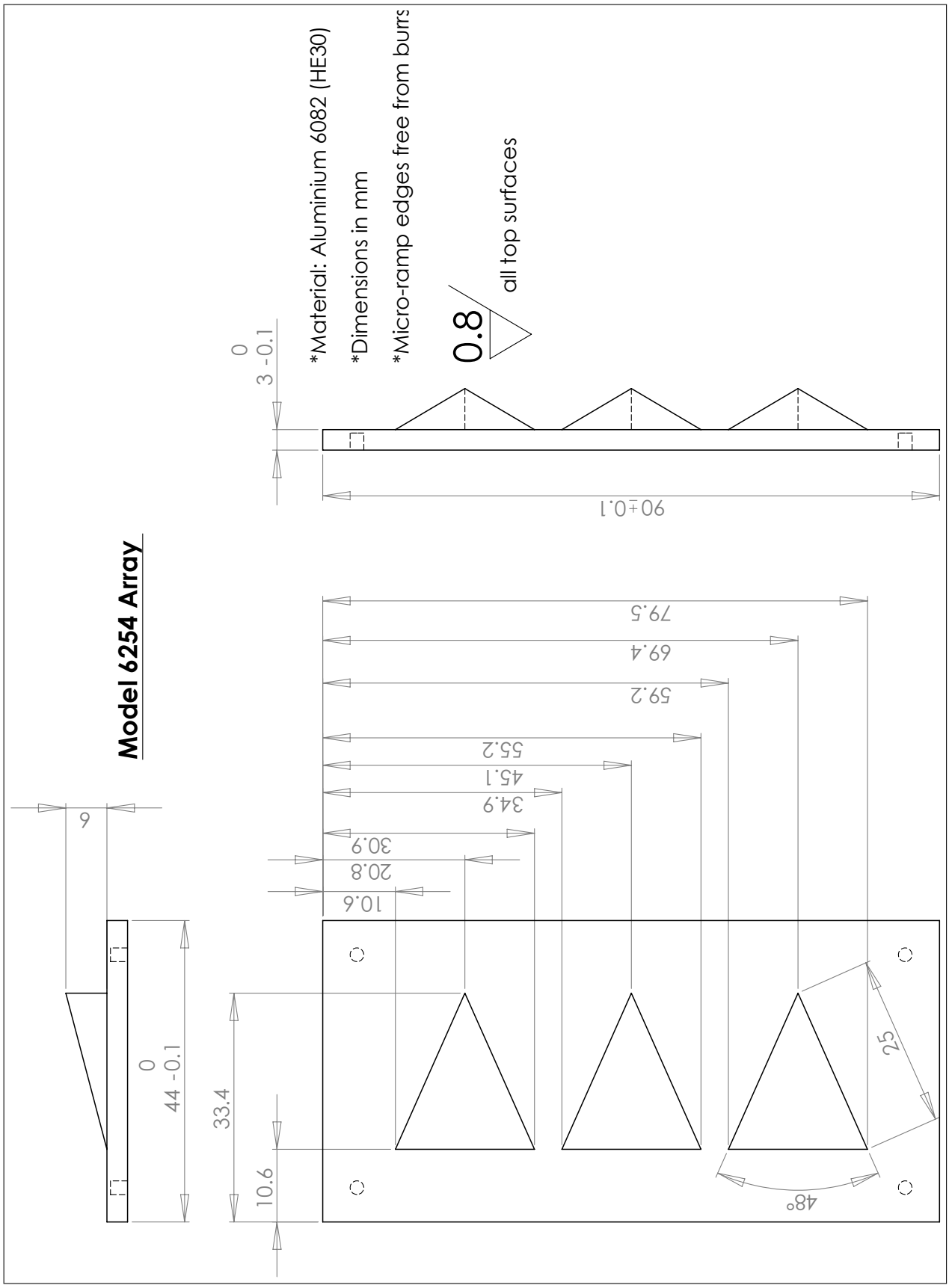


Figure B.12: CAD drawing of optimisation model 6254.

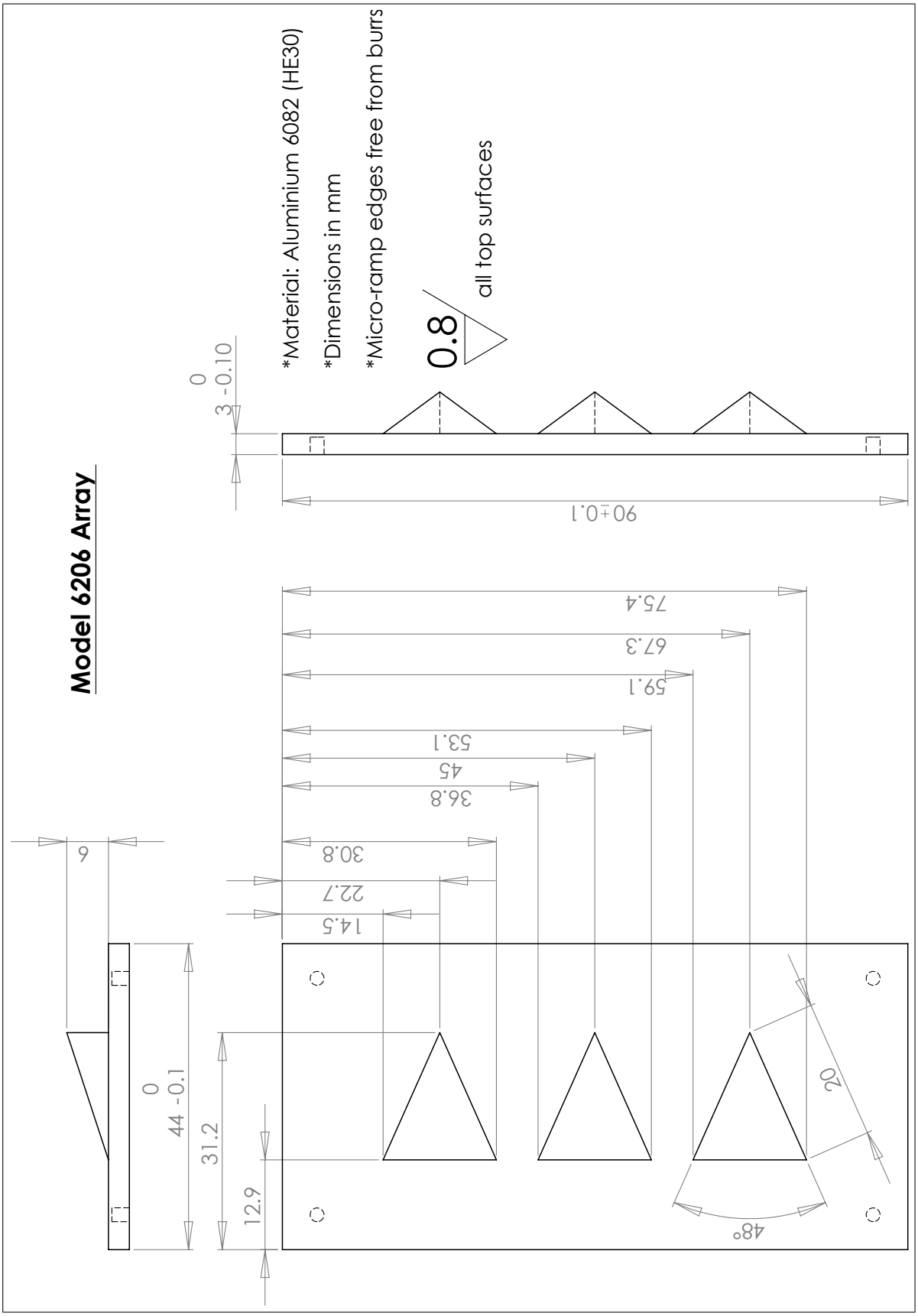


Figure B.13: CAD drawing of optimisation model 6206.

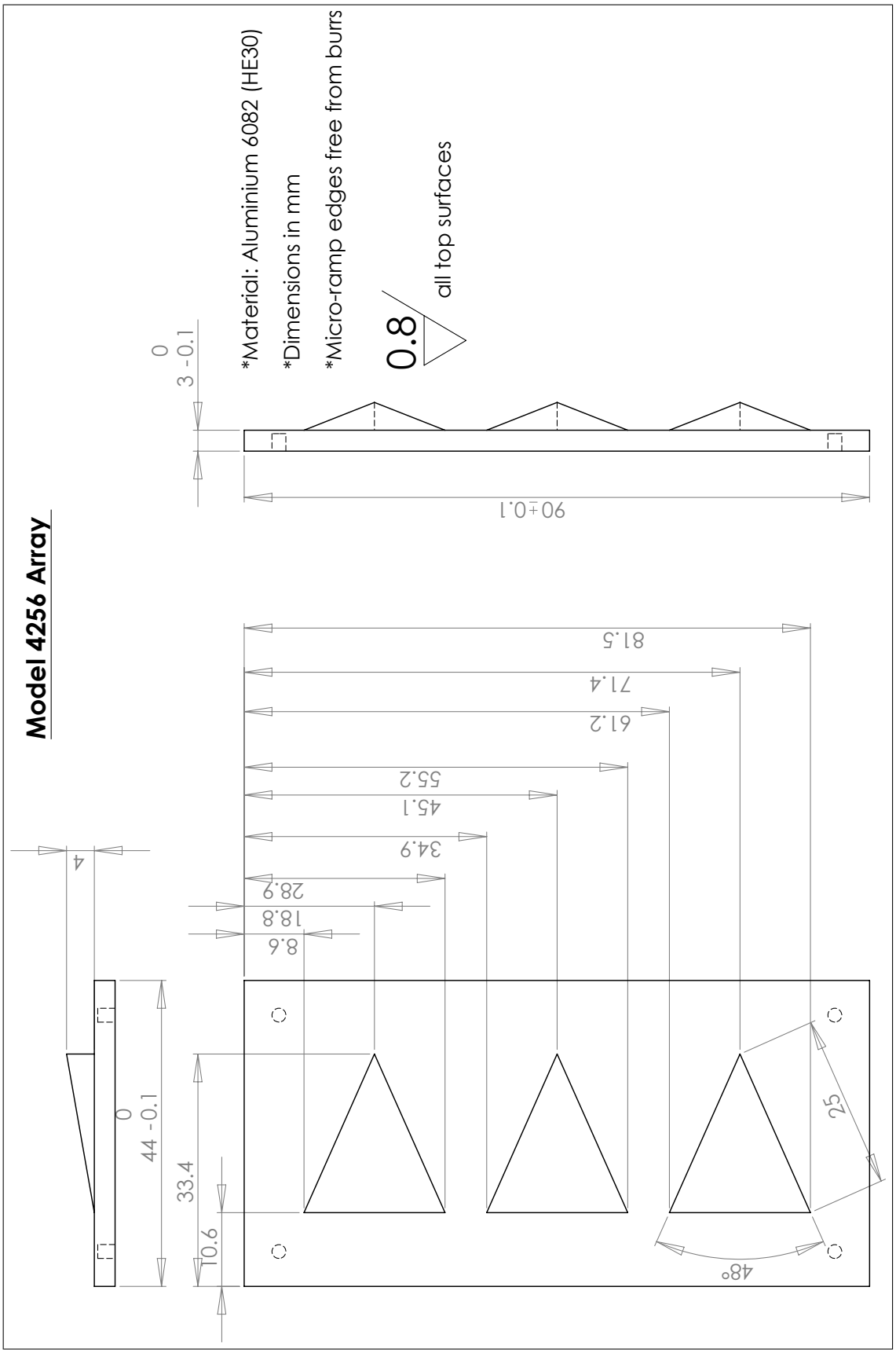


Figure B.14: CAD drawing of optimisation model 4256.

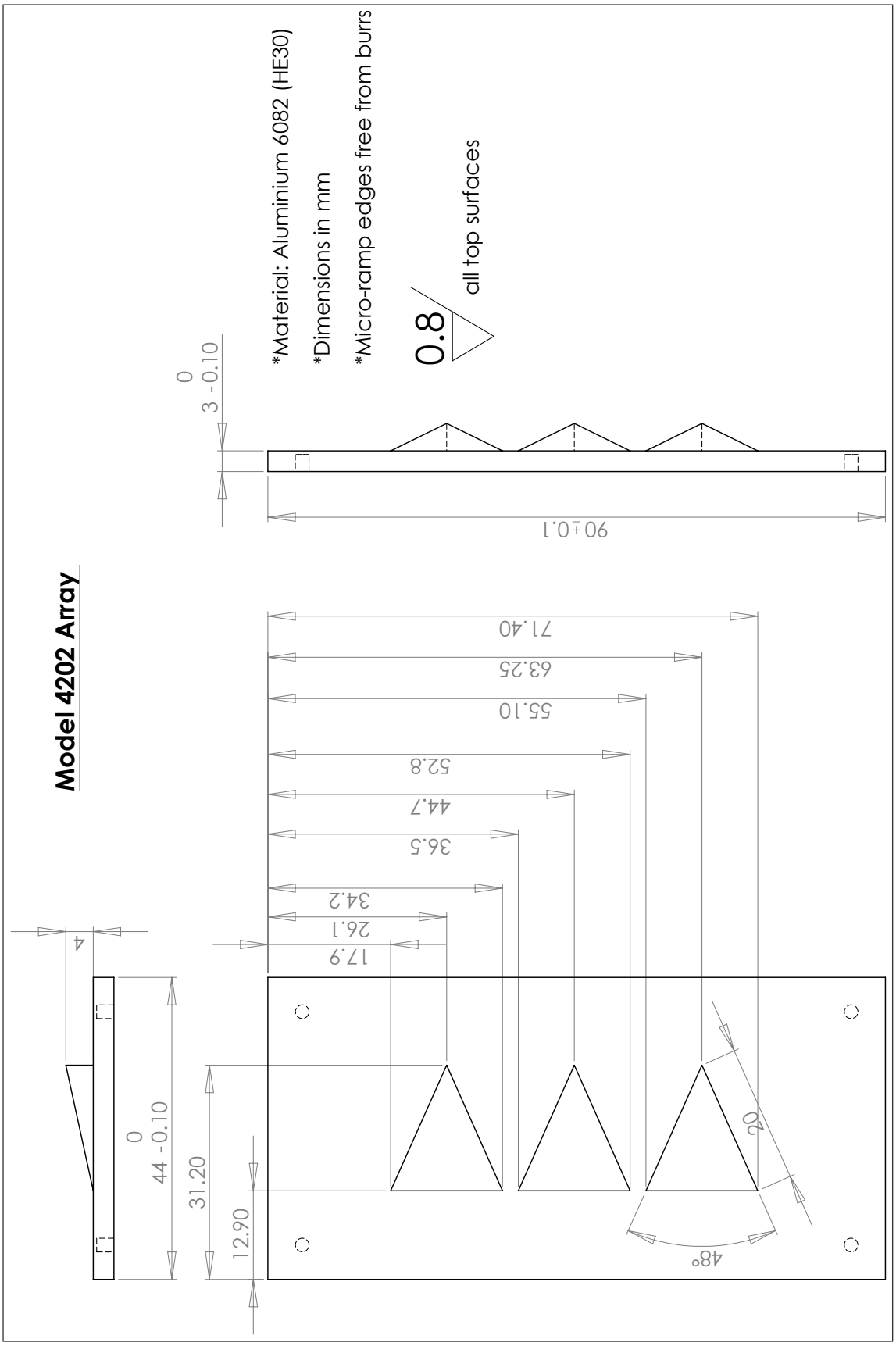


Figure B.15: CAD drawing of optimisation model 4202.

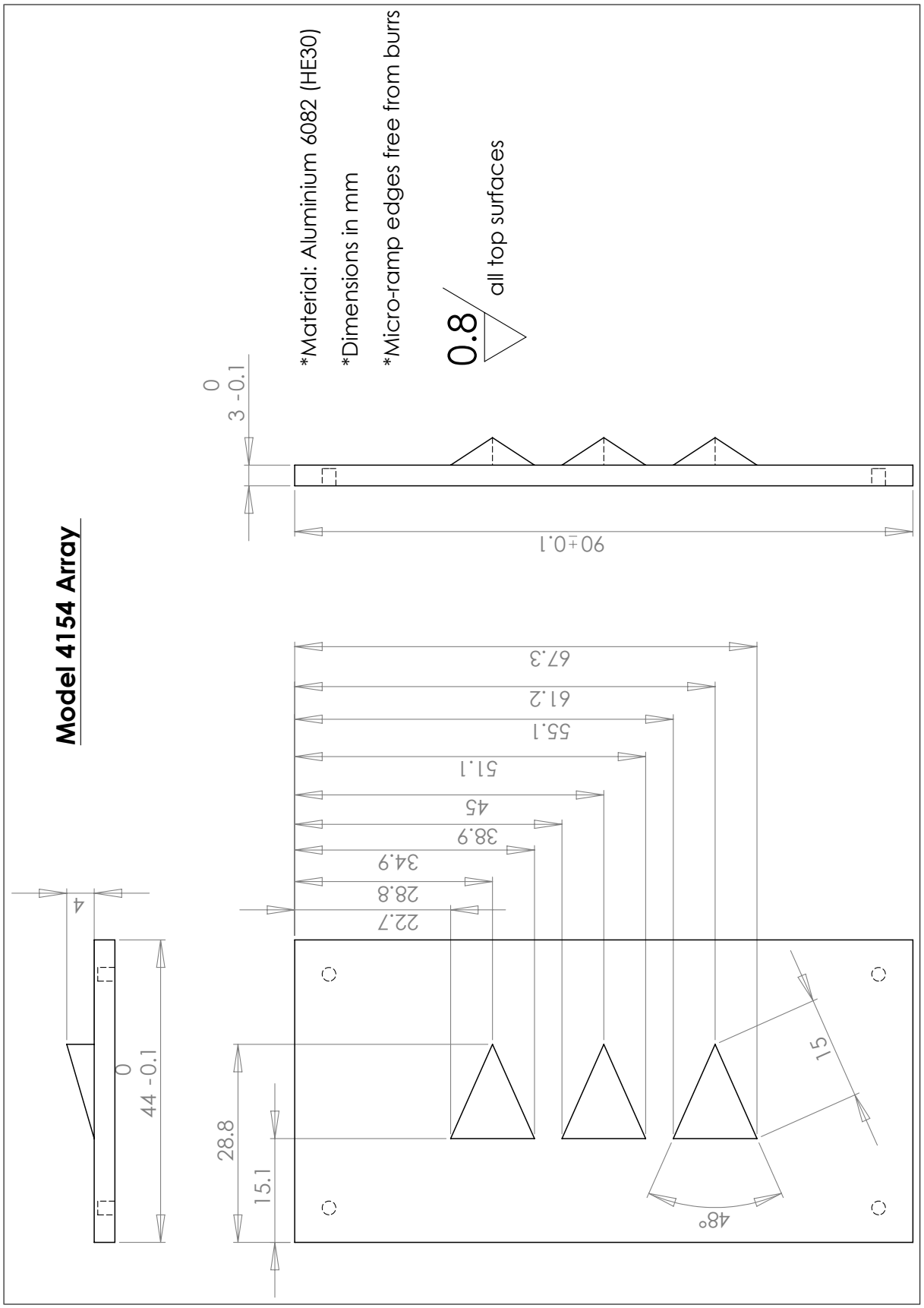


Figure B.16: CAD drawing of optimisation model 4154.